BIS(PHOSPHINE) PLATINUM(II) SUPRAMOLECULAR COORDINATION COMPLEXES: A STRUCTURAL, PHOTOPHYSICAL, AND COMPUTATIONAL INVESTIGATION

by

James Bryant Pollock

A dissertation submitted to the faculty of
The University of Utah
in partial fulfillment of the requirements for the degree of

Doctor of Philosophy

Department of Chemistry

The University of Utah

May 2014

The University of Utah Graduate School

STATEMENT OF DISSERTATION APPROVAL

The following faculty members served as the supervisory committee chair and members for the dissertation of James Bryant Pollock .

Dates at right indicate the members' approval of the dissertation.

Peter J. Stang	, Chair	11/12/2013 Date Approved
Janis Louie	, Member	11/12/2013 Date Approved
Haitao Ji	, Member	11/12/2013 Date Approved
Bethany Buck-Koehntop	, Member	11/12/2013 Date Approved
Ling Zang	, Member	11/12/2013 Date Approved

The dissertation has also been approved by Cynthia J. Burrows

Chair of the Department of Chemistry

and by David B. Kieda, Dean of The Graduate School.

ABSTRACT

Since pioneering work in the early 1990s, supramolecular coordination complexes (SCCs) have attracted attention from researchers because complex, discrete systems can readily be self-assembled from highly symmetric, complementary molecular subunits that display a high-level of modularity and fidelity. Classically, in the Stang lab, SCCs are synthesized using bis(phosphine) platinum(II) metal nodes and rigid, pyridyl-based organic ligands. Flexible SCCs, however, are very rare and are attractive for host-guest applications due to their fluid cavity sizes and shapes that can autonomously adapt to specific substrates. Utilizing a recently developed methodology for constructing multicomponent SCCs that exploits the electronic nature of the coordinating ligands and platinum metal center, a series of 2D and 3D flexible SCCs was synthesized using alkyl-based dicarboxylic acid and pyridyl-based subunits. Moreover, insight into the thermodynamic preference for the coordination motif was explored using computational methods, which was determined to originate from orbital effects in conjunction with shape complementarily and electrostatic effects.

Platinum-based SCCs have been proposed for photon emitting applications due to the assumed preservation of the unique and attractive photophysical properties of known mononuclear platinum complexes. However, reports on the photophysical properties of platinum-based SCCs are rare, which severely limits

their utility. Platinum-based SCCs that display low-energy optical transitions, have high quantum yields, and are readily tunable need to be developed if they are to fulfill this purpose. Using aniline-based core scaffolds, a series of SCCs that emit above 500 nm with quantum yields greater than 20% was synthesized. Utilizing computational methods, the nature of the observed optical transitions were determined to arise from π-type molecular orbitals that are ligand centered with modest contributions from the metal center. By functionalizing the periphery of the aniline-based core scaffolds, a series of rhomboidal-shaped SCCs was synthesized that emit from 500 to 600 nm. The low-energy absorption and emission band of the series was determined to be tunable in a predictive manner by altering the Hammett sigma constants of the peripheral functional group.

This dissertation describes our investigations into bis(phosphine) platinum(II) SCCs. In particular, a novel series of flexible SCCs was synthesized and the construction method was probed via molecular modeling. Then, a series of highly emissive endohedral functionalized SCCs is described, characterized, and investigated via computational methods. Model complexes were synthesized to further investigate the nature of the observed photophysical properties for the endohedral functionalized SCCs, culminating with a series of SCCs that displayed facile tunability in a predictive manner with emission profiles spanning the visible spectral window.

TABLE OF CONTENTS

LIST OF ABBREVIATIONS

Å – angstroms
k – rate constant
λ – wavelength
Φ – quantum yield
τ_o – excited-state lifetime
2D – two dimensional
3D – three dimensional
AO – atomic orbitals
B3LYP – Becke-three parameter Lee-Yang-Par
BODIPY – boron dipyrromethene
$CDCl_3$ – deuterated chloroform
CD_2Cl_2 – deuterated methylene chloride
DCM – dichloromethane
DFT – density functional theory
DMF – dimethylformamide
DMSO – dimethylsulfoxide
ECP – effective core potential
ESI-MS – electrospray ionization mass spectrometry
ESI-ToF – electrospray ionization time of flight
Et_3N – triethylamine
EtOAc – ethyl acetate
FT-ICR – fourier transform ion cyclotron resonance
HF – Hartree-Fock
HOMO – highest occupied molecular orbital
HRMS – high resolution mass spectrometry
Hz – hertz
IC – internal conversion
IEFPCM – integral equation formalism polarizable continuum model
ISC – intersystem crossing
LANL2-DZ – Los Alamos National Laboratory double-zeta
LLCT – ligand to ligand charge transfer
LMCT – ligand to metal charge transfer
LUMO – lowest occupied molecular orbital
M06 – Minnesota 06
m/z – mass/charge
MeOH – methanol
MLCT – metal to ligand charge transfer
MMFF – molecular modeling force field

MO – molecular orbital
MOF – metal-organic framework
mPW1PW91 – modified Purdue-Wang-1-Purdue-Wang-91
NBO – natural bond order
NLO – nonlinear optics
NaOH – sodium hydroxide
nm – nanometers
NMR – nuclear magnetic resonance
NPA – natural population analysis
PCM – polarizable continuum model
PEt_3 – triethyl phosphine
SCC – supramolecular coordination complex
TCSPC – total correlated single photon counting
TD-DFT – time-dependent DFT
ToF – time of flight
UV/Vis – ultraviolet/visible

LIST OF TABLES

LIST OF SCHEMES

ACKNOWLEDGEMENTS

Foremost, I would like to express my sincerest gratitude to my Ph.D. advisor, Professor Peter J. Stang. His guidance and support allowed the research described in the following dissertation to be possible. His enthusiasm for science and mentoring has served as a model that I will try to emulate in my academic pursuits. Moreover, the freedom and latitude he allowed afforded me a unique opportunity to explore my chemical interests, driving my passion to utilize chemistry as a tool for impacting or making a difference in the world.

My committee members Professor Janis Louie, Professor Bethany Buck-Koehntop, Professor Haitao Ji, and Professor Ling Zang deserve special thanks for their guidance, support, and thoughtful suggestions.

I would also like to extend a heartfelt thanks to Professor Timothy R. Cook, coworkers, collaborators, and the chemical community at large for insightful discussions and words of encouragement.

Last, but most importantly, I would like to thank my wife and family for their patience and unwavering support during this academic endeavor.

1. INTRODUCTION

1.1 Supramolecular Self-Assembly

Supramolecular chemistry is often referred to as "chemistry beyond the molecule".[1] Meaning, supramolecular chemistry refers to a domain of chemistry where ensembles are constructed from complementary, discrete molecules; self-assembly is the process of two or more complementary molecules interacting and forming a supramolecular complex. The intermolecular forces responsible for the spatial organization of complementary subunits are, typically, noncovalent in nature (e.g., hydrogen bonding, π–π stacking, electrostatic interactions, and van der Waals) and weak (ca. 0.1–30 kcal/mol) when compared to sp^3 carbon–carbon covalent bonds (ca. 80 kcal/mol) that are used in traditional chemistry. Moreover, the reversible nature of these noncovalent intermolecular interactions often allows for the thermodynamic product to be synthesized without requiring stimulus from an outside source. As an example, nature has utilized a billion years of evolution to manipulate and exploit these weak, noncovalent interactions to self-assemble systems with deoxyribonucleic acid (DNA) being the pinnacle for biological systems.

DNA, a macromolecule that encodes the genetic material needed for all known living organisms and most viruses, is comprised of two complementary

polymeric strands of nucleotides which utilize hydrogen bonding and π–π stacking to form a double-helix.[2] While each individual intermolecular interaction between the two strands is weak, the two strands are oriented to maximize these interactions, and the cumulative effect of all of these interactions results in a stable structure. It is complex, self-assembled systems such as DNA that were the inspiration for the pioneering work of Donald J. Cram,[3] Jean-Marie Lehn,[4] and Charles J. Pedersen[5] in supramolecular chemistry. However, the most impressive examples of supramolecular macromolecules synthesized in the lab pale in comparison to nature's ability to utilize multiple, weak intermolecular forces in concert for the construction of large ensembles. The potential of supramolecular complexes to be utilized for applications in the areas of microelectronics, medicine, environmental remediation, catalysis, and advanced materials necessitates that researchers become more adept at controlling these noncovalent interactions.

1.2 Supramolecular Coordination Complexes

Supramolecular systems are synthesized by utilizing our knowledge of reactivity at the atomic scale; however, manipulating noncovalent interactions with the dexterity required to synthesize elaborate, discrete supramolecular systems has been met with a great deal of difficulty. Instead of trying to master the manipulation of noncovalent bonds, prefabricated construction elements that have stronger and highly directional bonds could be employed to simplify the self-assembly process. Since the first examples by Verkade and coworkers in 1983,[6] a wealth of knowledge has been obtained about the self-assembly

process by using transition-metals, which have well-defined coordination geometries and stronger bonding interactions than noncovalent interactions. Complexes that utilize transition-metals as infrastructural nodes have since been coined supramolecular coordination complexes (SCCs),[7] and over the past several decades a variety of two- (2D) and three-dimensional (3D) SCCs[7b,7c,8] have been synthesized and proposed for catalysis,[9] chemo-sensing,[10] light harvesting,[11] and biological applications.[12]

The impetus for the formation of discrete SCCs is the encoded information between complementary metal nodes (Lewis acid) and organic ligands (Lewis base). The highly predictive and rigid coordination geometries that transition-metals can adopt allow for a plethora of metal nodes to be readily synthesized. Moreover, metal-ligand coordination bonds, which are typically 15–50 kcal mol^{-1},[13] are weaker than sp^3 carbon–carbon bonds (ca. 80 kcal mol^{-1}) and are kinetically labile.[14] The kinetic reversibility between complementary building blocks (Figure 1.1; i and ii), reaction intermediates (Figure 1.1; iii), and self-assembled architectures (Figure 1.1; iv) allows for a "self-healing" process to occur in certain reaction conditions, resulting in the thermodynamic product (as illustrated in Figure 1.1). This simple, yet efficient, process of constructing discrete SCCs using mild conditions has blossomed over the past two decades to afford structures with increasing complexity. The increase in structural diversity and characterization techniques has lead to a proliferation of approaches for the construction of discrete SCCs with the most widely studied dubbed the *weak-link*, *symmetry-interaction*, *directional-bonding*, and *molecular-paneling* approaches.

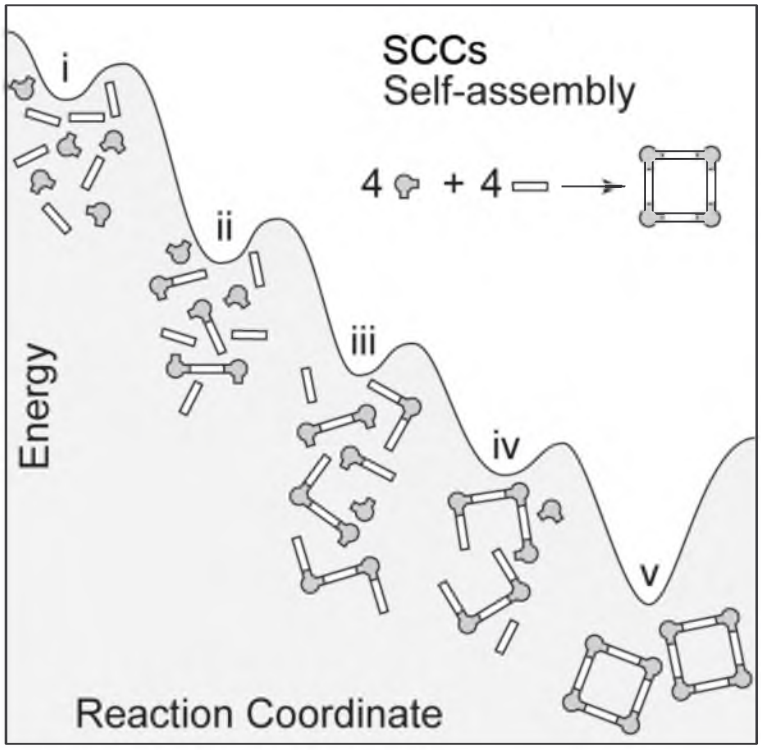

Figure 1.1: The kinetic lability of the metal coordination bond allows for a "self-healing" process of the SCCs to form the thermodynamic product wherein (i) is the reactant pool; (ii) coordination bonds are formed; (iii) scaffolds are further extended; (iv) if necessary, scaffolds are reoriented to form discrete structures; (v) discrete SCCs are the thermodynamic minimum.

1.3 Approaches to the Construction of SCCs

The various synthetic strategies (*weak-link*, *symmetry-interaction, directional-bonding*, and *molecular-paneling* approaches) used for the construction of 2D and 3D SCCs all hinge on the judicious choice of metal nodes, organic ligands, and reaction conditions. The kinetic lability of the metal-ligand coordination bond is at the center of each methodology, wherein the thermodynamic global minimum is the desired product; however, it should be noted that under certain conditions the kinetic product can be obtained using the *weak-link* approach.

1.3.1 Weak-link Approach

The crux of the *weak-link* approach, developed by Mirkin and coworkers,[7b,8e] is centered on the use of flexible, hemi-labile chelating ligands that undergo post-self-assembly modification (Figure 1.2[7c]). The formation of the self-assembled product is dictated by the bis(chelating) ligand, which often contains an ethylene spacer for the formation of favorable five- or six-member chelate rings and the reaction conditions. The bis(chelating) ligand is designed in such a manner that one of the metal-ligand bonds is weaker than the other. The self-assembled structure can then undergo further modification by introducing an exogenous ligand that has a greater affinity for the metal center than the weaker metal-ligand bond of the bis(chelating) ligand. The introduction of the new ancillary ligand (Figure 1.2; L) displaces the weaker ligand and leads to a new structure that is now the thermodynamic minimum. Typically, during this process, the structure expands since the bis(chelating) ligand contains a flexible ethylene spacer. Only a limited number of architectures have been constructed using this method, however, and it has largely been confined to macrocycles.

1.3.2 Symmetry-interaction Approach

In the *symmetry-interaction* approach, the construction of SCCs is predicated on understanding and controlling the relationship between the symmetry elements present in the desired geometry and replicating them in the ligands and metal centers. SCCs synthesized using this method are almost exclusively constructed from bidentate ligands and the “naked” octahedral metal centers. For

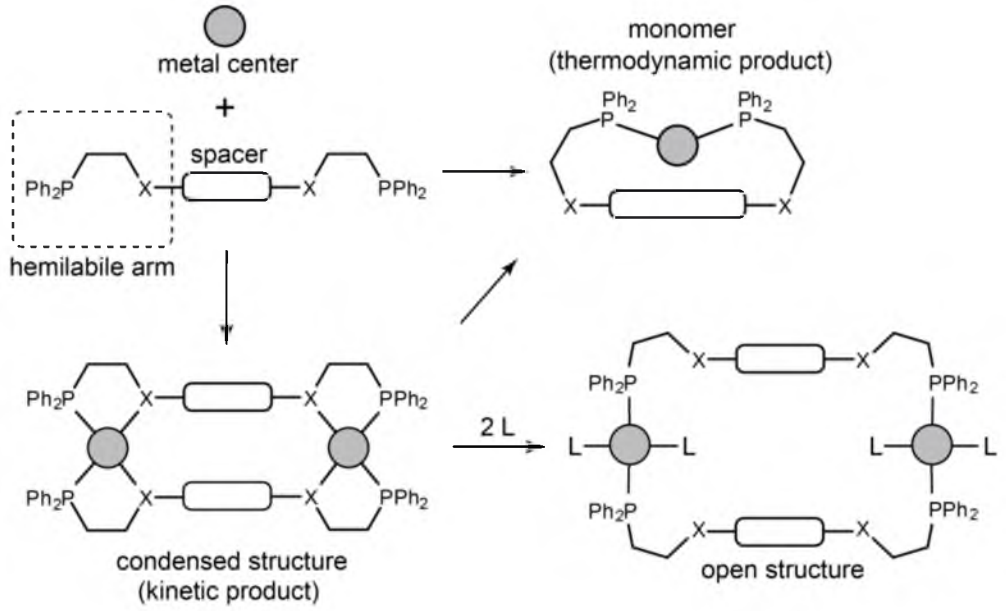

Figure 1.2: The weak-link approach first forms a kinetically stable complex which can then undergo post-self-assembly modification by adding a ligand (L) that has a higher affinity for the metal center than one of the two chelating atoms (X).

example, the principle axis of a M_4L_6 (four metal centers at the vertices and six ligands acting as the edges) tetrahedron has C_3 symmetry and bisects the metal nodes (Figure 1.3). A secondary C_2 axis exists along the edges of the tetrahedron that the ligands occupy. When considering the intimate relationship between the symmetry elements in desired geometry and the ligands and metal centers, it is often easier to first consider the octahedral metal center which must, in this case, relate to the principle C_3 axis of the tetrahedron. The plane perpendicular to the principle C_3 axis of the metal center is referred to as the chelate plane. Each metal center can be thought of as containing three sites for coordinating bidentate ligands that bisect the chelate plane (Figure 1.3[7c]). The spatial orientation that each bidentate ligand occupies and projects from the chelate plane is the coordination vector. The ligand, which occupies the edges of

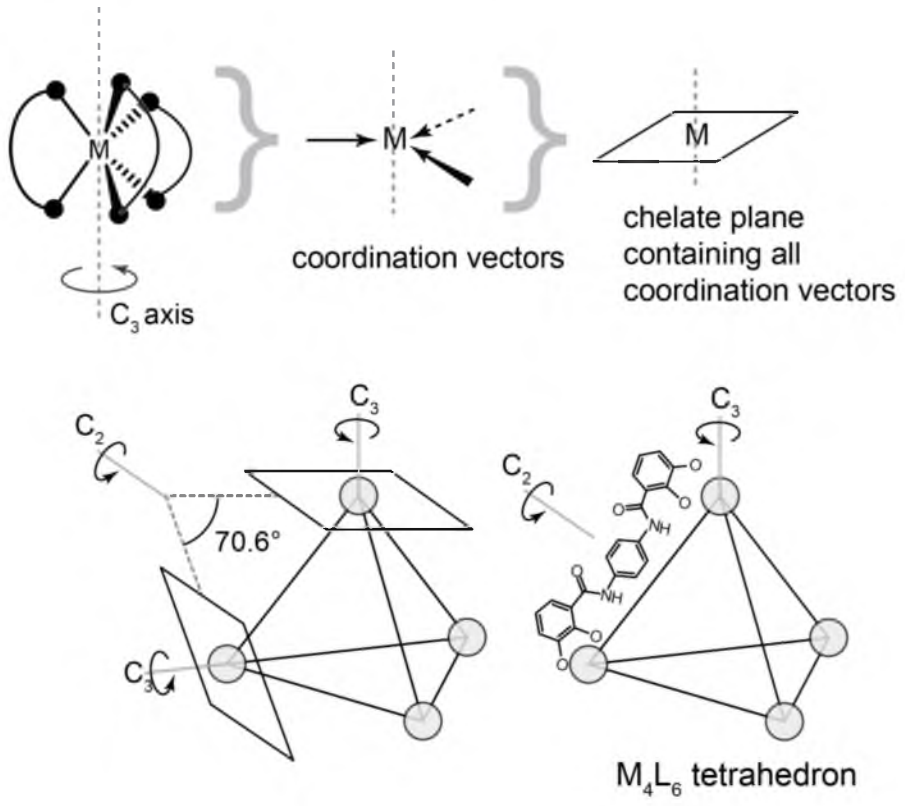

Figure 1.3: The symmetry-interaction approach requires careful consideration of the relationship between the symmetry elements present in the principal components to construct 3D architectures such as a tetrahedron.

the structure, must relate to the secondary C_2 axis, which bisects the edges of the tetrahedron. By synthesizing a bidentate ligand with C_2 symmetry that can occupy the three coordination vectors of the metal center, a M_4L_6 tetrahedron can be synthesized. A variety of transition-metal and main group metal-based shapes and architectures (e.g., helicates,[15] tetrahedra,[16] and adamantoids[17]), mainly from Raymond et al. and Saalfrank et al.,[8e,18] have been synthesized using this method and are currently being investigated as catalysts for various reactions.[9d,9e] However, the subtle interactions driving the formation of these structures are not fully understood, and it has hindered progress in developing rationale synthetic schemes.

1.3.3 Directional-Bonding Approach

Unlike the previous methods that utilize uncapped square planar metal centers, this approach, pioneered by the Stang lab,[8h,8j,19] utilizes capping ligands to form a rigid metal node "acceptor" with encoded directionality. Each square planar metal center has four vectors that are 90° degrees with respect to each other radiating from a single point. Using known synthetic protocols, specific vectors can be capped with ligands, allowing for 90° (*cis*) or 180° (*trans*) metal nodes to be accessed. Further chemistry can then be performed on the 180° metal centers to generate a library of multinuclear organometallic complexes with varying angles. Classically, the Stang lab has utilized third-row, d^8 square planar platinum(II) transition-metal centers since they maintain strict coordination geometries and have a high affinity for pyridyl-based ligands "donors."

The *directional-bonding* approach also dictates that the pyridyl-based ligands are rigid and have encoded directionality; this method can be likened to a molecular set of "tinker toys" wherein a variety of 2D and 3D structures can be afforded by using complementary acceptors and donors, as shown in Figure 1.4. An example relevant to this thesis is of a D_{2h} rhomboidal-shaped SCC (Figure 1.5) constructed from two dinuclear platinum 60° metal nodes and two 120° dipyridyl organic ligands.

1.3.4 Molecular-Paneling Approach

All of the approaches discussed previously have been used to construct a variety of architectures by placing organic ligands and metal nodes on the edges and vertices of constructs. For instance, as shown in Figure 1.6,[7c] a $M_{12}L_8$ cube

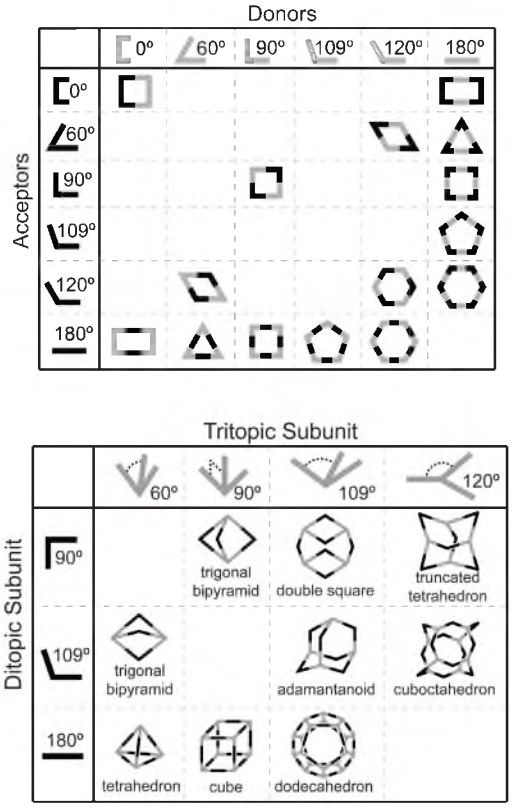

Figure 1.4: 2D and 3D SCCs that have been constructed with the *directional-bonding* approach by using complementary subunits.

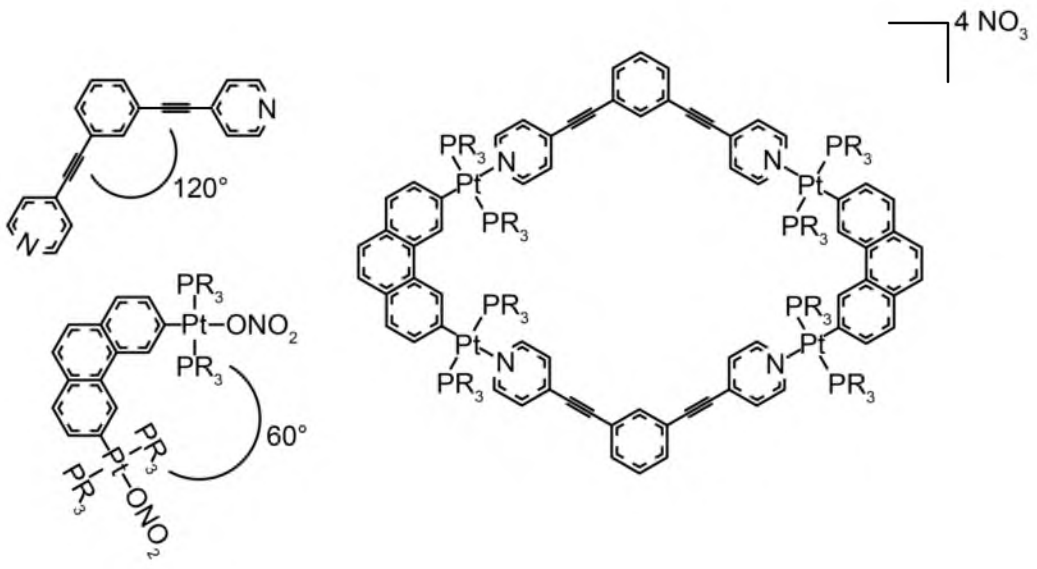

Figure 1.5: A D_{2h} rhomboidal-shaped SCC can be constructed from two 120° and two 60° subunits.

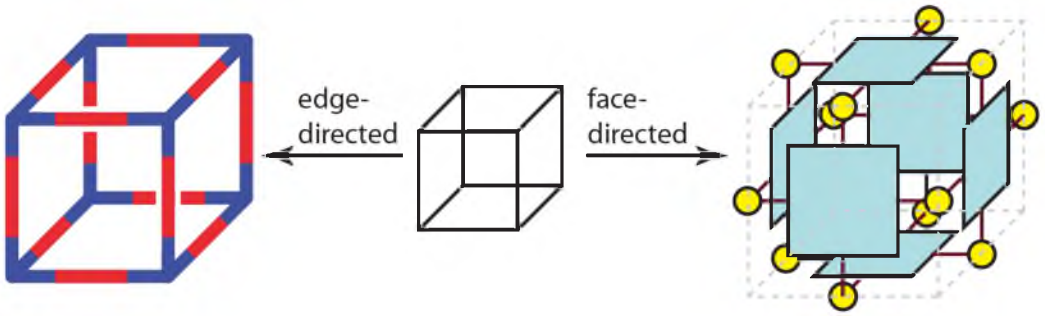

Figure 1.6: The construction of SCCs can be edge-directed or face-directed.

can be synthesized via edge-directed self- assembly from 8 tritopic organic ligands at the vertices and 12 metal nodes along the edges of the cube. Another method for constructing a cube, however, would be to occupy the faces of the cube by using 6 tetratopic organic ligands and connecting them with 12 metal nodes ($M_{12}L_6$) at the edges. This construction method has been used to synthesize a variety of Platonic and Archimedean solids and has been dubbed the *molecular-paneling* approach.[8c,20] It should be noted that this method has also been extended to synthesize prisms and several tetrahedral and octahedral-based systems, some of which have been utilized by Fujita and coworkers as "molecular flasks" to enhance reaction rates.[9i] However, unlike the *directional-bonding* approach, a *cis*-protected 90° metal center must be employed for 3D structures to converge. In doing so, the utility of one of the two principle components in this construction method is limited. For example, as shown in Figure 1.7, a truncated tetrahedron (M_6L_8) can be synthesized by mixing eight equivalents of 1,3,5-tripyridyl triazine—a tritopic organic ligand with D_{3h} symmetry that is triangular in shape—and six equivalents of a *cis*-protected ethylenediamine palladium (II) 90° metal node in appropriate reaction

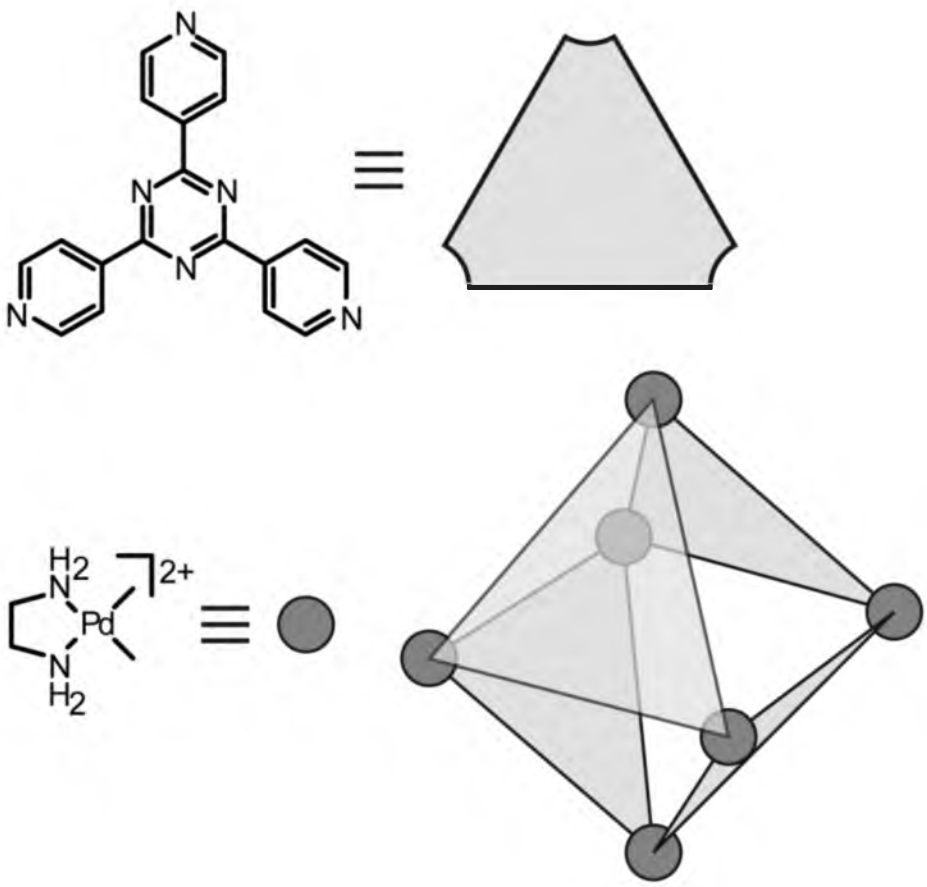

Figure 1.7: Using the molecular-paneling approach a M_6L_8 truncated tetrahedron can be constructed from *cis*-protected metal nodes and tritopic organic ligands.

conditions.[8c]

Despite the increasing complexity of structures afforded by utilizing these synthetic approaches, the limited number of components used in these systems inhibits further development. For the past 2 decades, the construction of SCCs has largely been limited to two-component systems. Moreover, in general, SCCs have been limited to utilizing principal components that are rigid to limit the number of possible reaction pathways; however, nature rarely employs such strict constraints when self-assembling biomolecules. For SCCs to fulfill their

purpose, a paradigm shift in the ideology of constructing SCCs must occur.

1.4 Multicomponent Self-Assembly: A Pathway to Flexible Architectures

In the previous section, the synthesis of SCCs was confined to two components—one type of organic ligand and one type of metal node. SCCs containing multiple, different molecular subunits are more complex and are more difficult to control due to the multiple reaction pathways that may exist in the solution. Elegant examples exist where multiple components have been utilized to give rise to discrete, predictable architectures and not statistical mixtures through the exploitation of geometric and electronic properties of molecular subunits.[21]

The self-assembly of SCCs with multiple components in solution using geometric constraints has been extensively studied and several methods have been developed.[8h,21e,22] One such method, dubbed *self-sorting*, relies on the thermodynamic preference for complementary subunits in a complex mixture to organize and form multiple, different discrete systems as shown in Figure 1.8.[23] This method demonstrates the high fidelity of subunits and gives insight into the formation of multiple structures from a single pool of subunits; however, the final structure in these systems is still comprised of two components. Systems comprised of three or more subunits have been constructed using the *self-sorting* shown in Figure 1.9.[24]

The self-assembly of SCCs comprised of three or more components has also been accomplished by controlling the size and shape of the incoming ligands and

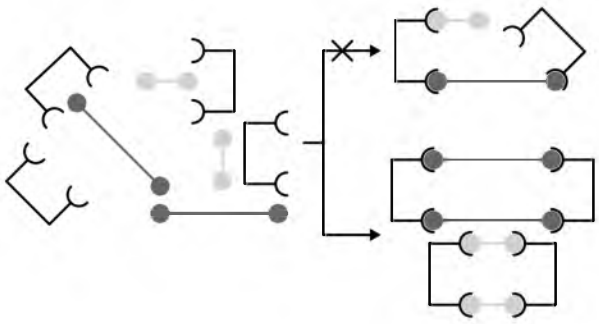

Figure 1.8: The self-sorting of three different subunits to form two different sizes of rectangles.

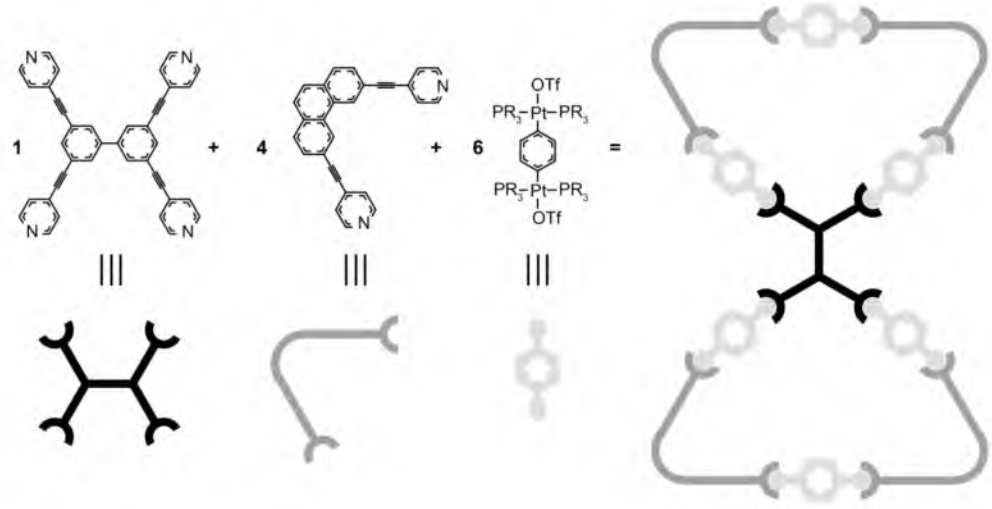

Figure 1.9: A three component bowtie-like structure was synthesized by stoichiometrically controlling the subunits utilized during the *self-sorting* method.[24c]

their spatial orientation around the metal center.[25] For example, Fujita and coworkers demonstrated that a bulkier pyridyl-based ligand would preferentially form a heteroligated coordination sphere with a less sterically demanding pyridyl-based ligand, as shown in Figure 1.10.[25b] The thermodynamically preferred heteroligated coordination sphere around the metal center allowed for the synthesis of a single three component macrocycle.[25b]

The previously discussed systems have been predicated on the judicious

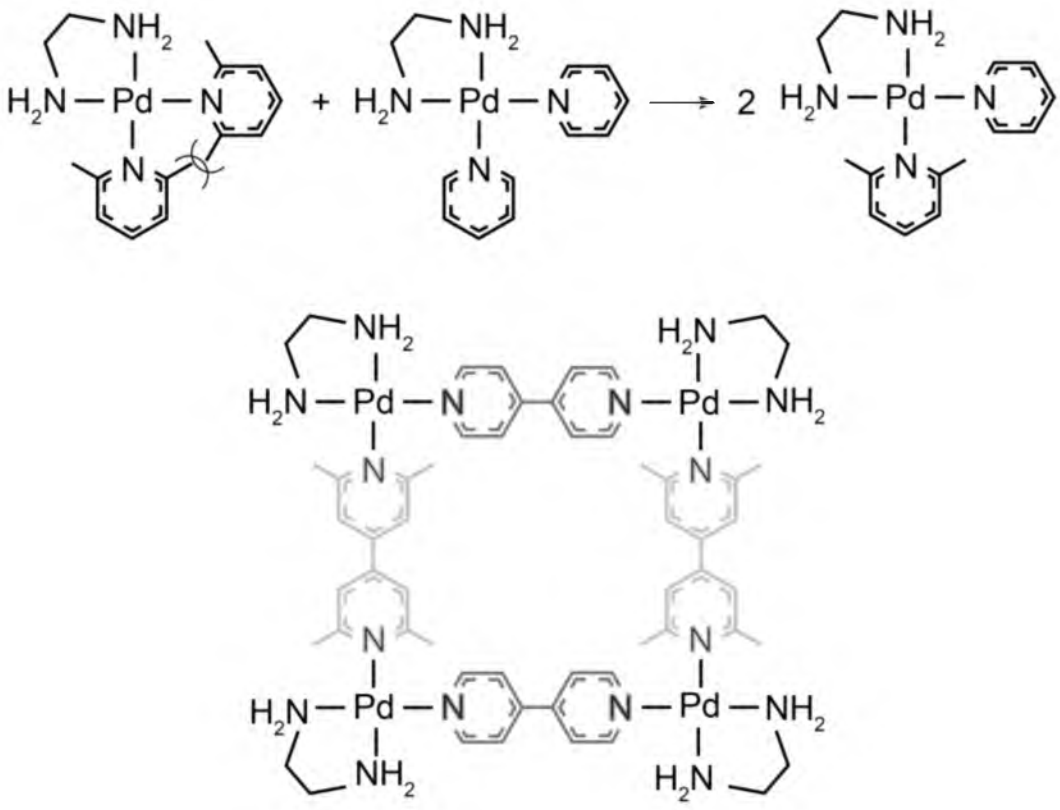

Figure 1.10: Three-component macrocycle synthesized by using a bulky 2,6-dimethyl pyridyl and pyridyl-based ligands that preferentially form the overall less sterically cumbersome species in solution.

choice of organic ligands that allow for geometric constraints such as steric bulk, size and complementarity to be exploited for the selective formation of discrete SCCs in complex mixtures. However, the thermodynamic preference for a heteroligated coordination sphere around a metal node based on the electronic properties of the incoming ligands has only recently been explored as a method for constructing multicomponent SCCs.

Since the pioneering work of Hor et al.,[26] bis(phosphine) platinum(II) metal nodes have experimentally been shown to preferentially form a heteroligated coordination sphere with carboxylate and pyridyl-based ligands (Figure 1.11), and several examples of SCCs have been constructed utilizing this coordination

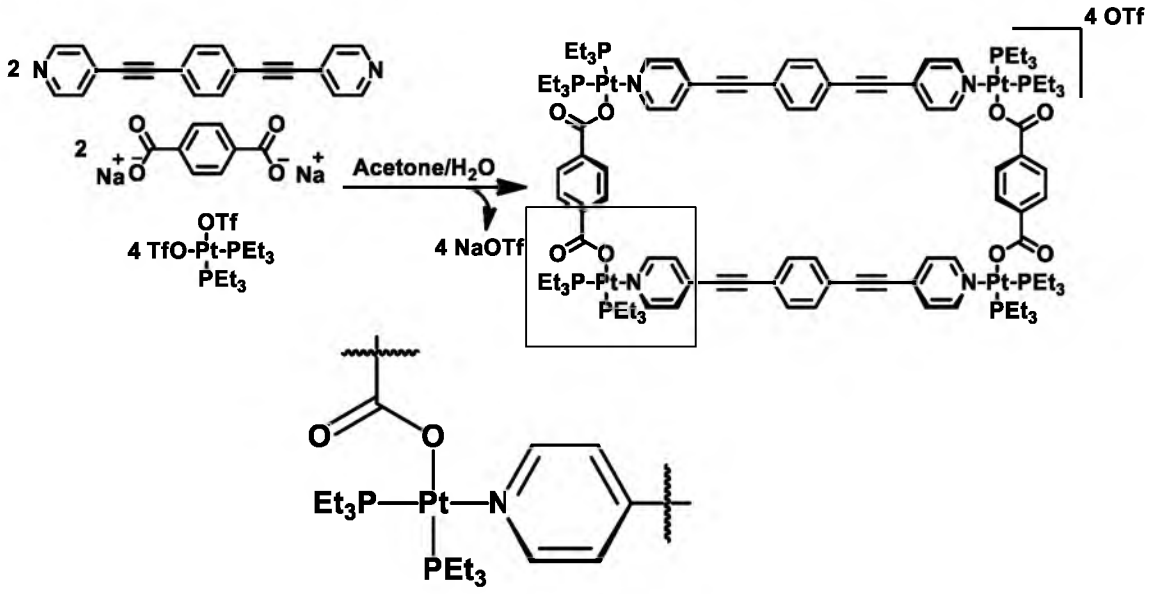

Figure 1.11: Three-component SCC constructed using the *charge-separation* method.

motif.[27] This strategy, dubbed the "*charge-separation*" method, obtained its moniker from the minimization of electrostatic effects on incoming or coordinated ligands; however, ongoing investigations using molecular modeling (*vide infra*) are providing further insight into this phenomenon which is likely due to multiple factors including orbital effects (i.e., *cis* and *trans* effect), relaxation of steric strain at the metal center, and electrostatic effects.

Other more exotic methods have been utilized to synthesize multicomponent systems and hinge on the use of rigid subunits to direct the self-assembly process. Rarely are subunits that contain alkyl linkers between the two Lewis basic sites on the donor subunit used in the self-assembly process, which is presumably due to the unpredictable reaction pathways that are introduced (e.g., polymers, dimers, oligomers, etc.) when using flexible subunits. To date, most studies that have utilized alkyl-based linkers have been restricted to methyl or

ethyl-based linkers between the two Lewis basic sites, while larger alkyl spacers have not been reported (Figure 1.12).[28] Currently, functional groups such as alkenes (*cis*/*trans* isomerization) are utilized to afford some level of spatial control; however, the final constructs are fairly rigid and lack the level of fluidity often seen in biological systems.[10h,22,24d,29] As such, synthesizing systems that preserve flexibility even after SCC formation are attractive because they could be used to construct SSCs without predefined cavities and volumes for host-guest recognition and catalysis.

Previous two component designs did not maintain the geometric control required during the self-assembly process to afford such flexible architectures because the metal center would indiscriminately coordinate with incoming ligands, leading to a complex mixture of products. Fortunately, the previously described *charge-separation* method circumvents this issue by exploiting the electronic properties of the incoming ligands to preferentially form a heteroligated coordination sphere. Dicarboxylates that have varying alkyl spacers are readily available, and by utilizing rigid pyridyl-based ligands with platinum nodes, a novel series of flexible 2D and 3D SCCs was synthesized (*vide infra*).

As the structural designs and methods used to construct SCCs continue to increase in complexity, the unique chemistry of transition-metals will provide and unlock new strategies for building SCCs. However, researchers should continue to concurrently explore the utility and properties of current systems, especially due to the lack of understanding of the photophysical properties in these systems since they are often proposed for photon-emitting applications.

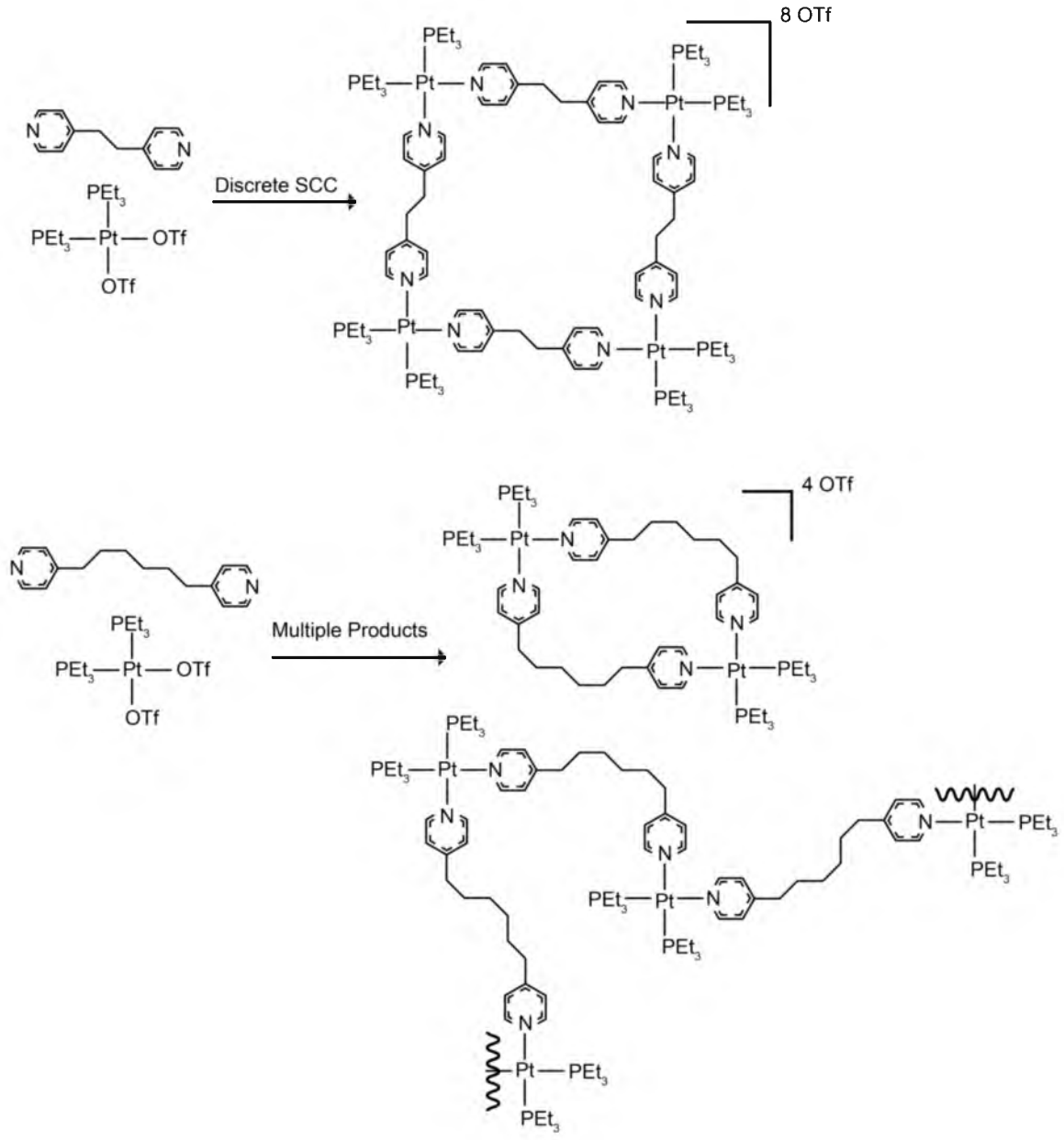

Figure 1.12: Rectangular SCC synthesized using an ethylene spacer between the two Lewis basic sites on a donor, but larger alkyl-based linkers on a dipyridyl donor lead to a mixture of products.

1.5 Basics of Photophysics

Electromagnetic radiation consists of two transverse, in-phase, perpendicular propagating waves of electric and magnetic fields and is classified by the frequency of the resulting wave.[30] The frequency (ν) of a wave multiplied by Planck's constant (h) is directly proportional to the energy (E) of the electromagnetic radiation, as shown in eq. 1.1. The electromagnetic spectrum was devised as a method for grouping electromagnetic radiation of similar energy with the most pertinent regions, grouped by wavelengths (nm), to this discussion being the ultraviolet (UV; 10-380 nm) and visible (Vis; 380-750 nm) spectral windows. However, since wavelengths are nonlinear with respect to energy, a difference in spectral wavelengths is often reported as a change in frequency or wavenumbers with the units cm^{-1} for the regions discussed.

$$E = h\nu = \frac{hc}{\lambda} \tag{1.1}$$

Optical spectroscopy, which will be discussed heavily in this thesis, investigates the interaction between light and matter. The nature of these interactions that we are most concerned with, herein, will be discussed individually and represented with a Jablonski diagram (Figure 1.13).

Molecules in their resting state or ground state (S_o) can absorb photons in the electromagnetic spectrum. Upon absorbing the energy of a photon, electrons in the ground state can be promoted to an antibonding molecular orbital or higher-energy excited-state (S_1) via a vertical transition. The energy required for the vertical transition from the S_o to the S_1 states is the energy required to promote an electron from the highest occupied molecular orbital (HOMO) to the lowest

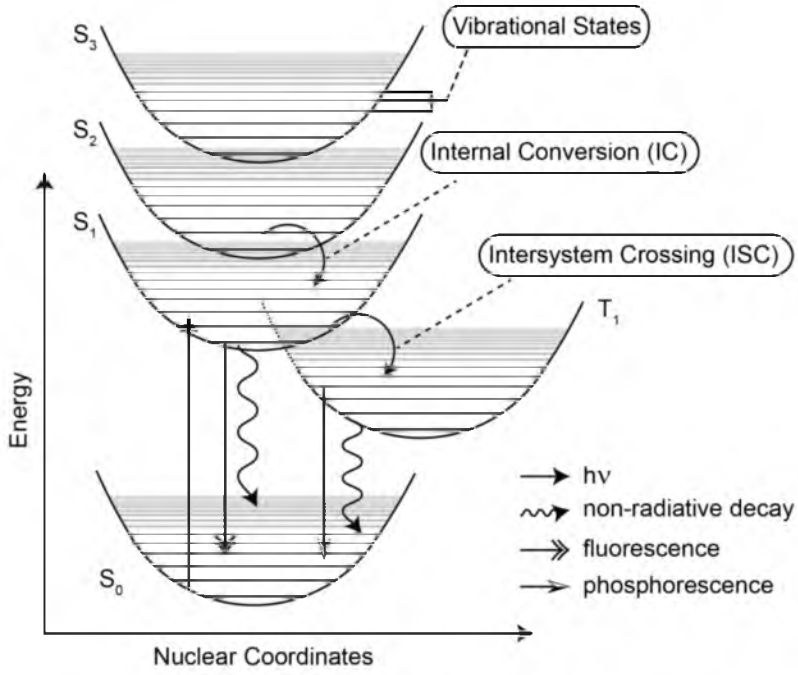

Figure 1.13: Jablonski diagram displaying the absorption process and various fates of excited-states.

unoccupied molecular orbital (LUMO).The total number of energy manifolds that can be present is limited to the number of molecular orbitals that a compound can have with each molecular orbital being progressively higher in energy, as shown on the y-axis of the Jablonski diagram. So, S_3 would represent an excited-state molecular orbital that is two energy manifolds higher than the S_1, noted as LUMO+2. Within each energy manifold (e.g., S_o) there are horizontal lines representing the various vibrational energy levels that can exist for each molecular orbital. Depending on the amount of energy absorbed, an electron may be promoted to a vibrational level not at the bottom of an excited-state manifold; however, the electron rapidly relaxes (~10^{-12} s) to the lowest vibrational level within a given excited-state energy manifold. The lower the energy gap between the ground-state and excited-state molecular orbitals, the higher the wavelength

of incident light needed for the electronic transition to occur.

The wavelengths of incident light required to illicit an electronic response in an absorbing material can be monitored using ultraviolet/visible (UV/Vis) spectroscopy, which measures the difference between the intensity of light before and after passing through a sample. The Beer–Lambert Law states that when a photon has the appropriate energy, the transmittance of light is directly proportional to the concentration of an absorbing species in solution and the pathlength that the photon must travel. The Beer–Lambert Law can be expressed as

$$A = \log_{10} \frac{I_o}{I} = \varepsilon c l \qquad (1.2)$$

where A is the measured absorption, I_o is the incident light at a single wavelength, I is the amount of transmitted light from I_o, c is the concentration (M) of the species in solution, and l is the pathlength (cm^{-1}) through the sample. The molar absorption coefficient (ε; $cm^{-1}M^{-1}$) is a physical property of the absorbing species at a particular wavelength and is dependent on the solvent, temperature and pressure.

Once in the excited-state an electron can then either undergo nonradiative (Figure 1.13; curved line) or radiative (Figure 1.13; double arrow) decay to the S_o state. The radiative decay process from an S_1–S_n to S_o state is termed fluorescence and normally occurs on the nanosecond timescale. Sometimes, though, enough energy is absorbed from a photon to promote an electron to a high-level excited-state molecular orbital (e.g., S_3). Through a rapid process (10^{-12} s) called internal conversion (IC), the electron can relax to a lower level

excited-state molecular orbital (e.g., S_1) before decaying to the ground-state. Excited-states that have radiative decay pathways are termed "bright states," while states that have nonradiative decay pathways are termed "dark states."

The previous discussion has strictly dealt with vertical transitions of the same multiplicity because of certain formal constraints within optical spectroscopy. The spin selection rule dictates that when exciting an electron from the ground-state to an excited-state molecular orbital, the multiplicity of the molecule must be conserved. Multiplicity is the number associated with differentiating degenerate wavefunctions based on the spin angular momenta of unpaired electrons. The S_o–S_n states get their moniker because of the singlet multiplicity of the molecular orbitals. Sometimes, however, when an electron is in an excited-state it is possible to break the spin selection rule by enhancing spin-orbit coupling, resulting in a change of multiplicity. This spin-forbidden process called intersystem crossing (ISC) results in the electron relaxing to a low-lying triplet-state (T_1–T_n). The electron can then either nonradiatively or radiatively (Figure 1.13; half arrow) decay. The radiative decay process from a triplet excited-state is termed phosphorescence and can often last minutes or hours. As a point of interest, ISC can often be enhanced by incorporating very heavy atoms, such as platinum, into materials that are photo-excited. Another selection rule that dictates whether an electronic transition is allowed is the Laporte selection rule, which states that electronic transitions that conserve parity in molecules or atoms (i.e., those that contain an inversion center) are forbidden.

The Jablonski diagram shown in Figure 1.13 has nuclear coordinates as the

x-axis. The Franck–Condon principle is the approximation that electronic transitions that can occur will do so without changes to the positions of the nuclei since the absorption process is on the femtosecond timescale. As a result, vertical transitions between ground-state to excited-state molecular orbitals that have a higher level of overlap have a higher probability. The time-scale for radiative decay processes, however, can vary greatly. Long radiative decay processes can greatly affect the excited-state to ground-state orbital overlap and probability of a radiative transition. The probability of a radiative transition is directly related to the luminescence intensity of a system, which can be quantified.

The probability of a photon being absorbed and decaying via a radiative pathway is a photophysical property that is of great interest when discussing emissive systems because it is a metric that allows for the direct comparison of the luminescence intensities between systems. The quantum yield (Φ) of a system is a measurement of emission intensity, which is defined by the number of photons emitted (η_e) versus the number of photons absorbed (η_a).

$$\Phi = \frac{\eta e}{\eta a} = \frac{k_r}{k_r + k_n} \tag{1.3}$$

Quantum yields can also be defined as the rate constant for the radiative pathway (k_r) versus the sum of the rate constants for all decay pathways. The rate constant for all nonradiative pathways is termed k_n.

The measurements previously discussed are all termed steady-state, that is to say that the molecule is constantly irradiated and the population of the ground and excited-states remain constant over time. Conversely, time-resolved

measurements utilize a short excitation pulse to populate the excited-state, which allows for kinetic information about the decay pathways to be accessed. By using an observable such as emission, the excited-state lifetime (τ_o) can be measured. The excited-state lifetime can be expressed as

$$\tau_o = \frac{1}{k_r + k_n} \quad (1.4)$$

From the excited-state lifetime, the rate constants for the radiative and nonradiative decay pathways can be calculated using the quantum yield.

$$k_r = \Phi {\tau_o}^{-1} \quad (1.5)$$

$$k_n = {\tau_o}^{-1} - k_r \quad (1.6)$$

Steady-state and time-resolved optical spectroscopy can provide a wealth of information about the electronic structure of systems. Absorption spectroscopy can probe the energy differences between the ground and excited-state molecular orbitals and determine which transitions are allowed. Emission can be monitored spectroscopically and the luminescence intensity can be quantified, while time-resolved spectroscopy allows for the fate of excited-states to be probed by mapping the full kinetic profile of the decay processes. Using these methods in conjunction with modern molecular modeling techniques, the photophysical properties of a system can be fully characterized and differences between systems can be analyzed to give insight into future designs.

1.6 Molecular Modeling

Over the past several decades, the accuracy and utility of molecular modeling has increased to the extent that molecular modeling has become an instrumental

tool in augmenting photophysical studies for metal-based systems. As such, it is prudent to discuss in general terms some of the techniques that have been utilized in previous studies and are utilized in this thesis for describing the photophysical properties of platinum-based SCCs.

Density functional theory (DFT) has gained popularity over the past couple of decades due to the accuracy of the calculations afforded by the increased emphasis on the electron correlation and energies associated with electron-electron interactions; terms that previous Hatree–Fock (HF) methods lacked.[31] Moreover, the significant increase in accuracy comes at only a modest increase in computational cost when compared to previous HF methods. DFT utilizes functions of the electron density to calculate the energy of a molecule, where the electron density is represented by functions which partition the electronic energy into multiple components: Coulombic repulsion, kinetic energy, electron-nuclear attraction and an electron-correlation term accounting for all effects arising from the multiplicity of the system. The electron correlation term is then inserted into the Kohn–Sham equation[32] and solved iteratively and self-consistently until it remains constant and is within some set tolerance.

In a practical sense, one must define a functional and a basis set when performing geometry optimization calculations using DFT. There are many different functionals and basis sets that can be utilized in DFT calculations and, in the interest of brevity, functionals and basis sets will only be discussed in very general terms.

Functionals are defined by the way they treat the exchange-correlation term

and, currently, some of the most widely used and accurate are hybrid functionals. Hybrid functionals utilize linear combinations of the various functionals for calculating spin densities that were formulated for previous methods. One of the well-known and popular hybrid functionals is the Becke three-parameter functional due to its accuracy when predicting experimental molecular properties.[33]

A basis set is an approximation of the molecular orbitals, which are represented as a linear combination of predefined atomic orbitals. Generally, a larger basis set allows for a more accurate molecular orbital model. This can be accomplished by adding diffuse and polarized functions, when appropriate, to the basis set. A diffuse function defines for larger atomic orbitals than normal to occupy a larger space for atoms with lone pairs or point charges, while polarized functions add atomic orbitals with higher angular momentum than required for an atom (i.e., d-orbitals are added for carbon). However, when performing calculations with large atoms or transition-metals such as platinum, it is best to utilize a contracted basis set that approximates the inner atomic orbitals by using an effective core potential (ECP) to save on computational cost. These basis sets also include relativistic effects that are important for electrons near the nucleus in large atoms.

An extension of DFT is time-dependent DFT (TD-DFT), and it utilizes the same practical formalism as DFT; however, TD-DFT utilizes the Runge–Gross theorem which allows for the properties of a system to be investigated by applying time-dependent potentials.[34] For example, the application of a time-

dependent electric potential on a density field allows for excitations to be probed. Meaning, TD-DFT predicts the electronic transitions for a system in the ground-state and determines the probability and molecular orbitals involved in an electronic transition. This method is often used to augment photophysical experiments and has been instrumental in furthering our understanding of the observed optical properties of systems.

1.7 Photophysical Properties of SCCs

Organometallic complexes are well-known for their attractive photophysical properties (e.g., facile tunability, low energy and long lived excited-states, and high quantum yields) and have been used extensively in bioimaging,[35] photodynamic therapies,[36] photocatalysis[37] and photovoltaics.[38] SCCs are often implicated for applications stemming from their photophysical properties which are assumed to be unique and attractive due to the metal centers that are integral in their construction. However, studies probing the photophysical properties of discrete 2D and 3D SCCs are rare, especially for platinum-based SCCs.

Mono- and multinuclear platinum complexes have been investigated thoroughly for their inherent photophysical properties and have exhibited low-energy absorption bands, long-lived and low-energy excited-states, and high quantum yields.[39] These properties make a multinuclear Pt(II) self-assembled metallacycle an attractive target. Although the photophysics of mono- and multinuclear Pt(II) complexes have been investigated extensively, the photophysics of Pt-pyridyl metallacycles have largely been understudied.[40] One

rare example is the study of rhomboids constructed with 1,2-bis(3-pyridyl)ethyne and 1,4-bis(3-pyridyl)-1,3-butadiyne (Figure 1.14) using TD-DFT calculations.[41]

The low-energy transitions of both rhomboids correspond to transitions between molecular orbitals that contain a large amount of ligand character. It was observed that increasing the size of the π-system by the addition of ethylene spacers within the ligand resulted in red-shifted emission of the rhomboidal SCC. Goodson et al. studied the ultrafast optical excitation and relaxation of a series of Pt-pyridyl rectangles and triangles (Figure 1.15).[42] It was determined that for SCCs with multiple platinum centers, increased amounts of intersystem crossing occurred due to spin-orbit coupling. This "heavy atom effect" manifested itself in decreased excited-state lifetimes and since the triplet excited-state was plagued by nonemissive decay pathways, low quantum yields were observed.

Recently, Pistolis et al. synthesized a boron dipyrromethene (BODIPY) Pt metallacycles (Figure 1.16) whose emission was significantly red-shifted compared to that of the free ligand (λ_{em} = 592 versus 545 nm).[43] However, the quantum yield of the metallacycle species was low compared to that of the ligand (6% versus 47%). When an ethylene spacer was added between the

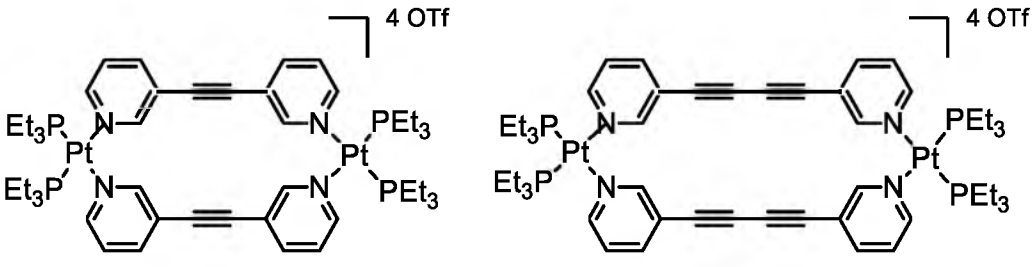

Figure 1.14: The inclusion of a larger π system within the coordinating ligand led to red-shifted emission profiles of the metallacycles.

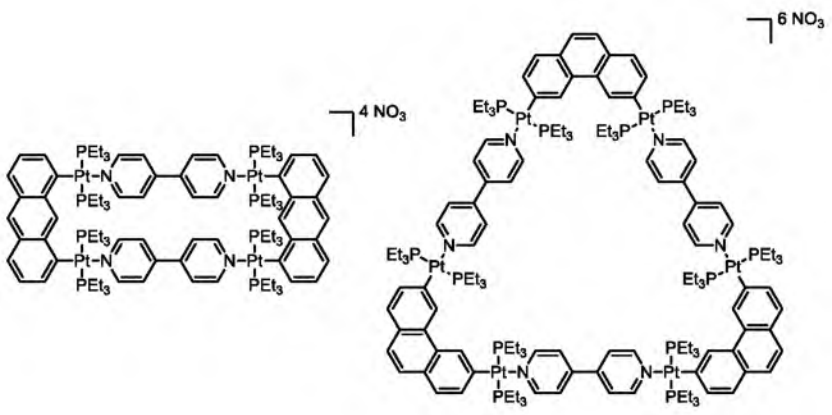

Figure 1.15: Two representative SCCs studied by Goodson et al. using ultrafast dynamics.

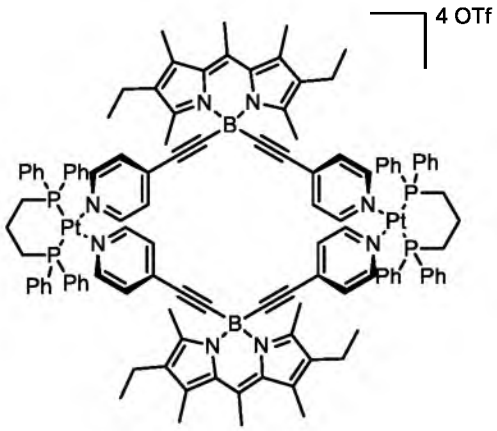

Figure 1.16: BODIPY incorporated SCC synthesized by Pistolis et al. that has a visible wavelength emission profile.

coordinating pyridyl units and the BODIPY backbone, the photophysical properties of the BODIPY ligand were conserved after coordination with the platinum acceptor. This study demonstrates the delicate balance between the isolation of the pyridyl–based ligand centered electronic transitions and the bis(phosphine) platinum (II) metal center's ability to perturb the ligand centered excited-state. Too much Pt character and spin-orbit coupling opens up nonradiative decay pathways—too little, and the emissive characteristics of the

assembly do not differ enough from the building blocks to allow them to be distinguished from one another.

Concurrently with the work presented in this thesis, Han et al. studied a suite of SCCs (Figure 1.17) using steady-state and time-resolved spectroscopic techniques in conjunction with DFT and TD-DFT.[44] It was determined that some the lumniscence intensity was very weak. Unlike in the Goodson study, the ligand utilized in these systems had a radiative triplet-state and the inclusion of platinum facilitated a higher rate constant for intersystem crossing, which led to phosphorescence. Moreover, it was also shown that the fate of the excited-states in multiplatinum SCCs is complex and that a variety of decay pathways can exist for a given system, giving rise to varying optical properties. The SCCs studied, systems had increased phosphorescence due to the "heavy atom effect"; albeit however, did not emit above 400 nm which limits their use in the proposed applications for platinum-based SCCs.

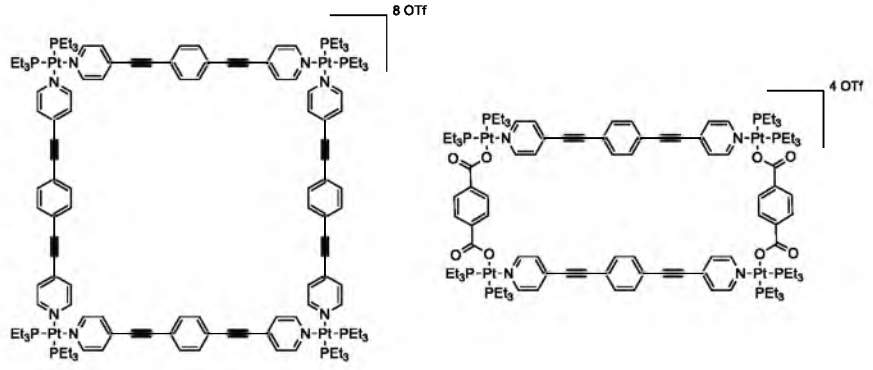

Figure 1.17: Two representative SCCs that were studied by Han et al. with homoligated Pt-pyridyl (left) and heteroligated carboxylate-Pt-pyridyl (right) coordination spheres.

1.8 Summary

The self-assembly of discrete systems in a laboratory setting has been greatly simplified through the use of transition-metals. Over the past couple of decades, a variety of techniques has proven to be useful in the construction of both 2D and 3D SCCs. However, during the self-assembly process, most SCCs still utilize two principle components. Recent advancements in the formation of three or more component systems have opened avenues for the synthesis of flexible systems, unlike previous constructs. As the methodologies for synthesizing novel SCCs continue to grow, the utility and properties of SCCs for proposed applications need to be investigated.

The photophysical properties of platinum-based SCCs have largely been understudied despite the unique and attractive properties of mono- and mutlinuclear platinum complexes. Current platinum-based SCCs have poor quantum yields and do not emit well in the visible region. Moreover, the inclusion of platinum metal centers has been shown to be a "double-edged sword" with the emission profile of coordinating ligands being red-shifted upon complexation, but having a deleterious effect on the quantum yield in systems lacking radiative triplet-states. As such bis(phosphine) platinum(II) SCCs that have high quantum yields and are tunable in the visible spectral window need to be developed and are necessary if they are to be used for photocatalysis, bio-imoaging, photovolatics, and optical chemosensors.

In the chapters that follow (i) a novel series of flexible SCCs is synthesized using the "charge-separation" method, which is further examined via molecular

modeling, and (ii) the photophysical properties of bis(phosphine) platinum(II) SCCs and model complexes are investigated experimentally and computationally, culminating with a novel series of rhomboidal-shaped SCCs that have predictable emission profiles spanning the visible region.

1.9 References

(1) (a) Steed, J. W.; Atwood, J. L. *Supramolecular Chemistry*, 2 ed.; John Wiley & Sons, Inc., London, UK, 2009; (b) Ariga, K.; Kunitake, T. *Supramolecular Chemistry–Fundamentals and Applications*; Springer, New York, NY, 2006.

(2) Nelson, D. L.; Cox, M. M. *Lehninger Principles of Biochemistry*, 5 ed.; Freeman, W.H. & Company, New York, NY, 2008.

(3) (a) Cram, D. J.; Cram, J. M. *Acc. Chem. Res.* **1978**, *11*, 8; (b) Cram, D. J.; Cram, J. M. *Acc. Chem. Res.* **1971**, *4*, 204.

(4) Lehn, J. M. *Acc. Chem. Res.* **1978**, *11*, 49.

(5) Pedersen, C. J. *J. Am. Chem. Soc.* **1967**, *89*, 7017.

(6) Stricklen, P.; Verkade, J. *J. Am. Chem. Soc.* **1983**, *105*, 2494.

(7) (a) Mamula, O.; von Zelewsky, A. *Coord. Chem. Rev.* **2003**, *242*, 87; (b) Oliveri, C. G.; Ulmann, P. A.; Wiester, M. J.; Mirkin, C. A. *Acc. Chem. Res.* **2008**, *41*, 1618; (c) Cook, T. R.; Zheng, Y.-R.; Stang, P. J. *Chem. Rev.* **2012**, *113*, 734.

(8) (a) Cotton, F. A.; Lin, C.; Murillo, C. A. *Acc. Chem. Res.* **2001**, *34*, 759; (b) Cotton, F. A.; Lin, C.; Murillo, C. A. *Proc. Natl. Acad. Sci. U.S.A.* **2002**, *99*, 4810; (c) Fujita, M.; Tominaga, M.; Hori, A.; Therrien, B. *Acc. Chem. Res.* **2005**, *38*, 369; (d) Farha, O. K.; Hupp, J. T. *Acc. Chem. Res.* **2010**, *43*, 1166; (e) Gianneschi, N. C.; Masar, M. S.; Mirkin, C. A. *Acc. Chem. Res.* **2005**, *38*, 825; (f) Caulder, D. L.; Brückner, C.; Powers, R. E.; König, S.; Parac, T. N.; Leary, J. A.; Raymond, K. N. *J. Am. Chem. Soc.* **2001**, *123*, 8923; (g) Caulder, D. L.; Raymond, K. N. *Acc. Chem. Res.* **1999**, *32*, 975; (h) Chakrabarty, R.; Mukherjee, P. S.; Stang, P. J. *Chem. Rev.* **2011**, *111*, 6810; (i) Kryschenko, Y. K.; Seidel, S. R.; Arif, A. M.; Stang, P. J. *J. Am. Chem. Soc.* **2003**, *125*, 5193; (j) Seidel, S. R.; Stang, P. J. *Acc. Chem. Res.* **2002**, *35*, 972.

(9) (a) Breiner, B.; Clegg, J. K.; Nitschke, J. R. *Chem. Sci.* **2011**, *2*; (b) Dydio, P.; Dzik, W. I.; Lutz, M.; de Bruin, B.; Reek, J. N. H. *Angew. Chem. Int. Ed.* **2011**, *50*, 396; (c) Koblenz, T. S.; Wassenaar, J.; Reek, J. N. H. *Chem. Soc. Rev.* **2008**, *37*; (d) Fiedler, D.; Leung, D. H.; Bergman, R. G.; Raymond, K. N. *Acc. Chem. Res.* **2004**, *38*, 349; (e) Pluth, M. D.; Bergman, R. G.; Raymond, K. N. *Acc. Chem. Res.* **2009**, *42*, 1650; (f) Lee, J.; Farha, O. K.; Roberts, J.; Scheidt, K. A.; Nguyen, S. T.; Hupp, J. T. *Chem. Soc. Rev.* **2009**, *38*; (g) Lee, S. J.; Lin, W. *Acc. Chem. Res.* **2008**, *41*, 521; (h) Yamauchi, Y.; Fujita, M. *Chem. Comm.* **2010**, *46*; (i) Yoshizawa, M.; Klosterman, J. K.; Fujita, M. *Angew. Chem., Int. Ed.* **2009**, *48*, 3418.

(10) (a) Mishra, A.; Vajpayee, V.; Kim, H.; Lee, M. H.; Jung, H.; Wang, M.; Stang, P. J.; Chi, K.-W. *Dalton Trans.* **2012**, *41*; (b) Vajpayee, V.; Kim, H.; Mishra, A.; Mukherjee, P. S.; Stang, P. J.; Lee, M. H.; Kim, H. K.; Chi, K.-W. *Dalton Trans.* **2011**, *40*, 3112; (c) Müller, C.; Whiteford, J. A.; Stang, P. J. *J. Am. Chem. Soc.* **1998**, *120*, 9827; (d) Whiteford, J. A.; Stang, P. J.; Huang, S. D. *Inorg. Chem.* **1998**, *37*, 5595; (e) Ghosh, S.; Chakrabarty, R.; Mukherjee, P. S. *Inorg. Chem.* **2008**, *48*, 549; (f) Amouri, H.; Desmarets, C.; Moussa, J. *Chem. Rev.* **2012**, 10.1021/cr200345v; (g) Barry, N. P. E.; Therrien, B. *Eur. J. Inorg. Chem.* **2009**, *2009*, 4695; (h) Takezawa, H.; Murase, T.; Fujita, M. *J. Am. Chem. Soc.* **2012**, *134*, 17420.

(11) (a) Flamigni, L.; Ventura, B.; Oliva, A. I.; Ballester, P. *Chem. Eur. J.* **2008**, *14*, 4214; (b) Oliva, A. I.; Ventura, B.; Wurthner, F.; Camara-Campos, A.; Hunter, C. A.; Ballester, P.; Flamigni, L. *Dalton Trans.* **2009**; *20*, 4023; (c) Indelli, M. T.; Chiorboli, C.; Scandola, F.; Iengo, E.; Osswald, P.; Würthner, F. *J.Phys. Chem. B* **2010**, *114*, 14495; (d) Jensen, R. A.; Kelley, R. F.; Joong Lee, S.; Wasielewski, M. R.; Hupp, J. T.; Tiede, D. M. *Chem. Comm.* **2008**; *16*, 1886; (e) Kelley, R. F.; Lee, S. J.; Wilson, T. M.; Nakamura, Y.; Tiede, D. M.; Osuka, A.; Hupp, J. T.; Wasielewski, M. R. *J. Am. Chem. Soc.* **2008**, *130*, 4277; (f) Sprafke, J. K.; Kondratuk, D. V.; Wykes, M.; Thompson, A. L.; Hoffmann, M.; Drevinskas, R.; Chen, W.-H.; Yong, C. K.; Kärnbratt, J.; Bullock, J. E.; Malfois, M.; Wasielewski, M. R.; Albinsson, B.; Herz, L. M.; Zigmantas, D.; Beljonne, D.; Anderson, H. L. *J. Am. Chem. Soc.* **2011**, *133*, 17262.

(12) (a) Fyles, T. M.; Tong, C. C. *New J. Chem.* **2007**, *31*; (b) Hannon, M. J. *Chem. Soc. Rev.* **2007**, *36*; (c) Hannon, M. J.; Moreno, V.; Prieto, M. J.; Moldrheim, E.; Sletten, E.; Meistermann, I.; Isaac, C. J.; Sanders, K. J.; Rodger, A. *Angew. Chem. Int. Ed.* **2001**, *40*, 879; (d) Kieltyka, R.; Englebienne, P.; Fakhoury, J.; Autexier, C.; Moitessier, N.; Sleiman, H. F. *J. Am. Chem. Soc.* **2008**, *130*, 10040; (e) Ma, D.-L.; Che, C.-M.; Yan, S.-C. *J. Am. Chem. Soc.* **2008**, *131*, 1835; (f) Barry, N. P. E.; Edafe, F.; Dyson, P. J.; Therrien, B. *Dalton Trans.* **2010**, *39*, 2816; (g) Barry, N. P.

E.; Edafe, F.; Therrien, B. *Dalton Trans.* **2011**, *40*, 7172; (h) Barry, N. P. E.; Zava, O.; Furrer, J.; Dyson, P. J.; Therrien, B. *Dalton Trans.* **2010**, *39*, 5272; (i) Paul, L. E. H.; Therrien, B.; Furrer, J. *Inorg. Chem.* **2011**, *51*, 1057; (j) Yi, J. W.; Barry, N. P. E.; Furrer, M. A.; Zava, O.; Dyson, P. J.; Therrien, B.; Kim, B. H. *Bioconjugate Chem.* **2012**, 10.1021/bc200472n; (k) Zava, O.; Mattsson, J.; Therrien, B.; Dyson, P. J. *Chem.-Eur. J.* **2010**, *16*, 1428; (l) Vajpayee, V.; Song, Y. H.; Jung, Y. J.; Kang, S. C.; Kim, H.; Kim, I. S.; Wang, M.; Cook, T. R.; Stang, P. J.; Chi, K.-W. *Dalton Trans.* **2012**; *41*, 3046; (m) Vajpayee, V.; Song, Y. H.; Yang, Y. J.; Kang, S. C.; Kim, H.; Kim, I. S.; Wang, M.; Stang, P. J.; Chi, K.-W. *Organometallics* **2011**, *30*, 3242; (n) Vajpayee, V.; Yang, Y. J.; Kang, S. C.; Kim, H.; Kim, I. S.; Wang, M.; Stang, P. J.; Chi, K.-W. *Chem. Comm.* **2011**, *47*; 5184; (o) Cook, T. R.; Vajpayee, V.; Lee, M. H.; Stang, P. J.; Chi, K.-W. *Acc. Chem. Res.* **2013**, 10.1021/ar400010v.

(13) (a) Cotton, A. F.; Wilkinson, G.; Murillo, C. A.; Bochmann, M. *Advanced Inorganic Chemistry*, 5 ed.; John Wiley & Sons, Inc., United Kingdom, 1999; (b) Wu, D.-Y.; Ren, B.; Xu, X.; Liu, G.-K.; Yang, Z.-L.; Tian, Z.-Q. *J. Chem. Phys.* **2003**, *119*, 1701; (c) Al Takhin, G.; Skinner, H. A.; Zaki, A. A. *J. Chem. Soc., Dalton Trans.* **1983**, *10* ,2323.

(14) Zheng, Y.-R.; Stang, P. J. *J. Am. Chem. Soc.* **2009**, *131*, 3487.

(15) Yeh, R. M.; Ziegler, M.; Johnson, D. W.; Terpin, A. J.; Raymond, K. N. *Inorg. Chem.* **2001**, *40*, 2216.

(16) Yeh, R. M.; Xu, J.; Seeber, G.; Raymond, K. N. *Inorg. Chem.* **2005**, *44*, 6228.

(17) Saalfrank, R. W.; Demleitner, B.; Glaser, H.; Maid, H.; Bathelt, D.; Hampel, F.; Bauer, W.; Teichert, M. *Chem.-Eur. J.* **2002**, *8*, 2679.

(18) Saalfrank, R. W.; Maid, H.; Scheurer, A.; Puchta, R.; Bauer, W. *Eur. J. Inorg. Chem.* **2010**, *2010*, 2903.

(19) Stang, P. J.; Olenyuk, B. *Acc. Chem. Res.* **1997**, *30*, 502.

(20) Fujita, M. *Chem. Soc. Rev.* **1998**, *27*, 417.

(21) (a) Albertí, F. M.; Zielinski, W.; Morell Cerdà, M.; Sanz Miguel, P. J.; Troeppner, O.; Ivanović-Burmazović, I.; Lippert, B. *Chem.-Eur. J.* **2013**, *19*, 9800; (b) Baxter, P.; Lehn, J.-M.; DeCian, A.; Fischer, J. *Angew. Chem., Int. Ed.* **1993**, *32*, 69; (c) Shankar, B.; Elumalai, P.; Hussain, F.; Sathiyendiran, M. *J. Organomet. Chem.* **2013**, *732*, 130; (d) Johnson, A. M.; Young, M. C.; Hooley, R. J. *Dalton Trans.* **2013**, *42*, 8394; (e) Smulders, M. M. J.; Riddell, I. A.; Browne, C.; Nitschke, J. R. *Chem. Soc.*

Rev. **2013**, *42*, 1728; (f) Wu, T.; Lin, Y.-J.; Jin, G.-X. *Dalton Trans.* **2013**, *42*, 82.

(22) Saha, M. L.; De, S.; Pramanik, S.; Schmittel, M. *Chem. Soc. Rev.* **2013**, *42*, 6860.

(23) (a) Zheng, Y.-R.; Yang, H.-B.; Northrop, B. H.; Ghosh, K.; Stang, P. J. *Inorg. Chem.* **2008**, *47*, 4706; (b) Safont-Sempere, M. M.; Fernández, G.; Würthner, F. *Chem. Rev.* **2011**, *111*, 5784; (c) Zhao, L.; Northrop, B. H.; Zheng, Y.-R.; Yang, H.-B.; Lee, H. J.; Lee, Y. M.; Park, J. Y.; Chi, K.-W.; Stang, P. J. *J. Org. Chem.* **2008**, *73*, 6580; (d) Northrop, B. H.; Zheng, Y.-R.; Chi, K.-W.; Stang, P. J. *Acc. Chem. Res.* **2009**, *42*, 1554; (e) Rowan, S. J.; Hamilton, D. G.; Brady, P. A.; Sanders, J. K. M. *J. Am. Chem. Soc.* **1997**, *119*, 2578; (f) Zheng, Y.-R.; Northrop, B. H.; Yang, H.-B.; Zhao, L.; Stang, P. J. *J. Org. Chem.* **2009**, *74*, 3554.

(24) (a) Smulders, M. M. J.; Jiménez, A.; Nitschke, J. R. *Angew. Chem., Int. Ed.* **2012**, *51*, 6681; (b) Bar, A. K.; Raghothama, S.; Moon, D.; Mukherjee, P. S. *Chem.-Eur. J.* **2012**, *18*, 3199; (c) Lee, J.; Ghosh, K.; Stang, P. J. *J. Am. Chem. Soc.* **2009**, *131*, 12028; (d) Wang, M.; Zheng, Y.-R.; Ghosh, K.; Stang, P. J. *J. Am. Chem. Soc.* **2010**, *132*, 6282; (e) Lee, S. J.; Cho, S.-H.; Mulfort, K. L.; Tiede, D. M.; Hupp, J. T.; Nguyen, S. T. *J. Am. Chem. Soc.* **2008**, *130*, 16828; (f) Mahata, K.; Schmittel, M. *J. Am. Chem. Soc.* **2009**, *131*, 16544; (g) Samanta, D.; Shanmugaraju, S.; Joshi, S. A.; Patil, Y. P.; Nethaji, M.; Mukherjee, P. S. *Chem. Commun.* **2012**, *48*, 2298.

(25) (a) Neogi, S.; Lorenz, Y.; Engeser, M.; Samanta, D.; Schmittel, M. *Inorg. Chem.* **2013**, *52*, 6975; (b) Yoshizawa, M.; Nagao, M.; Kumazawa, K.; Fujita, M. *J. Organomet. Chem.* **2005**, *690*, 5383; (c) Yamanaka, M.; Yamada, Y.; Sei, Y.; Yamaguchi, K.; Kobayashi, K. *J. Am. Chem. Soc.* **2006**, *128*, 1531; (d) Schmittel, M.; Mahata, K. *Inorg. Chem.* **2009**, *48*, 822; (e) Schmittel, M.; Saha, M. L.; Fan, J. *Org. Lett.* **2011**, *13*, 3916.

(26) Teo, P.; Koh, L. L.; Hor, T. S. A. *Inorg. Chem.* **2003**, *42*, 7290.

(27) (a) Zheng, Y.-R.; Zhao, Z.; Wang, M.; Ghosh, K.; Pollock, J. B.; Cook, T. R.; Stang, P. J. *J. Am. Chem. Soc.* **2010**, *132*, 16873; (b) Li, S.; Huang, J.; Cook, T. R.; Pollock, J. B.; Kim, H.; Chi, K.-W.; Stang, P. J. *J. Am. Chem. Soc.* **2013**, *135*, 2084; (c) Wang, M.; Zheng, Y.-R.; Cook, T. R.; Stang, P. J. *Inorg. Chem.* **2011**, *50*, 6107; (d) Zheng, Y.-R.; Lan, W.-J.; Wang, M.; Cook, T. R.; Stang, P. J. *J. Am. Chem. Soc.* **2011**, *133*, 17045.

(28) (a) Bar, A. K.; Chakrabarty, R.; Mukherjee, P. S. *Inorg. Chem.* **2009**, *48*, 10880; (b) Chuang, C.-H.; Sathiyendiran, M.; Tseng, Y.-H.; Wu, J.-Y.; Hsu, K.-C.; Hung, C.-H.; Wen, Y.-S.; Lu, K.-L. *Organometallics* **2009**, *29*, 283; (c) Chi, K.-W.; Addicott, C.; Stang, P. J. *J. Org. Chem.* **2004**, *69*,

2910; (d) Li, X.-J.; Jiang, F.-L.; Wu, M.-Y.; Zhang, S.-Q.; Zhou, Y.-F.; Hong, M.-C. *Inorg. Chem.* **2012**, *51*, 4116; (e) Olenyuk, B.; Fechtenkotter, A.; Stang, P. J. *J. Chem. Soc., Dalton Trans.* **1998**, *0*, 1707; (f) McQuillan, F. S.; Chen, H.; Hamor, T. A.; Jones, C. J.; Jones, H. A.; Sidebotham, R. P. *Inorg. Chem.* **1999**, *38*, 1555; (g) Tabellion, F. M.; Seidel, S. R.; Arif, A. M.; Stang, P. J. *J. Am. Chem. Soc.* **2001**, *123*, 11982; (h) Fujita, M.; Nagao, S.; Ogura, K. *J. Am. Chem. Soc.* **1995**, *117*, 1649; (i) Fujita, M.; Ibukuro, F.; Seki, H.; Kamo, O.; Imanari, M.; Ogura, K. *J. Am. Chem. Soc.* **1996**, *118*, 899; (j) Liu, X.; Eisenberg, A. H.; Stern, C. L.; Mirkin, C. A. *Inorg. Chem.* **2001**, *40*, 2940; (k) Bell, Z. R.; Harding, L. P.; Ward, M. D. *Chem. Commun.* **2003**, *0*, 2432; (l) Müller, I. M.; Spillmann, S.; Franck, H.; Pietschnig, R. *Chem.-Eur. J.* **2004**, *10*, 2207; (m) Schweiger, M.; Seidel, S. R.; Schmitz, M.; Stang, P. J. *Org. Lett.* **2000**, *2*, 1255; (n) Childs, L. J.; Alcock, N. W.; Hannon, M. J. *Angew. Chem., Int. Ed.* **2002**, *41*, 4244.

(29) (a) Mukherjee, P. S.; Das, N.; Stang, P. J. *J. Org. Chem.* **2004**, *69*, 3526; (b) Benkstein, K. D.; Hupp, J. T.; Stern, C. L. *J. Am. Chem. Soc.* **1998**, *120*, 12982; (c) Kuehl, C. J.; Yamamoto, T.; Seidel, S. R.; Stang, P. J. *Org. Lett.* **2002**, *4*, 913; (d) Shanmugaraju, S.; Bar, A. K.; Chi, K.-W.; Mukherjee, P. S. *Organometallics* **2010**, *29*, 2971; (e) Shanmugaraju, S.; Jadhav, H.; Patil, Y. P.; Mukherjee, P. S. *Inorg. Chem.* **2012**, *51*, 13072; (f) Shanmugaraju, S.; Joshi, S. A.; Mukherjee, P. S. *Inorg. Chem.* **2011**, *50*, 11736; (g) Moon, D.; Kang, S.; Park, J.; Lee, K.; John, R. P.; Won, H.; Seong, G. H.; Kim, Y. S.; Kim, G. H.; Rhee, H.; Lah, M. S. *J. Am. Chem. Soc.* **2006**, *128*, 3530; (h) Qin, Z.; Jennings, M. C.; Puddephatt, R. J. *Chem. Commun.* **2001**, *0*, 2676.

(30) (a) Lakowicz, J. R. *Principles of Fluorescence Spectroscopy*, 3 ed., Springer, New York, NY, 2006; (b) McHale, J. L. *Molecular Spectroscopy*, 1 ed., Prentice Hall, Upper Saddle River, NJ, 1999; (c) Crews, P.; Rodriguez, J.; Jaspars, M. *Organic Structure Analysis*, 1 ed., Oxford University Press, London, UK, 1998.

(31) (a) Cramer, C. J. *Essentials of Computational Chemistry: Theories and Models*; 2 ed., John Wiley & Sons, Ltd., London, UK, 2004; (b) Foresman, J. B.; Frisch, E. *Exploring Chemistry with Electronic Structure Methods*; 2 ed.; Gaussian, Inc., Pittsburgh, PA, 1996; (c) Parr, R. G.; Weitao, Y. *Density-Functional Theory of Atoms and Molecules*, 1 ed.; Oxford University Press, London, UK,1994.

(32) Kohn, W.; Sham, L. J. *Physical Review* **1965**, *140*, A1133.

(33) (a) Becke, A. D. *J. Chem. Phys.* **1993**, *98*, 1372; (b) Perdew, J. P.; Ernzerhof, M.; Burke, K. *J. Chem. Phys.* **1996**, *105*, 9982.

(34) (a) Runge, E.; Gross, E. K. U. *Phys. Rev. Lett.* **1984**, *52*, 997; (b)

Petersilka, M.; Gossmann, U. J.; Gross, E. K. U. *Phys. Rev. Lett.* **1996**, *76*, 1212.

(35) (a) Guo, Z.; Sadler, P. J. *Angew. Chem. Int. Ed.* **1999**, *38*, 1512; (b) Zhao, Q.; Huang, C.; Li, F. *Chem. Soc. Rev.* **2011**, *40*, 2508; (c) McRae, R.; Bagchi, P.; Sumalekshmy, S.; Fahrni, C. J. *Chem. Rev.* **2009**, *109*, 4780; (d) Clarke, M. J.; Zhu, F.; Frasca, D. R. *Chem. Rev.* **1999**, *99*, 2511.

(36) (a) Celli, J. P.; Spring, B. Q.; Rizvi, I.; Evans, C. L.; Samkoe, K. S.; Verma, S.; Pogue, B. W.; Hasan, T. *Chem. Rev.* **2010**, *110*, 2795; (b) Lovell, J. F.; Liu, T. W. B.; Chen, J.; Zheng, G. *Chem. Rev.* **2010**, *110*, 2839; (c) Lau, J. T. F.; Lo, P.-C.; Fong, W.-P.; Ng, D. K. P. *J. Med. Chem.* **2012**, *55*, 5446; (d) Schmitt, F.; Govindaswamy, P.; Süss-Fink, G.; Ang, W. H.; Dyson, P. J.; Juillerat-Jeanneret, L.; Therrien, B. *J. Med. Chem.* **2008**, *51*, 1811; (e) Fry, N. L.; Mascharak, P. K. *Acc. Chem. Res.* **2011**, *44*, 289.

(37) (a) Shilov, A. E.; Shul'pin, G. B. *Chem. Rev.* **1997**, *97*, 2879; (b) Fagnoni, M.; Dondi, D.; Ravelli, D.; Albini, A. *Chem. Rev.* **2007**, *107*, 2725; (c) Fox, M. A.; Dulay, M. T. *Chem. Rev.* **1993**, *93*, 341.

(38) (a) Cook, T. R.; Dogutan, D. K.; Reece, S. Y.; Surendranath, Y.; Teets, T. S.; Nocera, D. G. *Chem. Rev.* **2010**, *110*, 6474; (b) Walter, M. G.; Warren, E. L.; McKone, J. R.; Boettcher, S. W.; Mi, Q.; Santori, E. A.; Lewis, N. S. *Chem. Rev.* **2010**, *110*, 6446; (c) Nazeeruddin, M. K.; Grätzel, M. *Photofunctional Transition Metal Complexes*; Springer, New York, 2007; Vol. 123, p 113; (d) Heimer, T. A.; Bignozzi, C. A.; Meyer, G. J. *J. Phys. Chem.* **1993**, *97*, 11987.

(39) (a) Hui, C.-K.; Chu, B. W.-K.; Zhu, N.; Yam, V. W.-W. *Inorg. Chem.* **2002**, *41*, 6178; (b) Wong, H.-L.; Tao, C.-H.; Zhu, N.; Yam, V. W.-W. *Inorg. Chem.* **2010**, *50*, 471; (c) Wong, K. M.-C.; Yam, V. W.-W. *Acc. Chem. Res.* **2011**, *44*, 424; (d) Adamson, A. W.; Waltz, W. L.; Zinato, E.; Watts, D. W.; Fleischauer, P. D.; Lindholm, R. D. *Chem. Rev.* **1968**, *68*, 541; (e) Brooks, J.; Babayan, Y.; Lamansky, S.; Djurovich, P. I.; Tsyba, I.; Bau, R.; Thompson, M. E. *Inorg. Chem.* **2002**, *41*, 3055; (f) Caspar, J. V. *J. Am. Chem. Soc.* **1985**, *107*, 6718; (g) Chan, S.-C.; Chan, M. C. W.; Wang, Y.; Che, C.-M.; Cheung, K.-K.; Zhu, N. *Chem.-Eur. J.* **2001**, *7*, 4180; (h) Danilov, E. O.; Rachford, A. A.; Goeb, S. b.; Castellano, F. N. *J. Phys. Chem. A* **2009**, *113*, 5763; (i) Eryazici, I.; Moorefield, C. N.; Newkome, G. R. *Chem. Rev.* **2008**, *108*, 1834; (j) Fleischauer, P. D.; Fleischauer, P. *Chem. Rev.* **1970**, *70*, 199; (k) Forniés, J.; Fuertes, S.; Martín, A.; Sicilia, V.; Lalinde, E.; Moreno, M. T. *Chem.-Eur. J.* **2006**, *12*, 8253; (l) Goeb, S.; Prusakova, V.; Wang, X.; Vezinat, A.; Salle, M.; Castellano, F. N. *Chem. Comm.* **2011**, *47*; (m) Ho, Y.-M.; Koo, C.-K.; Wong, K.-L.; Kong, H.-K.; Chan, C. T.-L.; Kwok, W.-M.; Chow, C.-F.; Lam, M. H.-W.; Wong, W.-Y. *Dalton Trans.* **2012**, *41*; 1792; (n) Kui, S. C. F.; Hung, F.-F.; Lai, S.-L.;

Yuen, M.-Y.; Kwok, C.-C.; Low, K.-H.; Chui, S. S.-Y.; Che, C.-M. *Chem.-Eur. J.* **2012**, *18*, 96; (o) Lees, A. J. *Chem. Rev.* **1987**, *87*, 711; (p) Pomestchenko, I. E.; Luman, C. R.; Hissler, M.; Ziessel, R.; Castellano, F. N. *Inorg. Chem.* **2003**, *42*, 1394; (q) Rausch, A. F.; Murphy, L.; Williams, J. A. G.; Yersin, H. *Inorg. Chem.* **2011**, *51*, 312; (r) Wang, Z.; Turner, E.; Mahoney, V.; Madakuni, S.; Groy, T.; Li, J. *Inorg. Chem.* **2010**, *49*, 11276; (s) Weinstein, J. A.; Tierney, M. T.; Davies, E. S.; Base, K.; Robeiro, A. A.; Grinstaff, M. W. *Inorg. Chem.* **2006**, *45*, 4544; (t) Wong, K. M.-C.; Yam, V. W.-W. *Coordination Chem. Rev.* **2007**, *251*, 2477; (u) Yam, V. W.-W. *Acc. Chem. Res.* **2002**, *35*, 555.

(40) (a) Zhao, G.-J.; Yu, F.; Zhang, M.-X.; Northrop, B. H.; Yang, H.; Han, K.-L.; Stang, P. J. *J. Phys. Chem. A* **2011**, *115*, 6390; (b) Zhao, G.-J.; Northrop, B. H.; Han, K.-L.; Stang, P. J. *J. Phys. Chem. A* **2010**, *114*, 9007; (c) Ghosh, S.; Mukherjee, P. S. *Organometallics* **2008**, *27*, 316.

(41) Zhao, G.-J.; Northrop, B. H.; Stang, P. J.; Han, K.-L. *J. Phys. Chem. A* **2010**, *114*, 3418.

(42) Flynn, D. C.; Ramakrishna, G.; Yang, H.-B.; Northrop, B. H.; Stang, P. J.; Goodson, T. *J. Am. Chem. Soc.* **2010**, *132*, 1348.

(43) KaloudiChantzea, A.; Karakostas, N.; Raptopoulou, C. P.; Psycharis, V.; Saridakis, E.; Griebel, J.; Hermann, R.; Pistolis, G. *J. Am. Chem. Soc.* **2010**, *132*, 16327.

(44) Chen, J.-S.; Zhao, G.-J.; Cook, T. R.; Han, K.-L.; Stang, P. J. *J. Am. Chem. Soc.* **2013**, *135*, 6694.

2. MULTICOMPONENT COORDINATION-DRIVEN SELF-ASSEMBLY: ALKYL-BASED STRUCTURES AND MOLECULAR MODELING

2.1 Introduction

A prerequisite for the construction of SCCs using the *directional-bonding*[1] approach is for the components to be inherently rigid and have encoded directionality; as such, flexible building blocks are not usually employed due to the multiple products that may form (dimers, polymers, cyclic oligomers, etc).

The length of the alkyl chain of a flexible subunit is an important determinant of the outcome of a given self-assembly. When using a subunit with Lewis basic sites linked by alkyl spacers, the selective formation of flexible SCCs is possible; however, existing examples are limited to methyl and ethyl spacers, presumably due to the concurrent formation of polymers, dimers, and discrete SCCs that arise when longer chains are used.[2] Furthermore, when designing 3D prismatic structures wherein two multitopic panel-like ligands are held cofacially, care must be taken that the molecular components intended to span the two panels are not size-matched to simply bridge two sites of a single panel ligand, which results in a planar 2D assembly rather than the 3D metallacage (Figure 2.1).[3] Similarly, if

---

Portions of this work have appeared previously:
Pollock, J.B.; Cook, T.R.; Schneider, G.L.; Stang, P.J. Multi-Component Coordination-Driven Self-Assembly: Construction of Alkyl-Based Structures and Molecular Modeling; *Chem–Asian J* **2013**, *8(10)*, 2423-2429.

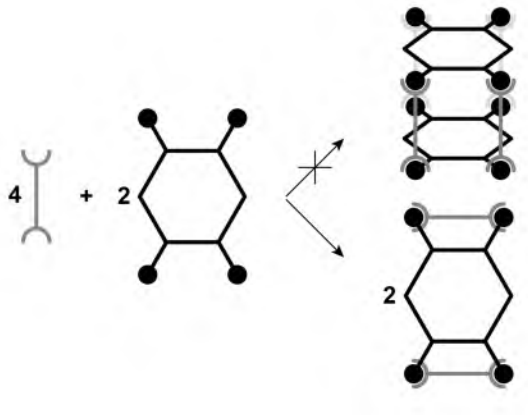

Figure 2.1: If a bridging ligand is large enough, a 2D SCC will be furnished instead of a 3D SCC.

adjacent Lewis bases on a given ligand are within a certain proximity, complexation with a single metal node can occur, furnishing a bridged complex rather than a 3D SCC.[2c]

Despite these difficulties associated with increases to structural complexity, much progress has been made into the incorporation of functional groups within subunits. For example, alkene moieties,[4] which can undergo *cis*- and *trans*-isomerization, and amide linkages[5] have been incorporated into building blocks for the constructruction of predictable architectures. However, after the self-assembly process is complete, these designs are still fairly rigid. As such, systems that preserve a degree of flexibility even after SCC formation (e.g., subunits containing alkyl groups larger than ethylene spacers) are rare. These designs are attractive since they could be used to construct host-guest or catalysis ensembles without predefined cavity sizes or shapes, thus allowing the assembly to adapt to a specific substrate. As such, we have sought new methods to utilize long-chain alkyl-based subunits in efforts to define a new paradigm for the construction of SCCs.

Since the pioneering work of Hor et al.[6] there have been several examples of multicomponent SCCs prepared by using a self-selection process wherein dicarboxylate, dipyridyl, and platinum-containing building blocks self-assembled from a complex mixture;[7] this method has also been extended to systems containing other metal centers.[7,8] In this case, a heteroligated coordination sphere was preferentially formed by coordinating a single neutral pyridyl donor and an anionic carboxylate donor on a single bis(phosphine) Pt(II) metal center (Figure 2.2, top). In fact, it was reported that when homoligated Pt-pyridyl-based squares and Pt-carboxylate-based triangles were mixed in appropriate stoichiometries, rectangular SCCs with heteroligated coordination spheres formed (Figure 2.2, bottom); this result was important because it firmly established the heteroligated coordination sphere as the thermodynamic product for these systems.[7a] This new multicomponent mode of synthesis for SCCs fundamentally differs from the *directional-bonding* approach because it is the platinum node that dictates the thermodynamic structure afforded.

When considering the preference for heteroligation, electronic effects are an obvious avenue of investigation. Thus, the thermodynamic preference for a heteroligated coordination sphere and one contributing factor could be the minimization of charge repulsion between coordinated ligands. Orbital effects such as the *trans* or *cis*-effect could contribute to this as well. An additional factor is the relaxation of the enthalpic penalty for distorting the internal angle between coordinated ligands within the square planar platinum coordination sphere (i.e., deviations from the idealized internal 90° angles around the Pt metal center).

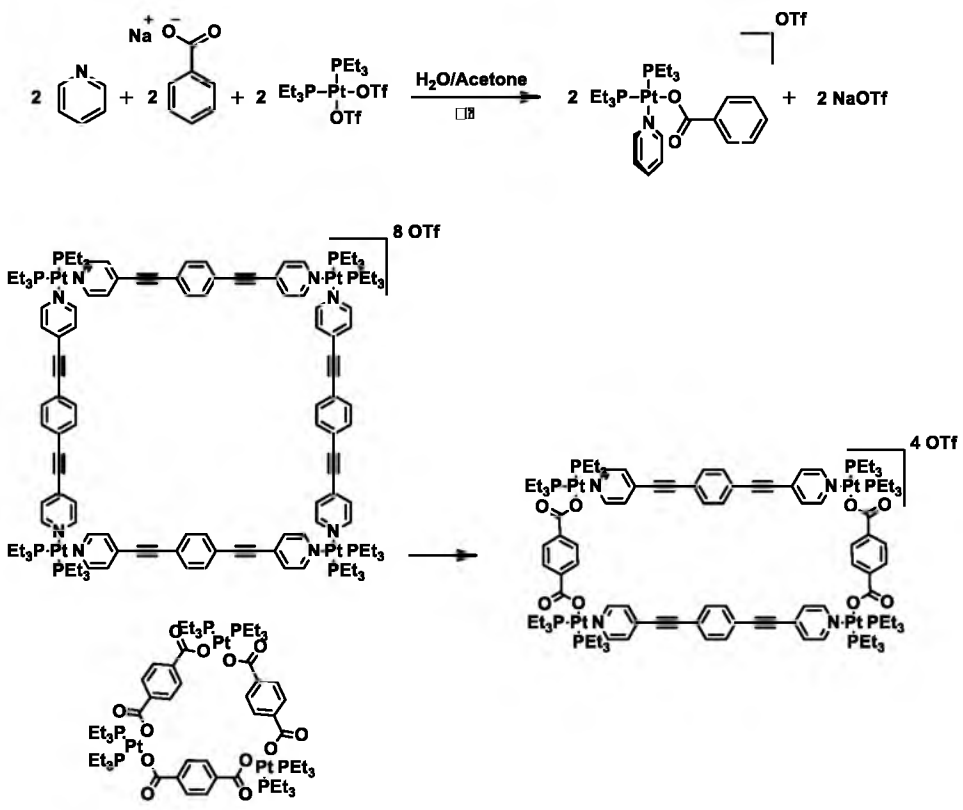

Figure 2.2: Synthesis of three-component systems can be accomplished using the "*charge-seperation"* method. Mixtures of Pt(II), pyridyl, and carboxylate-based compounds favor heteroligated products (*top*). Pt-pyridyl and Pt-carboxylate SCCs will reassemble to furnish heteroligated structures (*bottom*).

Exploiting the multicomponent construction method, a series of 2D metallacycles and a 3D metallacage were constructed from 90° bis(phosphine) Pt(II) metal nodes, alkyl-based dicarboxylates, and rigid pyridyl-containing subunits. Also, to further understand the thermodynamics of the heteroligated coordination sphere, density functional theory and natural population analysis (NPA) calculations were performed on small models wherein deprotonated isonicotinic acid is the coordinating ligand. DFT calculations were also performed on the full constructs shown in the bottom of Figure 2.2 to probe structural and electronic effects not present in the small models.

2.2 Results and Discussion

Flexible, two-dimensional, [4_{Pt}+2_{cb}+2_{py}] rectangular bis(phosphine) Pt(II)-based SCCs **2.05a-b** were prepared by stirring Pt acceptor **2.01** (Scheme 2.1), the dibasic sodium salt of two different length alkyl dicarboxylates **2.02a** or **2.02c**, and a linear dipyridyl subunit **2.03** in a 9:1 (v:v) acetone:H_2O solution. The mixtures were heated to 40°C and allowed to stir for 3 h. The homogenous solutions were then dried overnight *in vacuo*, redissolved in acetone-d_6, and filtered to remove insoluble NaOTf. The SCCs were then characterized by ^{1}H and ^{31}P{^{1}H} NMR and electrospray ionization mass spectrometry (ESI-MS). In each case, characteristic upfield shifts of the pyridyl protons were observed, supporting that the pyridyl nitrogen atoms were coordinated to the Pt metal center. The ^{31}P{^{1}H} NMR of **2.05b**, Figure 2.3, displays two sets of doublets since each phosphorous atom is magnetically inequivalent. This result can be rationalized by having a carboxylate and pyridyl donor bound to the same platinum metal node. However, for **2.06** in Scheme 2.2, two singlets in the ^{31}P{^{1}H} NMR were observed as the predominate species, which is indicative of two species with homoligated coordination spheres. This result is consistent with two unique species, each with their own unique phosphorus environment; such is the case when two donor ligands on the platinum metal node are the same (i.e., carboxylate–Pt–carboxylate or pyridyl–Pt–pyridyl). A plausible explanation for the monomeric nature of SCC **2.06** is the favorable chelation that can occur with the methylene- spaced carboxylate donor, similar to what is observed in malonato-bis(phosphine) Pt(II) systems, shown in Scheme 2.2.[9]

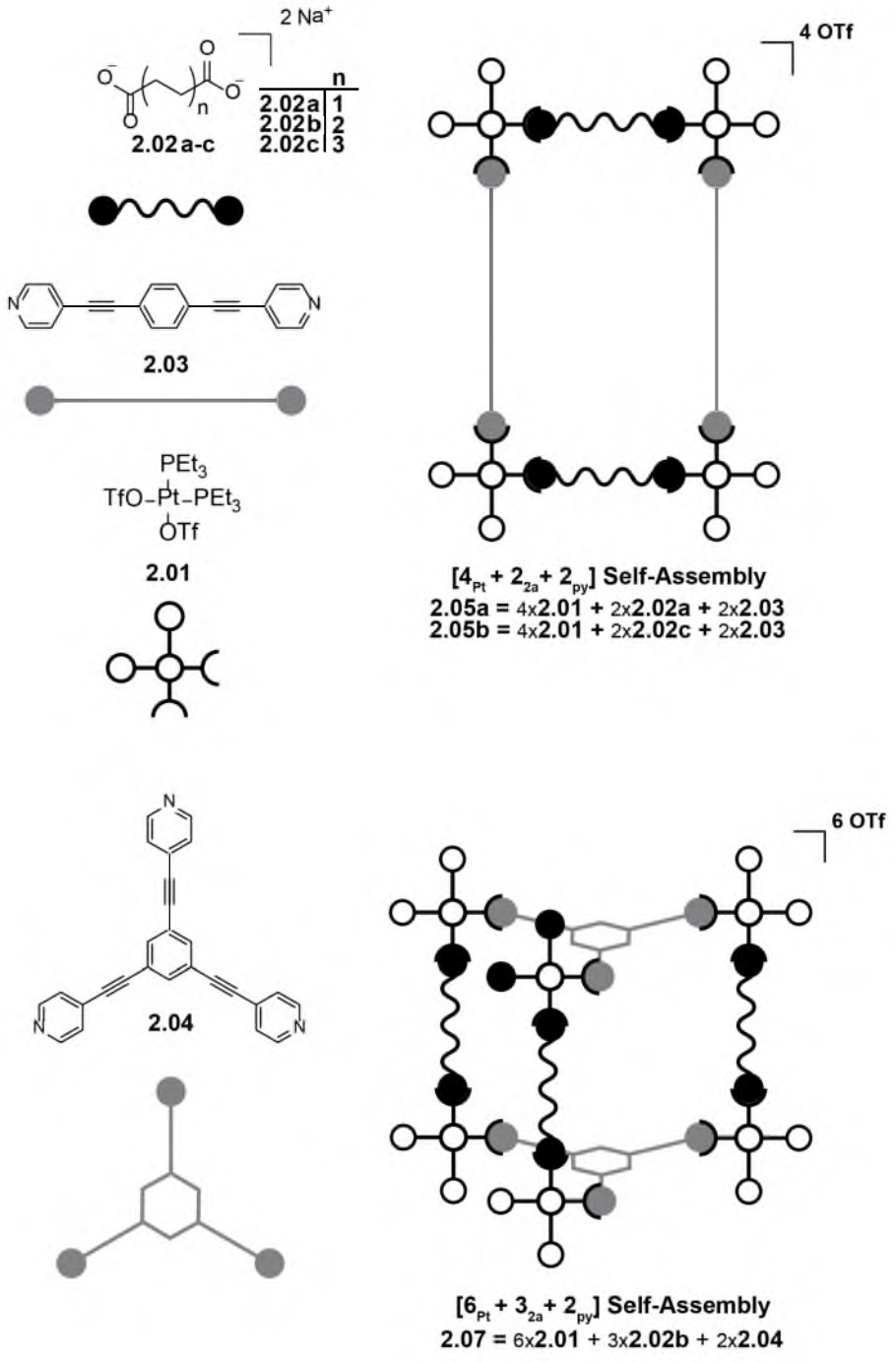

Scheme 2.1: The synthesis of flexible rectangles **2.05a–b** and trigonal prismatic cage **2.07**.

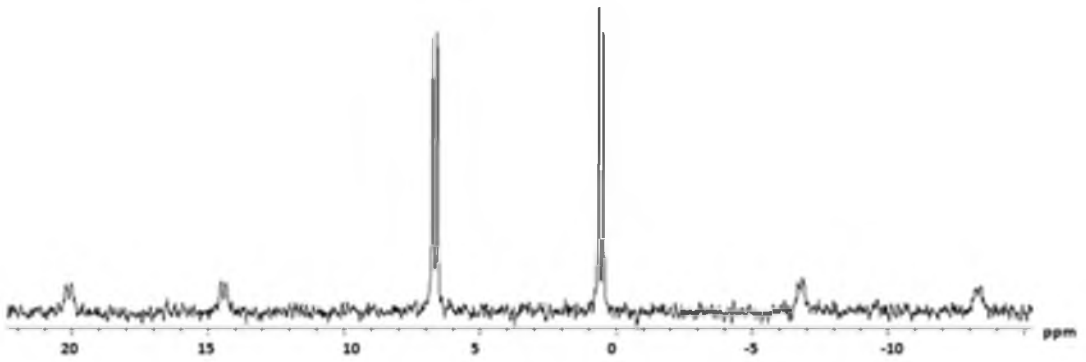

Figure 2.3: $^{31}P\{^{1}H\}$ NMR spectra of **2.05c**.

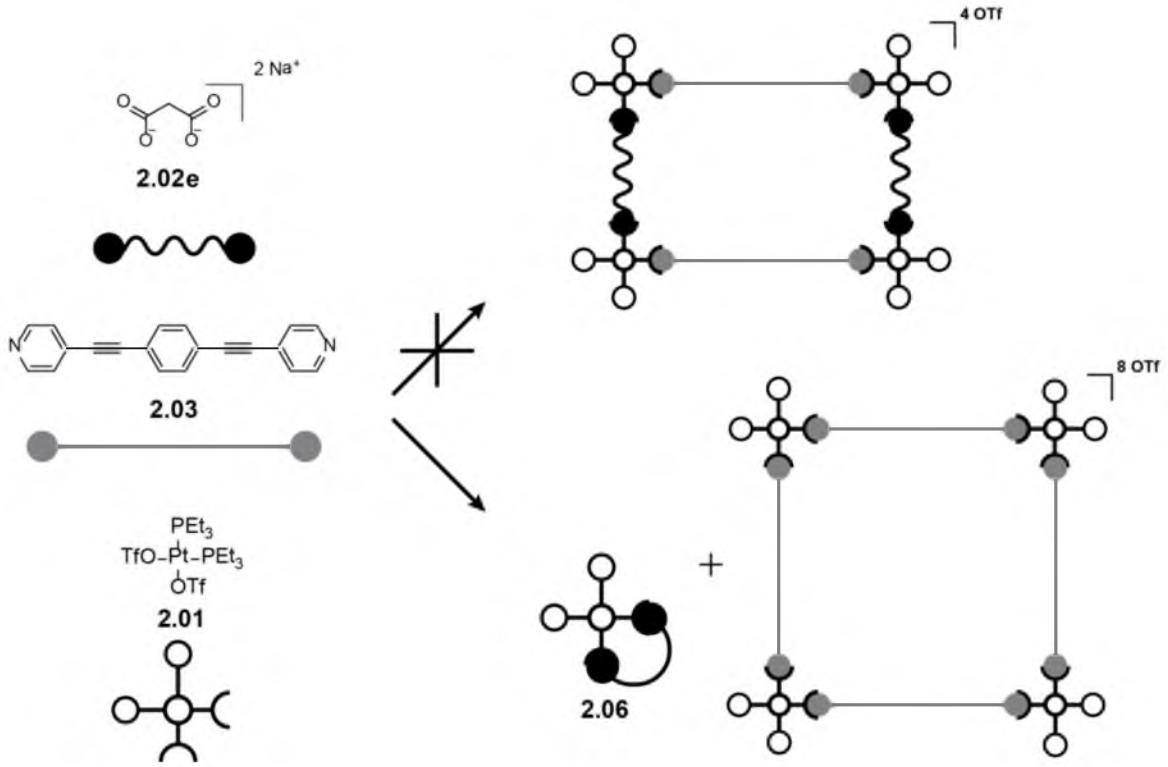

Scheme 2.2: The synthesis of metallacomplex **2.06**.

Dipyridyl linker **2.03** can coordinate two molecules of **2.01** and if the carboxylate linker can bridge those two platinum nodes, a dimer will preferentially form instead of a more complex structure. To probe this effect, sodium n-heptadecanoate dibasic **2.02d** (Scheme 2.3) was specifically chosen since the covalent bond distance, as determined by a Merck molecular force field (MMFF)[10] calculation, between the anionic coordinating oxygen atoms is 19.85Å, while the covalent bond distance between the coordinating nitrogen atoms of the dipyridyl linker **2.03** is 16.90Å. Therefore, since the dicarboxylate unit is longer than the dipyridyl linker, a $[2_{Pt}+1_{cb}+1_{py}]$ dimer complex **2.05c** is expected ratherthan the rectangular $[4_{Pt}+2_{cb}+2_{py}]$ SCC **2.08**. While distinguishing **2.05c** from **2.08** by $^{31}P\{^{1}H\}$ and ^{1}H NMR is difficult, the isotopic spacing of peaks in the ESI-MS spectra are unique to specific intact assemblies; thus, providing evidence that the $[2_{Pt}+1_{cb}+1_{py}]$ assembly, **2.05c**, was formed as the sole product.

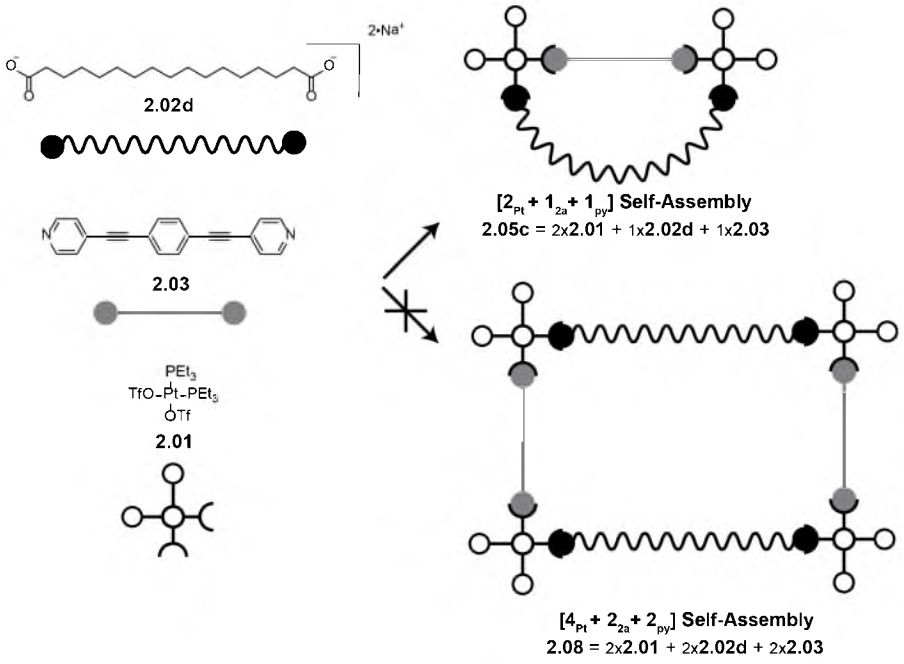

Scheme 2.3: The formation of a $[2_{Pt}+1_{cb}+1_{py}]$ SCC **2.05c**.

Extending the structural library of alkyl-based SCCs, a 3D flexible, trigonal prismatic cage **2.07** (Scheme 2.1) was synthesized by carefully selecting an appropriately sized dicarboxylate ligand **2.02b**, a D_{3h} tripodal ligand **2.04**, and the 90° bis(phosphine) Pt(II) acceptor **2.01**.

2.3 Molecular Modeling

Three sets of single point calculations were performed on the three small models **A**–**C** using three different functionals, which are the Becke three-parameter hybrid exchange with the Lee–Yang–Parr correlation (B3LYP),[11] Minnesota 06 (M06),[12] and a Perdew–Wang exchange[13] modified by Adamo and Barone with Perdew–Wang 91 correlation[14] (mPW1PW91) functionals. In each calculation a 6-31+G** basis set[15] was used for C, H, N, O, and P atoms while the Los Alamos National Laboratory (LANL2-DZ)[16] basis set and pseudopotential were used for Pt. To minimize computational cost, $P(CH_3)_3$ ligands were utilized instead of PEt_3. The ground state energies of the complexes were computed using a polarizable continuum model (PCM)[17] with acetone as the solvent in G09.[18] Natural population analysis (NPA)[19] calculations and frequency analysis were also performed on the optimized structures to gain insight about atomic charges and to confirm the absence of imaginary frequencies.

2.3.1 Small Model Complexes

Table 2.1 summarizes the pertinent information from the calculations of the three models shown in Figure 2.4 using the functionals B3LYP, M06, and mPW1PW91. Since we were interested in probing the energetics arising from the

Table 2.1: Energies of optimized structures for **A**–**C**.

Compound	B3LYP / kcal•mol^{-1}	M06 / kcal•mol^{-1}	mPW1PW91 / kcal•mol^{-1}
A	2.833	0.877	1.710
B	0.000	0.350	0.419
C	0.197	0.000	0.000

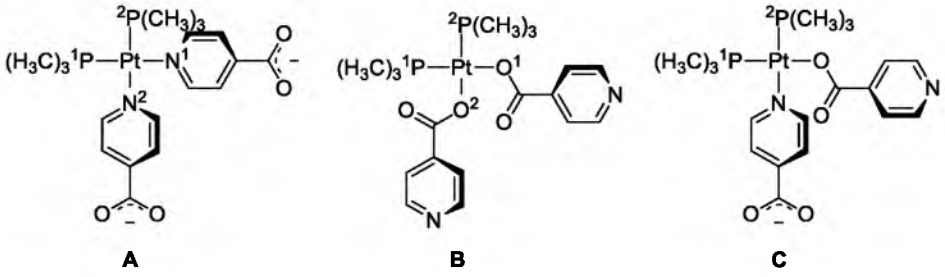

Figure 2.4: The models used in molecular calculations wherein A (homoligated pyridyl), B (homoligated carboxylate), and C (heteroligated) are shown.

coordination sphere around the bis(phosphine) Pt(II) metal center, deprotonated isonicotinic acid was used in these computations since it allows for a direct comparison of the homoligated pyridyl model **A**, homoligated carboxylate model **B**, and heteroligated model **C**. The overall energies listed are relative to the model (**B** for B3LYP and **C** for M06 and mPW1PW91) that had the lowest energy. It should be noted that the largest energy difference observed in the calculations was 2.833 kcal•mol^{-1}, which is small enough of an energy difference to be considered within error of the calculation. However, calculations with both the M06 and mPW1PW91 functionals determined the heteroligated coordination sphere to be the lowest in energy. Morever, a trend is observed when one consideres the energies involved in the synthesis of a heteroligated coordination

sphere such as **C**, which can be accomplished by stirring two homoligated species together (**A** plus **B**); the energies can be calculated by adding each homoligated species (**A** plus **B**; for B3LYP: 2.833 kcal•mol^{-1}) and multiplying the heteroligated species **C** by two since two of **C** (B3LYP: 0.394 kcal•mol^{-1}) would be synthesized in such a case. When doing so, each calculation predicts the heteroligated coordination sphere **C** to be the lowest in energy. However, the largest energy difference observed is 2.439 kcal•mol^{-1} using the B3LYP functional.

To determine whether the models utilized in the calculations were appropriate, the angles and bond lengths were compared to those in a crystal structure of a square bis(triphenylphosphine) Pt(II) SCC with a carboxylate-Pt-pyridyl heteroligated coordination sphere.[20] Table 2.2 lists the data from the B3LYP functional while similar tables can be found in the Appendix for the M06 and mPW1PW91 functionals. From Table 2.2, the internal angle between the coordinated N–Pt–O atoms in model **C** (84.423°) was determined to be close to that of the reported crystal structure (85°), and the Pt–O (2.14±0.01 Å) and Pt–N (2.14±0.01 Å) interatomic distances in each model are in good agreement with those in the previously described crystal structure (Pt–N and Pt–O; interatomic distances of 2.10±0.5 Å).

Point charges from the B3LYP functional NPA calculation are summarized in Table 2.2, and point charges for the M06 and mPW1PW91 functionals can be found in the Appendix. Since each calculation had energies that were very close to each other, only trends consistent with each calculation are briefly discussed.

Table 2.2: Energies, bond lengths, natural point charges, and internal angles

Compound	Bond Length / Å	Natural Point Charges	Angles / °	Optimized Energy / kcal•mol^{-1}
A	Pt–N^1 2.14459	N^1 -0.078	N^1–Pt–N^2 84.151	2.83
	Pt–N^2 2.14450	N^2 -0.078	N^1–Pt–P^2 89.819	
	Pt–P^1 2.33058	P^1 1.279	N^2–Pt–P^1 89.809	
	Pt-P^2 2.33061	P^2 1.280	P^1–Pt–P^2 96.236	
		Pt -1.081		
B	Pt–O^1 2.14080	O^1 -0.0471	O^1–Pt–O^2 86.521	0.00
	Pt–O^2 2.13915	O^2 -0.0472	O^1–Pt–P^2 84.706	
	Pt–P^1 2.29296	P^1 1.407	O^2–Pt–P^1 85.363	
	Pt-P^2 2.29229	P^2 1.337	P^1–Pt–P^2 103.409	
		Pt -0.739		
C	Pt–O 2.14502	O -0.404	O–Pt–N 84.422	0.20
	Pt–N 2.14066	N -0.126	N–Pt–P^1 91.782	
	Pt–P^1 2.30111	P^1 1.563	O–Pt–P^2 85.077	
	Pt-P^2 2.32230	P^2 1.205	P^1–Pt–P^2 98.704	
		Pt -0.949		

The Pt metal center in each model had a large negative value. The electron density on the coordinating *N* of the pyridyl group is lower in model **A** when compared to that of the heteroligated model **C**. The electron density of the coordinating *O* atom of the carboxylate is lower in complex **C** when compared to the average of the densities in **B**, and in each model the phosphine atoms have large positive values with the greatest deviation being between the two phosphine atoms in model **C**.

In summary, the energy differences calculated by each functional are small and therefore imply that shape complementarity or nonfavorable steric interactions may also have a role in determining the thermodynamic outcome of the self-assembly process for SCCs with heteroligated coordination spheres. From the calculations performed, significant differences in the electron density on the phosphine atoms *trans* to the coordinating atoms implicate that a molecular orbital effect (*cis*- and *trans*-influence) may account for the small observed differences in the overall ground-state energies, and it may be the cumulative effect of these small energetic differences in multiPt SCCs that account for the overall thermodynamic preference. Further, more sophisticated calculations with complete SCCs may shed light on the thermodynamic preference for the heteroligated SCCs.

2.3.2 Supramolecular Coordination Complexes

In section 2.3.1, DFT calculations were performed on small complexes to probe the electronic effects of the heteroligated coordination sphere around the metal center; however, it was determined that that shape complementarity or

nonfavorable steric interactions may also have a role in determining the thermodynamic outcome of the self-assembly process for SCCs with heteroligated coordination spheres. Moreover, the heteroligated coordination motif in SCCs may stem from the cumulative effect of the small observed differences in the overall ground-state energies of **A**–**C**.

It was previously reported that when homoligated Pt-pyridyl-based squares and Pt-carboxylate-based triangles were mixed in appropriate stoichiometries, rectangular SCCs with heteroligated coordination spheres formed in solution (Figure 2.2, bottom). This result was important because it established that the thermodynamic preference for a heteroligated coordination sphere could overcome the enthalpic and entropic penalties for deconstructing already formed SCCs. As such, the three SCCs shown in the bottom of Figure 2.2 were modeled by DFT using the B3LYP functional in an acetone solvent field to further understand this phenomenon.

Unlike the small model complexes, the energies associated with each SCC cannot be directly compared since they have differing number and types of atoms. However, the stoichiometric recombination of 3 homoligated Pt-pyridyl-based squares with 4 homoligated Pt-carboxylate-based triangles in solution to form 6 heteroligated rectangular-shaped SCC allows for the energies to be compared since all atoms are conserved in this process. By multiplying the energies of the homoligated species by the correct stoichiometry and adding them (3 homoligated Pt-pyridyl-based squares + 4 homoligated Pt-carboxylate-based triangles; B3LYP, $-2.688 \cdot 10^{7}$ kcal•mol^{-1}), the overall energy of the

homoligated species in solution can then be directly compared to the minimized energy of 6 heteroligated rectangular-shaped SCC ($-2.688 \cdot 10^7$ kcal•mol^{-1}). After comparing the two energies, the system containing the heteroligated rectangular-shaped SCC was determined to be preferred by 121.8 kcal•mol^{-1}. The thermodynamic preference for each individual heteroligated rectangular-shaped SCC was then calculated by dividing 121.8 kcal•mol^{-1} by 6, which was determined to be 20.30 kcal•mol^{-1}.

In the previous section small complex **C** was determined to be the lowest energy complex using the B3LYP functional after the recombination of **A** and **B** with the thermodynamic preference being 2.439 kcal•mol^{-1}. The impetus for the formation of full SCC constructs was assumed to be the cumulative effect of this small energy difference; however, 20.30 kcal•mol^{-1} is much larger than expected. This result clearly demonstrates that the small complexes are not good models for the full constructs and thermodynamic parameters accounting for the larger energy difference in the SCCs are not fully accounted for in **A**–**C**.

It was hypothesized that the thermodynamic preference for the heteroligated rectangular-shaped SCC in Figure 2.2 may also stem from the relaxation of steric strain in the coordiation sphere around the metal center for the triangular-shaped SCCs. The smaller internal angles required for a triangle was expected to account for a level of destabilization in the triangular-shaped SCC, making it higher in energy than the homoligated Pt-pyridyl square. However, from the DFT calculations, it was determined that the triangular-shaped SCC could be synthesized while maintaining internal angles (O-Pt-O) of 81.639°, 82.126°, and

85.004°, which are close in value to those reported for the small model complex **B**. As such, arguments that invoke minimization of steric strain at the metal center must be deemphasized for this system.

In summary, it was determined that the heteroligated rectangular-shaped SCC (Figure 2.2; bottom) is preferred thermodynamically by 20.30 kcal•mol^{-1} over the homoligated squareshaped Pt-pyridyl and homoligated triangle-shaped Pt-carboxylate SCCs. Also, relaxation of any steric strain around the metal center for the homoligated triangle-shaped SCC may have a minimal effect in the thermodynamic outcome for this system; however, the energetic preference for the heteroligated SCC was determined to exceed that expected from the cumulative effects associated with small complex **C**. This result implies that **A**–**C** are not sufficient small models for the SCC transformation from homoligated to heteroligated systems and do not account for all of the thermodynamic parameters necessary to fully understand this phenomenon.

2.4 Conclusion

SCCs have largely been confined to structurally rigid architectures with increasing complexity coming from the inclusion of more subunits and functional groups. It was previously reported that discrete SCCs can be synthesized from three components by preferentially forming a heteroligated coordination sphere around bis(phosphine) Pt(II) metal nodes with carboxylate and pyridyl donors; however, examples of this new construction method were still limited to rigid components with predefined angularities. Utilizing this method, 2D and 3D flexible SCCs were synthesized using alkyl-based dicarboxylates, which could

find applications in catalysis and sensing.

DFT and NPA calculations on small model complexes **A**–**C** determined that the overall energies between the homoligated and heteroligated coordination spheres are not as signficant as previously reported. Moreover, the explanations based on electrostatic effects may not explain the preferential formation of a heteroligated coordination sphere using bis(phosphine) Pt(II) and carboxylate and pyridyl-based donors. Instead, the calculations suggest that an orbital effect can account for the small energy differences in the coordination modes and that shape complementarity may play a significant role in the structural outcome.

Calculations performed on homoligated SCCs that are known to undergo a transformation in solution to form heteroligated SCCs were also performed via DFT. These calculations suggest that during the self-assembly process there may be additional effects that dictate the thermodynamic preference for the heteroligated SCCs in this system that can not be probed by modeling the full constructs or small complexes **A**–**C**. Moreover, deleterious effects due to steric strain within the coordination sphere for heteroligated and homoligated species were determined to be minimal. Instead, this phenomenon needs to be further investigated to fully understand the thermodynamic parameters leading to the heteroligated SCCs before it can be applied to other systems.

2.5 Experimental

The sodium salts **2.02a**–**e** of dicarboxylic acids were prepared in a similar method via neutralization with NaOH in MeOH. Dipyridyl donor **2.03**,[21] D_{3h} tritopic pyridyl ligand **2.04**,[22] and Pt acceptor **2.01**[23] were prepared as reported in the

literature. Deuterated solvents (CD_2Cl_2, $CDCl_3$, D_2O, and Acetone-d_6) were purchased from Cambridge Isotope Laboratory (Andover, MA). NMR spectra were recorded on a Varian Unity 300 spectrometer. The ^1H NMR chemical shifts are reported relative to residual solvent signals. Mass spectra for all SCCs were analyzed using MassLynx software and recorded on a high-resolution Micromass Quattro II triple-quadrupole mass spectrometer using electrospray ionization.

General Procedure for 2D Self-Assembly **2.05a–c** and **2.06**:1.00 μm of sodium dicarboxylate dibasic **2.02a–e**, 0.28 mg (1.00 μm) of **2.03**, and 1.43 mg (2.00 μm) of **2.01** were weighed into a 2 dram glass vial followed by the addition of 1.0 mL of solvent 9:1 (v:v; Acetone/H_2O). The mixture was sealed and immersed in an oil bath at 60–65°C for 1 hr. The solution was then dried via N_2 (*g*) flow and placed *in vacuo* overnight. 1.0 mL of acetone-d_6 was added, and the vial was sealed and immersed in a 60-65°C oil bath for 1 hr. The yellow, homogenous solution was then filtered and transferred to a NMR tube for characterization. Each SCC was synthesized quantitatively.

2.05a: Reaction Scale: 0.44 mg (2.70 μm) of sodium succinate dibasic **2.02a**, 0.76 mg (2.70 μm) of **2.03**, and 4.00 mg (5.40 μm) of **2.01**. ^1H (Acetone-d_6, 300 MHz) δ 8.91 (s, 8H, H_α–Py), δ 7.80 (d, 8H, J = 6.0 Hz, H_β–Py), δ 7.70 (s, 8H, Ar*H*), δ 2.96 (s, 24H, H_2–H_3), δ 1.88–1.93 (m, 56H, H_1 & PCH_2CH_3), δ 1.18–1.37 (m, 72H, PCH_2CH_3). $^{31}P\{^1H\}$ NMR (Acetone-d_6, 121.4 MHz) δ 0.5 (d, J = 21.4 Hz; br, ^{195}Pt satellites, $^1J_{Pt-P}$ 3400 Hz), δ 6.5 (d, J = 21.6; br, ^{195}Pt satellites, $^1J_{Pt-P}$ 3300 Hz). ESI–MS: $[C_{100}H_{152}F_{12}N_4O_{20}P_8Pt_4S_4]$, $[M–3\cdot OTf]^{3+}$ 888.91, $[M–2\cdot OTf]^{2+}$ 1407.90.

2.05b: Reaction Scale: 0.59 mg (2.70 μm) of sodium suberate dibasic **2.02c**, 0.76 mg (2.70 μm) of **2.03**, and 4.00 mg (5.40 μm) of **2.01**. ^{1}H (Acetone–d_6, 300 MHz) δ 8.95 (s, 8H, H_α–Py), δ 7.85 (d, 8H, *J* = 5.7 Hz, H_β–Py), δ 7.65 (s, 8H, Ar*H*), δ 2.96 (s, 24H, H_2–H_4), δ 2.86 (s, 16H, H_5–H_6), δ 1.87–1.94 (m, 56H, H_1 & PCH_2CH_3), δ 1.16–1.36 (m, 72H, PCH_2CH_3), δ 0.76 (s, 12H, H_7–H_8). $^{31}P\{^{1}H\}$ NMR (Acetone–d_6, 121.4 MHz) δ 0.4 (d, *J* = 21.1; br, ^{195}Pt satellites, $^{1}J_{Pt-P}$ 3400 Hz), δ 6.6 (d, *J* = 21.0; br, ^{195}Pt satellites, $^{1}J_{Pt-P}$ 3300 Hz). ESI–MS: $[C_{108}H_{168}F_{12}N_4O_{20}P_8Pt_4S_4]$, $[M–3\cdot OTf]^{3+}$ 926.30, $[M–2\cdot OTf]^{2+}$ 1463.41.

2.05c: Reaction Scale: 0.93 mg (2.70 μm) of sodium n–heptadecanoate dibasic **2.02d**, 0.76 mg (2.70 μm) of **2.03**, and 4.00 mg (5.40 μm) of **2.01**. ^{1}H (Acetone–d_6, 300 MHz) δ 8.93 (s, 8H, H_α–Py), δ 7.79 (d, 8H, *J* = 6.0 Hz, H_β–Py), δ 7.39 (s, 8H, Ar*H*), δ 2.91 (s, 8H, H_2)δ 1.93–2.00 (m, 56H, H_1 & PCH_2CH_3), δ 1.16–1.36 (m, 72H, PCH_2CH_3), δ 1.01 (s, 24H, H_3–H_5), δ 0.76 (s, 16H, H_5–H_6), δ 0.76 (s, 12H, H_7–H_8). $^{31}P\{^{1}H\}$ NMR (Acetone–d_6, 121.4 MHz) δ 0.5 (d, *J* = 20.8; br, ^{195}Pt satellites, $^{1}J_{Pt-P}$ 3400 Hz), δ 6.6 (d, *J* = 23.7; br, ^{195}Pt satellites, $^{1}J_{Pt-P}$ 3300 Hz). ESI–MS: $[C_{63}H_{102}F_6N_2O_{10}P_4Pt_2S_2]$, $[M–2\cdot OTf]^{2+}$ 720.3.

2.06: Reaction Scale: 0.40 mg (2.70 μm) of sodium malonate dibasic **2.02e**, 0.76 mg (2.70 μm) of **2.03**, and 4.00 mg (5.40 μm) of **2.01**. ^{1}H (Acetone–d_6, 300 MHz) δ 9.27 (d, 16H, *J* = 6.0 Hz, H_α–Py), δ 7.77 (d, 16H, *J* = 6.0 Hz, H_β–Py), δ 7.69 (s, 16H, Ar*H*), δ 3.20 (s, 2H, H_1), δ 1.28–1.40 (m, 50H, PCH_2CH_3), δ 1.14–1.25 (m, 90H, PCH_2CH_3). $^{31}P\{^{1}H\}$ NMR (Acetone–d_6, 121.4 MHz) δ 0.3 (s; br, ^{195}Pt satellites, $^{1}J_{Pt-P}$ 3100 Hz), δ 6.0 (s; ^{195}Pt satellites, $^{1}J_{Pt-P}$ 3500 Hz). ESI–MS: $[C_{15}H_{32}O_4P_2Pt]$, $[M]^+$ 533.4; ESI–MS: $[C_{136}H_{168}N_8O_{24}F_{24}P_8Pt_4S_8]$, $[M–4\cdot OTf]^{4+}$

860.2.

Self-Assembly **2.07:** 0.78 mg (4.10 μm) of sodium adipate dibasic **2.02b**, 1.04 mg (2.70 μm) of **2.04**, and 6.00 mg (8.20 μm) of **2.01** were weighed into a 2 dram glass vial followed by the addition of 1.0 mL of solvent 9:1 (Acetone/H_2O). The mixture was sealed and immersed in an oil bath at 60–65°C for 1 h. The solution was then dried via N_2 (g) flow and placed *in vacuo* for 3 h. 1.0 mL of acetone–d_6 was added, and the vial was sealed and immersed in a 60–65°C oil bath for 1 hr. The yellow, homogenous solution was then transferred to a NMR tube for characterization. ^{1}H (Acetone–d_6, 300 MHz) δ 8.99 (s, 8H, H_α–Py), δ 7.86–7.90 (m, 16H, H_β–Py & Ar*H*), δ 1.93–2.00 (m, 52H, H_1 & PC*H*$_2$CH$_3$), δ 1.16–1.36 (m, 72H, PCH$_2$C*H*$_3$), δ 1.01 (s, 24H, H_2–H_4), δ 0.76 (s, 16H, H_5–H_6), δ 0.76 (s, 12H, H_7–H_8). ^{31}P{^{1}H} NMR (Acetone–d_6, 121.4 MHz) δ 0.5 (d, *J* = 21.3; br, ^{195}Pt satellites, $^1J_{Pt-P}$ 3371 Hz), δ 6.4 (d, *J* = 20.6; br, ^{195}Pt satellites, $^1J_{Pt-P}$ 3251 Hz). ESI–MS: [$C_{144}H_{226}F_{18}N_6O_{26}P_{12}Pt_6S_6$], [M–3·OTf]$^{3+}$ 1020.29, [M–2·OTf]$^{2+}$ 1410.04.

Molecular Modeling: Three sets of single point calculations were performed on the three small models **A**–**C** using three different functionals, which are the B3LYP[11], M06,[12] and mPW1PW91[13,14] functionals. The three SCCs that were modeled utilized the B3LYP functional. In each calculation a 6-31+G** basis set[15] was used for C, H, N, O, and P atoms while the LANL2-DZ[16] basis set and pseudopotential were used for Pt. All geometry optimizations were performed with C1 symmetry in an acetone solvent field that was modeled using the integral equation formalism variant of the Polarizable Continuum Model (IEFPCM). On models **A**–**C** a full Natural Bond Orbital (NBO) analysis was performed using

NBO version 3. To minimize computational cost $P(CH_3)_3$ ligands were utilized instead of PEt_3.

2.6 Contributions

All primary work (i.e., synthesis, molecular modeling, spectroscopy, analysis, etc.) was performed by J. Bryant Pollock, while Gregory L. Schneider, an undergraduate in the Stang lab, and Timothy R. Cook assisted in synthesis and served an advisory role, respectively.

2.7 Future Directions

The incorporation of alkyl-based subunits into SCCs has opened a new avenue of investigation with regards to the construction of architectures. The methodology, outlined in section 2.2, is currently being applied to construct porphyrin-based trigonal prisms for host-guest applications and to interrogate electronic communication between cofacial porphyrins. Further, molecular modeling is being applied to similar carboxylate-pyridyl-based SCCs to gain insight into the nature of the heteroligated coordination motif, outlined in scheme 2.1, so that it can be applied to synthesize a library of novel heteroligated SCCs. In turn, the structural complexity of SCCs can be increased giving rise to modes of inquiry for the construction of higher-order multicomponent SCCs.

2.8 References

(1) (a) Chakrabarty, R.; Mukherjee, P. S.; Stang, P. J. *Chem. Rev.* **2011**, *111*, 6810; (b) Seidel, S. R.; Stang, P. J. *Acc. Chem. Res.* **2002**, *35*, 972; (c) Stang, P. J.; Olenyuk, B. *Acc. Chem. Res.* **1997**, *30*, 502.

(2) (a) Olenyuk, B.; Fechtenkotter, A.; J. Stang, P. *J. Chem. Soc., Dalton*

Trans. **1998**, *0*, 1707; (b) McQuillan, F. S.; Chen, H.; Hamor, T. A.; Jones, C. J.; Jones, H. A.; Sidebotham, R. P. *Inorg. Chem.* **1999**, *38*, 1555; (c) Tabellion, F. M.; Seidel, S. R.; Arif, A. M.; Stang, P. J. *J. Am. Chem. Soc.* **2001**, *123*, 11982; (d) Fujita, M.; Ibukuro, F.; Yamaguchi, K.; Ogura, K. *J. Am. Chem. Soc.* **1995**, *117*, 4175; (e) Fujita, M.; Ibukuro, F.; Seki, H.; Kamo, O.; Imanari, M.; Ogura, K. *J. Am. Chem. Soc.* **1996**, *118*, 899; (f) Liu, X.; Eisenberg, A. H.; Stern, C. L.; Mirkin, C. A. *Inorg. Chem.* **2001**, *40*, 2940; (g) Bell, Z. R.; Harding, L. P.; Ward, M. D. *Chem. Commun.* **2003**, *0*, 2432; (h) Müller, I. M.; Spillmann, S.; Franck, H.; Pietschnig, R. *Chem.-Eur. J.* **2004**, *10*, 2207; (i) Fujita, M.; Nagao, S.; Ogura, K. *J. Am. Chem. Soc.* **1995**, *117*, 1649; (j) Schweiger, M.; Seidel, S. R.; Schmitz, M.; Stang, P. J. *Org. Lett.* **2000**, *2*, 1255; (k) Childs, L. J.; Alcock, N. W.; Hannon, M. J. *Angew. Chem. Int. Ed.* **2002**, *41*, 4244.

(3) (a) Sankarasekaran, S. D.; Samanta; P.; Mukherjee, P. *Beilstein J. Org. Chem.* **2012**, *8*, 313; (b) Huang, F.; Yang, H.-B.; Das, N.; Maran, U.; Arif, A. M.; Gibson, H. W.; Stang, P. J. *J. Org. Chem.* **2006**, *71*, 6623; (c) Chi, K.-W.; Addicott, C.; Stang, P. J. *J. Org. Chem.* **2004**, *69*, 2910.

(4) (a) Takezawa, H.; Murase, T.; Fujita, M. *J. Am. Chem. Soc.* **2012**, *134*, 17420; (b) Wang, M.; Zheng, Y.-R.; Ghosh, K.; Stang, P. J. *J. Am. Chem. Soc.* **2010**, *132*, 6282; (c) Kuehl, C. J.; Yamamoto, T.; Seidel, S. R.; Stang, P. J. *Org. Lett.* **2002**, *4*, 913; (d) Das, N.; Mukherjee, P. S.; Arif, A. M.; Stang, P. J. *J. Am. Chem. Soc.* **2003**, *125*, 13950; (e) Benkstein, K. D.; Hupp, J. T.; Stern, C. L. *J. Am. Chem. Soc.* **1998**, *120*, 12982; (f) Ghosh, S.; Chakrabarty, R.; Mukherjee, P. S. *Inorg. Chem.* **2008**, *48*, 549; (g) Kaim, W.; Schwederski, B.; Dogan, A.; Fiedler, J.; Kuehl, C. J.; Stang, P. J. *Inorg. Chem.* **2002**, *41*, 4025.

(5) (a) Shanmugaraju, S.; Joshi, S. A.; Mukherjee, P. S. *Inorg. Chem.* **2011**, *50*, 11736; (b) Shanmugaraju, S.; Jadhav, H.; Patil, Y. P.; Mukherjee, P. S. *Inorg. Chem.* **2012**, *51*, 13072; (c) Shanmugaraju, S.; Bar, A. K.; Chi, K.-W.; Mukherjee, P. S. *Organometallics* **2010**, *29*, 2971; (d) Ghosh, S.; Mukherjee, P. S. *J. Org. Chem.* **2006**, *71*, 8412; (e) Moon, D.; Kang, S.; Park, J.; Lee, K.; John, R. P.; Won, H.; Seong, G. H.; Kim, Y. S.; Kim, G. H.; Rhee, H.; Lah, M. S. *J. Am. Chem. Soc.* **2006**, *128*, 3530; (f) Chang, S.-Y.; Um, M.-C.; Uh, H.; Jang, H.-Y.; Jeong, K.-S. *Chem. Commun.* **2003**, *0*, 2026; (g) Qin, Z.; Jennings, M. C.; Puddephatt, R. J. *Chem. Commun.* **2001**, *0*, 2676.

(6) Teo, P.; Koh, L. L.; Hor, T. S. A. *Inorg. Chem.* **2003**, *42*, 7290.

(7) (a) Zheng, Y.-R.; Lan, W.-J.; Wang, M.; Cook, T. R.; Stang, P. J. *J. Am. Chem. Soc.* **2011**, *133*, 17045; (b) Wang, M.; Zheng, Y.-R.; Cook, T. R.; Stang, P. J. *Inorg. Chem.* **2011**, *50*, 6107; (c) Zheng, Y.-R.; Zhao, Z.; Wang, M.; Ghosh, K.; Pollock, J. B.; Cook, T. R.; Stang, P. J. *J. Am.*

Chem. Soc. **2010**, *132*, 16873.

(8) Bar, A. K.; Mostafa, G.; Mukherjee, P. S. *Inorg. Chem.* **2010**, *49*, 7647.

(9) Sampedro, F.; Molins-Pujol, A. M.; Ruiz, J. I.; Santaló, P.; Bonal, J.; Pueyo, M.; Llagostera, M.; Sánchez-Ferrando, F. *Eur. J. Med. Chem.* **1992**, *27*, 611.

(10) Halgren, T. A. *J. Comput. Chem.* **1996**, *17*, 490.

(11) (a) Becke, A. D. *J. Chem. Phys.* **1993**, *98*, 5648; (b) Lee, C.; Yang, W.; Parr, R. G. *Phys. Rev. B* **1988**, *37*, 785.

(12) Zhao, Y.; Truhlar, D. *Theor. Chem. Acc.* **2008**, *120*, 215.

(13) Adamo, C. B., Vincenzo *J. Chem. Phys.* **1998**, *108*, 664.

(14) Perdew, J. P.; Burke, K.; Wang, Y. *Phys. Rev. B* **1996**, *54*, 16533.

(15) Hehre, W. J.; Ditchfield, R.; Pople, J. A. *J. Chem. Phys.* **1972**, *56*, 2257.

(16) Hay, P. J.; Wadt, W. R. *J. Chem. Phys.* **1985**, *82*, 299.

(17) Tomasi, J.; Mennucci, B.; Cammi, R. *Chem. Rev.* **2005**, *105*, 2999.

(18) Frisch, M. J.; Trucks, G. W.; Schlegel, H. B.; Scuseria, G. E.; Robb, M. A.; Cheeseman, J. R.; Scalmani, G.; Barone, V.; Mennucci, B.; Petersson, G. A.; Nakatsuji, H.; Caricato, M.; Li, X.; Hratchian, H. P.; Izmaylov, A. F.; Bloino, J.; Zheng, G.; Sonnenberg, J. L.; Hada, M.; Ehara, M.; Toyota, K.; Fukuda, R.; Hasegawa, J.; Ishida, M.; Nakajima, T.; Honda, Y.; Kitao, O.; Nakai, H.; Vreven, T.; Montgomery, J. A., Jr.; Peralta, J. E.; Ogliaro, F.; Bearpark, M.; Heyd, J. J.; Brothers, E.; Kudin, K. N.; Staroverov, V. N.; Kobayashi, R.; Normand, J.; Raghavachari, K.; Rendell, A.; Burant, J. C.; Iyengar, S. S.; Tomasi, J.; Cossi, M.; Rega, N.; Millam, N. J.; Klene, M.; Knox, J. E.; Cross, J. B.; Bakken, V.; Adamo, C.; Jaramillo, J.; Gomperts, R.; Stratmann, R. E.; Yazyev, O.; Austin, A. J.; Cammi, R.; Pomelli, C.; Ochterski, J. W.; Martin, R. L.; Morokuma, K.; Zakrzewski, V. G.; Voth, G. A.; Salvador, P.; Dannenberg, J. J.; Dapprich, S.; Daniels, A. D.; Farkas, Ö.; Foresman, J. B.; Ortiz, J. V.; Cioslowski, J.; Fox, D. J., *Gaussian 09*, Gaussian, Inc., Wallingford CT, 2009.

(19) Foster, J. P.; Weinhold, F. *J. Am. Chem. Soc.* **1980**, *102*, 7211.

(20) Teo, P.; Koh, L. L.; Hor, T. S. A. *Inorg. Chem.* **2008**, *47*, 6464.

(21) Champness, N. R.; Khlobystov, A. N.; Majuga, A. G.; Schröder, M.; Zyk,

N. V. *Tetrahedron Lett.* **1999**, *40*, 5413.

(22) Lee, S. J.; Mulfort, K. L.; O'Donnell, J. L.; Zuo, X.; Goshe, A. J.; Wesson, P. J.; Nguyen, S. T.; Hupp, J. T.; Tiede, D. M. *Chem. Commun.* **2006**, *0*, 4581.

(23) Fochi, F.; Jacopozzi, P.; Wegelius, E.; Rissanen, K.; Cozzini, P.; Marastoni, E.; Fisicaro, E.; Manini, P.; Fokkens, R.; Dalcanale, E. *J. Am. Chem. Soc.* **2001**, *123*, 7539.

3. PHOTOPHYSICAL AND COMPUTATIONAL INVESTIGATIONS OF BIS(PHOSPHINE) PLATINUM(II) METALLACYCLES

3.1 Introduction

The use of discrete, metal-organic supramolecular structures in biological settings has garnered attention lately, primarily as vessels or capsules for the trafficking and delivery of therapeutic agents, biosensing, and bioimaging.[1] In addition, certain assemblies have demonstrated inherent drug activity often due to the transition-metal ions present in the structure. While reports for Pt(II)-based self-assemblies are very rare,[2] in the past few years, several reports have demonstrated that ruthenium-based metallacages show cytotoxicity towards cancerous cell lines *in vivo*.[3] However, little is known about the mechanism of uptake and release for these systems. The biological systems in which these supramolecular structures are used are complex, containing many ligands (e.g., amino acids, glutathione, etc.) that are capable of coordinating to a metal center and degrading the metal-organic structure. An *in vitro* study using several biological ligands and a cationic Ru(III) trigonal prism supports the previously proposed hypothesis that the cytotoxicity arises from degradation pathways.[4] While this study was insightful, the current paradigm of having to perform

---

Portions of this work have appeared previously:
Reproduced in part with permission from Pollock, J.B.; Cook, T.R.; Stang, P.J. *J. Am. Chem. Soc.* **2012**, *134*, 10607

separate experiments to access information on cytotoxicity and the species giving rise to cytotoxicity is laborious, and systems that can stream-line this process into a single experiment are attractive.

Monitoring structural integrity *in vivo*, cell uptake, localization, and cytotoxicity studies of a supramolecular assembly can be facilitated by using constructs with unique photophysical properties from their molecular components. One strategy to imbue emissive properties to a self-assembly is to tether a known fluorophore using common organic coupling techniques. The issue with such a design is that the emissive signature of the parent fluorophoreappended building block often matches that of the constructed assembly. Thus, it is impossible to distinguish between the self-assembly and decomposition products on the basis of emission alone, which is typically the handle used in the aforementioned biological applications. This problem is avoided by using systems in which the core of the final assembly is inherently emissive.

In an effort to synthesize a rhomboid-shaped metallacycle that displays low-energy and long-lived excited-states that have parent spectral signatures differing from the components used in its construction, 4-ethynyl pyridyl-based ligands with aniline core motifs were considered. Hooley et al.[5] recently reported the synthesis and photophysical characterization of 2,6-bis(pyridin-3-ylethynyl) aniline, which has a quantum yield of 36% with a low-energy absorption band at 441 nm. Altering the 2,6-bis(pyridin-3-ylethynyl) aniline structure slightly, a highly emissive ligand with the correct angularity and directionality was synthesized for the construction of Pt(II) incorporated metallacycles.

The synthesis and characterization of a series of novel bis(pyridyl) aniline ligands and their use in the self-assembly of rhomboids are now reported. Steady-state absorption and fluorescence spectra were collected for each ligand and compared to their respective D_{2h} rhomboids synthesized with a 60° phenanthrene-based Pt acceptor. Rhomboids amine-functionalized in the interior (endohedral) and on the periphery (exohedral) were synthesized; however, only the endohedral aniline metallacycles displayed red-shifted emission compared to the free ligands. TD-DFT calculations were employed to probe the nature of the optical transitions for the rhomboids. Also, a hexagon was synthesized using a 180° organoplatinum(II) acceptor to investigate whether size or shape of 2D metallacycles affects the photophysical properties. Herein, the synthesis, photophysical characterization, and quantum mechanical description of the electronic transitions are discussed for a series of metallacycles.

3.2 Ligand Synthesis and Photophysical Characterization

The endohedral, exohedral, and nonfunctionalized[6] ligand scaffolds employed for metallacycle synthesis are shown in Figure 3.1. Each ligand contains three components: (i) a central ring with or without amino groups for electronic tuning of the ligand; (ii) ethynyl spacers that are *meta* with respect to each other, which provides the requisite internal 120° angle for the synthesis of the D_{2h} rhomboids or D_{6h} hexagons; (iii) 4-pyridyl moieties at the periphery for metal complexation.

The exohedral and endohedral aniline-based ligands, **3.05** and **3.06**, were prepared step-wise using a Sonogashira coupling, deprotection, and second Sonogashira coupling. Ligand **3.06** was prepared in modest yields due to

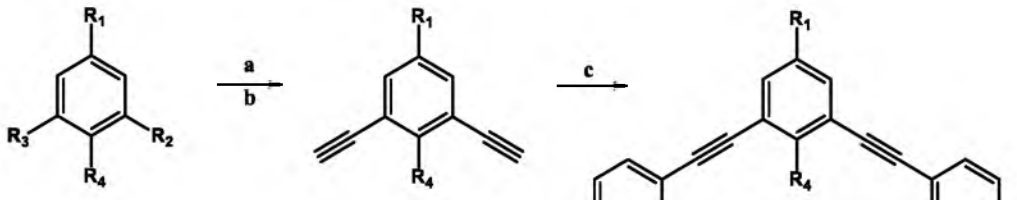

3.01: $R_1 = NH_2$, R_2 & R_3 = I, R_4 = H
3.02: R_1 = H, R_2 & R_3 = Br, $R_4 = NH_2$
3.03: $R_1 = NH_2$, R_4 = H
3.04: R_1 = H, $R_4 = NH_2$

3.05: $R_1 = NH_2$, R_4 = H (Exohedral Functionalized Ligand)
3.06: R_1 = H, $R_4 = NH_2$ (Endohedral Functionalized Ligand)
3.07: R_1 & R_4 = H (Non–Functionalized Ligand)

Figure 3.1: The synthesis of ligands **3.05–3.07**. (a). 10 mol% $Pd(PPh_3)_4$, 10 mol% CuI, acetylene-TMS, Et_3N, THF, 60°C, 24h. (b). KOH, MeOH, 24 h. (c). 10 mol% $Pd(PPH_3)_4$, 10 mol% CuI, 4-bromo pyridine hydrochloride, Et_3N, THF, 60°C, 24h 60°C, 24h.

alternate reaction pathways, mainly uncontrollable indole formation from the *ortho* aniline acetylene core during the Pd catalyzed 4-pyridyl insertion.[5]

Ligand **3.08** was prepared in modest yield (58%) via a Suzuki cross coupling of **3.02** with 4-bromopyridine HCl, as shown in Figure 3.2.

The absorption profiles of each of the four ligands **3.05**, **3.06**, **3.07**, and **3.08** are shown in Figure 3.3 (left). Ligand **3.07** has two sharp absorption bands at 282 and 300 nm with molar absorption coefficients (ε) of 52,000 and 45,900 cm^{-1} M^{-1}, respectively. These bands are present in both **3.05** and **3.06**, but with decreased intensity (see Table 3.1). **3.05** and **3.06** have broad, lower-energy

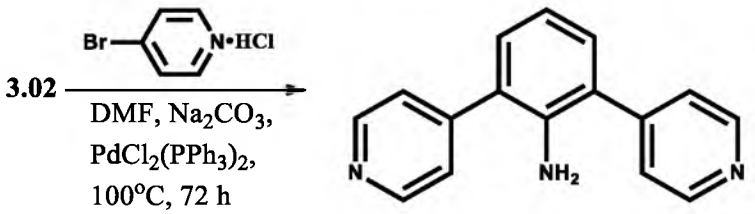

3.08 (Ethynyl–Free Ligand)

Figure 3.2: Ligand **3.08** was prepared via a Suzuki cross-coupling of **3.02** and 4-bromopyridine HCl.

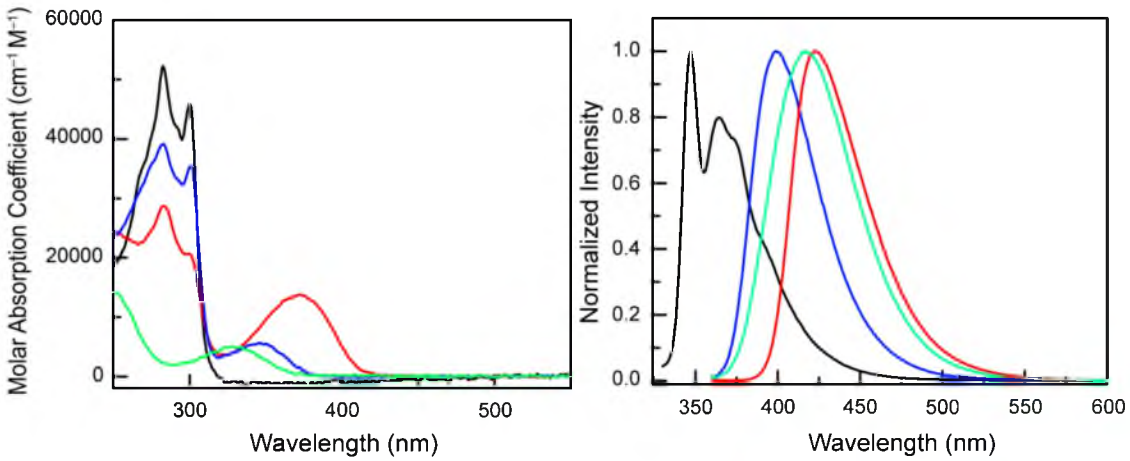

Figure 3.3: Absorption (left) and emission (right) profiles for ligands **3.05** (blue), **3.06** (red), **3.07** (black), and **3.08** (cyan). The spectra were collected using a 1 cm path length in aerated methylene chloride.

absorption bands at 347 and 373 nm, respectively, which are not present in **3.07**. These two absorption bands have molar absorption coefficients of 5,500 and 13,700 cm^{-1} M^{-1}, respectively. Ligand **3.08** does not maintain the two higher-energy absorption bands (found at 282 and 300 nm) that are present in **3.05**, **3.06**, and **3.07**. However, it does posses a broad absorption band centered at 329 nm with a molar absorption coefficient of 5,000 cm^{-1} M^{-1}.

The emission spectra (Figure 3.3, right) for **3.05**, **3.06**, and **3.08** all show similar single, broad bands with λ_{max} = 399, 422, and 417 nm, respectively. The quantum yields of **3.05**, **3.06**, and **3.08** are 41, 65, and 34%, respectively. Ligand **3.07** was determined to be weakly-emissive (Φ = 8.4%) with a sharp band centered at 347 nm and a broad band at 364 nm with a shoulder at 392 nm.

3.3 Metallacycle Synthesis and Characterization

Rhomboids **3.10**, **3.11**, and **3.12**, shown in Figure 3.4, were prepared by treating methylene chloride solutions of organoplatinum acceptor **3.09** with **3.05**,

Table 3.1: The molar absorption coefficients, λ_{emiss}, and quantum yield for each ligand and SCC.

Compound	Description	Absorption Bands λ_{max} / nm [ε x 10^3 / $cm^{-1} \cdot M^{-1}$]	λ_{exc} / nm	λ_{emis} / nm	Φ (%)[a]
3.05	*Exohedral Aniline Ligand*	282 [39.0], 300 [35.3], 347 [5.50]	356	399	41
3.06	*Endohedral Aniline Ligand*	282 [28.6], 300 *sh* [20.7], 373 [13.7]	356	422	65
3.07	*Nonfunctionalized Ligand*	282 [52.0], 300 [45.9]	324	347, 364, 392 *sh*	8.4
3.08	*Ethynyl-free Ligand*	329 [5.00]	356	417	34
3.10	*Exohedral Functionalized Rhomboid*	258 *sh* [100], 267 [103], 288 [77.5], 306 [86.6], 319 [91.2], 370 *sh* [20.1]	356	400	4.0
3.11	*Endohedral Functionalized Rhomboid*	258 [135], 267 *sh* [130], 288 [85.2], 317 [112], 430 [39.9]	430	522	28
3.12	*Nonfunctionalized Rhomboid*	258 *sh* [73.6], 267 [79.9], 288 [69.9], 306 [95.3], 319 [98.5], 356 *sh* [10.2]	356	no emiss[b]	—
3.13	*Ethynyl-free Rhomboid*	285 [167], 314 *sh* [76.3], 385 [37.8]	385	493	3.7
3.14	*Endohedral Functionalized Hexagon*	284 *sh* [95.2], 318 [139], 422 [87.6]	422	505	15

[a] Quinine sulfate and anthracene were used as standards for quantum yield determination

[b] A very weak emission profile was obtained with a signal-to-noise ratio unsuitable for quantum yield determination

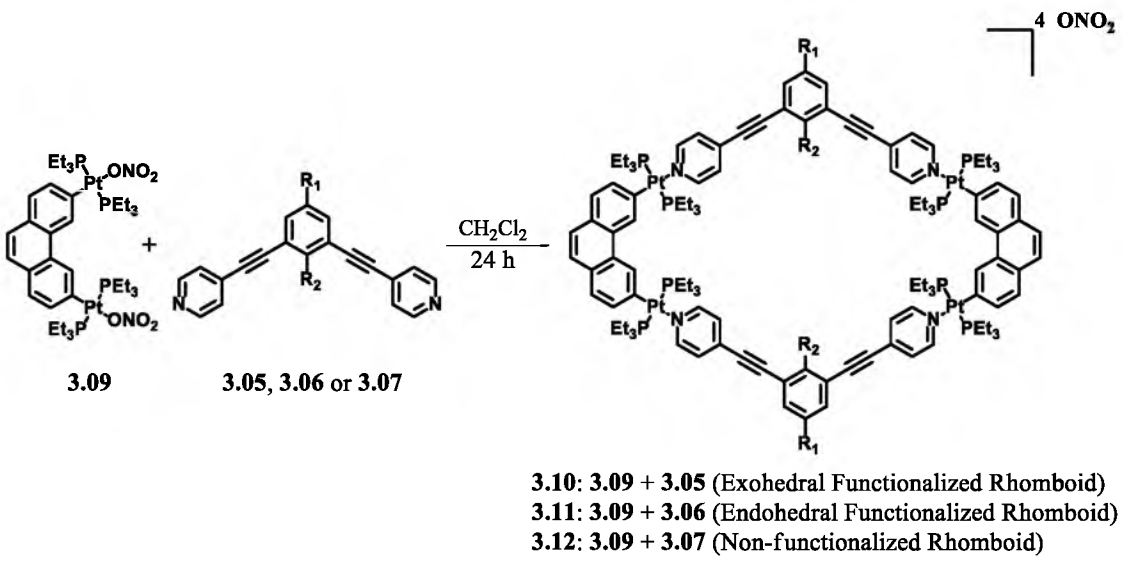

Figure 3.4: Compounds **3.09** with **3.05**, **3.06**, or **3.07** are stirred in a 1:1 stoichiometric fashion in CH_2Cl_2 for 24 h to afford D_{2h} rhomboids **3.10**, **3.11**, and **3.12**.

3.06, and **3.07**, respectively, in a (1:1) ratio. After 24 hours of stirring at room temperature, the rhomboids were precipitated out of solution using diethyl ether, isolated and redissolved in CD_2Cl_2. The final products were characterized by ^1H and $^{31}P\{^1H\}$ NMR and ESI-MS. In each $^{31}P\{^1H\}$ NMR spectrum of **3.10**, **3.11**, and **3.12**, an intense singlet with concomitant ^{195}Pt satellites was observed (see Appendix), indicating that all the phosphorus atoms in solution were equivalent. The $^{31}P\{^1H\}$ NMR of rhomboid **3.11** is shown in Figure 3.5. A singlet at δ = 12.61 ppm with the Pt satellites ($^1J_{Pt\text{-}P}$ 2684 Hz) was observed. Also, the expected downfield shifts of the α- and β–pyridyl protons upon coordination to the platinum were observed in the ^1H spectrum, consistent with previous observations of Pt-based metallacycles and cages.[7] As shown in Figure 3.5, the α and β protons on the pyridyl ring are split into two sets of two doublets upon coordination. The H_α–Py of **3.06**, shown in red at δ = 8.62 ppm, is split into two doublets at δ = 8.89

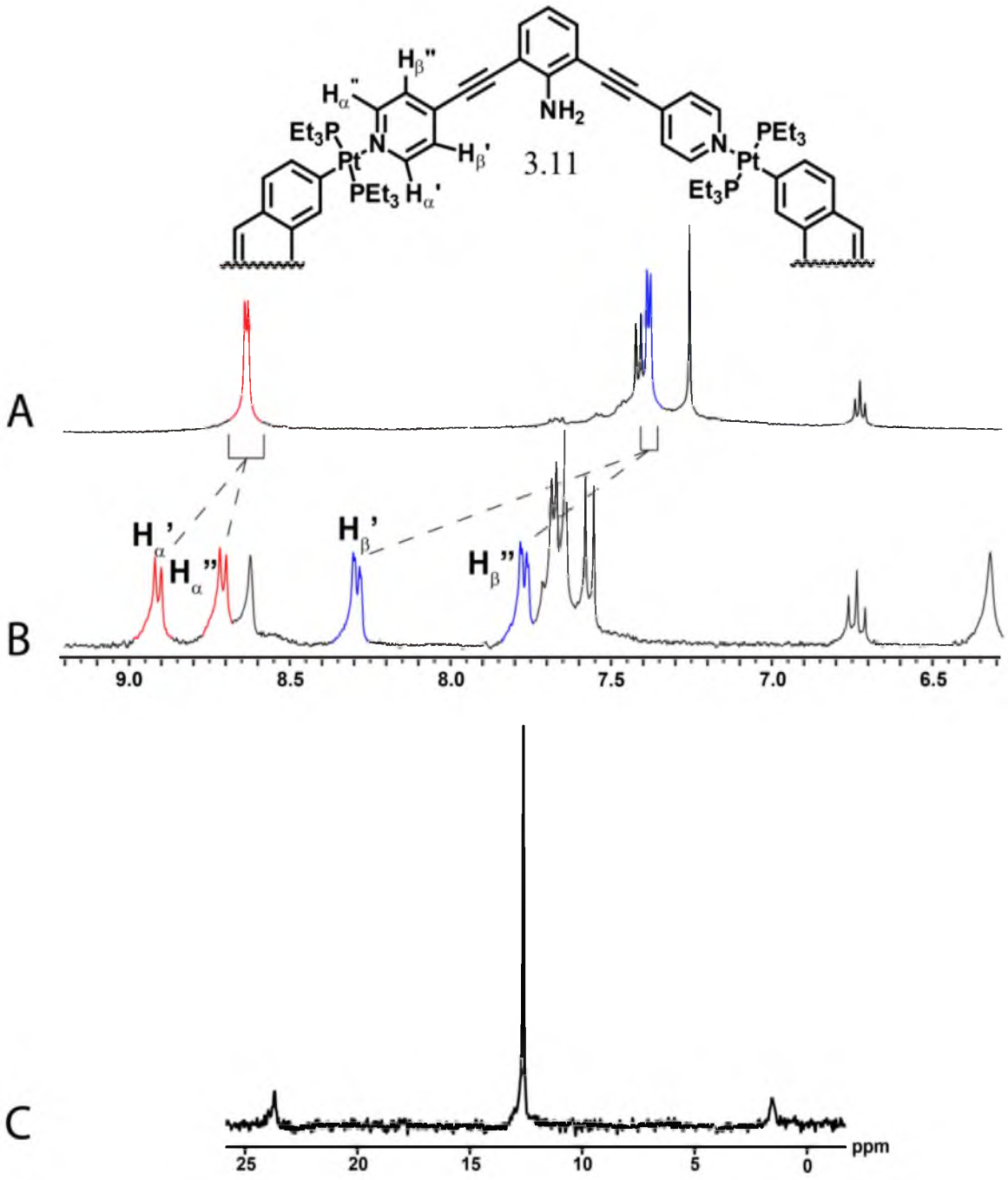

Figure 3.5: NMR spectra used to characterize the SCCs. (a) The ^{1}H NMR spectra for **3.06** with the *α*- and *β*-pyridyl proton signals colored in red and blue. (b) The ^{1}H NMR spectra for **3.11** demonstrates the downfield shift and splitting of the *α*- and *β*-protons on the pyridyl ring upon metal complexation. (c) The ^{31}P{^{1}H} spectrum for **3.11**.

and 8.69 ppm, while the H_β–Py of **3.06**, shown in blue at δ = 7.38, is split into two doublets at δ = 8.28 and 7.76 ppm. Isotopically resolved peaks for two of the charge states for **3.10**–**3.12** (see Appendix) from the loss of nitrate counterions in the ESI-MS spectra further supports the formation of a single, discrete rhomboid. Isotopically resolved signals for [**3.11** – 2 ONO_2]$^{2+}$ and [**3.11** – 3 ONO_2]$^{3+}$ are shown in Figure 3.6.

The synthesis of **3.13** (Figure 3.7) was accomplished by stirring **3.08** and **3.09** in a 1:1 ratio in MeOH at a temperature of 55°C for 24 h. Diethyl ether was added to the brightly-colored, green solution to precipitate the product. The product was then isolated.

Hexagon **3.14** (Figure 3.8) was synthesized by weighing 180° acceptor **3.15** and ligand **3.06** into separate vials and dissolving both with methylene chloride. The clear solution containing **3.15** was then added drop-wise to the yellow solution of **3.06**. The resulting brightly-colored, green solution was then allowed to stir for 24 h at room temperature. Then, the product was precipitated, isolated, and redissolved in CD_2Cl_2 for characterization (see Appendix) and redissolved in CD_2Cl_2 for characterization (see Appendix). It should be noted that if both compounds are weighed into the same vial and dissolved together, a low yield will be obtained due to insoluble kinetic by-products. Parent ions of the hexagon structure were not observed in the ESI spectra (both ToF and FT-ICR detectors were utilized with and without acid) due to fragmentation; however, several unique fragments were observed that support the formation of the hexagonal structure when analyzed in conjunction with the NMR spectra (see Appendix).

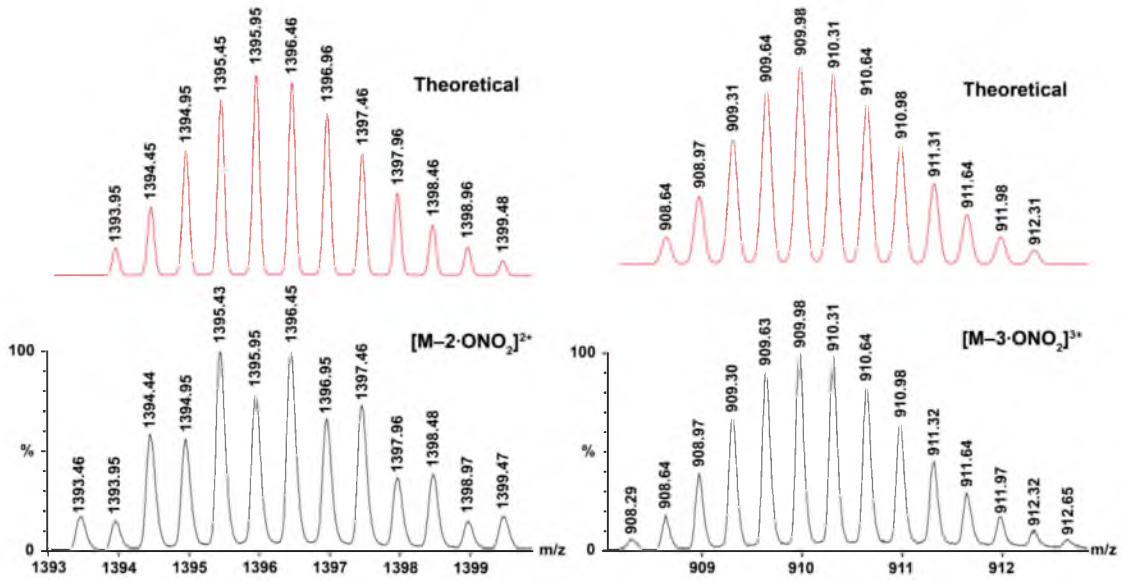

Figure 3.6: ESI-MS spectra of [**3.11** – 2•ONO_2]$^{2+}$ and [**3.11** – 3•ONO_2]$^{3+}$ (black) and simulated spectra (red).

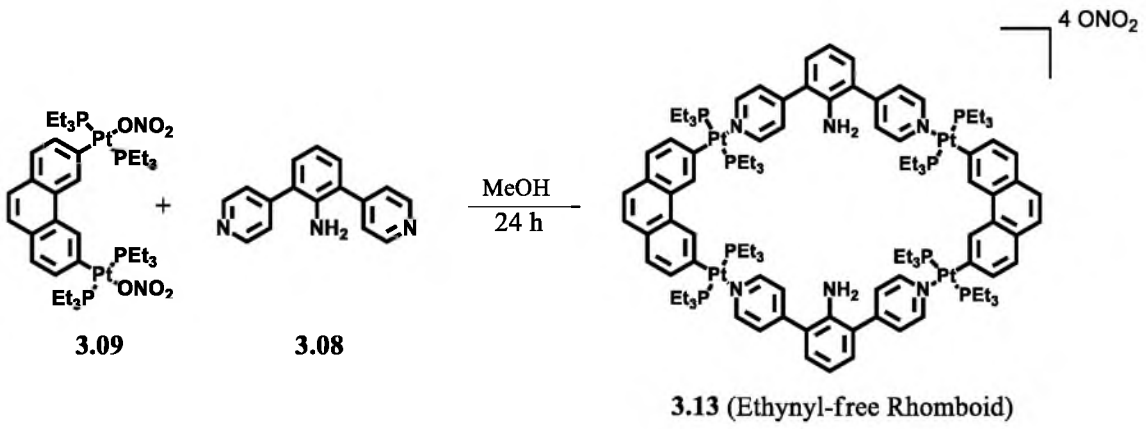

Figure 3.7: Compounds **3.09** and **3.08** are stirred in a 1:1 stoichiometric fashion in MeOH for 24 h to afford **3.13**.

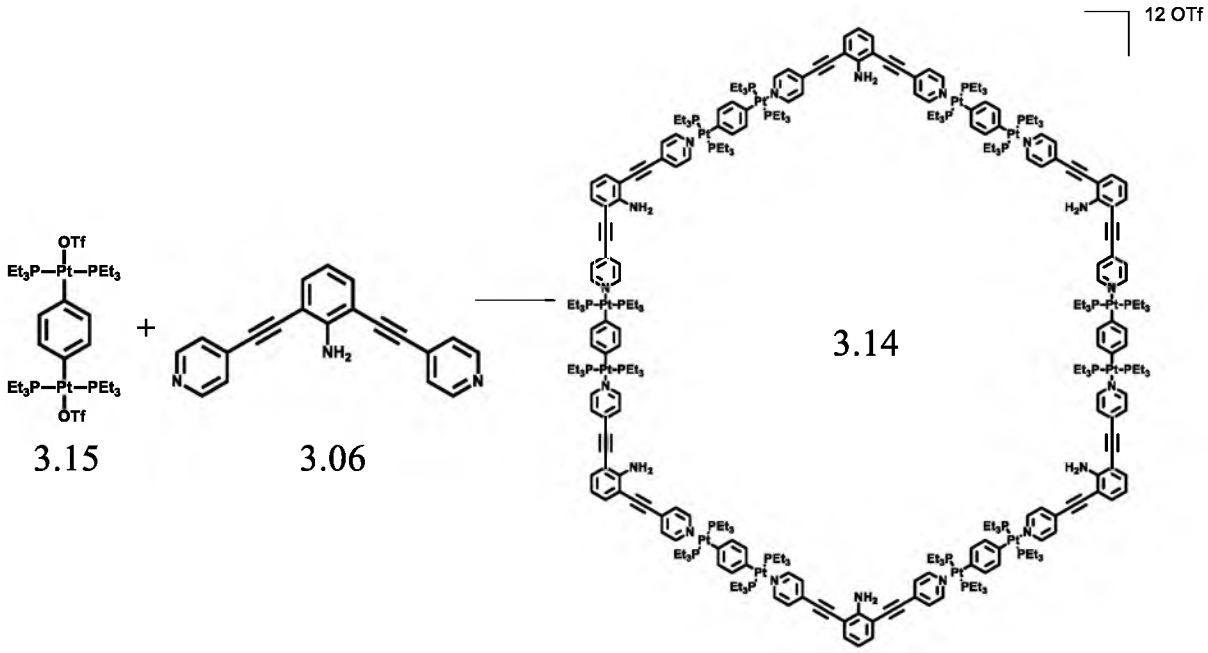

Figure 3.8: Solutions of **3.15** and **3.06** were prepared using CH_2Cl_2. **3.15** was then added drop-wise to a solution of **3.06** and the mixture is stirred for 24 h to afford **3.14**.

Figure 3.9 (left) displays the absorption profiles for rhomboids **3.10**, **3.11**, and **3.12.** Each of the rhomboids has two high-energy absorption bands centered at 258 and 267 nm. Interestingly, **3.11** has a higher molar absorption coefficient for the 258 nm band (ε = 135,000 cm^{-1} M^{-1}) with respect to the 267 nm band (ε = 130,000 cm^{-1} M^{-1}), while the converse is observed for **3.12**; it has a higher molar absorption coefficient for the 267 nm band (ε = 79,900 cm^{-1} M^{-1}) than the 258 nm band (ε = 73,600 cm^{-1} M^{-1}). SCCs **3.10**, **3.11**, and **3.12** all have an absorption band centered at 288 nm with molar absorption coefficients of 77,500, 85,200, and 69,900 cm^{-1} M^{-1}, respectively. Both **3.10** and **3.12** have two absorption bands centered at 288 and 306 nm, while **3.11** has a single, broad absorption band centered at 317 nm. There is a weak shoulder for **3.12** centered at 356 nm

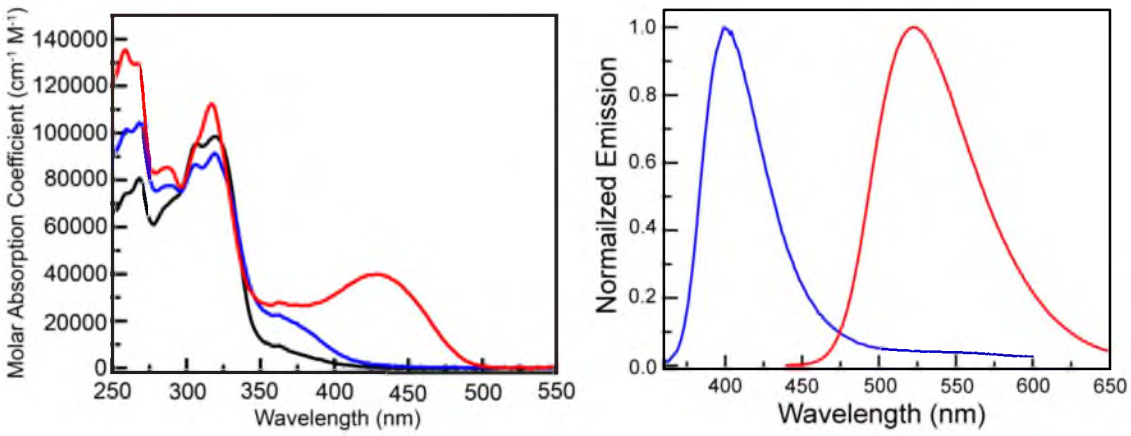

Figure 3.9: The absorption (left) and emission (right) profiles for **3.10** (blue), **3.11** (red) and **3.12** (black). Spectra were recorded in aerated CH_2Cl_2.

with a molar absorption coefficient of 10,200 cm^{-1} M^{-1}. For metallarhomboid **3.10**, there is a weak, broad absorption band centered at 370 nm with a molar absorption coefficient of 20,100 cm^{-1} M^{-1}. **3.11** has the lowest energy absorption band of the three rhomboids with a band centered at 430 nm. This absorption band also has the highest molar absorption coefficient (ε = 39,900 cm^{-1} M^{-1}) of the lowest energy absorption bands for **3.10**–**3.12**.

Figure 3.9 (right) displays the emission profiles for **3.10** and **3.11** with both rhomboids having a single, broad emission band centered at 400 and 522 nm, respectively. The quantum yield of **3.10** and **3.11** are 4.0 and 28%. The emission profile for **3.12** is not shown because the quantum yield was too low.

Figure 3.10 displays the absorption and emission profiles for rhomboid **3.13**. In the absorption spectrum there is an intense, high-energy absorption band centered at 285 nm with a molar absorption coefficient of 167,000 cm^{-1} M^{-1}. This band has a shoulder at 314 nm (ε = 76,300 cm^{-1} M^{-1}). A broad, low-energy absorption band appears at 385 nm with a molar absorption coefficient of 37,800

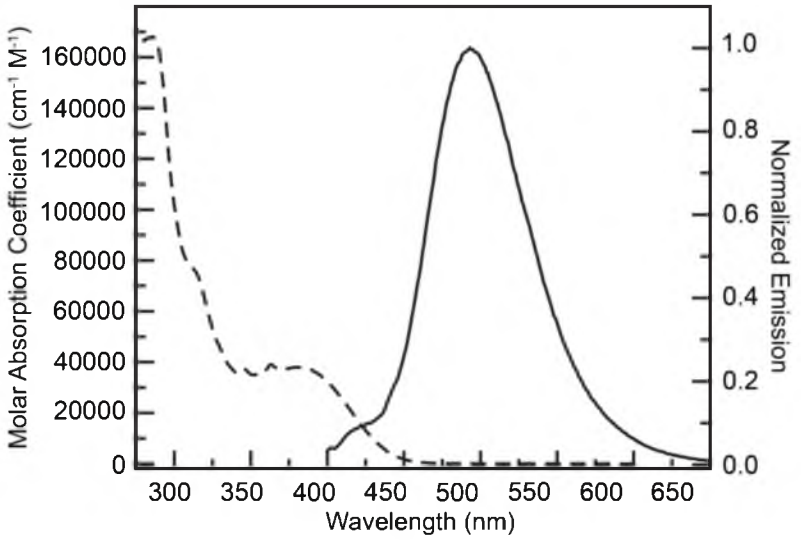

Figure 3.10: The absorption (solid) and emission (dashed) profiles for **3.13**. The spectra were collected using 1 cm path length in aerated CH_2Cl_2.

cm^{-1} M^{-1}. Within this broad band there are two optical transitions that overlap and have slightly higher molar absorption coefficients at 344 and 362 nm.

Figure 3.11 displays the absorption and emission profile for **3.14**. The absorption spectrum displays a high-energy, sharp-band centered at 318 nm with a shoulder at 284 nm, while a lower-energy broad band is centered at 422 nm. The two higher-energy bands have molar absorption coefficients of 139,000 and 95,200 cm^{-1} M^{-1}, respectively, while the lower-energy band has a molar absorption coefficient of 87,600 cm^{-1} M^{-1}. The emission profile of **3.14** (solid) has a single, broad band centered at 505 nm, and **3.14** has a quantum yield of 15%.

3.4 Discussion

3.4.1 Ligands

The photophysical properties of aniline have been widely studied. In general, intense absorption bands for aniline are due to $\pi \rightarrow \pi^*$ transitions.[8] Typically,

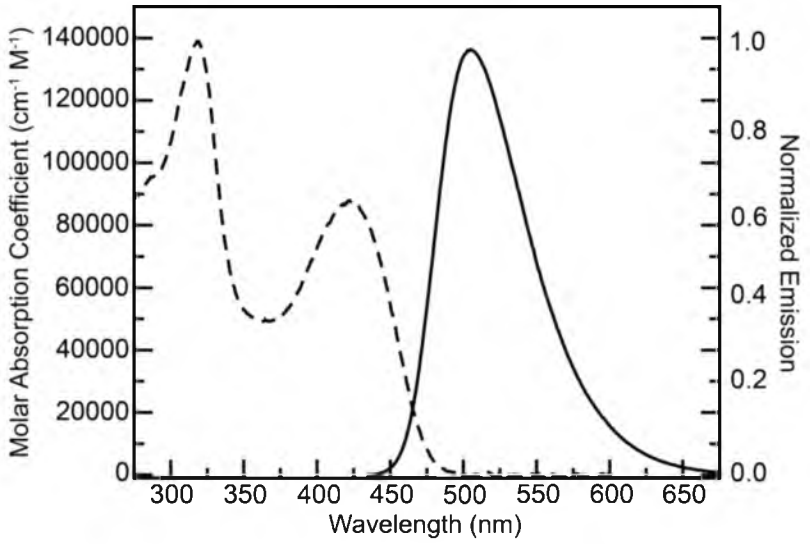

Figure 3.11: The absorption (solid) and emission (dashed) profiles for **3.14**. The spectra were collected using 1 cm path length in aerated CH_2Cl_2.

there are two electronic transitions that correspond to the $S_0 \rightarrow S_1$ and $S_0 \rightarrow S_2$ excited-states with both transitions being red-shifted for larger arene-aniline systems. For simple anilines, the main pathway for nonradiative decay is intersystem crossing from the S_1 to T_1 state, wherein the $T_1 \rightarrow S_0$ conversion does not phosphoresce.[8a] For larger arene-anilines the rate constant for ISC is smaller, which leads to higher quantum yields.[9]

Ligands **3.05**, **3.06**, and **3.07** follow a similar trend where two excited-states S_1 and S_2 are modulated by the presence and position of the aniline amine. For **3.07**, we assign the $S_0 \rightarrow S_1$ transition to the lower-energy band at 300 nm. Decay from this state appears to be significantly nonradiative compared to the other aniline-based ligands, which is supported by the lower quantum yield for **3.07** (Φ = 8.4%) with respect to **3.05** (Φ = 41%) and **3.06** (Φ = 65%). The major pathway for nonradiative decay is believed to be through ISC followed by a nonemissive $T_1 \rightarrow S_0$ transition. The S_1 excited-state for **3.05** and **3.06** is lower-

energy than that of **3.07** while the S_2 state (300 nm) is similar in energy to that of the S_1 state for **3.07** (300 nm); it is possible that a lower-energy, dark S_1 state exists for **3.07** that can be accessed through internal conversion. The variation in quantum yield between **3.05**, **3.06**, and **3.07** may be rationalized by considering these two excited-states. If the emissive singlet state, which is S_2 in compound **3.07**, is stabilized in compounds **3.05** and **3.06**, it may be stabilized and approach the S_1 state. This stabilization makes it populated upon excitation of **3.05** and **3.06**, leading ultimately to increased emission since ISC is attenuated. Evidence for this claim comes from the observed quantum yields for **3.05** (Φ = 41%) and **3.06** (Φ = 65%) as well as absorption features among the series of compounds. The trend for the band centered at 300 nm to decrease with the growing lower-energy bands of **3.05** (347 nm) and **3.06** (373 nm) suggests that an intimate relationship between these two electronic transitions exists. The lack of electronic transitions at 282 and 300 nm in **3.08** provides evidence linking the two transitions to the presence of the ethynyl moieties.

The lower-energy excited-state of **3.06** compared to **3.05** can be attributed to the position of the amine group on the central ring. The amine in **3.05** is *meta* to the ethynyl moieties and while the lone pair on the amine nitrogen is not in direct resonance with the ethynyl moieties, the σ_{meta} value is negative (-0.16).[10] However, when the amine is *ortho* to the ethynyl moieties it is in direct resonance, lowering the energy of the excited state of **3.06**. This is manifested in a 23 nm (1366 cm^{-1}) red-shift of the emission of **3.06** relative to **3.05**.

Compound **3.08** lacks the ethynyl moieties responsible for absorption bands

at 282 and 300 nm. It does have a lower-energy broad absorption band centered at 329 nm; however, it is blue-shifted compared to **3.05** (347 nm) and **3.06** (373 nm). This blue-shift is attributed to the smaller π-system present in the ethynyl-free ligand. Interestingly though, the ethynyl spacer does not seem to have a significant effect on the emission spectra. When comparing the lowest-energy absorption bands between **3.06** (373 nm) and **3.08** (329 nm), there is a 44 nm (3585 cm^{-1}) red-shift; however, a 5 nm (283 cm^{-1}) red-shift is observed between the emission spectra. This indicates that the excited-state from which the radiative pathway decays is similar in energy to that of **3.06** despite being a higher-energy transition. Moreover, the quantum yield of **3.08** is almost half that of **3.06**, providing evidence that the excited-state has a much lower rate constant for the radiative pathway. The major component for the nonradiative pathway could be attributed to ISC, as a similar phenomenon has been observed with simple aniline compounds (i.e., a smaller π system has a higher rate constant for ISC).

3.4.2 SCCs

In all cases, the SCCs have red-shifted lower-energy absorption bands and lower quantum yields than their constituent ligands. However, only SCCs constructed using endohedral aniline ligands (**3.11**, **3.13**, and **3.14**) displayed appreciable red-shifts in the emission spectra when compared to endohedral aniline ligands **3.06** and **3.08**. A 17 nm (645 cm^{-1}) blue-shift in the emission was observed for **3.14** when compared to that of **3.11**. Each of these observed results will be addressed individually.

When comparing the ligands and their respective SCCs, a red-shift was observed for the lower-energy electronic transitions. For example, the lowest-energy electronic transition for endohedral aniline ligand **3.06** is centered at 373 nm, while the SCCs constructed from this ligand **3.11** and **3.14** have bands centered at 430 and 422 nm, respectively. This phenomenon was attributed to the metal center coordinating with the pyridyl nitrogen and perturbing the electronic structure of the ligand. As will be shown in the TD-DFT section, the molecular orbitals involved with the electronic transitions are of π-type symmetry. Therefore, it is hypothesized that π-backbonding from the metal center to the nitrogen π* orbital enriches the ligand π system and lowers the energy required for excitation.

The quantum yield of each self-assembly is lower than the quantum yields of the ligands from which they are constructed. As previously discussed, aniline undergoes $S_1 \rightarrow T_1$ ISC and then nonradiatively decays back to the ground-state, S_0. Heavy atoms are known to enhance the rate of spin-forbidden processes such as ISC. Therefore, inclusion of platinum metal centers in the SCCs will increase the rate constant for ISC for the ligand-centered transitions. This manifests itself in the quantum yields being lower in the SCCs than in the ligand used for its construction. For example, **3.08** has a quantum yield of 8.4% while **3.12** is nonemissive. In a more impressive example, **3.05** has a quantum yield of 41% while **3.10** has a quantum yield of 4.0%.

Interestingly, the exohedral aniline ligand, **3.05**, and **3.10** have similar λ_{max} for emission, 399 and 400 nm, despite **3.10** having a lower-energy absorption band

than **3.05** (370 nm versus 347 nm). This implies that **3.05** and **3.10** have ligand-centered excited-states with similar energies.

Unlike **3.10**, SCCs constructed using endohedral aniline ligands (**3.11**, **3.13**, and **3.14**) displayed appreciable red-shifts in the emission spectra when compared to that of the endohedral aniline ligands **3.06** and **3.08**; however, **3.10** has an emission profile similar to that of ligand **3.05**. The low-energy optical transition for **3.11** in the absorption spectrum is 430 nm and the λ_{max} for emission is 522 nm, while **3.13** has a low-energy absorption band of 385 nm and a λ_{max} for emission of 493 nm. This trend is continued for **3.14** which has a low-energy absorption band of 422, while the λ_{max} for emission is 505 nm.

A 17 nm (645 cm^{-1}) blue-shift in the emission spectrum for **3.14** was observed as compared to that of **3.11**. While organoplatinum(II) acceptor **3.15** is different than that of **3.09** and could account for this difference in the emission spectra, the purpose of making a larger self-assembly was to determine whether the photophysical properties and shape or size of the metallacycle were intimately related. By increasing the size of the metallacycle, there was only a small blue-shift of 8 nm (441 cm^{-1}) in the lower-energy absorption band, which could be attributed to the difference between **3.15** and **3.09**. Also, the molar absorption coefficient of this lower-energy band is higher in **3.14** (ε = 87,600 cm^{-1} M^{-1}) versus **3.11** (ε = 39,900 cm^{-1} M^{-1}). This is to be expected if each metallacycle consists of multiple localized π-systems; however, it does not manifest itself as a strictly linear relationship when comparing the molar absorption coefficients for **3.14** and **3.11**. This does implicate, though, that the self-assembly's inherent

photophysical properties are ligand centered. This is evidence that for Pt-based constructs of this type, the specific ligands used in a given self-assembly have a larger influence on the photophysical properties than the particular size or shape of the assembly.

3.5 DFT and TD-DFT General Information

Single point calculations were performed using a split basis set where the B3LYP[11] functional and 6-31G** basis set[12] was used for C, H, N, and P atoms while the LANL2-DZ[13] basis set and pseudopotential was used for Pt. To minimize computational cost PH_3 ligands were utilized instead of PEt_3; therefore, the model used to approximate self-assembly **3.10** will be termed **3.10**–*PH_3*. This nomenclature was applied to all models. The vertical singlet transition energies of the complexes were computed at the TD-DFT level within G09[14] using the ground state optimized structure. For the structures that were calculated, 1486 to 1598 molecular orbitals are observed and each molecular orbital number that is listed is real and in its absolute energetic order. The nomenclature that will be utilized to discuss these molecular orbitals will be relative to the HOMO and LUMO (i.e. HOMO-1 is the molecular orbital directly below the HOMO).

3.6 TD-DFT Results and Discussion

3.6.1 Rhomboid **3.11**

For endohedral aniline rhomboid **3.11**–*PH_3*, Table 3.2 lists the wavelengths for the theoretical electronic transitions that have oscillator strengths over 0.3 from the output of the TD-DFT calculation. For each electronic transition at a

Table 3.2: Three electronic transitions are predicted for **3.11**–PH_3. For each transition the wavelength, molecular orbitals involved, oscillator strength, and description are listed.

Compound	Wavelength / nm	Orbital transitions	Orbital transitions	Oscillator strength, *f*	Description
3.11–PH_3	458.3	349 → 354 350 → 353	HOMO-3 → LUMO+1 HOMO-2 → LUMO	1.1438	Loss of e^- density on aniline nitrogen ethynyl $^1\pi \rightarrow {}^1\pi^*$
	353.4	345 → 356 346 → 355	HOMO-7 → LUMO+3 HOMO-6 → LUMO+2	2.3945	e^- density increases on aniline nitrogen ethynyl $^1\pi \rightarrow {}^1\pi^*$
	343.0	345 → 353 346 → 354	HOMO-7 → LUMO HOMO-6 → LUMO+1	0.8230	ethynyl $^1\pi \rightarrow {}^1\pi^*$

particular energy, the following are listed: the orbitals associated with that transition, the oscillator strength, and a general description of the changes between the ground-state and excited-state molecular orbitals involved in the transition. Each molecular orbital has π-type symmetry and has two regions of electron density that are ligand-centered and are separated by the phenathrene moieties of the organoplatinum(II) units on the D_{2h} rhomboid. Rhomboid **3.11** has three predicted optical transitions at 458.3, 353.4, and 343.0 nm with oscillator strengths of 1.1438, 2.3945, and 0.8230 (see Table 3.2). All three predicted transitions involve filled molecular orbitals with bonding character between the

carbons of the ethynyl moieties. The corresponding virtual or unoccupied molecular orbitals have an antibonding character between the carbon atoms in the ethynyl moieties, which leads to a weakening of the π system on the ethynyl moiety during the electronic transition. This transition is ascribed as $^1\pi \rightarrow {}^1\pi^*$. Both transitions at 353.4 and 343.0 nm originate from low-lying (HOMO-6 and HOMO-7) occupied molecular orbitals. The molecular orbitals for the lowest-energy transition at 458.3 nm have electron density on the central aniline amine group which is not present in the corresponding virtual molecular orbitals. The opposite is observed for the electronic transition at 353.4 nm where the occupied molecular orbitals have electron density on the central aniline amine group, while the unoccupied orbitals have significantly less. Figure 3.12 displays the predicted electronic transitions and the molecular orbitals involved. After comparing the energies of the eight molecular orbitals involved in the three theoretical optical transitions, it was observed that there are four subsets of grouped molecular orbitals with each subset consisting of two molecular orbitals that are close in energy. Moreover, each electronic transition consists of one energetically similar occupied ground-state "pair" going to an unoccupied excited-state "pair." These two energetically similar molecular orbitals are thought to be degenerate, as discussed below.

Rhomboid **3.11**–PH_3 has D_{2h} symmetry and each molecular orbital has two regions of electron density with π-symmetry. HOMO-7 and HOMO-6 contain a homologous ligand centered π-system that is separated from the second ligand centered π-system by the phenanthrene moiety on the Pt acceptor **3.09**. The

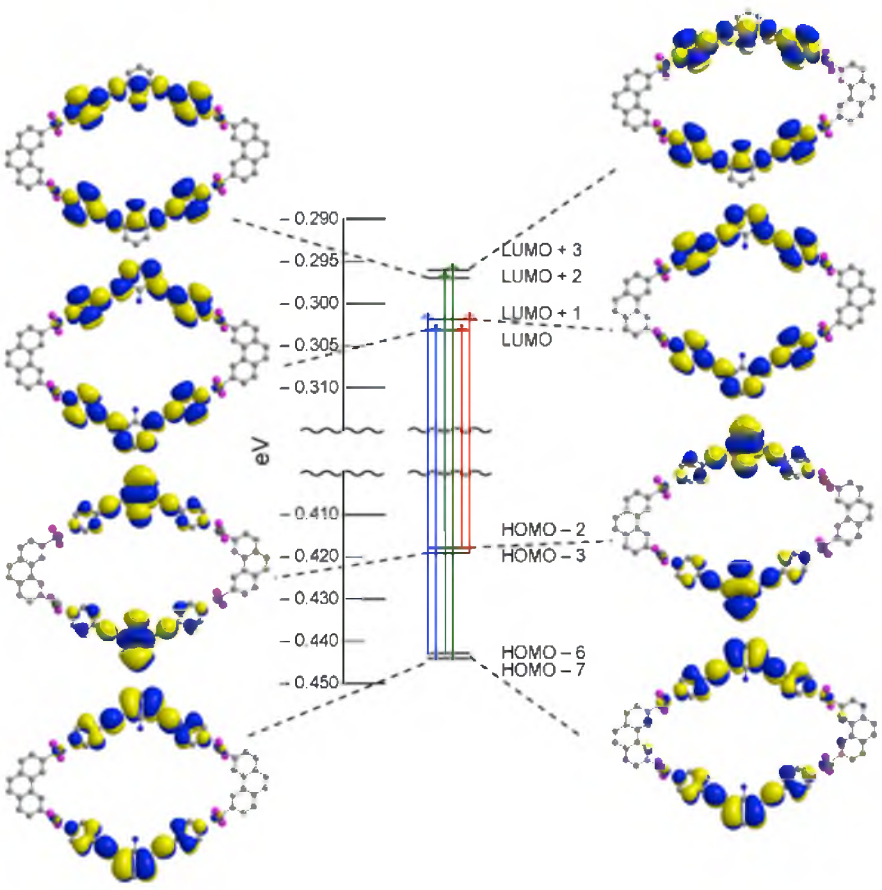

Figure 3.12: Predicted TD-DFT transitions for a rhomboid model with oscillator strengths above 0.3. Three excited states are predicted, corresponding to absorptions at 458.3 nm (red), 353.4 nm (green), and 343.0 nm (blue).

second π system is either identical to the localized π-system across from it (HOMO-7) or inverted (HOMO-6), which results in a change in the overall orbital symmetry.

Performing a population analysis on each molecular orbital corroborated the experimental conclusion that the optical transitions arise from ligand-centered transitions; it was calculated that over 96% of the electron density resides on ligand-based orbitals. That said, the inclusion of Pt afforded new photophysical properties relative to those of the free ligands. This implies that the metal center

perturbs the electronic structure of the ligands. Since each molecular orbital is of π-type symmetry and extends onto the Pt metal center, it is hypothesized that π-backbonding from Pt to the pyridyl nitrogen π* could be stabilizing the ligand-centered excited-state, thus giving rise to the red-shifted absorption and emission bands.

The emission profile for **3.11** has a broad band centered at 522 nm, while **3.10** has a band centered at 400 nm. The difference in emission wavelength maxima was previously discussed and attributed to the difference in the σ values and resonance structures. Further analysis of the molecular orbitals determined that the unique positioning of the aniline nitrogen *ortho* to both ethynyl moieties allows for direct "bridging" of the two π systems. This can be seen in molecular orbitals HOMO-3 and HOMO-2 where the p-orbital of the aniline nitrogen is in phase with the ethynyl π system. This allows for the electrons in the p-orbital on the aniline nitrogen to participate in the π system on the ethynyl moieties without having to traverse the central benzene ring, resulting in the large red-shift observed.

It should be noted that between molecular orbitals 352 (HOMO) and 353 (LUMO) there is a considerable amount of charge transfer from the metal acceptor unit and ligand; the organo-Pt(II) acceptor unit includes orbital contributions from the platinum, phenanthrene, and phosphine. In the HOMO 98.12% of the electron density resides on the metal acceptor while in the LUMO there is only 0.88 (for the ligand: 0.31% in HOMO and 95.48% in the LUMO).

3.6.2 Rhomboid **3.10** and **3.12**

The exohedral aniline rhomboid model **3.10**–PH_3 has two predicted electronic transitions at 361.5 and 345.8 nm (Table 3.3) with oscillator strengths of 2.4633 and 0.7839. The orbitals utilized in both transitions are deep, low-lying HOMO-6 and HOMO-7 orbitals and for both electronic transitions, the electron is promoted to low-lying LUMO orbitals. The occupied molecular orbitals HOMO-7 and HOMO-6 involved with the electronic transition at 361.5 nm have carbons that are bonding in the ethynyl moieties, while the unoccupied destination molecular orbitals LUMO+3 and LUMO+2 have carbons that are antibonding within the ethynyl moieties. This transition is ascribed as $^1\pi \rightarrow {}^1\pi^*$. Also, HOMO-7 and HOMO-6 have little electron density on the aniline nitrogen but some electron density is present in the unoccupied molecular orbitals LUMO+2 and LUMO+3. This implies that the aniline amine is actively participating in the electronic transitions even though it is meta to the ethynyl moieties. The electronic transition at 345.8 nm has an oscillator strength of 0.7839 and is comprised of two molecular orbital transitions (HOMO-7 → LUMO and HOMO-6 → LUMO+1). Occupied molecular orbitals HOMO-7 and HOMO-6 both have the carbons in the ethynyl moieties bonding, while the destination unoccupied molecular orbitals have the carbons in the ethynyl moieties antibonding ($^1\pi \rightarrow {}^1\pi^*$). Therefore, the ethynl moieties seem to be critical to the observed photophysical properties.

Rhomboid **3.10**–PH_3, also, displays a significant amount of charge transfer between the 352 (HOMO) and 353 (LUMO) molecular orbitals. Molecular orbital 352 has 88.73% of the electron density residing on the organo–Pt(II) acceptor

Table 3.3: Two electronic transitions are predicted for **3.10**–PH_3 while three are predicted for **3.12**–PH_3. For each transition the wavelength, molecular orbitals involved, oscillator strength, and description are listed.

Compound	Wavelength / nm	Orbital transitions	Orbital transitions	Oscillator strength, *f*	Description
3.10–PH_3	361.5	345 → 356 346 → 355	HOMO-7 → LUMO+3 HOMO-6 → LUMO+2	2.4633	increase of e^- density on aniline nitrogen ethynyl $^1\pi \rightarrow {}^1\pi^*$
	345.8	345 → 353 346 → 354	HOMO-7 → LUMO HOMO-6 → LUMO+1	0.7839	ethynyl $^1\pi \rightarrow {}^1\pi^*$
3.12–PH_3	361.2	337 → 346 339 → 348 340 → 347	HOMO-7 → LUMO+1 HOMO-5 → LUMO+3 HOMO-4 → LUMO+2	1.5737	ethynyl $^1\pi \rightarrow {}^1\pi^*$
	342.6	339 → 345 340 → 346	HOMO-5 → LUMO HOMO-4 → LUMO+1	0.6351	ethynyl $^1\pi \rightarrow {}^1\pi^*$
	338.7	335 → 345 337 → 346 338 → 345 340 → 347	HOMO-9 → LUMO HOMO-7 → LUMO+1 HOMO-6 → LUMO HOMO-4 → LUMO+2	2.5610	ethynyl $^1\pi \rightarrow {}^1\pi^*$ charge transfer from phenanthrene to ligand

unit with 10.08% on the ligand, while molecular orbital 353 has 2.68% on the organo-Pt(II) acceptor unit and 96.96% on the ligand.

Rhomboid **3.12**–PH_3 has three predicted electronic transitions at 361.2, 342.6, and 338.7 nm with oscillator strengths of 1.5737, 0.6351, and 2.5610. The electronic transitions at 361.22 and 342.57 nm both correspond to a weakening of the ethynyl moieties ($^1\pi \rightarrow {}^1\pi^*$). It was predicted that **3.12** would have a higher-energy electronic transition centered at 338.7 nm that utilizes deep, low-lying HOMO-9 and HOMO-7 molecular orbitals, wherein the ethynyl moieties ($^1\pi \rightarrow {}^1\pi^*$) are weakened, and a phenanthrene (acceptor) to ligand charge transfer occurs. After performing a population analysis on the molecular orbitals associated with this charge transfer, it was determined that 41% of electron density on the phenanthrene moiety of acceptor **3.09** moiety is transferred to **3.05**.

It should be noted that there is a considerable amount of charge transfer from the metal acceptor unit and ligand between molecular orbitals 344 (HOMO) and 345 (LUMO) for rhomboid **3.12.** Molecular orbital 344 has 96.63% of the electron density residing on the organo-Pt(II) acceptor unit while in molecular orbital 345 there is only 2.20% (for the ligand: 0.43% in HOMO and 95.64% in the LUMO).

The experimental absorption spectra for **3.12** and **3.10** with the predicted lower-energy electronic transition for **3.10**–PH_3 overlaid are shown in Figure 3.13. The theoretical lowest-energy electronic transition for **3.10**–PH_3 (361.5 nm) closely matches the experimentally observed wavelength maximum for the low-energy absorption band, 370 nm. Also, the lowest-energy electronic transition for

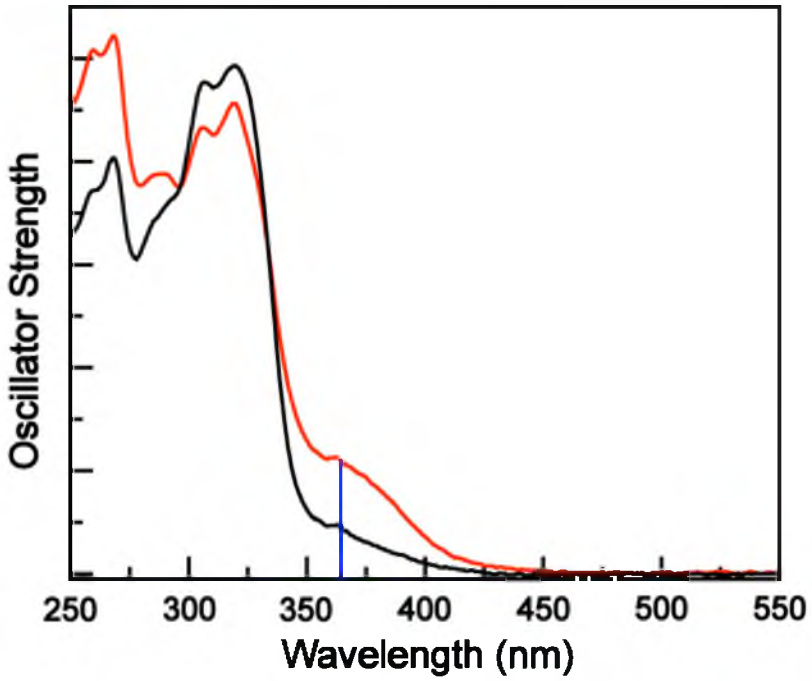

Figure 3.13: The experimental absorption spectra of **3.12** (black) and **3.10** (red) with the predicted optical transition at 361 nm (blue) overlaid.

3.12–PH_3 was predicted to be centered at 361.2 nm, while it was experimentally observed at 356 nm. The theoretical oscillator strengths, which are related to the molar absorption coefficients, for **3.10**–PH_3 and **3.12**–PH_3 follow what is observed experimentally with **3.10** having a larger molar absorption coefficient at 361 nm than that of **3.12**.

3.6.3 Rhomboid **3.13**:

Unlike rhomboids **10**–PH_3, **11**–PH_3, and **12**–PH_3, rhomboid **13**–PH_3 has C_{2v} symmetry. Rhomboid **13**–PH_3 was predicted to have a single electronic transition at 378.23 nm with an oscillator strength of 0.5194 (Table 3.4). Both occupied molecular orbitals HOMO-5 and HOMO-4 have electron density centered on the

Table 3.4: The electronic transition predicted for **3.13**–PH_3 is listed. For the transition the wavelength, molecular orbitals involved, oscillator strength, and description are listed.

Compound	Wavelength / nm	Orbital transitions	Orbital transitions	Oscillator strength, *f*	Description
3.13–PH_3	378.2	323 → 330 324 → 329	HOMO-5 → LUMO+1 HOMO-4 → LUMO	0.5194	loss of e^- density from aniline nitrogen

central aniline core with density on the nitrogen, while the unoccupied molecular orbitals LUMO+1 and LUMO have little electron density on the aniline nitrogen.

Moreover, the unoccupied molecular orbitals have more electron density displaced on the pyridyl moieties than in the occupied molecular orbitals. This demonstrates that without the ethynyl moiety spacers, the ligand centered transitions are significantly altered and the pyridyl π-systems contribution to the observed optical properties is greatly increased. Also, like **3.10**–PH_3, **3.11**–PH_3, and **3.12**–PH_3, it was determined that rhomboid **3.13**–PH_3 has a large charge transfer between molecular orbitals 328 (HOMO) and 329 (LUMO). Molecular orbital 328 has 98.79% of the electron density on the organo–Pt(II) acceptor unit and 0.31% on the ligand while in molecular orbital 329 there is 3.35% on the organo–Pt(II) acceptor unit and 95.48% on the ligand.

3.7 Conclusion

A series of novel Pt(II)-metallacycles was synthesized and their photophysical properties were investigated experimentally and computationally. During this

investigation it was determined that the emissive properties of bis(phosphine) Pt(II) metallacycles arise from ligand-centered transitions involving π-type symmetry molecular orbitals that extend onto the metal center. Interestingly, an endohedral aniline rhomboid **3.11** had markedly different photophysical properties than that of the ligand **3.6** used for its construction. Rhomboid **3.11** has a low-energy excited-state that is in the visible regime, and the assembly emits at wavelengths above 500 nm. This novel property makes **3.11** a promising candidate for applications such as bioimaging and biosensing, since the degradation of the rhomboid can be monitored by its fluorescence.

Currently, there are ongoing efforts to probe the metal center and its effect on the photophysical properties of the endohedral aniline rhomboid **3.11.** By altering the electronic nature of the ancillary phosphine ligands, it is our intention to synthesize red-shifted rhomboids that retain the novel properties demonstrated in this work.

3.8 Experimental Procedures

3,5-diiodo-aniline[15] (**3.01**), m-Bis(pyridin-4-ylethynyl)benzene[6] (**3.02**), and 2,9-Bis[*trans*-Pt(PEt_3)$_2$$NO_3$]phenanthrene[16] (**3.09**) were prepared using known procedures. 2,6-dibromo-aniline (**3.03**) was purchased from Sigma-Aldrich. Deuterated solvents were purchased from the Cambridge Isotope Laboratory (Andover, MA). ^{1}H, ^{31}P{^{1}H}, and ^{13}C NMR spectra were recorded on a Varian 300 spectrometer, and the mass spectra were recorded on a Micromass LCT Premier XE ToF mass spectrometer using electrospray ionization with a MassLynx operating system. The ESI-MS samples were dissolved in methylene chloride

then diluted with acetone unless otherwise noted. All $^{31}P\{^{1}H\}$ spectra were referenced using a 10% H_3PO_4 *aq* solution. Elemental Analysis was performed by Atlantic Microlab, Inc.

3,5-diethynyl aniline **(3.03)**: A Schlenk flask was charged with 1.035 g (3.001 mmol) of 3,5-diiodo-aniline, 693.5 mg (20.00 mol%) of $Pd(PPh_3)_4$, and 114.3 mg (20.00 mol%) of CuI. The Schlenk flask was evacuated and placed under positive N_2 pressure. 30 mL of distilled THF, 10 mL of dry Et_3N, and 5.0 mL (35.00 mmol) of trimethylsilylacetylene were added via syringe. The reaction mixture was stirred for 4 h at room temperature before placing the Schlenk flask in a 60°C oil bath for 20 h. The solvent was removed by reduced pressure. The crude product, yellow oil, was isolated after column chromatography (Mobile Phase: 5:1 Hexanes/EtOAc). The crude product was then placed into a round bottom flask and 25 mL of a MeOH/KOH (1 g) solution was added. The mixture was allowed to stir for 24 h. After removing the solvent by reduced pressure, the product was isolated by column chromatography (Mobile Phase: 2:1 Hexanes/EtOAc). 280 mg (65% yield). ^{1}H ($CDCl_3$, 300 MHz): δ 7.02 (t, 1H, Ar*H,* J = 1.32 Hz), δ 6.78 (d, 2H, Ar*H,* J = 1.32 Hz), δ 3.75 (s, 2H, NH_2), δ 3.01 (s, 2H, C*H*); ^{13}C ($CDCl_3$, 75 MHz): δ 146.38 (1C), δ 126.34 (1C), δ 123.32 (2C), δ 119.06 (2C), δ 83.08 (2C), δ 77.39 (2C); ESI-MS $[M+H]^+$ 142.07; Anal. Calcd. for $C_{10}H_7N$: C, 85.08; H, 5.00; N, 9.92. Found: C, 84.07; H, 9.43, N, 4.93.

2,6-diethynyl aniline **(3.04)**: A Schlenk flask was charged with 3.000 g (0.012 mol) of 2,6-dibromo aniline, 10 mol% of CuI (0.230 g), and 10 mol% $Pd(PPh_3)_4$ (1.400 g). The Schlenk flask was then evacuated via reduced pressure and

placed under an N_2 atmosphere. 20 mL of distilled THF and 20 mL of dry Et_3N were then added via syringe. Lastly, 10 Eq of acetylene-TMS (17 mL) was added. The reaction was heated to 60°C and allowed to stir for 48 h. After cooling, the solvent was removed and the compound was purified by column chromatography (Mobile Phase: 10% EtOAc/Hexanes). The resulting crude mixture, yellow oil, was used during the next step. A round bottom was charged with the crude mixture from the previous step. A KOH/MeOH solution was prepared by dissolving 1.000 g into 25 mL. The KOH/MeOH solution was then added to the round bottom and the mixture was allowed to stir overnight. The solvent was then removed by reduced pressure and the compound was purified by column chromatography (Mobile Phase: 30% EtOAc/Hexanes). 0.980 g (58% yield) of a yellow colored solid was afforded. ^1H ($CDCl_3$, 300 MHz): δ 7.30 (d, 2H, *Ar*H, J = 7.68 Hz), δ 6.61 (t, 1H, *Ar*H, J = 7.71 Hz), δ 4.86 (*b*s, 2H, NH_2), δ 3.41 (s, 2H, C*H*); ^{13}C ($CDCl_3$, 75 MHz): δ 133.59 (1C), δ 117.14 (2C), δ 106.40 (1C), δ 98.81 (2C), δ 83.16 (2C), δ 80.20(2C); ESI-MS $[M+H]^+$ 142.07; Anal. Calcd. for $C_{10}H_7N$: C, 85.08; H, 5.00; N, 9.92. Found: C, 83.32; H, 5.15, N, 9.63.

3,5-bis(4-pyridyl ethynyl) aniline **(3.05)**: A Schlenk flask was charged with 275 mg (1.95 mmol) of 3,5-diethynyl aniline, 225 mg (10.0 mol%) of $Pd(PPh_3)_4$, 37.1 mg (10.0 mol%) of CuI, and 758 mg (3.89 mmol) of 4-bromopyridine hydrochloride. The Schlenk flask was evacuated and charged with N_2. 20 mL of distilled THF and 20 mL of dry Et_3N were then added via syringe. The reaction mixture was stirred at 60°C for 48 h. The solvent was removed by reduced pressure and the product was purified via column chromatography (Mobile

Phase: 10:1 EtOAc/Hexanes). 82% yield ^{1}H ($CDCl_3$, 300 MHz) δ 8.61 (d, 4H, H_α–Py, J = 5.88 Hz), δ 7.36 (d, 4H, H_β–Py, J = 5.91 Hz), δ 7.13 (*b*s, 1H, Ar*H*), δ 6.87 (d, 2H, Ar*H*, J = 0.96 Hz), δ 3.82 (*b*s, 2H, NH_2); ^{13}C ($CDCl_3$, 75 MHz): δ 150.06 (4C), δ 146.77 (1C), δ 131.37 (2C), δ 125.76 (5C), δ 123.53 (2C), δ 118.86 (2C), δ 93.4 (2C), δ 86.9 (2C); ESI-MS $[M+H]^+$ 296.03; Anal. Calcd. for $C_{20}H_{13}N_3$: C, 81.34; H, 4.44; N, 14.23 Found: C, 80.25; H, 4.50, N, 13.62.

2,6-bis(4-pyridyl-ethynyl) aniline **(3.06)**: 0.975 g (6.91 mmol) of 2,6-bis(4-pyridyl-ethynyl) aniline was weighed into a Schlenk flask with 132 mg (10.0 mol%) CuI, 798 mg (10.0 mol%) $Pd(PPh_3)_4$, and 2.50 mol equivalents (1.34 g) of 4-bromopyridine HCl. The Schlenk flask was then evacuated by reduced pressure and back-filled with N_2. 20 mL of freshly distilled THF and 20 mL of dry Et_3N were then added. The mixture was heated to 60°C and left to stir for 48 h. The solvent was removed by reduced pressure and purified via column chromatography (Mobile Phase: EtOAc) to afford 450 mg of a bright yellow solid. (23% yield); ^{1}H ($CDCl_3$, 300 MHz): δ 8.62 (d, 4H, H_α–Py, J = 3.39 Hz), δ 7.41 (d, 2H, H_β–Py, J = 4.62 Hz), δ 7.38 (d, 4H, Ar*H*, J = 3.48 Hz), δ 6.74 (t, 1H, Ar*H,* J = 4.59 Hz), δ 4.93 (*b*s, 2H, NH_2); ^{13}C ($CDCl_3$, 75 MHz): δ 150.13 (4C), δ 149.57 (1C), δ 133.98 (2C), δ 131.26 (1C), δ 125.54 (4C), δ 117.82 (2C), δ 106.74 (2C), δ 94.99 (2C), δ 92.82 (2C), δ 89.99 (2C); ESI-MS $[M+H]^+$ 296.06; Anal. Calcd. for $C_{20}H_{13}N_3$: C, 81.34; H, 14.23; N, 4.44 Found: C, 80.56; H, 13.42, N, 4.67.

2,6-(4-pyridine) aniline **(3.08)**: A Schlenk flask was charged with 1.0 g (4.0 mmol) of 2,6-dibromo aniline and 10 mL of degassed DMF (purged with N_2 for 15 min) and kept under N_2 atomosphere. A 2 M solution of Na_2CO_3 was prepared

and purged with N_2 for 15 min and added to the Schlenk flask via syringe. Then, a solution containing 2.5 mol equivalents (1.2 g) of pyridine-4-boronic acid and 15 mol% $PdCl_2(PPh_3)_2$ (280 mg) was prepared using 5 mL of degassed DMF and was added to the Schlenk flask via syringe. The mixture was then heated to 100°C and allowed to stir for 72 h. The solvent was removed by reduced pressure and the product was purified via column chromatography (Mobile Phase: 10% EtOAc/ Hexanes) and afforded 575 mg of a light orange solid. (58.0% yield); ^1H ($CDCl_3$, 300 MHz): δ 8.67 (d, 4H, H_α–Py, J = 5.7), δ 7.42 (d, 4H, H_β–Py, J = 6.03), δ 7.14 (d, 2H, Ar*H*, J = 7.62), δ 6.92 (t, 1H, Ar*H*, J = 7.95), δ 3.90 (*b*s, 2H, NH_2); ^{13}C ($CDCl_3$, 75 MHz): δ 150.69 (4C), δ 147.51 (2C), δ 140.49 (1C), δ 130.74 (2C), δ 125.52 (2C), δ 124.29 (4C), δ 119.00 (1C); ESI-MS $[M+H]^+$ 248.06; Anal. Calcd. for $C_{16}H_{13}N_3$: C, 77.71; H, 16.99; N, 5.30 Found: C, 76.94; H, 16.79, N, 5.28.

General Procedure for Rhomboid Formation **(3.10–3.13)**: In a 1:1 stoichiometric fashion, ligand **3.5**, **3.6**, **3.7**, or **3.8** were added to the 60° bis(phosphine) organoplatinum(II) acceptor **3.9** in a 2 dram vial. The solids were dissolved in dichloromethane (methanol for **3.13**) and allowed to stir at room temperature overnight. For rhomboid **3.13**, the solution was allowed to stir at 55°C for 24 h. To the resulting homogenous solution, diethyl ether was added to precipitate the product, which was then isolated and dried under reduced pressure for 4 h and redissolved in CD_2Cl_2 for characterization.

3.10: ^1H (CD_2Cl_2, 300 MHz) δ 9.33 (d, 4H, $H_{\alpha'}$–Py, J = 5.58 Hz), δ 8.86 (s, 4H, Phen*H*), δ 8.66 (d, 4H, $H_{\alpha''}$–Py, J = 5.73 Hz), δ 7.91 (d, 4H, $H_{\beta'}$–Py, J = 5.43 Hz),

δ 7.78 (d, 4H, $H_{\beta''}$–Py, J = 4.23 Hz), δ 7.59 (d, 12H, Phen*H*, J = 5.61 Hz), δ 7.34 (s, 2H, Ar*H*), δ 7.13 (s, 4H, Ar*H*), δ 4.56 (*b*s, 4H, $–NH_2$), δ 1.3–1.4 (m, 48H, PCH_2CH_3), δ 1.12–1.27 (m, 72H, PCH_2CH_3). ^{31}P {^1H} NMR (CD_2Cl_2, 121.4 MHz) δ 8.04 (*b*s; ^{195}Pt satellites, $^1J_{Pt–P}$, 2707 Hz); ESI-MS ($C_{116}H_{162}N_{10}O_{12}P_8Pt_4$) m/z: [**3.10**–2•$ONO_2$]$^{2+}$ 1396.40; [**3.10**–3•ONO_2]$^{3+}$ 909.96.

3.11: ^1H (CD_2Cl_2, 300 MHz) δ 8.87 (d, 4H, $H_{\alpha'}$–Py, J = 5.79 Hz), δ 8.67 (d, 4H, $H_{\alpha''}$–Py, J = 5.67 Hz), δ 8.59 (s, 4H, Phen*H*), δ 8.25 (d, 4H, $H_{\beta'}$–Py, J = 5.82 Hz), δ 7.74 (d, 4H, $H_{\beta''}$–Py, J = 5.88 Hz), δ 7.78 (s, 2H, $H_{b'}$–Py), δ 7.62 (d, 8H, Phen*H*, J = 4.44 Hz), δ 7.61 (s, 4H, Phen*H*), δ 7.53 (d, 4H, Ar*H*, J = 7.68 Hz), δ 6.72 (t, 2H, Ar*H*, J = 7.68 Hz), δ 6.31 (*b*s, 4H, $–NH_2$), δ 1.3–1.4 (m, 48H, PCH_2CH_3), δ 1.11–1.27 (m, 72H, PCH_2CH_3). ^{31}P {^1H} NMR (CD_2Cl_2, 121.4 MHz) δ 12.61 (s; br, ^{195}Pt satellites, $^1J_{Pt–P}$ 2684 Hz); ESI-MS ($C_{116}H_{162}N_{10}O_{12}P_8Pt_4$) m/z: [**3.11**–2•$ONO_2$]$^{2+}$ 1396.45; [**3.11**–3•ONO_2]$^{3+}$ 909.98.

3.12: ^1H (CD_2Cl_2, 300 MHz) δ 9.36 (d, 4H, $H_{\alpha'}$–Py, J = 5.85 Hz), δ 8.85 (s, 4H, Phen*H*), δ 8.72 (d, 4H, $H_{\alpha''}$–Py, J = 5.76 Hz), δ 8.06 (s, 2H, Ar*H*), δ 7.97 (d, 4H, $H_{b'}$–Py, J = 5.82 Hz), δ 7.75–7.82 (m, 10H, $H_{b''}$–Py & Ar*H*), δ 7.53–7.63 (m, 12H, Phen*H*), δ 1.28–1.45 (m, 48H, PCH_2CH_3), δ 1.09–1.23 (m, 72H, PCH_2CH_3). ^{31}P {^1H} NMR (CD_2Cl_2, 121.4 MHz) δ 13.32 (*b*s; ^{195}Pt satellites, $^1J_{Pt–P}$ 2704 Hz); ESI-MS ($C_{116}H_{160}N_8O_{12}P_8Pt_4$) m/z: [**3.12**–2•$ONO_2$]$^{2+}$ 1381.44; [**3.12**–3•ONO_2]$^{3+}$ 899.97.

3.13: ^1H (CD_2Cl_2, 300 MHz) δ 9.06 (d, 4H, $H_{\alpha'}$–Py, J = 5.85 Hz), δ 8.77 (s, 4H, Phen*H*), δ 8.69 (d, 4H, $H_{\alpha''}$–Py, J = 5.67 Hz), δ 8.50 (d, 4H, $H_{\beta'}$–Py, J = 4.17 Hz), δ 8.02 (*b*s, 4H, $–NH_2$), δ 7.82 (d, 4H, $H_{\beta''}$–Py, J = 4.14 Hz), δ 7.55–7.65 (m, 12H,

Phen*H*), δ 7.44 (d, 4H, Ar*H*, J = 7.65 Hz), δ 7.03 (t, 2H, Ar*H*, J = 7.62 Hz), δ 1.35–1.45 (m, 24H, PCH_2CH$_3$), δ 1.1–1.27 (m, 36H, PCH$_2$CH_3). ^{31}P {^{1}H} NMR (CD_2Cl_2, 121.4 MHz) δ 8.97 (*b*s, ^{195}Pt satellites, $^1J_{Pt-P}$ 2692 Hz); ESI-MS ($C_{108}H_{162}N_{10}O_{12}P_8Pt_4$) m/z: [**3.13**–2•$ONO_2$]$^{2+}$ 1348.41; [**3.13**–3•ONO_2]$^{3+}$ 877.27.

Hexagon **3.14**: 180° organoplatinum(II) acceptor μ-1,4-phenylenetetrakis-(triethylphosphine)bis(1,1,1-trifluoromethanesulfonato-κO) diplatinum **3.15** and ligand **3.06** were weighed into separate 2 dram vials and dissolved with methylene chloride (0.5 mL for **3.06** and 1.0 mL for **3.15**). The clear solution containing **3.15** was then added drop-wise to the yellow solution of **3.06**. The brightly-colored, green solution was then allowed to stir for 24 h at room temperature. The product was then precipitated with diethyl ether, isolated and redissolved in CD_2Cl_2 for characterization. ^{1}H (CD_2Cl_2, 300 MHz) δ 8.61(*b*s, 24H, H_α–Py), δ 7.87 (*b*s, 24H, H_β–Py), δ 7.49 (d, 24H, Ar*H,* J = 7.8 Hz), δ 7.05 (*b*s, 12H, Ar*H*), δ 6.72 (*b*s, 6H, Ar*H*), δ 5.79 (*b*s, 12H, NH_2), δ 1.36 (*b*s, 144H, PCH_2CH$_3$), δ 1.00–1.25 (m, 216H, PCH$_2$CH_3). ^{31}P {^{1}H} NMR (CD_2Cl_2, 121.4 MHz) δ 12.14 (*b*s, ^{195}Pt satellites, $^1J_{Pt-P}$ 2716 Hz); ESI-MS ($C_{316}H_{462}N_{18}F_{48}O_{48}P_{24}Pt_{12}$). See Appendix for spectra of fragments.

UV-Vis and Fluorescence: Absorption spectra were recorded on a Hitachi U-4100 Spectrophotometer and fluorescence spectra were recorded on a Horiba Jobin-Yvon Fluoromax-3 using aerated spectro-photometric grade dichloromethane (Sigma-Aldrich) at room temperature. The cells used for the following experiments were all 1-cm path-length quartz cuvettes from Starna Cells, Inc. Molar absorption coefficients were determined by measuring four

solutions at concentrations ranging from 0.6 to 30 μM. The molar absorptivities for each solution were then calculated using Beer's Law, and the four were averaged. Subsequent samples were then prepared to confirm the molar absorption coefficients. For fluorescence, metallacycles were freshly prepared for each measurement. The quantum yield for the instrument was determined by cross-calibrating with two standards: quinine sulfate in 0.1M H_2SO_4 (Φ = 54%) and anthracene in ethanol (Φ = 27%).

DFT and TD-DFT Calculations*:* All calculations were performed using the Gaussian09 (G09) program package revision B.01,[14] with the Becke three-parameter hybrid exchange and the Lee–Yang–Parr correlation functionals (B3LYP).[11] The 6-31G** basis set[12] was used for H, C, N, and P atoms, while the LANL2-DZ[13] basis set and pseudopotential was used for Pt. All geometry optimizations were performed without a solvent field in C_1 symmetry; the results are in the gas phase. To minimize computational cost, the PEt_3 ligands on Pt were modeled as PH_3 ligands. Orbitals were visualized using Chem3D and GaussView 5.0 with an isovalue of 0.02.

The percentage of platinum, phenanthrene, phosphine, or ligand character in the occupied (canonical) MOs and virtual orbitals discussed for the previous complexes was calculated from a full population analysis, using equation 3.1,

$$\%\ \text{Orbital Character}_{(\text{Pt,Phen,Phosphine,Lig})} = \frac{\Sigma\phi^2_{(\text{Pt,Phen,Phosphine,Lig})}}{\Sigma\phi^2_{(\text{all})}} \times 100\% \qquad (3.1)$$

where $\Sigma\varphi_i$ (i = Pt, Phen, Phosphine, Lig or all) is the sum of the squares of the eigenvalues associated with the atomic orbital (AO) of interest and all of the AOs in a particular MO, respectively. The vertical singlet transition energies of the

complexes were computed at the TD-DFT level within G09 using the ground state optimized structure.

3.9 Contributions

All primary work (i.e., synthesis, molecular modeling, spectroscopy, analysis, etc.) was performed by J. Bryant Pollock while Timothy R. Cook served an advisory role.

3.10 Future Directions

Having established the photophysical properties of a series of endohedral functionalized and characterized the nature of the molecular orbitals involved in the optical transitions, rhomboid **3.11** is well-suited to act as a host for guests in its internal cavity via hydrogen bonding, and the inherent emission of **3.11** can be used as a reporter for a recognition event. Moreover, since the aniline p-orbital seems to be critical for the observed photophysical properties, guests such as nitrobenzene may alter the electronics of the system via hydrogen bonding, thereby resulting in an observable change in optical properties. The modularity of the directional bonding approach also allows for SCCs of varying size and shape to be constructed from ligand **3.06**, which will allow for tuning of the host-guest recognition modes. As such, a natural extension of this study would be to interrogate **3.11** and other SCCs constructed from **3.06** as a sensor for explosives.

3.11 References

(1) (a) Fyles, T. M.; Tong, C. C. *New J. Chem.* **2007**, *31,* 296; (b) Hannon, M. J. *Chem. Soc. Rev.* **2007**, *36,* 280; (c) Hannon, M. J.; Moreno, V.; Prieto, M. J.; Moldrheim, E.; Sletten, E.; Meistermann, I.; Isaac, C. J.; Sanders, K. J.; Rodger, A. *Angew. Chem. Int. Ed.* **2001**, *40*, 879; (d) Kieltyka, R.; Englebienne, P.; Fakhoury, J.; Autexier, C.; Moitessier, N.; Sleiman, H. F. *J. Am. Chem. Soc.* **2008**, *130*, 10040; (e) Ma, D.-L.; Che, C.-M.; Yan, S.-C. *J. Am. Chem. Soc.* **2008**, *131*, 1835; (f) Tashiro, S.; Tominaga, M.; Yamaguchi, Y.; Kato, K.; Fujita, M. *Angew. Chem. Int. Ed.* **2006**, *45*, 241; (g) Barry, N. P. E.; Edafe, F.; Dyson, P. J.; Therrien, B. *Dalton Trans.* **2010**, *39*, 1673; (h) Horcajada, P.; Gref, R.; Baati, T.; Allan, P. K.; Maurin, G.; Couvreur, P.; Férey, G.; Morris, R. E.; Serre, C. *Chem. Rev.* **2011**, *112*, 1232.

(2) Mounir, M.; Lorenzo, J.; Ferrer, M.; Prieto, M. J.; Rossell, O.; Avilès, F. X.; Moreno, V. *J. Inorg. Biochem.* **2007**, *101*, 660.

(3) (a) Ang, W. H.; Grote, Z.; Scopelliti, R.; Juillerat-Jeanneret, L.; Severin, K.; Dyson, P. J. *J. Organometallic Chem.* **2009**, *694*, 968; (b) Barry, N. P. E.; Edafe, F.; Therrien, B. *Dalton Trans.* **2011**, *40, 7172*; (c) Barry, N. P. E.; Zava, O.; Furrer, J.; Dyson, P. J.; Therrien, B. *Dalton Trans.* **2010**, *39,* 2816; (d) Linares, F. t.; Galindo, M. A.; Galli, S.; Romero, M. A.; Navarro, J. A. R.; Barea, E. *Inorg. Chem.* **2009**, *48*, 7413; (e) Therrien, B.; Süss-Fink, G.; Govindaswamy, P.; Renfrew, A. K.; Dyson, P. J. *Angew. Chem. Int. Ed.* **2008**, *47*, 3773; (f) Vajpayee, V.; Song, Y. H.; Jung, Y. J.; Kang, S. C.; Kim, H.; Kim, I. S.; Wang, M.; Cook, T. R.; Stang, P. J.; Chi, K.-W. *Dalton Trans.* **2012**, *41*, 3046; (g) Vajpayee, V.; Song, Y. H.; Yang, Y. J.; Kang, S. C.; Kim, H.; Kim, I. S.; Wang, M.; Stang, P. J.; Chi, K.-W. *Organometallics* **2011**, *30*, 3242; (h) Vajpayee, V.; Yang, Y. J.; Kang, S. C.; Kim, H.; Kim, I. S.; Wang, M.; Stang, P. J.; Chi, K.-W. *Chem. Comm.* **2011**, *47,* 5184; (i) Yi, J. W.; Barry, N. P. E.; Furrer, M. A.; Zava, O.; Dyson, P. J.; Therrien, B.; Kim, B. H. *Bioconjugate Chem.* **2012**, *23*, 461; (j) Zava, O.; Mattsson, J.; Therrien, B.; Dyson, P. J. *Chem.-Eur. J.* **2010**, *16*, 1428.

(4) Paul, L. E. H.; Therrien, B.; Furrer, J. *Inorg. Chem.* **2011**, *51*, 1057.

(5) Johnson, A. M.; Moshe, O.; Gamboa, A. S.; Langloss, B. W.; Limtiaco, J. F. K.; Larive, C. K.; Hooley, R. J. *Inorg. Chem.* **2011**, *50*, 9430.

(6) Amoroso, A. J.; Thompson, A. M. W. C.; Maher, J. P.; McCleverty, J. A.; Ward, M. D. *Inorg. Chem.* **1995**, *34*, 4828.

(7) (a) Wang, M.; Zheng, Y.-R.; Ghosh, K.; Stang, P. J. *J. Am. Chem. Soc.* **2010**, *132*, 6282; (b) Ghosh, K.; Hu, J.; Yang, H.-B.; Northrop, B. H.;

White, H. S.; Stang, P. J. *J. Org. Chem.* **2009**, *74*, 4828; (c) Zheng, Y.-R.; Northrop, B. H.; Yang, H.-B.; Zhao, L.; Stang, P. J. *J. Org. Chem.* **2009**, *74*, 3554; (d) Zheng, Y.-R.; Stang, P. J. *J. Am. Chem. Soc.* **2009**, *131*, 3487.

(8) (a) Knee, J. L.; Johnson, P. M. *J. Chem. Phys.* **1984**, *80*, 13; (b) Rückert, I.; Demeter, A.; Morawski, O.; Kühnle, W.; Tauer, E.; Zachariasse, K. A. *J. Phys. Chem. A* **1999**, *103*, 1958; (c) Scheps, R.; Florida, D.; Rice, S. A. *J. Chem. Phys.* **1974**, *61*, 1730; (d) Yang, J.-S. *PATAI'S Chemistry of Functional Groups*; John Wiley & Sons, Ltd., London, UK, 2009, doi:10.1002/9780470682531.pat0396.

(9) Lewis, F. D.; Hougland, J. L.; Markarian, S. A. *J. Phys. Chem. A* **2000**, *104*, 3261.

(10) Hansch, C. L., A., *Substituent Constants for Correlation Analysis in Chemistry and Biology*; 1 Ed.; Wiley-Interscience: New York, NY, 1979.

(11) (a) Becke, A. D. *J. Chem. Phys.* **1993**, *98*, 5648; (b) Lee, C.; Yang, W.; Parr, R. G. *Phys. Rev. B* **1988**, *37*, 785.

(12) Hehre, W. J.; Ditchfield, R.; Pople, J. A. *J. Chem. Phys.* **1972**, *56*, 2257.

(13) Hay, P. J.; Wadt, W. R. *J. Chem. Phys.* **1985**, *82*, 299.

(14) Frisch, M. J.; Trucks, G. W.; Schlegel, H. B.; Scuseria, G. E.; Robb, M. A.; Cheeseman, J. R.; Scalmani, G.; Barone, V.; Mennucci, B.; Petersson, G. A.; Nakatsuji, H.; Caricato, M.; Li, X.; Hratchian, H. P.; Izmaylov, A. F.; Bloino, J.; Zheng, G.; Sonnenberg, J. L.; Hada, M.; Ehara, M.; Toyota, K.; Fukuda, R.; Hasegawa, J.; Ishida, M.; Nakajima, T.; Honda, Y.; Kitao, O.; Nakai, H.; Vreven, T.; Montgomery, J. A., Jr.; Peralta, J. E.; Ogliaro, F.; Bearpark, M.; Heyd, J. J.; Brothers, E.; Kudin, K. N.; Staroverov, V. N.; Kobayashi, R.; Normand, J.; Raghavachari, K.; Rendell, A.; Burant, J. C.; Iyengar, S. S.; Tomasi, J.; Cossi, M.; Rega, N.; Millam, N. J.; Klene, M.; Knox, J. E.; Cross, J. B.; Bakken, V.; Adamo, C.; Jaramillo, J.; Gomperts, R.; Stratmann, R. E.; Yazyev, O.; Austin, A. J.; Cammi, R.; Pomelli, C.; Ochterski, J. W.; Martin, R. L.; Morokuma, K.; Zakrzewski, V. G.; Voth, G. A.; Salvador, P.; Dannenberg, J. J.; Dapprich, S.; Daniels, A. D.; Farkas, Ö.; Foresman, J. B.; Ortiz, J. V.; Cioslowski, J.; Fox, D. J., *Gaussian 09*, Gaussian, Inc., Wallingford CT, 2009.

(15) Chimenti, F.; Bolasco, A.; Secci, D.; Chimenti, P.; Granese, A. *Syn. Comm.* **2004**, *34*, 2549.

(16) Kryschenko, Y. K.; Seidel, S. R.; Arif, A. M.; Stang, P. J. *J. Am. Chem. Soc.* **2003**, *125*, 5193.

4. THE PHOTOPHYSICAL PROPERTIES OF ENDOHEDRAL AMINE-FUNCTIONALIZED BIS(PHOSPHINE) PLATINUM(II) COMPLEXES: MODELS FOR EMISSIVE METALLACYCLES

4.1 Introduction

The well-established photophysical properties of mono- and multinuclear bis(phosphine) platinum coordination complexes (e.g., low-energy and long-lived excited-states, facile tunablity, and high quantum yields) has set the foundation for studying SCCs constructed using bis(phosphine) platinum metal centers that may preserve these useful absorption and emission characteristics.[1] Recently, a D_{2h} [2+2] endohedral amine-functionalized rhomboid (**4.08**; Scheme 4.1) constructed from 2,6-bis(pyrid-4ylethynyl) aniline (**4.01**; Scheme 4.1) and 2,9-bis[*trans*-$Pt(PEt_3)_2NO_3$] phenanthrene[2] was reported, which displayed a low-energy absorption band in the visible region and emitted above 500 nm.[3] The emissive properties were attributed to ligand-centered transitions involving π-type molecular orbitals with modest contributions from metal-based atomic orbitals. Further investigations of these systems are critical for designing SCCs that possess the attractive photophysical properties established for mono- and multinuclear bis(phosphine) platinum coordination complexes.

Portions of this work have appeared previously:
Reproduce in part with permission from Pollock, J.B.; Cook, T.R.; Schneider, G.L.; Lutterman, D.A.; Davies, A.S.; Stang, P.J. *Inorg. Chem.,* **2013**, *52*, 9254

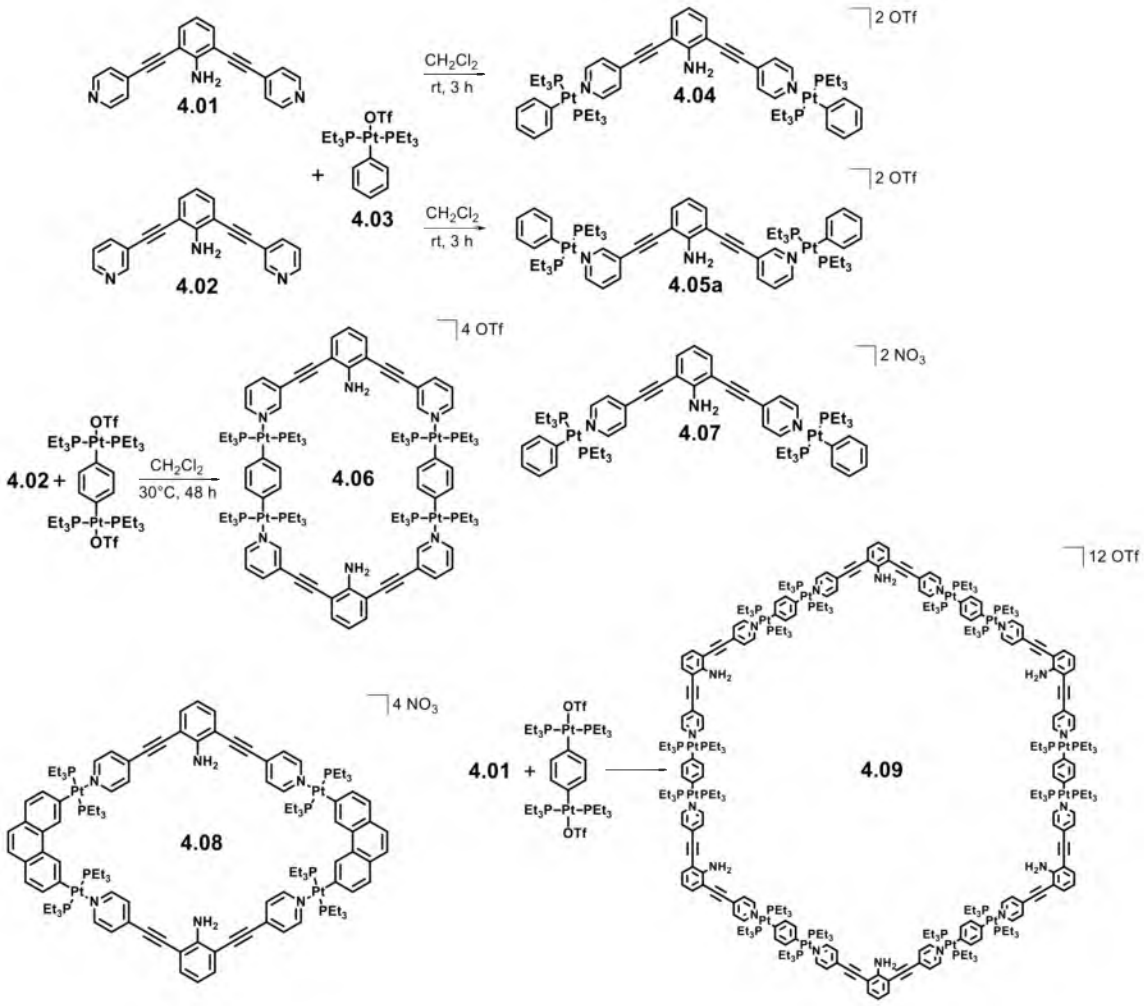

Scheme 4.1: Systems for investigating the effects of structural isomerism

Investigations probing the effects of size and shape on the photophysical properties of Pt-based SCCs are relatively rare when compared to synthetic and structural studies.[4] For instance, while it is clear that the position of the coordinating nitrogen dictates the architectural outcome of a self-assembly, the photophysical ramifications of structural isomerism are not well understood. Here, two isomeric ligands are employed: the previously mentioned 120° 2,6-bis(pyrid-4ylethynyl) aniline[2] donor (**4.01**) that has the coordinating nitrogen *para* to the ethynyl moiety and 2,6-bis(pyrid-3-ylethynyl) aniline[5] (**4.02**), with its nitrogen *meta* to the ethynyl moiety, represents a clip-like 0° donor (Scheme 4.1). Since the different angularities of donors **4.01** and **4.02** necessarily obviate the ability to form structurally analogous SCCs, a platinum acceptor (**4.03**) was synthesized to effectively cap each ligand. Given that the photophysical properties of the aforementioned rhomboidal SCC containing **4.01** were attributed to ligand-centered transitions, it was anticipated that the emissive behavior of such SCCs could be largely preserved in model systems wherein a ligand is capped by two Pt-centers, truncating a metallacycle to a single Pt-ligand-Pt fragment. As models of the Pt–ligand–Pt fragment of SCCs, **4.04** and **4.05a** reveal the effects of structural isomerism for ligands commonly used in metallacycle formation (Scheme 4.1).[4] While **4.05a** can exist as two additional conformers, the configuration shown in Scheme 4.1 is the energetic minimum as indicated by DFT calculations (*vide infra*). Interestingly, the nature of the molecular orbitals involved with the low-energy optical transition for **4.04** are significantly different from that of the previously reported system.

It has been established that the molecular orbitals involved with the observed optical transitions from endodedral amine-functionalized systems arise from mainly ligand-centered transitions, with only modest contributions from the metal center. Despite the lack of metal character in the orbitals involved in allowed electronic transitions, complexation of the dipyridyl ligands gives marked spectral shifts, as high as 100 nm (4540 cm^{-1}) when **4.01** coordinates to Pt.[3] As such, a complementary suite of compounds was synthesized to probe the photophysical influence stemming from the metal-containing fragment of these model systems. To accomplish this, the *trans* aryl group on the bis(phosphine) Pt(II) metal center was functionalized with either a methoxy (**4.13**; Scheme 4.2) or nitro (**4.14**; Scheme 4.2) group. These molecules were investigated using computational methods to determine the origins of any observed spectral changes. Also, an isoelectronic bis(phosphine) Pd(II) analog of **4.04** (**4.15**; Scheme 4.2) was prepared to determine: (i) can ISC be attenuated using a metal less prone to exhibit spin-orbit coupling, thus circumventing the main nonradiative decay pathway of these aniline compounds? and (ii) are desirable photophysical properties (visible wavelength emission, tunable bands, etc.) retained when using a second row d^8 metal center versus a third row d^8 Pt(II) metal center? Herein, the synthesis and steady-state absorption and emission and excited-state lifetime measurements of these SCC model systems are described with the intention of establishing the effects of structural isomers and effects originating from the perturbations of the electronics of the metal nodes by incorporating auxiliary functional groups on the bis(phosphine) aryl–Pt(II) capping unit and substituting

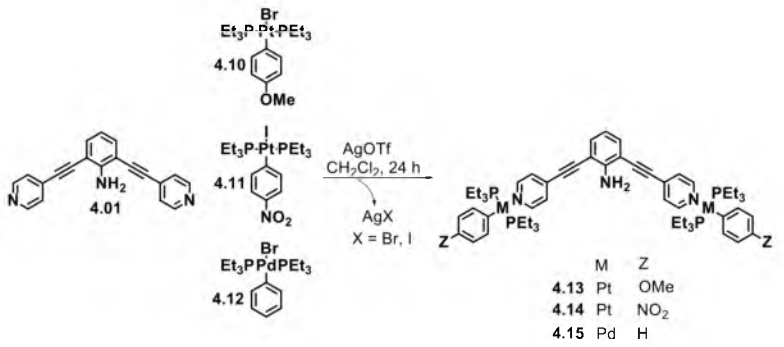

Scheme 4.2: Systems for probing the effects of the metal-containing fragments

Pt(II) for Pd(II) metal centers. These experiments are augmented by DFT and TD-DFT calculations to probe the nature of the observed optical transitions.

4.2 Results

4.2.1 Synthesis

The Pt-capped dipyridyl aniline compounds in Scheme 4.1 were obtained under synthetic conditions similar to those used for SCC formation. A CH_2Cl_2 solution of **4.01** or **4.02** with **4.03**, reflecting the 2:1 stoichiometry of acceptor to donor, furnished the Pt-ligand-Pt triads after three hours of stirring at room temperature and precipitation by diethyl ether. The combination of **4.02** and a linear diplatinum donor[6] in a 1:1 ratio extends the Pt-ligand-Pt motif to a closed metallacycle, **4.06**, which was used to validate **4.05a** as an appropriate model for larger SCCs. Similarly, the combination of **4.01** with the linear donor furnished a hexagonal metallacycle **4.09**[3] whose properties were useful in comparison to model system **4.04**. These systems were characterized via ESI-MS and $^{31}P\{^1H\}$ and ^1H NMR (see Appendix).

The M-ligand-M triads in Scheme 4.2 (**4.13**–**4.15**) were synthesized by stirring

4.01 with **4.10**,[7] **4.11**,[8] or **4.12**[9] in 1:2 stoichiometry with 2 equivalents of silver triflate in CH_2Cl_2. After 24 h of stirring at room temperature in the dark, the solutions were filtered to remove insoluble silver halide. Diethyl ether was then added to the homogenous solution to precipitate the product. The solids were then dried overnight *in vacuo* and redissolved in CD_2Cl_2 for characterization (see Appendix). Figure 4.1 displays the $^{31}P\{^1H\}$ NMR spectra for **4.14** (top, left) and **4.15** (bottom, left) where the loss of ^{195}Pt satellites for **4.15** is evident. The electrospray ionization mass spectrum of the doubly charged $[M–2•OTf]^{2+}$ ion for **4.13** is shown in Figure 4.1 (right) and is in good agreement with the theoretical isotopic distribution pattern (shown in red). In each case, a characteristic downfield shift of the pyridyl protons was observed upon coordination to the metal centers.

4.2.2 Photophysical Properties

As shown in Table 4.1, ligands **4.01** and **4.02** were determined to have low-energy absorption bands centered at 373 and 362 nm, respectively, with similar molar absorption coefficients (**4.01**, 13,700 cm^{-1} M^{-1}; **4.02**, 12,200 cm^{-1} M^{-1}). A single emission band was observed for **4.01** and **4.02** with each being centered at 422 and 408 nm, respectively. The quantum yield for **4.01** (Φ = 65%) is roughly double that of **4.02** (Φ = 30%).

Figure 4.2 displays the absorption and emission spectra for **4.04–4.07** with the relevant metrics summarized in Table 4.1. Each compound is characterized by a high-energy absorption band between 300 and 350 nm, with the largest molar absorption coefficient being observed for **4.04**. In addition, all four species

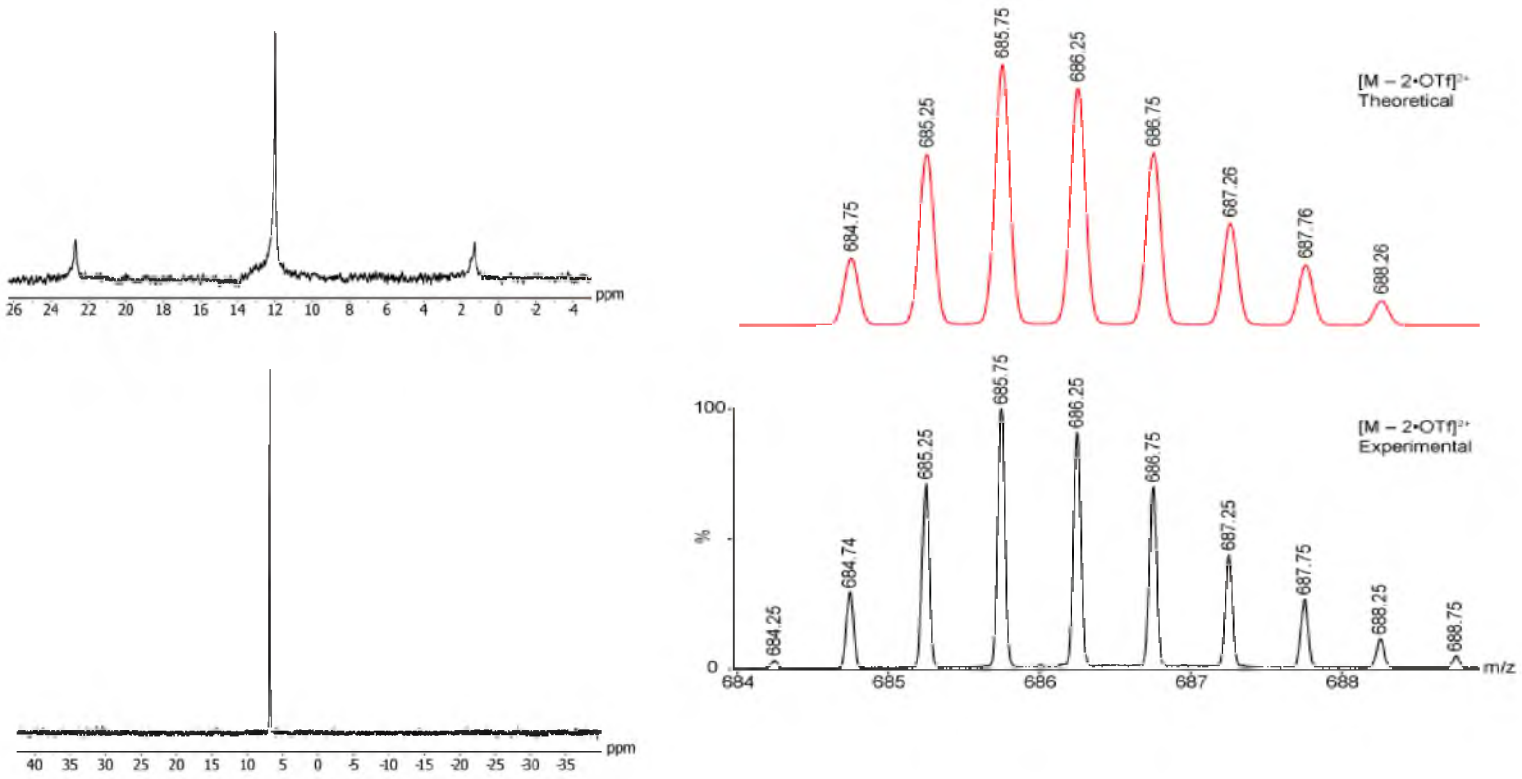

Figure 4.1: $^{31}P\{^{1}H\}$ NMR spectra of **4.14** (left, top) and **4.15** (left, bottom) and ESI mass spectrum of **4.13** (right).

Table 4.1: Photophysical data of compounds **4.04**, **4.05a**, and **4.06–4.09**.

Compound	Absorption Bands λ_{max} / (nm) [ε x 10^{-3} /(cm^{-1} M^{-1})]	λ_{exc} / (nm)	λ_{emiss} / (nm)	Φ / (%)[a]	τ / (10^{-9} s)	k_{rad} / (10^8 s^{-1})[b]	k_{nr} / (10^8 s^{-1})[b]
4.01[c]	282 [28.6], 300 *sh* [20.7], 373 [13.7]	356	422	65	2.55	2.55	1.37
4.02	300 *sh* [17.7], 362 [12.2]	365	408	30	2.59	1.16	2.70
4.04	318 [44], 423 [26]	423	500	32	1.37	2.34	4.96
4.05a	292 [35], 393 [16]	393	461	19	2.58	0.74	3.14
4.06	293 [16], 402 [10]	402	466	12			
4.07	321 [36], 425 [20]	425	510	34			
4.08[c]	258 [135], 267 *sh* [130], 288 [85.2], 317 [112], 430 [39.9]	430	522	28			
4.09[c]	284 *sh* [95.2], 318 [139], 422 [87.6]	422	505	15			

[a]Quinine sulfate at 365 nm was used for quantum yield determination. [b]$k_{rad} = \Phi \bullet \tau^{-1}$; $k_{nr} = \tau^{-1} - k_{rad}$. [c]Absorption and quantum yield data obtained from Ref. 6.

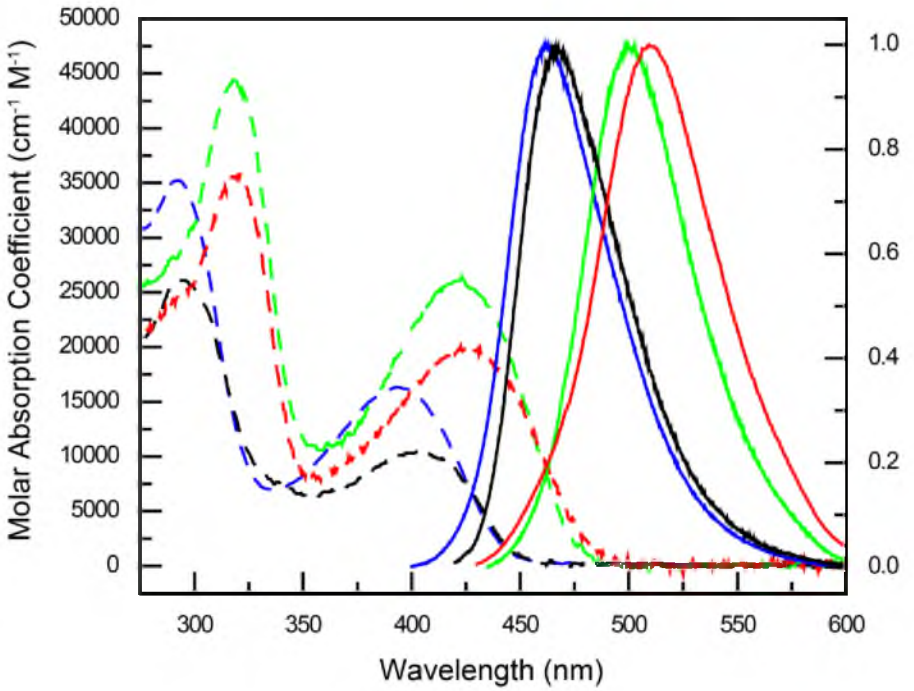

Figure 4.2: Absorption (dashed) and emission (solid) spectra for **4.04** (—green), **4.05a** (—blue), **4.06** (—black) and **4.07** (—red). The spectra were collected in aerated CH_2Cl_2 at room temperature.

contain a less intense band at longer wavelengths ~400–450 nm. The molar absorption coefficients of the second bands (~10,000 –25,000 cm^{-1} M^{-1}) are roughly half those of the higher energy bands (~15,000 –45,000 cm^{-1} M^{-1}). The single emission bands for this series of compounds are centered at 500 nm for **4.04**, 461 nm for **4.05a**, 466 nm for **4.06**, and 510 nm for **4.07** with quantum yields (Φ) of 32%, 19%, 12%, and 34%, respectively.

Excited-state lifetime measurements were performed using an 800 ps pulse width excitation at 336 nm. The decay of the excited-state was monitored by the loss of emission intensity at the wavelength maxima for each sample, as determined from steady-state measurements. The decay profiles were fit to bi-

exponential functions where τ_1 corresponded to the intact platinated species of **4.04** (1.37 ns) and **4.05a** (2.58 ns) with 83.6% and 97.7% contributions, respectively. All excited-state lifetime traces can be found in the Appendix.

Figure 4.3 displays the absorption and emission spectra for **4.13–4.15** with the relevant metrics summarized in Table 4.2. Each compound is characterized by a high-energy band between 306 and 325 nm, with the largest molar absorption coefficient being observed for **4.14**. In addition, all species contain a less intense band at longer wavelengths ~400–425 nm. The molar absorption coefficient of the higher-energy band (~35,000–65,000 cm^{-1} M^{-1}) is roughly double that of the low-energy band (~20,000–23,000 cm^{-1} M^{-1}).

The single emission bands for this series of compounds were centered at 500 nm for **4.13**, 508 nm for **4.14**, and 494 nm for **4.15** with quantum yields (Φ) of 20%, 13%, and 41%, respectively.

The effect of excitation wavelength on the lifetimes of **4.13–4.15** was investigated by employing both 336 nm and 458 nm light in the measurements to determine whether the lifetime was independent of wavelength. The decay profiles were fit to bi-exponential functions where the average of τ_1 corresponded to the intact platinated species of **4.13** (2.20 ns) and **4.14** (2.62 ns) and the palladium bound **4.15** (3.26 ns) with 95.8%, 95.5%, and 88.5% contributions, respectively, at 336 nm. Similar lifetimes were observed at 458 nm (Table 4.2) indicating that the excited-state leading to radiative decay is accessed through internal conversion and is thus independent of the wavelength of excitation.

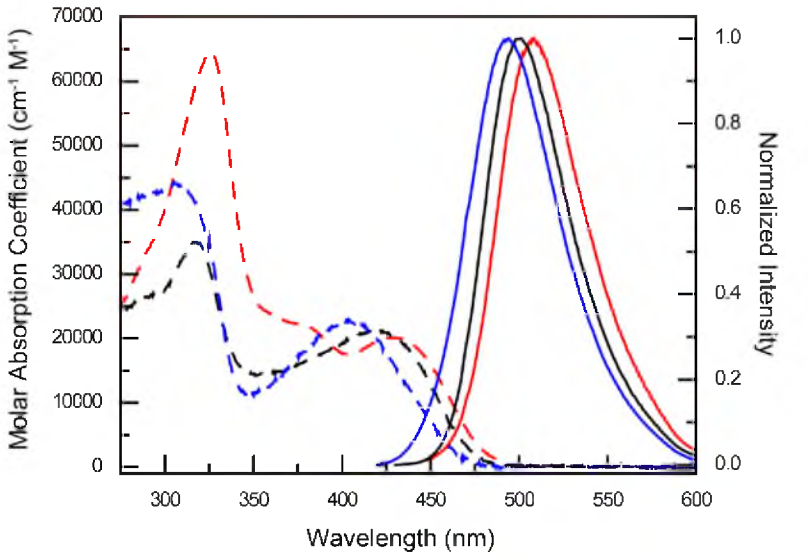

Figure 4.3: Absorption (dashed) and emission (solid) spectra for **4.13** (—; black), **4.14** (—; red) and **4.15** (—; blue). The spectra were collected in aerated CH_2Cl_2 at room temperature.

Table 4.2: Photophysical data of compounds **4.13–4.15**

Compound	Absorption Bands λ_{max} / (nm) [ε x 10^{-3} /(cm^{-1} M^{-1})]	λ_{exc} / (nm)	λ_{em} / (nm)	Φ / (%)[a]	τ / (10^{-9} s)	k_{rad} / (10^8 s^{-1})[b]	k_{nr} / (10^8 s^{-1})[b]
4.13	317[35], 420 [21]	420	500	20	2.20	0.91	3.64
4.14	325 [65], 377 *sh* [22], 429 [20]	429	508	13	2.62	0.50	3.32
4.15	306 [44], 404 [23]	404	494	41	3.26	1.26	1.81

[a]Quinine sulfate at 365 nm was used for quantum yield determination. [b]$k_{rad} = \Phi \bullet \tau^{-1}$; $k_{nr} = \tau^{-1} - k_{rad}$.

4.2.3 Photophysical Discussion

It is readily apparent that the position of the pyridyl nitrogen atom has an effect on the resulting photophysical properties of **4.01** and **4.02**, as evidenced by the red-shifted low-energy absorption and emission band maxima of **4.01** (373 and 422 nm, respectively) when compared to that of **4.02** (362 and 408 nm, respectively). The quantum yield of **4.01** (Φ = 65%) was determined to be more than double that of **4.02** (Φ = 30%). It should be noted that previous reports have determined that the main nonradiative decay pathway from the S_1 excited-state of aniline-based compounds is via ISC to a nonradiative triplet state.[10]

Interestingly, upon platination, ligands **4.01** and **4.02** have marked shifts in the low-energy absorption and emission bands. When comparing ligand **4.01** to complex **4.04**, the low-energy absorption band maximum is red-shifted by 50 nm (3169 cm^{-1}), and the emission band maximum is red-shifted by 78 nm (3697 cm^{-1}). Similarly, but to a lesser degree, the low-energy absorption and emission band maxima of **4.02** are red-shifted when compared to **4.05a** by 31 (2179 cm^{-1}) and 53 nm (2818 cm^{-1}), respectively. An overall loss of quantum yield is also observed upon platination with **4.04** (Φ = 32%) being 33% lower than that of **4.01**, while **4.05a** (Φ = 19%) is 11% lower than that of **4.02**.

The apparent differences in the photophysical properties that arise from the position of the pyridyl nitrogen atom in ligands **4.01** and **4.02** are preserved when comparing **4.04** and **4.05a**, as evidenced by the blue-shift of the low-energy absorption and emission peak maxima of **4.05a** (30 and 39 nm or 1804 and 1692 cm^{-1}, respectively) when compared to that of **4.04**. In addition, the molar

absorption coefficient for the low-energy absorption band was 16,000 cm^{-1} M^{-1} (393 nm) for **4.05a** but was less than that of **4.04** at 26,000 cm^{-1} M^{-1} (423 nm).

The photophysical differences between isomers **4.04** and **4.05a** were further manifested in the quantum yields, wherein that of **4.05a** (Φ = 19%) is lower than that of **4.04** (Φ = 32%). To better understand these differences, excited-state lifetime measurements were employed to probe the radiative and nonradiative rate constants of the excited-state.

The excited-state lifetimes (τ_1) of **4.01** (2.55 ns), **4.02** (2.59 ns), **4.04** (1.37 ns), and **4.05a** (2.58 ns) are all similar in magnitude, as are the rate constants for the radiative decay pathway of **4.01** (k_{rad} = 2.55•10^8 s^{-1}) and **4.04** (k_{rad} = 2.34•10^8 s^{-1}), which were calculated using the quantum yields and excited-state lifetimes. However, the rate constant for the nonradiative decay pathway for **4.04** (k_{nr} = 4.96•10^8 s^{-1}) is more than double that of **4.01** (k_{nr} = 1.37•10^8 s^{-1}). Since k_{nr} is the sum of the rate constants for all nonemissive processes, this indicates that **4.04** either has access to more nonradiative decay pathways or has better overlap with a nonradiative excited-state; moreover, the inclusion of platinum in these systems enhances the rate of spin-forbidden processes, coined the "heavy atom effect." From the TD-DFT calculations (*vide infra*) it was determined that **4.04** utilizes the frontier orbitals during the lowest energy electronic transition. Therefore, while it is advantageous in some Pt-based systems to increase ISC,[1d,11] the decrease in the quantum yield of **4.04** (Φ = 32%) when compared to that of **4.01** (Φ = 65%) could be attributed to better overlap between the nonradiative triplet and S_1 excited-states (shown in Figure 4.4); no

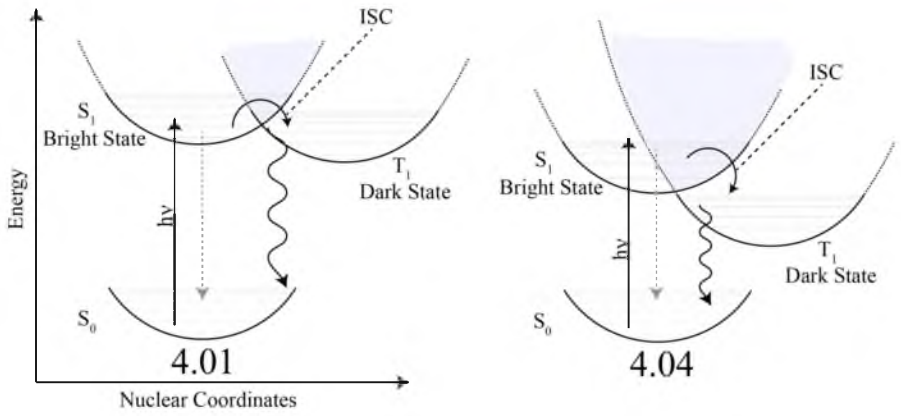

Figure 4.4: Jablonski diagrams for **4.01** (left) and **4.04** (right).

phosphorescence was observed in the platinated species in degassed, oxygen free solvent. Interestingly, the rate constants for the radiative decay pathways for **4.02** (k_{rad} = 1.16•10^8 s^{-1}) and **4.05a** (k_{rad} = 0.74•10^8 s^{-1}) are different, indicating that platination not only induces both ISC, as was seen in the case of **4.01** versus **4.04**, but also affects the radiative decay pathway.

Both the rate constants for the radiative and nonradiative decay pathways of **4.04** (k_{rad} = 2.34•10^8 s; k_{nr} = 4.96•10^8 s^{-1}) are higher than that of **4.05a** (k_{rad} = 0.74•10^8 s^{-1}; k_{nr} = 3.14•10^8 s^{-1}), which implicates that the higher quantum yield of **4.04** is due to ligand **4.01** (Φ = 65%) when compared to **4.02** (Φ = 30%). Also, the quantum yield of **4.04** (Φ = 32%) is half that of **4.01** (Φ = 65%) while the quantum yield of **4.05a** (Φ = 19%) is two-thirds that of **4.02** (Φ = 30%). Understanding these differences requires an analysis of the molecular orbitals involved with the relevant optical transitions (*vide infra*).

Platinum complexes **4.04** and **4.05a** were then compared to metallacyclic SCC analogues to evaluate the use of capped M–L–M fragments as models for larger systems. Since computational investigations implicate ligand-centered

HOMO and LUMO orbitals in the low-energy optical transitions of **4.04** and **4.05a** (*vide infra*), it was expected that these truncated fragments were valid models.

Comparing **4.05a** to its hexagonal SCC counterpart, **4.06**, the low-energy absorption and emission bands of **4.05a** are blue-shifted by 9 nm (569 cm^{-1}) and 5 nm (233 cm^{-1}), respectively. The quantum yield of **4.05a** (Φ = 19%) is higher than that of **4.06** (Φ = 12%). The absorption and emission profiles are in good-agreement for **4.05a** versus **4.06** and the quantum yield difference can be accounted for by the inclusion of more Pt(II) metal centers, which will enhance the "heavy atom effect." Therefore, **4.05a** is a good model for **4.06**.

The previously reported endohedral amine-functionalized D_{2h} [2+2] rhomboid (**4.08**; Scheme 4.1) synthesized from ligand **4.01** and a 60° phenanthrene diplatinum nitrate acceptor (Scheme 4.1) has photophysical properties that show relatively greater discrepancies when compared with those of **4.04**. The low-energy absorption and emission peak maxima of **4.08** are both blue-shifted by 7 nm (385 cm^{-1}) and 22 nm (843 cm^{-1}), respectively. However, when compared to the endohedral amine-functionalized [6 + 6] hexagon[3] (**4.09**; Scheme 4.1), which contains ligand **4.01** and a 180° benzene-based diplatinum triflate acceptor, the low-energy absorption bands differs by only 1 nm (56 cm^{-1}), and the emission band of **4.09** is red-shifted by 5 nm (198 cm^{-1}) relative to that of **4.04**; the shifts in the observed optical transitions is thought to arise from the differences in the aromatic scaffolds (i.e., **4.03** has a benzene core scaffold much like the 180° benzene-based diplatinum acceptor while the rhomboid is synthesized from a 60° phenanthrene-based diplatinum acceptor). As such, **4.04** appropriately models

the photophysical properties of its analogous hexagonal SCC, but not its rhomboidal counterpart.

To probe the differences in the photophysical properties of **4.04** and **4.08**, the counterion and the aromatic group *trans* to the coordinating nitrogen were investigated. The nitrate counterion analogue to **4.04**, (**4.07**; Scheme 4.1), was prepared and possessed low-energy absorption and emission peak maxima that were red-shifted when compared to those of **4.04** by 2 nm (112 cm^{-1}) and 10 nm (392 cm^{-1}), respectively. This result is interesting since the counterions of a SCC are often thought to be outer-sphere and typically are not ascribed any photophysical relevance. Also, the low-energy absorption and emission peak maxima of **4.07** are blue-shifted by 5 nm (273 cm^{-1}) and 12 nm (451 cm^{-1}), respectively, when compared to those of **4.08**, which indicates that these systems are sensitive to the nature of the aryl group *trans* to the Pt-N.

To better understand and probe this effect, the aryl group *trans* to the coordinating nitrogen was functionalized at the *para* position to give systems with an electron donating methoxy group (**4.13**; Scheme 4.2) and an electron withdrawing nitro group (**4.14**; Scheme 4.2). Previous studies hypothesized that π-backbonding from the bis(phosphine) Pt(II) metal center to the coordinated pyridyl nitrogen accounted for the observed optical shifts between free ligands and their coordinated counterparts.[3,12,13] These two compounds allowed for a direct probe into the effects of perturbing the π-system of the metal-fragments. An isoelectronic bis(phosphine) Pd(II) metal complex (**4.15**; Scheme 4.2) was also utilized to attenuate spin-orbit coupling, thereby decreasing ISC. Since ISC

is a known nonradiative decay pathway for aniline-based compounds, this should result in a higher quantum yield.

The NO_2-aryl Pt system (**4.14**) displayed the lowest energy absorption (429 nm) and emission (508 nm) band maxima, which are red-shifted when compared to both the nonfunctionalized-aryl system, **4.04**, (λ_{abs} = 423 nm; λ_{em} = 500 nm) and OMe-aryl Pt system **4.13** (λ_{abs} = 420 nm; λ_{em} = 500 nm). The quantum yield, however, of system **4.14** (Φ = 13%) is lower than that of **4.13** (Φ = 20%) and **4.04** (Φ = 32%), while the excited-state lifetime of **4.14** (τ = 2.62 ns) is higher than that of **4.13** (τ = 2.20 ns) and **4.04** (τ = 1.37 ns). From these results it was calculated that the rate constants for the nonradiative (k_{rad}) and radiative (k_{nr}) decay pathway for **4.14** (k_{rad} = $0.50 \cdot 10^8$ s^{-1}; k_{nr} = $3.32 \cdot 10^8$ s^{-1}) were the lowest as compared to that of **4.13** (k_{rad} = $0.91 \cdot 10^8$ s^{-1}; k_{nr} = $3.64 \cdot 10^8$ s^{-1}) and of **4.04** (k_{rad} = $2.34 \cdot 10^8$ s^{-1}; k_{nr} = $4.96 \cdot 10^8$ s^{-1}).

Pd-based **4.15** displays a blue-shift in both the absorption and emission bands as compared to its isoelectronic Pt-based system, **4.04**. The low-energy absorption band of **4.15** was blue-shifted by 19 nm (1111 cm^{-1}), and the emission band maximum was blue-shifted by 6 nm (243 cm^{-1}) when compared to those of **4.04**. The excited-state lifetime, however, is much higher for **4.15** (τ = 3.26 ns) when compared to that of **4.04** (τ = 1.37 ns), which could account for the overall 9% higher quantum yield of the former over the latter. The k_{rad} for **4.15** is $1.26 \cdot 10^8$ s^{-1} while the k_{nr} is $1.81 \cdot 10^8$ s^{-1}, and the values calculated for **4.04** were k_{rad} = $2.34 \cdot 10^8$ $s^{-1}$and k_{nr} = $4.96 \cdot 10^8$ s^{-1}. The difference in k_{rad} implies that a different radiative pathway (i.e., the nature of the molecular orbitals involved in

the electronic transition) may exist and to better understand why the observed optical transitions are higher in energy for **4.15** when compared to **4.04**, time-dependent density functional (TD-DFT) calculation were employed (*vide infra*).

4.3 DFT and TD-DFT General Information

Geometry optimization calculations were performed using a split basis set where B3LYP[14] functionals and 6-31G** basis set[15] were used for C, H, N, and P atoms while the LANL2-DZ[16] basis set and pseudopotential were used for Pt and Pd. To minimize computational cost, $P(CH_3)_3$ ligands were utilized instead of PEt_3; therefore, the model used to approximate compound *X* is abbreviated as *X*–*P(CH$_3$)$_3$*, where *X* is the compound number. A frequency analysis was also performed to determine if any imaginary states exist below the energy minimum. The vertical singlet transition energies of the complexes were computed at the TD-DFT level within G09[17] using the ground state optimized structure. For the structures that were calculated, 1000 or more total molecular orbitals are observed and each molecular orbital number that is listed is real and in its absolute energetic order. The nomenclature that will be utilized to discuss these molecular orbitals will be relative to the HOMO and LUMO (i.e., HOMO-1 is the molecular orbital directly below the HOMO).

As mentioned previously, compound **4.05a** can exist as one of three conformers as shown in Figure 4.5. DFT optimizations of the three compounds determined that **4.05a**–*P(CH$_3$)$_3$* is the lowest in energy (Table 4.3) by 3.70 kcal/mol when compared to **4.05b**–*P(CH$_3$)$_3$* and 1.51 kcal/mol when compared to **4.05c**–*P(CH$_3$)$_3$*; therefore, despite having energies that are very closely related,

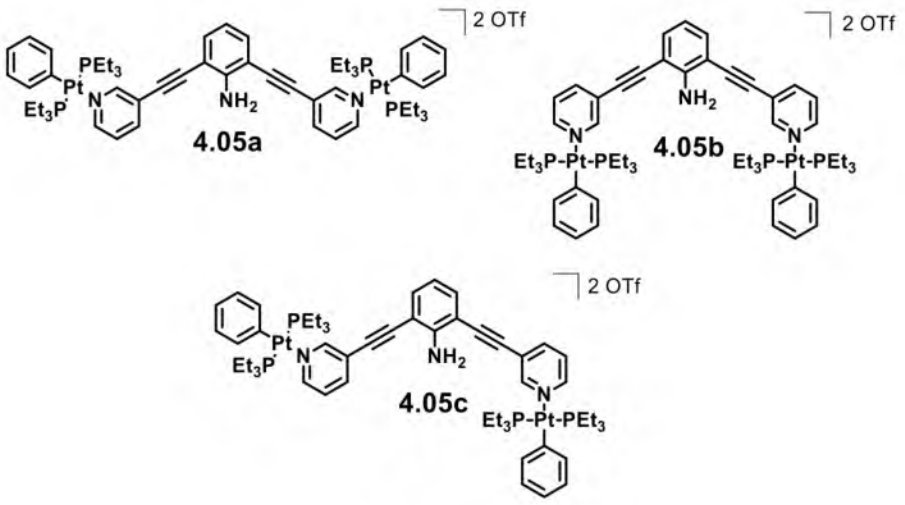

Figure 4.5: 4.05a and the two additional conformers that it can exist as

Table 4.3: DFT optimization energies for **4.05a**–*P(CH$_3$)$_3$* – **4.05c**–*P(CH$_3$)$_3$*.

Compound	Energy (Hartrees)	Δkcal/mol
4.05a–*P(CH$_3$)$_3$*	-3480.00293429	0.0000
4.05b–*P(CH$_3$)$_3$*	-3479.99704283	3.6970
4.05c–*P(CH$_3$)$_3$*	-3480.00052333	1.5129

configuration 5a–$P(CH_3)_3$ was used in subsequent TD-DFT calculations.

4.4 TD-DFT Results and Discussion

From the TD-DFT calculations of **4.04**–$P(CH_3)_3$ and **4.05a**–$P(CH_3)_3$, the low-energy optical transitions were determined to originate from a HOMO to LUMO electronic transition which involves ligand-centered molecular orbitals with π-type symmetry (Figure 4.6). The predicted observed low-energy optical transitions occur at 451 nm for **4.04**–$P(CH_3)_3$ and 424 nm for **4.05a**–$P(CH_3)_3$ (see Table 4.4).

In the low-energy transition for both **4.04**–$P(CH_3)_3$ and **4.05a**–$P(CH_3)_3$, the HOMO has the nitrogen p-orbital and ethynyl π-system in phase and bonding, while the LUMO has little electron density on the aniline nitrogen p-orbital, and the ethynyl π-system is antibonding; however, despite sharing similar

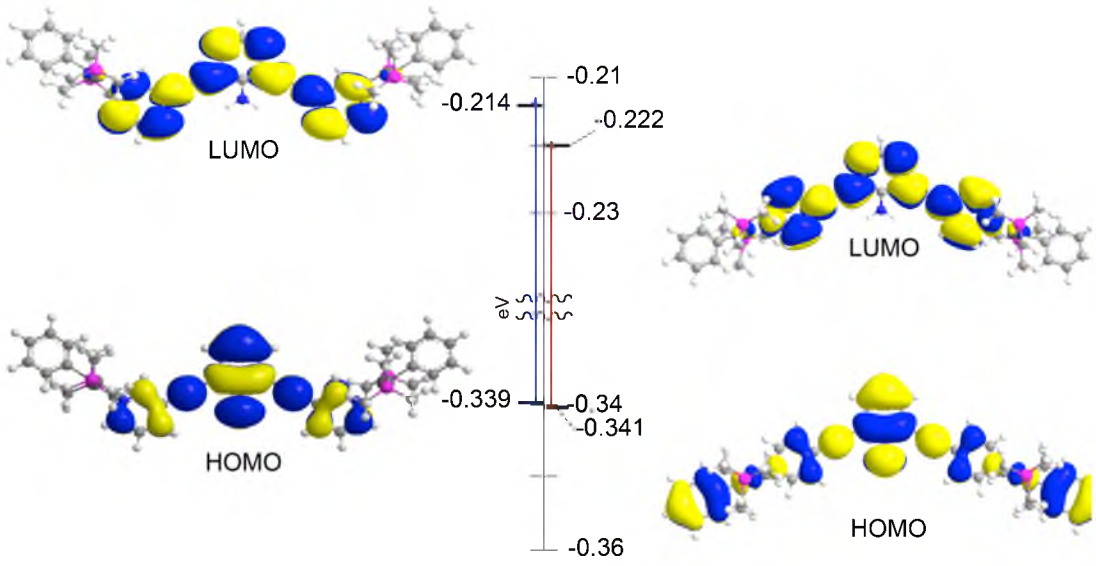

Figure 4.6: HOMO and LUMO of **4.04**–$P(CH_3)_3$ (*right*) and **4.05a**–$P(CH_3)_3$ (*left*).

Table 4.4: Electronic transitions predicted for **4.04**–$P(CH_3)_3$ and **4.05a**–$P(CH_3)_3$ with $f > 0.2$

Compound	Wavelength / nm	Orbital transitions	Orbital transitions	Oscillator strength, f	Description
4.04–$P(CH_3)_3$	451	219 → 220	HOMO → LUMO	0.925	MLCT LLCT $^1\pi \rightarrow {}^1\pi^*$
	343	214 → 221	HOMO-5 → LUMO+1	1.200	ILCT $^1\pi \rightarrow {}^1\pi^*$
4.05a–$P(CH_3)_3$	424	219 → 220	HOMO → LUMO	0.715	ILCT $^1\pi \rightarrow {}^1\pi^*$
	329	214 → 221 216 → 221	HOMO-5 → LUMO+1 HOMO-3 → LUMO+1	0.746	LLCT LMCT $^1\pi \rightarrow {}^1\pi^*$

characteristics, **4.04**–$P(CH_3)_3$ also has a significant amount of charge transfer character. After performing a population analysis it was determined that in the HOMO for **4.04**–$P(CH_3)_3$, 8% of the electron density is on the Pt-phosphine metal center and 15% of the electron density is on phenyl group while 5% and 0.1% of the electron density lie on the Pt-phosphine and phenyl group in the LUMO. The ligand gains an appreciable amount of electron density during the HOMO (77%) to LUMO (95%) transition, which leads to the charge transfer being described as a mixture of metal-ligand (MLCT) and ligand-ligand (LLCT) charge transfer; the

charge transfer character of the low-energy transition could explain why the emission of **4.04** is sensitive to the nature of the aromatic group trans to the coordinating *N* of the pyridyl group. Also, for the HOMO of **4.05a**–*P(CH$_3$)$_3$* (left, Figure 4.6), the coordinating nitrogen and platinum metal center are nonbonding versus antibonding in **4.04**–*P(CH$_3$)$_3$* (right, Figure 4.6), which could account for the apparent differences in the measured quantum yields and calculated rate constants between **4.04** and **4.05a**. The LUMO in both systems has an antibonding character between the coordinating nitrogen and platinum metal center. This modulation of the energies of the HOMO and LUMO with **4.05a**–*P(CH$_3$)$_3$* (0.125 eV) having a larger energy gap compared to **4.04**–*P(CH$_3$)$_3$* (0.119 eV) is in agreement with **4.04** having a lower-energy absorption band. It should be noted that the oscillator strengths of the lowest-energy predicted transitions from the calculations of **4.04** (0.925) and **4.05a** (0.715) reflect the trend observed in the experimental molar absorption coefficients of the low-energy optical transitions.

The predicted high-energy electronic transitions for **4.04**–*P(CH$_3$)$_3$* and **4.05a**–*P(CH$_3$)$_3$* were determined to originate from lower lying occupied molecular orbitals (e.g., HOMO-5 for **4.04**–*P(CH$_3$)$_3$* and HOMO-5 and HOMO-3 for **4.05a**–*P(CH$_3$)$_3$*) to unoccupied destination molecular orbitals that are higher than the LUMO (e.g., LUMO+1 for **4.04**–*P(CH$_3$)$_3$* and **4.05a**–*P(CH$_3$)$_3$*). The observed optical transitions arising from the electronic transitions are predicted to occur at 343 nm for **4.04**–*P(CH$_3$)$_3$* and 329 nm for **4.05a**–*P(CH$_3$)$_3$*. The molecular orbitals involved in the optical transition at 343 nm for **4.04**–*P(CH$_3$)$_3$* show that the

transition arises from the HOMO having the nitrogen p-orbital and ethynyl π-system in phase and bonding, while the LUMO has little electron density on the aniline nitrogen p-orbital and the ethynyl π-system is antibonding. Population analysis on the predicted high-energy electronic transition at 329 nm for **4.05a**–*P(CH$_3$)$_3$* determined that the singlet transition arises from a charge transfer between the Pt-aryl group to ligand **4.02** (>80% → <1%). Also, *ca.* 12% of the HOMO electron density lies on the Pt metal center for **4.05a**–*P(CH$_3$)$_3$*. In contrast, for the LUMO, more than 5% of the electron density is localized on the Pt metal centers; therefore, despite the mild ligand-to-metal charge transfer (LMCT) character, the HOMO → LUMO transition appears to be more appropriately described as a ligand-centered LLCT.

The TD-DFT calculation predicts three electronic transitions (see Table 4.5) to occur with oscillator strengths above 0.2 for **4.13**–*P(CH$_3$)$_3$*. The predicted low-energy transition arises from an electron being promoted from the HOMO-2 to the LUMO wherein the orbitals are largely ligand-centered (>95% electron density) and of π-type symmetry. The same electronic transition has a modest change in electron density on the platinum metal center (1.5% → 4.7%). A similar electronic transition was predicted at 455 nm for **4.14**–*P(CH$_3$)$_3$* wherein the HOMO and LUMO molecular orbitals are involved. The HOMO to LUMO transition involves π-type molecular orbitals with over 94% electron density being centered on the ligand, and it is accompanied by an increase in electron density on the platinum metal node (1.8% → 4.8%). This result is consistent with the previously discussed population analysis performed for **4.04**–*P(CH$_3$)$_3$* wherein the

Table 4.5: Electronic transitions predicted for **4.13**–$P(CH_3)_3$, **4.14**–$P(CH_3)_3$, and **4.15**–$P(CH_3)_3$ with $f > 0.2$

Compound	Wavelength / nm	Orbital transitions	Orbital transitions	Oscillator strength, f	Description
4.013–$P(CH_3)_3$	447	233 → 236	HOMO-2 → LUMO	0.839	ILCT $^1\pi \rightarrow {}^1\pi^*$
	343	230 → 237	HOMO-5 → LUMO+1	1.316	ILCT $^1\pi \rightarrow {}^1\pi^*$
	336	230 → 236 233 → 237	HOMO-5 → LUMO HOMO-2 → LUMO+1	0.253	ILCT $^1\pi \rightarrow {}^1\pi^*$
4.014–$P(CH_3)_3$	455	241 → 242	HOMO → LUMO	0.932	ILCT $^1\pi \rightarrow {}^1\pi^*$
	349	238 → 243 239 → 242 240 → 243	HOMO-3 → LUMO+1 HOMO-2 → LUMO HOMO-1 → LUMO+1	1.069	LLCT MLCT $^1\pi \rightarrow {}^1\pi^*$
4.15–$P(CH_3)_3$	446	219 → 220	HOMO → LUMO	0.872	ILCT $^1\pi \rightarrow {}^1\pi^*$
	342	216 → 221 218 → 221	HOMO-3 → LUMO+1 HOMO-1 → LUMO+1	1.166	LLCT MLCT $^1\pi \rightarrow {}^1\pi^*$
	335	216 → 220 219 → 221	HOMO-3 → LUMO HOMO-1 → HOMO+1	0.248	ILCT $^1\pi \rightarrow {}^1\pi^*$

ethynyl π system is weakened ($^1\pi \rightarrow {}^1\pi^*$) during the transition with a loss of electron density on the aniline nitrogen.

A higher energy optical transition with an oscillator strength of 1.316 is predicted to occur at 343 nm for **4.13**–*P(CH$_3$)$_3$* that utilizes the HOMO-5 and LUMO+1. This is very similar in nature to the predicted lowest energy transition where the molecular orbitals involved are of π-type symmetry and are ligand centered with modest contributions from the metal center. The HOMO-5 molecular orbital has 92% electron density on the ligand while 7.3% is on the metal center. The LUMO+1 molecular orbital has 94% of its electron density centered on the ligand and 5.9% on the metal center. The highest energy predicted electronic transition for **4.13**–*P(CH$_3$)$_3$* at 336 nm has an oscillator strength of 0.253. The electronic transition utilizes low lying occupied (HOMO-2 and HOMO-5) and low lying unoccupied (LUMO and LUMO+1) molecular orbitals that were discussed in the previous predicted electronic transitions for **4.13**–*P(CH$_3$)$_3$*.

The high-energy electronic transition for **4.14**–*P(CH$_3$)$_3$* is predicted to occur at 349 nm with an oscillator strength of 1.069 and, interestingly, can be characterized as a mixture of LLCT and MLCT bands. For the occupied molecular orbitals predicted to be involved (HOMO-3, HOMO-2, and HOMO-1), a population analysis was performed on the Pt-phosphine metal center (22%), aryl ligand (46%), and ligand **4.01** (31%); the percentages represent the average of the contributions for each molecular fragment. The destination molecular orbitals have 94.0% of the electron density on the ligand while 5.5% is on the metal

center. This predicted transition, however, is significantly different from **4.13**–*P(CH$_3$)$_3$* and previously studied systems.

Pd system **4.15**–*P(CH$_3$)$_3$* is predicted to have three electronic transitions with oscillator strengths over 0.20 with the lowest energy state corresponding to an excitation at 446 nm. This electronic transition involves the HOMO and LUMO orbitals and consists of π-type molecular orbitals with >96% of the electron density centered on the ligand. A loss of electron density on the aniline nitrogen is accompanied by weakening of the ethynyl π system ($^1\pi \rightarrow {}^1\pi^*$) during the transition. A similar transition was observed for the highest energy predicted transition at 335 nm.

The transition at 342 nm for **4.15**–*P(CH$_3$)$_3$* involves the HOMO-3 and HOMO-1 as the occupied molecular orbitals with the destination unoccupied molecular orbital being the LUMO+1. During this transition, the HOMO-1 has 73% of the electron density centered on the aryl group while 26.6% is centered on the Pd-Phosphine. The LUMO+1 molecular orbital has 0.8% electron density on the aryl group and 5.4% on Pd-Phosphine. This is a significant transfer of charge during the transition, unlike what is observed for system **4.04**–*P(CH$_3$)$_3$*, and is described as a mixture of LLCT and MLCT.

4.5 Conclusion

The photophysical properties of endohedral amine-functionalized bis(phosphine) Pt(II) SCCs can be tuned by using isomeric species. This is important since assembly reactions using isomeric donor ligands often times do not require synthetic redesigns and therefore offer a way to alter the absorption

and emission profiles of discrete SCCs without losing atom efficiency or changing synthetic conditions. Given the attractive photophysical properties observed for SCCs constructed from aniline-based donor ligands, developing a chemistry to tune these properties while maintaining the important aniline core is desirable. It was determined that the position of the coordinating nitrogen can greatly affect the photophysical properties of 2,6-diethynyl aniline-based ligands by using M–ligand–M fragments as suitable models for metallacyclic SCCs. The difference in the low-energy absorption bands was attributed to the different Pt-*N* coordination bonding modes in the HOMO. The M–ligand–M systems employed also allowed for this study to be extended to probing the metal fragment. Studies using functionalized aryl groups on the metal-based acceptor fragments showed no significant effects to the overall observed photophysical properties of the M–ligand–M systems despite having more significant charge transfer mechanisms. Also, a Pd analog, **4.15**, displayed an emission profile similar to that of its Pt counterpart, which suggests that cheaper systems employing bis(phosphine) Pd(II) nodes can be used in the synthesis of systems for photon-emitting devices without suffering a large penalty in the observed optical properties.

4.6 Experimental

Materials and Methods: 2, 6-Bis(pyrid-4ylethynyl) aniline[3] (**4.01**), 2, 6-bis(pyrid-3-ylethynyl) aniline[5] (**4.02**), bromophenylbis(triethylphosphine) platinum,[18] μ-1,4-phenylenetetrakis(triethylphosphine)bis(1,1,1-trifluoromethane-sulfonato-κO)diplatinum,[6] bromo(4-methoxy)bis(triethylphosphine)-, (*SP*-4-3)-platinum (**4.10**), [7] iodo(4-nitrophenyl)bis(triethylphosphine)-, (*SP*-4-3)-platinum

(**4.11**),[10] and bromophenylbis(triethylphosphine) palladium (**4.12**)[9] were prepared using known procedures. All compounds were used as bought from Sigma-Aldrich, Oakwood Chemicals, and TCI America while deuterated solvents were purchased from the Cambridge Isotope Laboratory (Andover, MA). ^{1}H and $^{31}P\{^{1}H\}$ NMR spectra were recorded on a Varian 300 spectrometer, and the mass spectra were recorded on a Micromass LCT Premier XE ToF mass spectrometer using electrospray ionization and analyzed using the MassLynx software suite. The ESI-MS samples were dissolved in methylene chloride then diluted with acetone unless otherwise noted. All $^{31}P\{^{1}H\}$ NMR spectra were referenced using a 10% H_3PO_4 *aq* solution. Elemental Analysis was performed by Atlantic Microlab, Inc.

(1, 1, 1-trifluoromethanesulfonato-κO)phenylbis(triethylphosphine)-platinum **(4.03)**: 99.5 mg of bromophenylbis(triethylphosphine) platinum (169 μmol) and 49.0 mg of silver triflate (57.9 μmol) were weighed into a Schlenk flask, evacuated by reduced pressure, placed under N_2 atmosphere, and covered with aluminum foil. In another Schlenk flask, 10 mL of methylene chloride was degassed by the freeze-pump-thaw method. The 10 mL of methylene chloride was then transferred via cannula to the Schlenk flask containing the starting materials. The reaction was allowed to stir at room temperature in the dark for 3 h. The resulting mixture was then filtered using air-free techniques. A clear, colorless solution was obtained and after the methylene chloride was removed via reduced pressure, an off-white solid was afforded. 88 mg (79% yield) ^{1}H NMR ($CDCl_3$, 300 MHz) δ 7.23 (d, 2H, ArH_{α}, J = 12.6 Hz), δ 6.85 (m, 3H, Ar*H*), δ 1.61

(*b*s, 12H, P*CH*$_2$), δ 1.11 (m, 18H, P*CH*$_3$). ^{31}P{^{1}H} NMR (CD_2Cl_2, 121.4 MHz) δ 20.79 (*b*s; ^{195}Pt satellites, $^1J_{Pt-P}$, 2847 Hz). ESI-MS ($C_{19}H_{35}F_3O_3P_2PtS$) m/z: [M–OTf] 508.19; [M–OTf + Acetone] 566.23. Anal. Calcd. for $C_{19}H_{35}F_3O_3P_2PtS$: C, 34.70; H, 5.36; Found: C, 34.85; H, 5.17.

General Procedure for Synthesis of Pt-Aryl OTf Capped Ligands: To a 2-dram vial, 2, 6-bis(pyrid-4ylethynyl) aniline (**4.01**; 1.0 mg, 3.4 μmol] or 2, 6-bis(pyrid-3-ylethynyl) (**4.02**) aniline (1.0 mg, 3.4 μmol) were added with (1,1,1-trifluoromethanesulfonato-*κO*)phenylbis(triethylphosphine)-platinum (**4.03**; 4.5 mg, 6.8 μmol) in a 1:2 stoichiometric ratio. 1 mL of deuterated methylene chloride was then added, and the mixture was allowed to stir for 3 h. The compound was then purified via precipitation by adding diethyl ether to the homogenous solution. The mixture was centrifuged and the supernatant was decanted.

Diphenyl[μ-[4,4'-(1-amino-2,6-ethynediylbenzene)bis[pyridine-κ*N*]]tetrakis-(triethylphosphine)diplatinum **(4.04)**: ^{1}H NMR ($CDCl_3$, 300 MHz) δ 8.56–8.60 (d, 4H, Py*H*$_\alpha$, J = 12 Hz), δ 7.85–7.87 (d, 4H, Py*H*$_\beta$, J = 3 Hz), δ 7.49–7.52 (d, 2H, Ar*H*, J = 9 Hz), δ 7.32–7.34 (*d*, 4H, PtAr*H*$_\alpha$, J = 6 Hz, J_{ArH-Pt}=51 Hz), δ 7.05–7.09 (t, 4H, PtAr*H*$_\beta$, J = 12 Hz) , δ 6.95–6.97 (t, 2H, PtAr*H*$_\gamma$, J = 6 Hz) , δ 6.69–6.74 (t, 1H, Ar*H*, J = 15 Hz) , δ 5.83 (*b*s, 2H, ArN*H*$_2$) , δ 1.31–1.35 (m, 24H, PC*H*$_2$) , δ 1.07–1.17 (m, 36H, P*CH*$_3$). ^{31}P {^{1}H} NMR (CD_2Cl_2, 121.4 MHz) δ 10.84 (*b*s; ^{195}Pt satellites, $^1J_{Pt-P}$, 2695 Hz). ESI-MS ($C_{58}H_{83}F_6N_3O_6P_4Pt_2S_2$) m/z: $[M–OTf]^{1+}$ 1460.44; $[M–2•OTf]^{2+}$ 655.74. Anal. Calcd. for $C_{58}H_{83}F_6N_3O_6P_4Pt_2S_2$: C, 43.26; H, 5.19; N, 2.61; Found: C, 43.29; H, 5.23; N, 2.55.

Diphenyl[μ-[3,3'-(1-amino-2,6-ethynediylbenzene)bis[pyridine-κ*N*]]tetrakis-

(triethylphosphine)diplatinum **(4.05a)**: ^{1}H NMR ($CDCl_3$, 300 MHz) δ 8.81 (s, 2H, PyH_{α}), δ 8.56–8.58 (d, 2H, Py$H_{\alpha'}$, J = 6 Hz), δ 8.30–8.32 (d, 2H, PyH_{γ}, J = 6 Hz), δ 7.68–7.73 (m, 2H, PyH_{β}), δ 7.48–7.50 (*d*, 2H, Ar*H*, J = 6 Hz), δ 7.37–7.40 (*d*, 4H, PtArH_{β}, J = 9 Hz), δ 7.08 (m, 4H, PtArH_{α}), δ 6.98–7.01 (m, 2H, PtArH_{γ}), δ 6.69–6.75 (t, 1H, Ar*H*, J = 18 Hz) , δ 5.73 (*b*s, 2H, ArNH_2) , δ 1.34 (m, 24H, PCH_2) , δ 1.08–1.178 (m, 36H, PCH_3). ^{31}P {^{1}H} NMR (CD_2Cl_2, 121.4 MHz) δ 10.84 (*b*s; ^{195}Pt satellites, $^{1}J_{Pt-P}$, 2695 Hz). ESI-MS ($C_{58}H_{83}F_6N_3O_6P_4Pt_2S_2$) m/z: $[M–2•OTf]^{2+}$ 655.74. Anal Calcd for $C_{58}H_{83}F_6N_3O_6P_4Pt_2S_2$ [Complex]•CH_2Cl_2•Et_2O: C, 42.76; H, 5.41; N, 2.37; Found: C, 42.81; H, 5.22; N, 2.51.

Self-Assembly **(4.06)**: In separate 2-dram vials, 1.0 mg (3.4 μmol) of 2, 6-bis(pyrid-3-ylethynyl) aniline (**4.02**) and 3.4 mg (2.7 μmol) of μ-1,4-phenylene-tetrakis(triethylphosphine)bis(1,1,1-trifluoromethanesulfonato-κ*O*)diplatinum were added. Both compounds were then dissolved in 0.5 mL of deuterated methylene chloride. The μ-1,4-phenylenetetrakis(triethylphosphine)-bis(1,1,1-trifluorometh-anesulfonato-κ*O*)diplatinum solution was then added drop-wise to a stirring solution of 2, 6-bis(pyrid-3-ylethynyl) aniline, and the mixture was heated to 30°C and allowed to stir for 48 h. After which, the chartreuse-colored solution was filtered to remove any insoluble kinetic by-products (i.e., polymers). The compound was then purified by precipitation by adding diethyl ether, centrifuging, and decantation of the supernatant. (>85% yield). ^{1}H NMR ($CDCl_3$, 300 MHz) δ 9.10 (s, 4H, PyH_{α}), δ 8.58–8.60 (d, 4H, Py$H_{\alpha'}$, J = 6 Hz), δ 8.07–8.09 (d, 4H, PyH_{γ}, J = 6 Hz), δ 7.63–7.68 (m, 4H, PyH_{β}), δ 7.47–7.50 (*d*, 4H, Ar*H*, J = 9 Hz), δ

7.21 (s, 4H, PtAr*H*) , δ 7.01 (s, 4H, PtAr*H*), δ 6.68–6.73 (t, 2H, Ar*H*, J = 15 Hz) , δ 5.99 (*b*s, 4H, ArNH_2) , δ 1.38 (m, 48H, PCH_2), δ 1.12–1.17 (m, 72H, PCH_3). ^{31}P {^{1}H} NMR (CD_2Cl_2, 121.4 MHz) δ 11.29 (*b*s; ^{195}Pt satellites, $^1J_{Pt-P}$, 2730 Hz). ESI-MS ($C_{104}H_{154}F_{12}N_6O_{12}P_8Pt_4S_4$) m/z: $[M–2•OTf]^{2+}$ 1382.39; $[M–3•OTf]^{3+}$ 871.94. Anal. Calcd. for $C_{104}H_{154}F_{12}N_6O_{12}P_8Pt_4S_4$ [Complex]: C, 40.76; H, 5.06; N, 2.74; Found: C, 41.09; H, 5.27; N, 3.07.

Diphenyl[μ-[4,4'-(1-amino-2,6-ethynediylbenzene)bis[pyridine-κN]]tetrakis(tri-ethylphosphine)diplatinum **(4.07)**: 1.0 mg (3.4 μmol) of 2, 6-bis(pyrid-4ylethynyl) aniline (**4.01**) was weighed into a 2-dram vial. Two equivalents of bromo-phenylbis(triethylphosphine) platinum (4.0 mg, 6.8 μmol) and $AgNO_3$ (1.2 mg, 6.8 μmol) were also added into the same vial. 2 mL of CD_2Cl_2 was then added and the mixture was stirred at room temperature for 48 h in the dark. The solution was then filtered twice with glass microfiber filters to remove insoluble AgBr; a green-colored solution of **4.07** was afforded (96% yield). ^{1}H NMR ($CDCl_3$, 300 MHz) δ 8.58–8.60 (d, 4H, PyH_α, J = 6 Hz), δ 7.90–7.92 (d, 4H, PyH_β, J = 6 Hz), δ 7.48–7.51 (d, 2H, Ar*H*, J = 9 Hz), δ 7.31–7.34 (d, 4H, $PtArH_\alpha$, J = 12 Hz, J_{ArH-Pt} = 24 Hz), δ 7.04–7.09 (t, 4H, $PtArH_\beta$, J = 15 Hz) , δ 6.95–6.97 (t, 2H, $PtArH_\gamma$, J = 6 Hz) , δ 6.66–6.71 (t, 1H, Ar*H*, J = 15 Hz) , δ 5.83 (bs, 2H, ArNH_2) , δ 1.31–1.35 (m, 24H, PCH_2) , δ 1.07–1.17 (m, 36H, PCH_3). ^{31}P{^{1}H} NMR (CD_2Cl_2, 121.4 MHz) δ 12.88 (bs; ^{195}Pt satellites, $^1J_{Pt-P}$, 2696 Hz). ESI-MS ($C_{56}H_{83}N_5O_6P_4Pt_2$) m/z: $[M–ONO_2]^{1+}$ 1373.47; $[M–2•ONO_2]^{2+}$ 655.74. Anal. Calcd. for $C_{56}H_{83}N_5O_6P_4Pt_2$: C, 46.83; H, 5.82; N, 4.88; Found: C, 47.08; H, 5.79; N, 5.26.

General Procedure for Synthesis of **4.13**–**4.15**: To a 2-dram vial, 2, 6-

bis(pyrid-4ylethynyl) aniline (**4.01**; 1.0 mg, 3.4 μmol) was weighed with bromo(4-methoxy)bis(triethylphosphine)-, (*SP*-4-3)-platinum (**4.10**; 4.2 mg, 6.8 μmol), iodo(4-nitrophenyl)bis(triethylphosphine)-, (*SP*-4-3)-platinum (**4.11**; 4.6 mg, 6.8 μmol) or bromophenylbis(triethylphosphine) palladium (**4.12**; 3.4 mg, 6.8 μmol) in a 1:2 stoichiometric ratio. Two equivalents of AgOTf (1.7 mg, 6.8 μmol) was then added to the vial. 1 mL of CH_2Cl_2 was then added and the mixture was allowed to stir for 24 h in the dark at room temperature. The solution was then filtered and purified via precipitation by adding diethyl ether to the solution. The mixture was centrifuged and the supernatant was decanted. The solid was redissolved in CD_2Cl_2 and characterized.

Pt-methoxybenzene OTf Capped Ligand **(4.13)**: ^{1}H NMR ($CDCl_3$, 300 MHz) δ 8.56–8.58 (d, 4H, PyH_α, J = 6 Hz), δ 7.84–7.86 (d, 4H, PyH_β, J = 6 Hz), δ 7.49–7.51 (d, 2H, Ar*H*, J = 6 Hz), δ 7.17–7.20 (d, 4H, PtArH_α, J = 9 Hz, JAr*H*–Pt=51 Hz), δ 6.71–6.74 (m, 5H, PtArH_β, Ar*H*), δ 5.83 (bs, 2H, ArNH_2), δ 3.76 (s, 6H, OCH_3), δ 1.25–1.40 (m, 24H, PCH_2) , δ 1.06–1.16 (m, 36H, PCH_3). ^{31}P{^{1}H} NMR (CD_2Cl_2, 121.4 MHz) δ 13.39 (bs; ^{195}Pt satellites, J_{Pt-P}, 2688 Hz). ESI-MS ($C_{60}H_{87}F_6N_3O_8P_4Pt_2S_2$) m/z: $[M–OTf]^{1+}$ 1520.46; $[M–2•OTf]^{2+}$ 685.75. Anal. Calcd. for $C_{60}H_{87}F_6N_3O_8P_4Pt_2S_2$ [Complex]•CH_2Cl_2•Et_2O: C, 42.67; H, 5.45; N, 2.30; Found: C, 42.58; H, 5.47; N, 2.48.

Pt-nitrobenzene OTf Capped Ligand **(4.14)**: ^{1}H NMR ($CDCl_3$, 300 MHz) δ 8.58–8.60 (d, 4H, PyH_α, J = 6 Hz), δ 7.91–7.66 (m, 8H, PyH_β, Pt–ArH_β), δ 7.61–7.63 (d, 4H, Pt–ArH_α, J = 6 Hz), δ 7.50–7.53 (d, 2H, Ar*H*, J = 9 Hz), δ 6.69–6.75 (t, 1H, Ar*H*, J = 18 Hz), δ 5.83 (bs, 2H, ArNH_2), δ 1.28–1.39 (m, 24H, PCH_2) , δ

1.06–1.19 (m, 36H, PCH_3). $^{31}P\{^1H\}$ NMR (CD_2Cl_2, 121.4 MHz) δ 11.98 (bs; ^{195}Pt satellites, J_{Pt-P}, 2597 Hz). ESI-MS ($C_{58}H_{81}F_6N_5O_{10}P_4Pt_2S_2$) m/z: $[M–OTf]^{1+}$ 1550.36; $[M–2•OTf]^{2+}$ 700.69. Anal. Calcd. for $C_{58}H_{81}F_6N_5O_{10}P_4Pt_2S_2$: C, 40.97; H, 4.80; N, 4.12; Found: C, 41.14; H, 4.92; N, 4.03.

Pd-benzene OTf Capped Ligand **(4.15)**: ^1H NMR ($CDCl_3$, 300 MHz) δ 8.52–8.54 (d, 4H, PyH_α, J = 6 Hz), δ 7.85–7.87 (d, 4H, PyH_β, J = 6 Hz), δ 7.48–7.50 (d, 2H, Ar*H*, J = 6 Hz), δ 7.30–7.32 (d, 4H, Pd–ArH_β, J = 6 Hz), δ 7.11–7.15 (t, 4H, Pd–ArH_α, J = 12), δ 6.99–7.02 (t, 2H, Pd–ArH_γ, J = 9 Hz), δ 6.69–6.73 (t, 1H, Ar*H*, J = 12 Hz), δ 5.78 (bs, 2H, ArNH_2), δ 1.28–1.39 (m, 24H, PCH_2) , δ 1.06–1.19 (m, 36H, PCH_3). $^{31}P\{^1H\}$ NMR (CD_2Cl_2, 121.4 MHz) δ 6.78. ESI-MS ($C_{58}H_{83}F_6N_3O_6P_4Pd_2S_2$) m/z: $[M–2•OTf]^{2+}$ 567.68. Anal. Calcd. for $C_{58}H_{83}F_6N_3O_6P_4Pd_2S_2$: C, 48.61; H, 5.84; N, 2.93; Found: C, 48.50; H, 5.92; N, 2.95.

Steady-State Absorption and Emission Spectroscopy and Quantum Yield Determination: Absorption and fluorescence spectra were recorded on a Hitachi U-4100 and Hitachi F-7000 Spectrophotometer, respectively, with aerated spectrophotometric grade methylene chloride (Sigma Aldrich) at room temperature. The cells used in the experiments were 1 cm quartz cuvettes from Starna Cells, Inc. All samples were freshly prepared for each measurement. The molar absorption coefficients were determined by preparing four samples ranging in absorption from 0.01–1.0. The molar absorption coefficients for each solution were then calculated using Beer's Law, and the four were averaged. Subsequent samples were then prepared to confirm the molar absorption coefficients.

Quantum yields were determined by first cross-calibrating the instrument with quinine sulfate in 0.1 M H_2SO_4 and anthracene in ethanol. Quinine sulfate was then used to determine the experimental quantum yields at an excitation wavelength of 365 nm with Φ = 0.55. The quantum yield measurements were performed in multiplicates with values that were within 10% error being averaged.

Excited-State Lifetime Measurement*:* Excited-state lifetime measurements were performed by Daniel S. Lutterman at Oak Ridge National Laboratory and the analysis and interpretation of the results was performed by J. Bryant Pollock. Time correlated single photon counting (TCSPC) experiments were performed on an IBH (Jobin Yvon Horiba) model 5000F instrument equipped with single monochromators on both the excitation and emission sides of the instrument. The excitation light source was a NanoLED with a short 800 ps pulse width at 336 nm (458 nm was also used for **4.13–4.15**). Emission signals were collected on a picosecond photon detection module (TBX-04) at an angle perpendicular to excitation for samples and blanks. Data were collected at the sample's peak maxima as determined by steady state experiments and averaged (30,000 counts) to obtain the decay profile. Decay analysis and curve fitting routines to determine the sample's lifetimes were performed by the software (DAS6) provided by the manufacturer (IBH). The instrument response for the setup used was determined to be 1 ns, and the error in the measurements was determined to be ± 350 ps after deconvoluting the signal. The bi-exponential function (4.1) that was utilized to calculate the excited-state lifetimes is:

$$A(t) = A_1 e^{-k_1 t_1} + A_2 e^{-k_2 t_2}. \quad (4.1)$$

Molecular Modeling: All calculations were performed using the Gaussian09 (G09) program package revision B.01[17], with the B3LYP[14] functional. The 6-31G** basis set[15] was used for H, C, N, and P atoms, while the LANL2-DZ[16] basis set and pseudopotential was used for Pt and Pd. All geometry optimizations were performed without a solvent field with C1 symmetry; the results are in the gas phase. To minimize computational cost, the PEt_3 ligands on Pt and Pd were modeled as $P(CH_3)_3$ ligands. Orbitals were visualized using Chem3D and GaussView 5.0 with an isovalue of 0.02.

The percentage of platinum, palladium, phosphine, platinum-aryl or ligand character in the occupied (canonical) molecular orbitals (MOs) and virtual orbitals discussed for the previous complexes were calculated from a full population analysis using eq. 4.2:

$$\%\ \text{Orbital Character}_{(\text{Pt,Phen,Phosphine,Lig})} = \frac{\Sigma\phi^2_{(\text{Pt,Phen,Phosphine,Lig})}}{\Sigma\phi^2_{(\text{all})}} \times 100\% \quad (4.2)$$

where $\Sigma\varphi_i$ (i = Pd, Pt, Pt-Ar, Lig or all) is the sum of the squares of the eigenvalues associated with the atomic orbital (AO) of interest and all of the AOs in a particular MO, respectively. The vertical singlet transition energies of the complexes were computed at the TD-DFT level within G09 using the ground state optimized structure.

4.7 Contributions

All primary work (i.e., synthesis, molecular modeling, analysis, etc.) was performed by J. Bryant Pollock, while Gregory L. Schneider and Andrew S. Davies, undergraduates in the Stang lab, assisted in the synthesis of complexes

when needed; Timothy R. Cook served an advisory role. Daniel A. Lutterman measured the excited-state lifetimes of the ligands and complexes; however, analysis and interpretation of the data was performed by J. Bryant Pollock.

4.8 Future Directions

One of the more interesting outcomes from this study was the electronic tuning of the emission band for the Pt-L-Pt system **4.04** by altering the counterion. This implies that the triflate or nitrate counterion is interacting with the excited-state, but not the ground-state. This can be rationalized if one of the counterions is considered to be more inner sphere and the excited-state can interact with the counterion. TD-DFT predicts an increase of electron density on the metal node in the excited-state, so this is consistent. Moreover, previous studies examining ligand exchange kinetics have shown that certain counterions facilitate ligand exchange via an associative mechanism. As such, a suite of complexes can be made with different counterions and the spectroscopic properties may give insight into nature of ligand exchange for these complexes.

The preservation of the photophysical properties from the full SCC constructs to the small capped complexes implies that the full constructs are not needed for the observed optical properties. Moreover, when comparing SCCs with varying shapes and sizes, there was no significant change in photophysical properties. This result implies that there may not be any electronic communication between fragments within the full constructs. More significant, the Pd analog **4.15** was determined to preserve the attractive photophysical properties of **4.07**, which means that Pd-based SCCs should be investigated for photo emitting

applications.

4.9 References

(1) (a) Wong, K. M.-C.; Yam, V. W.-W. *Coordination Chem. Rev.* **2007**, *251*, 2477; (b) Eryazici, I.; Moorefield, C. N.; Newkome, G. R. *Chem. Rev.* **2008**, *108*, 1834; (c) Fleischauer, P. D.; Fleischauer, P. *Chem. Rev.* **1970**, *70*, 199; (d) Kindahl, T.; Ellingsen, P. G.; Lopes, C.; Brännlund, C.; Lindgren, M.; Eliasson, B. *J Phys Chem A* **2012**, *116*, 11519; (e) Chan, K. H.-Y.; Chow, H.-S.; Wong, K. M.-C.; Yeung, M. C.-L.; Yam, V. W.-W. *Chem. Sci.* **2010**, *1*, 477; (f) Hui, C.-K.; Chu, B. W.-K.; Zhu, N.; Yam, V. W.-W. *Inorg. Chem.* **2002**, *41*, 6178; (g) Wong, K. M.-C.; Yam, V. W.-W. *Acc. Chem. Res.* **2011**, *44*, 424; (h) Adamson, A. W.; Waltz, W. L.; Zinato, E.; Watts, D. W.; Fleischauer, P. D.; Lindholm, R. D. *Chem. Rev.* **1968**, *68*, 541; (i) Brooks, J.; Babayan, Y.; Lamansky, S.; Djurovich, P. I.; Tsyba, I.; Bau, R.; Thompson, M. E. *Inorg. Chem.* **2002**, *41*, 3055; (j) Caspar, J. V. *J. Am. Chem. Soc.* **1985**, *107*, 6718; (k) Chan, S.-C.; Chan, M. C. W.; Wang, Y.; Che, C.-M.; Cheung, K.-K.; Zhu, N. *Chem.-Eur. J.* **2001**, *7*, 4180; (l) Pomestchenko, I. E.; Luman, C. R.; Hissler, M.; Ziessel, R.; Castellano, F. N. *Inorg. Chem.* **2003**, *42*, 1394; (m) Danilov, E. O.; Rachford, A. A.; Goeb, S. b.; Castellano, F. N. *J. Phys. Chem. A* **2009**, *113*, 5763; (n) Goeb, S.; Prusakova, V.; Wang, X.; Vezinat, A.; Salle, M.; Castellano, F. N. *Chem. Commun.* **2011**, *47*, 4397; (o) Forniés, J.; Fuertes, S.; Martín, A.; Sicilia, V.; Lalinde, E.; Moreno, M. T. *Chem.-Eur. J.* **2006**, *12*, 8253; (p) Keller, J. M.; Glusac, K. D.; Danilov, E. O.; McIlroy, S.; Sreearuothai, P.; R. Cook, A.; Jiang, H.; Miller, J. R.; Schanze, K. S. *J. Am. Chem. Soc.* **2011**, *133*, 11289; (q) Keller, J. M.; Schanze, K. S. *Organometallics* **2009**, *28*, 4210; (r) Liao, C.; Yarnell, J. E.; Glusac, K. D.; Schanze, K. S. *J. Phys. Chem. B* **2010**, *114*, 14763; (s) Rogers, J. E.; Slagle, J. E.; Krein, D. M.; Burke, A. R.; Hall, B. C.; Fratini, A.; McLean, D. G.; Fleitz, P. A.; Cooper, T. M.; Drobizhev, M.; Makarov, N. S.; Rebane, A.; Kim, K.-Y.; Farley, R.; Schanze, K. S. *Inorg. Chem.* **2007**, *46*, 6483.

(2) Kryschenko, Y. K.; Seidel, S. R.; Arif, A. M.; Stang, P. J. *J. Am. Chem. Soc.* **2003**, *125*, 5193.

(3) Pollock, J. B.; Cook, T. R.; Stang, P. J. *J. Am. Chem. Soc.* **2012**, *134*, 10607.

(4) Flynn, D. C.; Ramakrishna, G.; Yang, H.-B.; Northrop, B. H.; Stang, P. J.; Goodson, T. *J. Am. Chem. Soc.* **2010**, *132*, 1348.

(5) Johnson, A. M.; Moshe, O.; Gamboa, A. S.; Langloss, B. W.; Limtiaco, J. F. K.; Larive, C. K.; Hooley, R. J. *Inorg. Chem.* **2011**, *50*, 9430.

(6) Manna, J.; Kuehl, C. J.; Whiteford, J. A.; Stang, P. J.; Muddiman, D. C.; Hofstadler, S. A.; Smith, R. D. *J. Am. Chem. Soc.* **1997**, *119*, 11611.

(7) Arnold, D. P.; Bennett, M. A. *Inorg. Chem.* **1984**, *23*, 2117.

(8) Tam, W.; Calabrese, J. C. *Chem. Phys. Let.* **1988**, *144*, 79.

(9) Calvin, G.; Coates, G. E. *J. Chem. Soc.* **1960**, *0*, 2008.

(10) (a) Yang, J.-S. *PATAI'S Chem. Func. Groups*; John Wiley & Sons, Ltd: 2009, doi:10.1002/9780470682531.pat0396; (b) Hou, X.-J.; Quan, P.; Höltzl, T.; Veszprémi, T.; Nguyen, M. T. *J. Phys. Chem. A* **2005**, *109*, 10396; (c) Lewis, F. D.; Hougland, J. L.; Markarian, S. A. *J. Phys. Chem. A* **2000**, *104*, 3261; (d) Oosterbaan, W. D.; Koeberg, M.; Piris, J.; Havenith, R. W. A.; van Walree, C. A.; Wegewijs, B. R.; Jenneskens, L. W.; Verhoeven, J. W. *J. Phys. Chem. A* **2001**, *105*, 5984; (e) Rückert, I.; Demeter, A.; Morawski, O.; Kühnle, W.; Tauer, E.; Zachariasse, K. A. *J. Phys. Chem. A* **1999**, *103*, 1958.

(11) (a) Kohler, A.; Wilson, J. S.; Friend, R. H.; Al-Suti, M. K.; Khan, M. S.; Gerhard, A.; Bassler, H. *J. Chem. Phys.* **2002**, *116*, 9457; (b) Ricciardi, L.; Puoci, F.; Cirillo, G.; La Deda, M. *Dalton Trans.* **2012**, *41*, 10923.

(12) Weil, T. A.; Schmidt, P. J.; Rycheck, M.; Orchin, M. *Inorg. Chem.* **1969**, *8*, 1002.

(13) Vrieze, K.; Volger, H. C.; Gronert, M.; Praat, A. P. *J. Organomet. Chem.* **1969**, *16*, P19.

(14) (a) Becke, A. D. *J. Chem. Phys.* **1993**, *98*, 5648; (b) Lee, C.; Yang, W.; Parr, R. G. *Phys. Rev. B* **1988**, *37*, 785.

(15) Hehre, W. J.; Ditchfield, R.; Pople, J. A. *J. Chem. Phys.* **1972**, *56*, 2257.

(16) Hay, P. J.; Wadt, W. R. *J. Chem. Phys.* **1985**, *82*, 299.

(17) Frisch, M. J.; Trucks, G. W.; Schlegel, H. B.; Scuseria, G. E.; Robb, M. A.; Cheeseman, J. R.; Scalmani, G.; Barone, V.; Mennucci, B.; Petersson, G. A.; Nakatsuji, H.; Caricato, M.; Li, X.; Hratchian, H. P.; Izmaylov, A. F.; Bloino, J.; Zheng, G.; Sonnenberg, J. L.; Hada, M.; Ehara, M.; Toyota, K.; Fukuda, R.; Hasegawa, J.; Ishida, M.; Nakajima, T.; Honda, Y.; Kitao, O.; Nakai, H.; Vreven, T.; Montgomery, J. A., Jr.; Peralta, J. E.; Ogliaro, F.; Bearpark, M.; Heyd, J. J.; Brothers, E.; Kudin, K. N.; Staroverov, V. N.; Kobayashi, R.; Normand, J.; Raghavachari, K.; Rendell, A.; Burant, J. C.; Iyengar, S. S.; Tomasi, J.; Cossi, M.; Rega, N.; Millam, N. J.; Klene, M.; Knox, J. E.; Cross, J. B.; Bakken, V.; Adamo, C.; Jaramillo, J.; Gomperts,

R.; Stratmann, R. E.; Yazyev, O.; Austin, A. J.; Cammi, R.; Pomelli, C.; Ochterski, J. W.; Martin, R. L.; Morokuma, K.; Zakrzewski, V. G.; Voth, G. A.; Salvador, P.; Dannenberg, J. J.; Dapprich, S.; Daniels, A. D.; Farkas, Ö.; Foresman, J. B.; Ortiz, J. V.; Cioslowski, J.; Fox, D. J., *Gaussian 09*, Gaussian, Inc., Wallingford CT, 2009.

(18) Rieke, R. D.; Kavaliunas, A. V. *J. Org. Chem.* **1979**, *44*, 3069.

5. TUNABLE VISIBLE LIGHT EMISSION OF SELF-ASSEMBLED RHOMBOIDAL METALLACYCLES

5.1 Introduction

The ability to tune the emission of materials in a simple fashion is of great interest in the manufacturing of photovoltaics,[1] light-emitting diodes,[2] nonlinear optical (NLO) materials,[3] bio-imaging agents,[4] and other photon emitting devices, motivating efforts to develop novel systems that are readily tunable, particularly in the visible region. The synthesis of tunable transition-metal-based molecular organic frameworks (MOFs) has seen intense growth over the past several years with tunability afforded by various methods: (i) incorporating fluorescent ligands or luminescent metal nodes in the core structure, (ii) altering the shape and size of the framework, (iii) guest inclusion, or (iv) external stimulus.[5] MOFs, however, are prone to morphological changes when external sources or stimuli are used to facilitate luminescence and are fraught with solubility issues.[6] Supramolecular coordination complexes preserve the attractive features of MOFs, such as facile building block modularity, yet also afford increased solubilities and lend themselves to small-molecule characterization techniques owing to their discrete nature.[7] Reports of both MOF and SCC systems that display tunable

---

Portions of this work have appeared previously:
Reproduced in part with permission from Pollock, J.B.; Schneider, G.L.; Cook, T.R.; Davies, A.S.; Stang, P.J. *J. Am. Chem. Soc.*, **2013**, *135*, 13676.

wavelengths spanning the visible spectrum have largely been dominated by lanthanide-based systems or metal-organic structures that contain lanthanide cations as guests, and only recently have lanthanide-free systems received attention.[5b,8]

The attractive photophysical properties of mono- and multinuclear bis(phosphine) Pt(II) metal complexes (i.e., tunabiltiy, low-energy and long-lived excited-states)[9] have prompted their incorporation into SCCs, wherein these characteristics can be exploited in large metallacycles. In particular, we have developed highly emissive rhomboids based on aniline-containing donors and Pt-based metal acceptors.[10] Having established the chemistry of visibly emitting rhomboids with high quantum yields, we sought to achieve the second, hitherto unrealized, goal of tunable emission.

Herein, the synthesis of a series of D_{2h} [D_2A_2] rhomboidal complexes (Scheme 5.1; **5.07**–**5.11**), which only differ by the pendant functional group *para* to the aniline core, and display tunable wavelengths spanning the visible spectrum is reported. Moreover, when plotting the wavenumber (cm^{-1}) of the λ_{max} of emission profiles for each rhomboid versus the Hammett σ_{para} constant for the pendant functional groups, a linear relationship is obtained. The steady-state absorption and emission profiles were collected for each rhomboidal complex and precursor ligand and are discussed.

5.2 Results and Discussion

Ligand **5.01** was prepared via a Sonogashira reaction with 2,6-diiodo-4-nitroanline and 4-ethynylpyridine hydrochloride; ligands **5.02** and **5.04** were

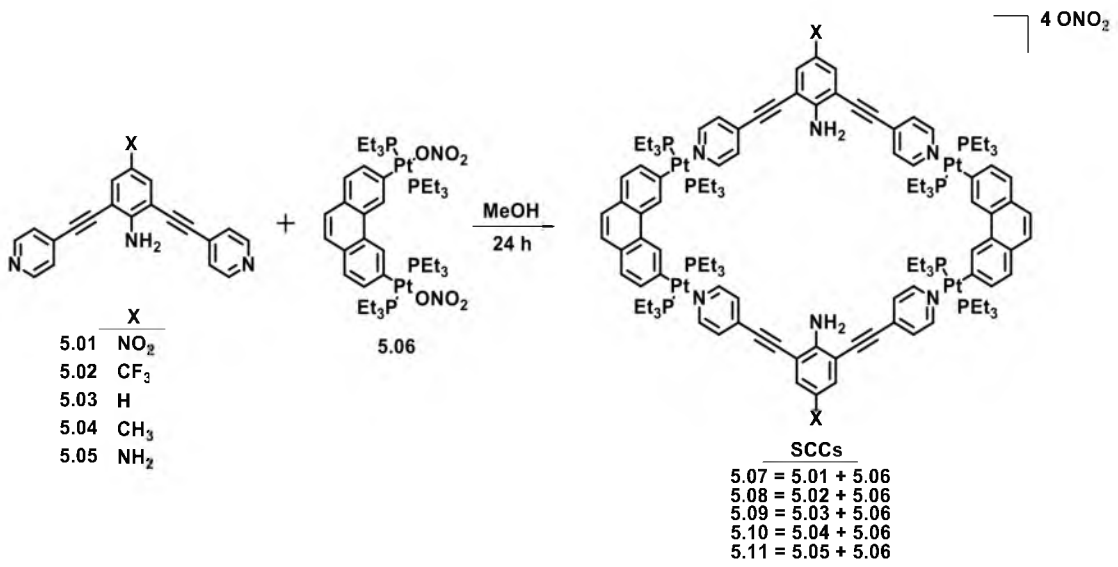

Scheme 5.1: The svnthesis of rhomboidal SCCs **5.07–5.11**

prepared in a similar manner while **5.05** was synthesized by reducing the nitro group in **5.01**. After 24 h of stirring, a solution containing a 1:1 stoichiometric mixture of ligand **5.01**, **5.02**, **5.03**, **5.04** or **5.05**, respectively, with **5.06** affords D_{2h} [D_2A_2] endohedral-amine exo-functionalized rhomboids **5.07–5.11** in quantitative yields (Scheme 5.1).

SCCs **5.07–5.11** have a high-energy band centered at 305–318 nm (Figure 5.1, left; Table 5.1) that increases in wavelength with the electron donating ability of the pendant functionality. This band was previously investigated for **5.09** and reported to be intimately related to the ethynyl group in ligand **5.03**.[10g] It was determined, unlike the low-energy band, that the molar absorption coefficient of this band is relatively unaffected by the nature of the functional group *para* to the aniline amine.[10g] SCC **5.07** has a high-energy band maximum of 305 nm with a molar absorption coefficient of 114,000 cm^{-1} M^{-1}, while **5.11** has a high-energy

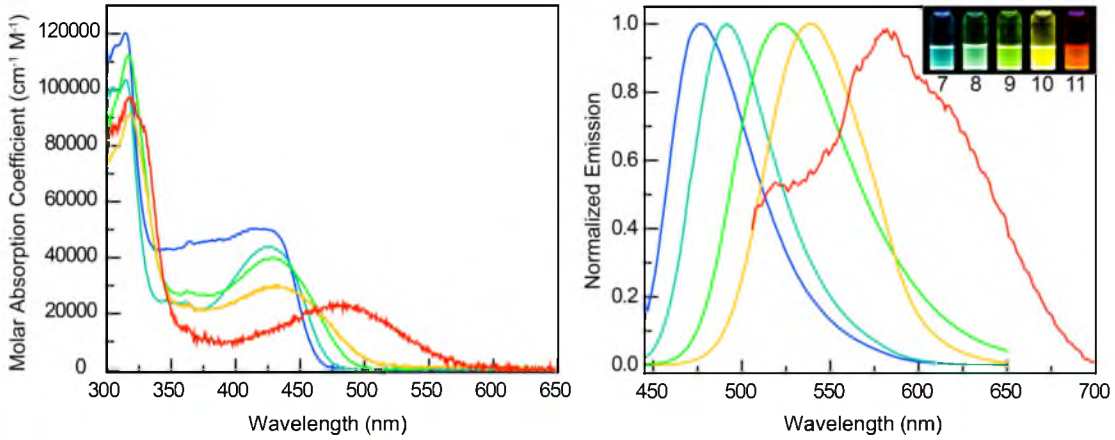

Figure 5.1: The absorption (left) and emission (right) profiles for **5.07** (—; blue), **5.08** (—; cyan), **5.09** (—; green), **5.10** (—; yellow) and **5.11** (—; red).

Table 5.1: Molar absorption coefficients, emission band maxima, and quantum yields for **5.07–5.11** in aerated methylene chloride.

SCC	Absorption Bands λ_{max} / (nm) [ε x 10^{-3} /(cm^{-1} M^{-1})]	λ_{exc} / (nm)	λ_{emis} / (nm)	Φ / (%)[a]
5.07	305 [114] *sh*, 314 [120], 420 [50.2]	420	476	1.1
5.08	304 [99.8] *sh*, 315 [104], 425 [43.6]	425	491	7.6
5.09[b]	317 [112], 430 [39.9]	430	522	28
5.10	318 [91.4], 432 [29.5]	430	538	12
5.11	317 [97.5], 480 [23.6]	480	581	< 1.0

[a]Quantum yield was determined using quinine sulfate at 365 nm (Φ = 0.56) except for **11** in which rhodamine 6G was utilized to determine the quantum yield (480 nm, Φ = 0.95).
[b]Data obtained from reference 10g.

band maximum of 317 nm and a molar absorption coefficient of 97,500 cm^{-1} M^{-1}. The low-energy absorption band, however, seems to be sensitive to the nature of the functional group *para* to the aniline amine, and the band maxima increases while the molar absorption coefficient decreases with the electron donating ability of the functional group *para* to the aniline amine. SCC **5.07** has a low-energy band maximum of 420 nm with a molar absorption coefficient of 50,200 cm^{-1} M^{-1} while **5.11** has a low-energy band maximum of 480 nm and a molar absorption coefficient of 23,6 00 cm^{-1} M^{-1}. Figure 5.1 (left) shows the emission profiles for SCCs **5.07**–**5.11**, which red-shift (**5.07**; 476 nm to **5.11**; 581 nm) with increasing electron donating ability of the functional group *para* to the aniline amine.

It was observed that the quantum yield increases from **5.07** to **5.09** (Φ = 0.011 to Φ = 0.28) and then decreases from **5.09**–**5.11** (Φ = 0.28 to Φ < 0.01); the loss of quantum yield upon Pt complexation (**5.03**, Φ = 0.66; **5.09**, Φ = 0.28) was previously hypothesized to originate from increased ISC due to the "heavy atom effect" to a nonradiative triplet-state which aniline-based species are known to posses.[11] The excited-state of related bis(phosphine) Pt-based endohedral amine systems, including system **5.09**, were previously explored and were determined not to phosphoresce in oxygen-free solvents due to a nonradiative triplet-state.[12]

Interestingly, when the emission band maxima are converted to wavenumbers (cm^{-1}) and plotted against the Hammett sigma constants for the functional groups *para* to the aniline amine, a linear relationship is obtained (Figure 5.2).[13] This allows for specific wavelengths between 476 to 581 nm to be

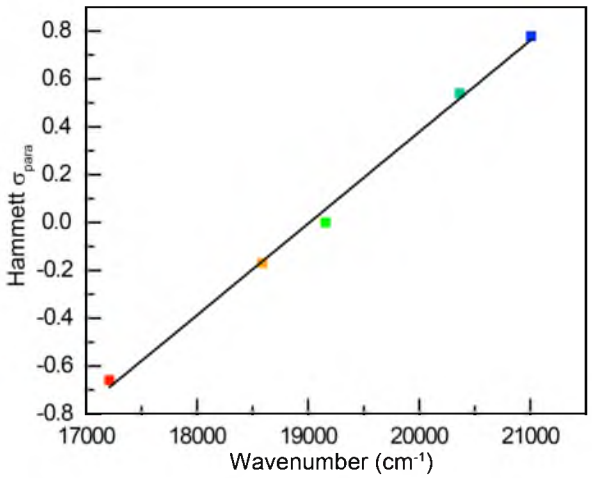

Figure 5.2: Hammett σ_{para} constants vs wavenumber (cm^{-1}) for **5.07** (■), **5.08** (■), **5.09** (■), **5.10** (■), and **5.11** (■). Fit to the equation: y = 0.0038x – 7.275 with a R^2 of 0.995.

chosen based on the Hammett σ_{para} value for a particular functional group. However, as previously noted, the quantum yields of **5.07**–**5.11** increase (**5.07**, Φ = 0.011; **5.09**, Φ = 0.28) while **5.09**–**5.11** decrease (**5.09**, Φ = 0.28; **5.11**, Φ < 0.01), which implies that there is an intimate relationship between the Hammett σ_{para} value and the quantum yield that is not fully understood. It can be assumed, however, that rhomboid **5.09** has an excited-state that allows for a higher radiative rate constant relative to the nonradiative rate constant when compared to that of **5.07**, **5.08**, **5.10**, and **5.11**.

The solvent effects on the absorption and emission profiles for **5.07**–**5.11** were probed using acetone, dimethylsulfoxide (DMSO), methanol (MeOH) and methylene chloride (DCM); however, there was no observable trend between the systems, and there was little effect (< 10 nm) on the λ_{max} for the absorption and emission profiles. As an example, the absorption and emission profiles for **5.09** can be found in Figure 5.3.

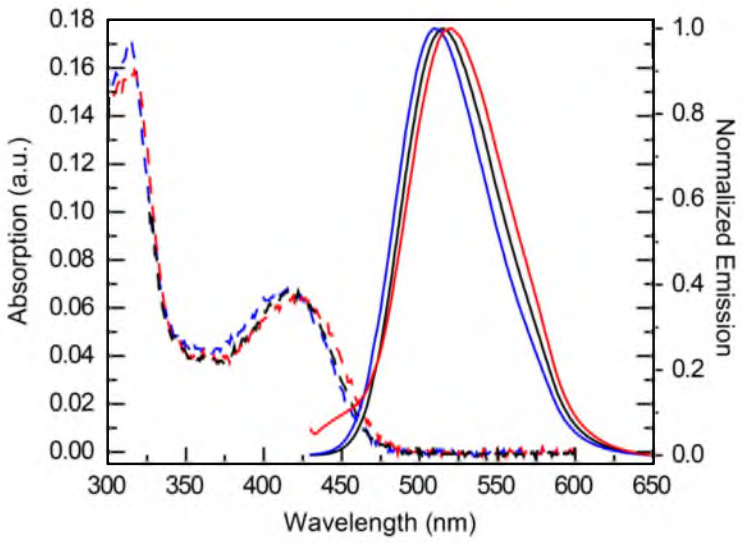

Figure 5.3: Solvent effects on the absorption (dashed) and emission (solid) profiles of **5.09**: MeOH (—; blue), Acetone (—; black), and DMSO (—; red).

As a control, the steady-state absorption (Figure 5.4) and emission (Figure 5.5) profiles for ligands **5.01**–**5.05** in aerated DMSO were obtained and the relevant metrics are listed in Table 5.2.

Ligands **5.01**–**5.05** were determined to have low-energy absorption bands that range from 388–437 nm with decreasing molar absorption coefficients from **5.01** to **5.05** (27,000 cm^{-1} M^{-1} to 8,100 cm^{-1} M^{-1}). The decrease in the molar absorption coefficients for the low-energy band maxima correlated with an increase in the electron donating ability of the functional group *para* to the aniline amine. This trend was also present in the emission band maxima **5.02**–**5.05** with **5.02** and and **5.05** having emission band maxima of 442 and 480 nm, respectively. As with **5.07**–**5.11**, the quantum yield increased from **5.01** to **5.03** ($\Phi < 0.01$ to $\Phi = 0.66$) and then decreased from **5.03** to **5.05** ($\Phi = 0.66$ to $\Phi = 0.23$).

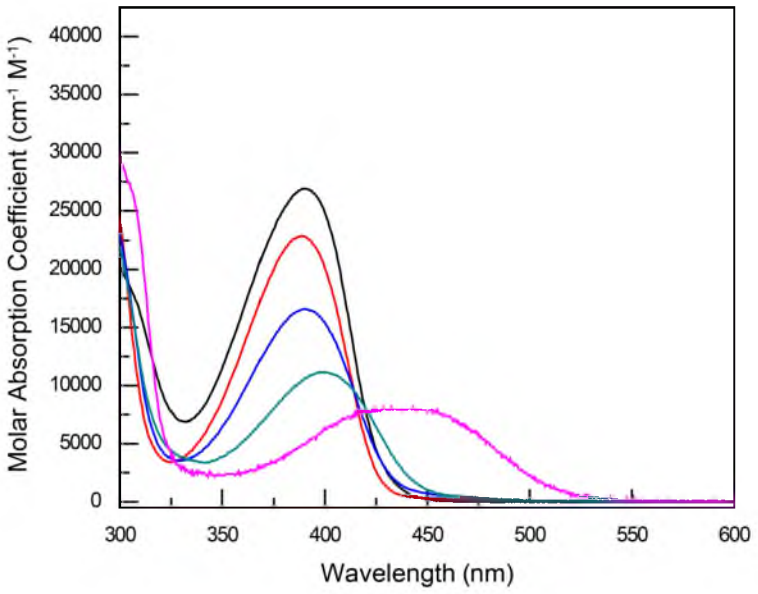

Figure 5.4: UV/Vis spectra for **5.01**-**5.05**. **5.01** (—; black), **5.02** (—; red), **5.03** (—; blue), **5.04** (—; cyan), and **5.05** (—; red).

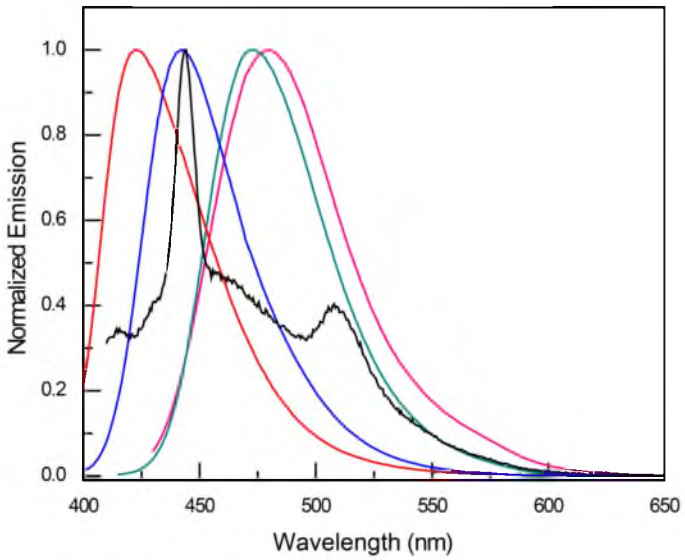

Figure 5.5: Emission spectra for **5.01**-**5.05**. **5.01** (—; black), **5.02** (—; red), **5.03** (—; blue), **5.04** (—; cyan), and **5.05** (—; pink).

Table 5.2: Molar absorption coefficients, emission band maxima, and quantum yields for **5.01**–**5.06**.

Ligand	Absorption Bands λ_{max} / (nm) [ε x 10^{-3} /(cm^{-1} M^{-1})]	λ_{exc} / (nm)	λ_{emiss} / (nm)	Φ / (%)[a]
5.01	390 [27.0]	390	443, 508	< 1.0
5.02	388 [22.8]	388	442	48
5.03	390 [16.7]	390	458	66
5.04	398 [11.2]	398	473	48
5.05	437 [8.1]	415	480	23
5.06	364 [1.1]; 346 [1.6]; 322 [20.1]; 308 [19.0]; 290 [24.0]	350	–	no emiss

[a]Quantum yield was determined using quinine sulfate at 365 nm (Φ = 0.56).

Also, the molar absorption coefficient of **5.06** was measured in aerated methylene chloride (Figure 5.6), which had multiple higher energy bands when compared to that of **5.01**–**5.05**; however, there was no observed emission in the visible region for **5.06**.

5.3 Conclusion

A method for forming easily-assembled rhomboidal-shaped [D_2A_2] SCCs (**5.07**–**5.11**) with predictive wavelengths that span the visible spectrum (476–581 nm) from 2,6-bis(4-ethynylpyridine) aniline-based ligands (**5.01**–**5.05**) was established. Moreover, by utilizing the linear relationship between the Hammett σ constants for the peripheral functional groups and the wavenumbers for the λ_{max}

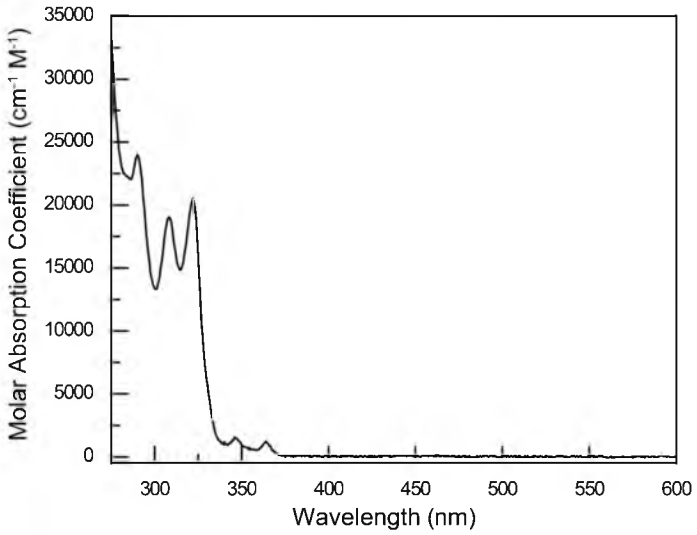

Figure 5.6: UV/Vis profile for **5.06**.

of the emission profiles, a rhomboid with a predetermined emission profile can be readily synthesized. As the fundamental science behind the quantum yields and other photophysical properties is developed by employing transient absorption and other techniques, such complexes can be adapted for a number of applications such as real-time cellular monitoring of the transport, internalization, and delivery of anticancer therapuetics.

5.4 Experimental

Materials and Methods*:* 2,6-bis(pyrid-4ylethynyl) aniline (**5.03**),[10g] 2,9-bis[*trans*-Pt(PEt_3)$_2$$NO_3$] phenanthrene (**5.06**),[14] and complex **5.09**[10g] were prepared using known procedures. All chemicals were purchased from Sigma-Aldrich, Oakwood Chemicals, Alfa Aesar, and TCI America while deuterated solvents were purchased from the Cambridge Isotope Laboratory (Andover, MA). ^{1}H and ^{31}P{^{1}H} NMR spectra were recorded on a Varian 300 spectrometer, and

the mass spectra were recorded using a Micromass LCT Premier XE ToF mass spectrometer using electrospray ionization and analyzed using the MassLynx software suite; high resolution mass spectrometry (HRMS) ESI-ToF with a mass accuracy within 0.003 m/z unit of the theoretical value was utilized to support the chemical formula for **5.01**, **5.02**, **5.04**, and **5.05**. The ESI-MS samples for **5.07**, **5.08**, **5.10**, and **5.11** were dissolved in methylene chloride then diluted with acetone unless otherwise noted. All $^{31}P\{^{1}H\}$ NMR spectra were referenced using a 10% H_3PO_4 *aq* solution. Elemental Analysis was performed by Atlantic Microlab, Inc.

General Procedure for the Synthesis of **5.01**, **5.02**, and **5.04**: To a Schlenk flask, 200 mg (0.760 mmol) of 2,6-dibromo-4-methylaniline, 200 mg (0.630 mmol) of 2,6-dibromo-4-trifluoromethylaniline, or 200 mg (0.510 mmol) of 2,6-diiodo-4-nitroaniline were weighed with 6 equivalents of 4-ethynylpyridine hydrochloride, 5 mol% of copper iodide, and 5 mol% of palladium tetrakis(triphenylphosphine). The Schlenk flask was then evacuated and put under inert N_2 atm. 20 mL of dimethylformamide (DMF) and 10 mL of triethylamine (Et_3N) that was sitting on a bed of potassium hydroxide (KOH) were sparged with N_2 for 30 min and syringed into the Schlenk flask. The reaction was heated to 80°C and allowed to stir for 48 h in the dark. The solution was then cooled to room temperature and poured into a separatory funnel containing *sat.* sodium bicarbonate ($NaHCO_3$), which was then extracted with ethyl acetate (EtOAc). The organic layer was then rotovaped and subjected to column chromatography using 5% methanol (MeOH) in dichloromethane (DCM) as the mobile phase. The product was obtained as a

yellow solid and recrystallized using a MeOH/H_2O mixture.

5.01: (15%). ^{1}H NMR (dmso–d_6; 300 MHz); 8.66–8.64 (*d*, 4H, Py_α, J = 6 Hz); 8.27 (*s*, 2H, Ar*H*); 7.70–7.69 (d, 4H, Py_β, J = 3 Hz); 7.39 (*bs*, 2H, NH_2); HRMS (ESI-ToF) m/z: $[M-H]^-$ Calc'd for $C_{20}H_{11}N_4O_2$ [339.0882]; Found 339.0884

5.02: (27%). ^{1}H NMR (dmso–d_6; 300 MHz); 8.64–8.63 (*d*, 4H, Py_α, J = 3 Hz); 7.73 (*s*, 2H, Ar*H*); 7.66–7.65 (d, 4H, Py_β, J = 3 Hz); 6.74 (*bs*, 2H, NH_2); HRMS (ESI-ToF) m/z: $[M+H]^+$ Calc'd for $C_{21}H_{13}F_3N_3$ [364.1062]; Found 364.1069

5.04: (28%). ^{1}H NMR (dmso–d_6; 300 MHz); 8.61–8.59 (*d*, 4H, Py_α, J = 6 Hz); 7.60–7.58 (d, 4H, Py_β, J = 6 Hz); 7.25 (*s*, 2H, Ar*H*); 5.83 (*bs*, 2H, NH_2); 2.15 (*s*, 3H, ArCH_3); HRMS (ESI-ToF) m/z: $[M+H]^+$ Calc'd for $C_{21}H_{16}N_3$ [310.1344]; Found 310.1354

2,6-bis(4-ethynylpyridine)-4-aminoaniline **(5.05)**: 330 mg (0.970 mmol) of **5.01** was weighed into a 50 mL round bottom flask and suspended in 20 mL of DMF and 5 mL of ethanol (EtOH). 2.19 g (9.71 mmol) of stannous chloride dihydrate ($SnCl_2$•$2H_2O$) was then added slowly. The mixture was heated to 90°C and allowed to stir for 24 h. Upon cooling, the mixture was filtered and poured into ~50 mL of EtOAc. The solution was then extracted with ~50 mL of H_2O multiple times. The organic layer was collected and rotovaped. The solid was purified via chromatography using a 5% MeOH/DCM mobile phase. The product was then recrystallized in a MeOH/H_2O solution to afford the pure product as an orange solid. (54%). ^{1}H NMR (dmso–d_6; 300 MHz); 8.60–8.59 (*d*, 4H Py_α, J = 3 Hz); 7.57–7.55 (*d*, 4H Py_α, J = 6 Hz); 6.74 (*s*, 2H, Ar*H*); 5.20 (*bs*, 2H NH_2); 4.64 (*bs*, 2H NH_2); HRMS (ESI-ToF) m/z: $[M+H]^+$ Calc'd for $C_{20}H_{15}N_4$ [311.1297]; Found

311.1302

General Procedure for **5.07–5.08** and **5.10–5.11**: To a 2-dram vial, 1.17 mg (3.45 μmol) of **5.01**, 1.25 mg (3.45 μmol) of **5.02**, 1.07 mg (3.45 μmol) of **5.04**, or 1.07 mg (3.45 μmol) of **5.05** was weighed with 4.00 mg (3.45 μmol) of **5.06**. ~1 mL of MeOH was then added and the vial was capped. The mixture was then heated to ~50°C and allowed to stir for 24 h. Upon cooling, the solution was dried overnight and then redissolved in methylene chloride-d_2 (CD_2Cl_2) for characterization. For further purification, if needed, ethyl ether was added to precipitate the complex. Centrifugation and decanting the supernatant afforded the complex as a pure solid (>95%).

5.07: ^{1}H NMR (CD_2Cl_2; 300 MHz); 8.91–8.92 (*d*, 4H $Py_{\alpha'}$, J = 3 Hz); 8.71–8.73 (*d*, 4H $Py_{\alpha''}$, J = 6 Hz); 8.58 (*s*, 4H Phen*H*); 8.43 (*s*, 4H, Ar*H*); 8.38–8.39 (*d*, 4H $Py_{\beta'}$, J = 3 Hz); 7.77–7.79 (*d*, 4H, $Py_{\beta''}$, J = 6 Hz); 7.65–7.66 (8H Phen*H*); 7.62 (*s*, 4H Phen*H*); 7.44 (*bs*, 4H NH_2); 1.37 (*bs*, 48H PCH_2CH$_3$); 1.19 (*m*, 72H PCH$_2$CH_3). ^{31}P{^{1}H} NMR (CD_2Cl_2, 121.4 MHz) δ 12.70 (bs; ^{195}Pt satellites, J_{Pt-P}, 2685 Hz); ESI-MS: $C_{116}H_{160}N_3O_{16}P_8Pt_4$; $[M–3•ONO_2]^{3+}$ 939.96; Elemental Analysis: Calcd: [**5.07**] + CH_2Cl_2; C, 45.45; H, 5.28; N, 5.44; Found: C, 45.57; H, 5.61; N, 5.28.

5.08: ^{1}H NMR (CD_2Cl_2; 300 MHz); 8.88–8.90 (*d*, 4H $Py_{\alpha'}$, J = 6 Hz); 8.69–8.71 (*d*, 4H $Py_{\alpha''}$, J = 6 Hz); 8.43 (*s*, 4H Phen*H*); 8.34–8.37 (*d*, 4H $Py_{\beta'}$, J = 9 Hz); 7.77 (*m*, 4H, $Py_{\beta''}$ and 4H Ar*H*); 7.65–7.66 (d, 8H Phen*H*, J = 3 Hz); 7.62 (*s*, 4H Phen*H*); 6.85 (*bs*, 4H NH_2); 1.37 (*bs*, 48H PCH_2CH$_3$); 1.19 (*m*, 72H PCH$_2$CH_3).^{31}P{^{1}H} NMR (CD_2Cl_2, 121.4 MHz) δ 16.72 (bs; ^{195}Pt satellites, J_{Pt-P},

2678 Hz); ESI-MS: $C_{118}H_{160}F_6N_{10}O_{12}P_8Pt_4$; $[M–3•ONO_2]^{3+}$ 955.28; Elemental Analysis: Calcd: [**5.08**] + 2•CH_2Cl_2; C, 44.72; H, 5.13; N, 4.35; Found: C, 45.00; H, 5.54; N, 4.36.

5.10: ^{1}H NMR (CD_2Cl_2; 300 MHz); 8.90–8.92 (*d*, 4H $Py_{\alpha'}$, J = 6 Hz); 8.65–8.67 (*d*, 4H $Py_{\alpha''}$, J = 6 Hz); 8.62 (*s*, 4H Phen*H*); 8.22–8.24 (*dd*, 4H $Py_{\beta'}$, J = 6 Hz); 7.72–7.74 (*dd*, 4H, $Py_{\beta''}$); 7.64–7.66 (d, 12H Phen*H*, J = 6 Hz); 7.61 (*s*, 4H Ar*H*); 7.38 (*bs*, 4H NH_2); 2.29 (*s*, 6H CH_3); 1.37 (*bs*, 48H PCH_2CH$_3$); 1.18 (*m*, 72H PCH$_2$CH_3); 3.35 (*q*, diethyl ether). ^{31}P{^{1}H} NMR (CD_2Cl_2, 121.4 MHz) δ 12.72 (bs; ^{195}Pt satellites, $J_{Pt–P}$, 2682 Hz); ESI-MS: $C_{118}H_{166}N_{10}O_{12}P_8Pt_4$; $[M–3•ONO_2]^{3+}$ 919.32; Elemental Analysis: Calcd: [**5.10**] + 2•CH_2Cl_2; C, 46.27; H, 5.50; N, 4.50; Found: C, 46.00; H, 5.89; N, 4.53.

5.11: ^{1}H NMR (CD_2Cl_2; 300 MHz); 8.96–8.98 (*d*, 4H $Py_{\alpha'}$, J = 6 Hz); 8.65 (*m*, 4H $Py_{\alpha''}$ and 4H Phen*H*); 8.16–8.18 (*d*, 4H $Py_{\beta'}$, J = 6 Hz); 7.72–7.74 (*d*, 4H $Py_{\beta''}$); 7.60–7.65 (d, 12H Phen*H* and 4H Ar*H*, J = 15 Hz); 7.00 (*bs*, 4H NH_2); 5.52 (*bs*, 4H NH_2); 1.37 (*bs*, 48H PCH_2CH$_3$); 1.17 (*m*, 72H PCH$_2$CH_3). ^{31}P{^{1}H} for NMR (CD_2Cl_2, 121.4 MHz) δ 14.58 (bs; ^{195}Pt satellites, $J_{Pt–P}$, 2688 Hz); ESI-MS: $C_{116}H_{164}N_{12}O_{12}P_8Pt_4$; $[M–3•ONO_2]^{3+}$ 919.98; Elemental Analysis: Calcd: [**5.11**] + 2•CH_2Cl_2; C, 45.47; H, 5.43; N, 5.39; Found: C, 45.15; H, 5.78; N, 5.55.

Steady-State Absorption and Emission Spectroscopy and Quantum Yield Determination: Absorption and fluorescence spectra were recorded on a Hitachi U-4100 and Hitachi F-7000 Spectrophotometer, respectively, with aerated spectrophotometric grade methylene chloride, acetone, dimethylsulfoxide and methanol (Sigma Aldrich) at room temperature. The cells used in the

experiments were 1 cm quartz cuvettes from Starna Cells, Inc. All samples were freshly prepared for each measurement. The molar absorption coefficients were determined by preparing four samples ranging in absorption from 0.01–1.0 in dimethylsulfoxide for ligands **5.01–5.05** and methylene chloride for **5.06–5.11**. The molar absorption coefficients for each solution were then calculated using Beer's Law and the four were averaged. Subsequent samples were then prepared to confirm the molar absorption coefficients. Quantum yields were determined by, first, cross-calibrating the instrument with quinine sulfate in 0.1 M H_2SO_4 and anthracene in ethanol. Quinine sulfate was then used to determine the experimental quantum yields at an excitation wavelength of 365 nm with Φ = 0.55 for compounds **5.01–5.05** and **5.07–5.10**; rhodamine 6G was used for **5.11** at an excitation wavelength of 480 nm with Φ = 0.95. The quantum yield measurements were performed in multiplicates with values that were within 10% error being averaged.

5.5 Contributions

All primary work (i.e., synthesis, molecular modeling, spectroscopy, analysis, etc.) was performed by J. Bryant Pollock, while Gregory L. Schneider and Andrew S. Davies, undergraduates in the Stang lab, assisted with the synthesis of ligands; Timothy R. Cook served an advisory role.

5.6 Future Directions

Currently, the rhomboidal SCCs are being investigated for bio-imaging applications. The nature of the spectroscopic red-shift upon metallation has been

investigated and is being exploited to interrogate structural integrity *in vivo* in real-time via confocal microscopy. Interestingly, the rhomboidal shaped SCCs are being internalized within the cell and are remaining intact. These preliminary results are indicating that Pt-based SCCs such as **5.10** can be used as delivery mechanisms for therapeutic agents. However, aqueous solubility of the rhomboidal SCCs is greatly limiting their utility in biological environments. As such, pegylated derivates are currently being synthesized to ascertain whether or not they retain their attractive photophysical properties in aqueous environments.

5.7 References

(1) (a) Kubacka, A.; Fernández-García, M.; Colón, G. *Chem. Rev.* **2011**, *112*, 1555; (b) Walter, M. G.; Warren, E. L.; McKone, J. R.; Boettcher, S. W.; Mi, Q.; Santori, E. A.; Lewis, N. S. *Chem. Rev.* **2010**, *110*, 6446; (c) Nozik, A. J.; Miller, J. *Chem. Rev.* **2010**, *110*, 6443.

(2) (a) Grimsdale, A. C.; Leok Chan, K.; Martin, R. E.; Jokisz, P. G.; Holmes, A. B. *Chem. Rev.* **2009**, *109*, 897; (b) Samuel, I. D. W.; Turnbull, G. A. *Chem. Rev.* **2007**, *107*, 1272; (c) Kido, J.; Okamoto, Y. *Chem. Rev.* **2002**, *102*, 2357.

(3) (a) Delaire, J. A.; Nakatani, K. *Chem. Rev.* **2000**, *100*, 1817; (b) Zyss, J.; Ledoux, I. *Chem. Rev.* **1994**, *94*, 77; (c) Oliva, M. M.; Juárez, R.; Ramos, M.; Segura, J. L.; Cleuvenbergen, S. V.; Clays, K.; Goodson, T.; Navarrete, J. T. L.; Casado, J. *J. Phys. Chem. C* **2012**, *117*, 626.

(4) Stender, A. S.; Marchuk, K.; Liu, C.; Sander, S.; Meyer, M. W.; Smith, E. A.; Neupane, B.; Wang, G.; Li, J.; Cheng, J.-X.; Huang, B.; Fang, N. *Chem. Rev.* **2013**, *113*, 2469.

(5) (a) Zhou, H.-C.; Long, J. R.; Yaghi, O. M. *Chem. Rev.* **2012**, *112*, 673; (b) Cui, Y.; Yue, Y.; Qian, G.; Chen, B. *Chem. Rev.* **2011**, *112*, 1126; (c) Ji, M.; Lan, X.; Han, Z.; Hao, C.; Qiu, J. *Inorg. Chem.* **2012**, *51*, 12389; (d) Allendorf, M. D.; Bauer, C. A.; Bhakta, R. K.; Houk, R. J. T. *Chem. Soc. Rev.* **2009**, *38*, 1330.

(6) Stock, N.; Biswas, S. *Chem. Rev.* **2011**, *112*, 933.

(7) (a) Stang, P. J.; Olenyuk, B. *Acc. Chem. Res.* **1997**, *30*, 502; (b) Seidel, S. R.; Stang, P. J. *Acc. Chem. Res.* **2002**, *35*, 972; (c) Gianneschi, N. C.; Masar, M. S.; Mirkin, C. A. *Acc. Chem. Res.* **2005**, *38*, 825; (d) Fujita, M. *Chem. Soc. Rev.* **1998**, *27*, 417; (e) Fujita, M.; Tominaga, M.; Hori, A.; Therrien, B. *Acc. Chem. Res.* **2005**, *38*, 369; (f) Cotton, F. A.; Lin, C.; Murillo, C. A. *Acc. Chem. Res.* **2001**, *34*, 759; (g) Caulder, D. L.; Raymond, K. N. *Acc. Chem. Res.* **1999**, *32*, 975; (h) Chakrabarty, R.; Mukherjee, P. S.; Stang, P. J. *Chem. Rev.* **2011**, *111*, 6810; (i) Cook, T. R.; Zheng, Y.-R.; Stang, P. J. *Chem. Rev.* **2012**, *113*, 734.

(8) (a) Binnemans, K. *Chem. Rev.* **2009**, *109*, 4283; (b) White, K. A.; Chengelis, D. A.; Gogick, K. A.; Stehman, J.; Rosi, N. L.; Petoud, S. *J. Am. Chem. Soc.* **2009**, *131*, 18069; (c) Dong, Y.-B.; Wang, P.; Ma, J.-P.; Zhao, X.-X.; Wang, H.-Y.; Tang, B.; Huang, R.-Q. *J. Am. Chem. Soc.* **2007**, *129*, 4872; (d) An, J.; Shade, C. M.; Chengelis-Czegan, D. A.; Petoud, S.; Rosi, N. L. *J. Am. Chem. Soc.* **2011**, *133*, 1220; (e) Bünzli, J.-C. G.; Piguet, C. *Chem. Rev.* **2002**, *102*, 1897; (f) Kreno, L. E.; Leong, K.; Farha, O. K.; Allendorf, M.; Van Duyne, R. P.; Hupp, J. T. *Chem. Rev.* **2011**, *112*, 1105.

(9) (a) Wong, K. M.-C.; Yam, V. W.-W. *Coordination Chem. Rev.* **2007**, *251*, 2477; (b) Eryazici, I.; Moorefield, C. N.; Newkome, G. R. *Chem. Rev.* **2008**, *108*, 1834; (c) Fleischauer, P. D.; Fleischauer, P. *Chem. Rev.* **1970**, *70*, 199; (d) Kindahl, T.; Ellingsen, P. G.; Lopes, C.; Brännlund, C.; Lindgren, M.; Eliasson, B. *J Phys Chem A* **2012**, *116*, 11519; (e) Chan, K. H.-Y.; Chow, H.-S.; Wong, K. M.-C.; Yeung, M. C.-L.; Yam, V. W.-W. *Chem. Sci.* **2010**, *1*, 477; (f) Hui, C.-K.; Chu, B. W.-K.; Zhu, N.; Yam, V. W.-W. *Inorg. Chem.* **2002**, *41*, 6178; (g) Wong, K. M.-C.; Yam, V. W.-W. *Acc. Chem. Res.* **2011**, *44*, 424; (h) Adamson, A. W.; Waltz, W. L.; Zinato, E.; Watts, D. W.; Fleischauer, P. D.; Lindholm, R. D. *Chem. Rev.* **1968**, *68*, 541; (i) Brooks, J.; Babayan, Y.; Lamansky, S.; Djurovich, P. I.; Tsyba, I.; Bau, R.; Thompson, M. E. *Inorg. Chem.* **2002**, *41*, 3055; (j) Caspar, J. V. *J. Am. Chem. Soc.* **1985**, *107*, 6718; (k) Chan, S.-C.; Chan, M. C. W.; Wang, Y.; Che, C.-M.; Cheung, K.-K.; Zhu, N. *Chem.-Eur. J.* **2001**, *7*, 4180; (l) Pomestchenko, I. E.; Luman, C. R.; Hissler, M.; Ziessel, R.; Castellano, F. N. *Inorg. Chem.* **2003**, *42*, 1394; (m) Danilov, E. O.; Rachford, A. A.; Goeb, S. B.; Castellano, F. N. *J. Phys. Chem. A* **2009**, *113*, 5763; (n) Goeb, S.; Prusakova, V.; Wang, X.; Vezinat, A.; Salle, M.; Castellano, F. N. *Chem. Commun.* **2011**, *47*, 4397; (o) Forniés, J.; Fuertes, S.; Martín, A.; Sicilia, V.; Lalinde, E.; Moreno, M. T. *Chem.-Eur. J.* **2006**, *12*, 8253; (p) Keller, J. M.; Glusac, K. D.; Danilov, E. O.; McIlroy, S.; Sreearuothai, P.; R. Cook, A.; Jiang, H.; Miller, J. R.; Schanze, K. S. *J. Am. Chem. Soc.* **2011**, *133*, 11289; (q) Keller, J. M.; Schanze, K. S. *Organometallics* **2009**, *28*, 4210; (r) Liao, C.; Yarnell, J. E.; Glusac, K. D.; Schanze, K. S. *J. Phys. Chem. B* **2010**, *114*, 14763; (s) Rogers, J. E.; Slagle, J. E.; Krein, D. M.; Burke, A. R.; Hall, B. C.; Fratini, A.; McLean, D.

G.; Fleitz, P. A.; Cooper, T. M.; Drobizhev, M.; Makarov, N. S.; Rebane, A.; Kim, K.-Y.; Farley, R.; Schanze, K. S. *Inorg. Chem.* **2007**, *46*, 6483.

(10) (a) Flynn, D. C.; Ramakrishna, G.; Yang, H.-B.; Northrop, B. H.; Stang, P. J.; Goodson, T. *J. Am. Chem. Soc.* **2010**, *132*, 1348; (b) Chen, J.-S.; Zhao, G.-J.; Cook, T. R.; Han, K.-L.; Stang, P. J. *J. Am. Chem. Soc.* **2013**, *135*, 6694; (c) Chen, J.-S.; Zhao, G.-J.; Cook, T. R.; Sun, X.-F.; Yang, S.-Q.; Zhang, M.-X.; Han, K.-L.; Stang, P. J. *J. Phys. Chem. A* **2012**, *116*, 9911; (d) Zhao, G.-J.; Northrop, B. H.; Han, K.-L.; Stang, P. J. *J. Phys. Chem. A* **2010**, *114*, 9007; (e) Zhao, G.-J.; Northrop, B. H.; Stang, P. J.; Han, K.-L. *J. Phys. Chem. A* **2010**, *114*, 3418; (f) Zhao, G.-J.; Yu, F.; Zhang, M.-X.; Northrop, B. H.; Yang, H.; Han, K.-L.; Stang, P. J. *J. Phys. Chem. A* **2011**, *115*, 6390; (g) Pollock, J. B.; Cook, T. R.; Stang, P. J. *J. Am. Chem. Soc.* **2012**, *134*, 10607.

(11) (a) Yang, J.-S. *PATAI'S Chem. Func. Groups*; John Wiley & Sons, Ltd: 2009, doi:10.1002/9780470682531.pat0396; (b) Hou, X.-J.; Quan, P.; Höltzl, T.; Veszprémi, T.; Nguyen, M. T. *J. Phys. Chem. A* **2005**, *109*, 10396; (c) Lewis, F. D.; Hougland, J. L.; Markarian, S. A. *J. Phys. Chem. A* **2000**, *104*, 3261; (d) Oosterbaan, W. D.; Koeberg, M.; Piris, J.; Havenith, R. W. A.; van Walree, C. A.; Wegewijs, B. R.; Jenneskens, L. W.; Verhoeven, J. W. *J. Phys. Chem. A* **2001**, *105*, 5984; (e) Rückert, I.; Demeter, A.; Morawski, O.; Kühnle, W.; Tauer, E.; Zachariasse, K. A. *J. Phys. Chem. A* **1999**, *103*, 1958.

(12) Pollock, J. B.; Cook, T. R.; Schneider, G. L.; Lutterman, D. A.; Davies, A. S.; Stang, P. J. *Inorg. Chem.* **2013**, *52*, 9254.

(13) Flynn, G. L. *J. Pharm. Sci.* **1980**, *69*, 1109.

(14) Kryschenko, Y. K.; Seidel, S. R.; Arif, A. M.; Stang, P. J. *J. Am. Chem. Soc.* **2003**, *125*, 5193.

APPENDIX

REFERENCE SPECTRA

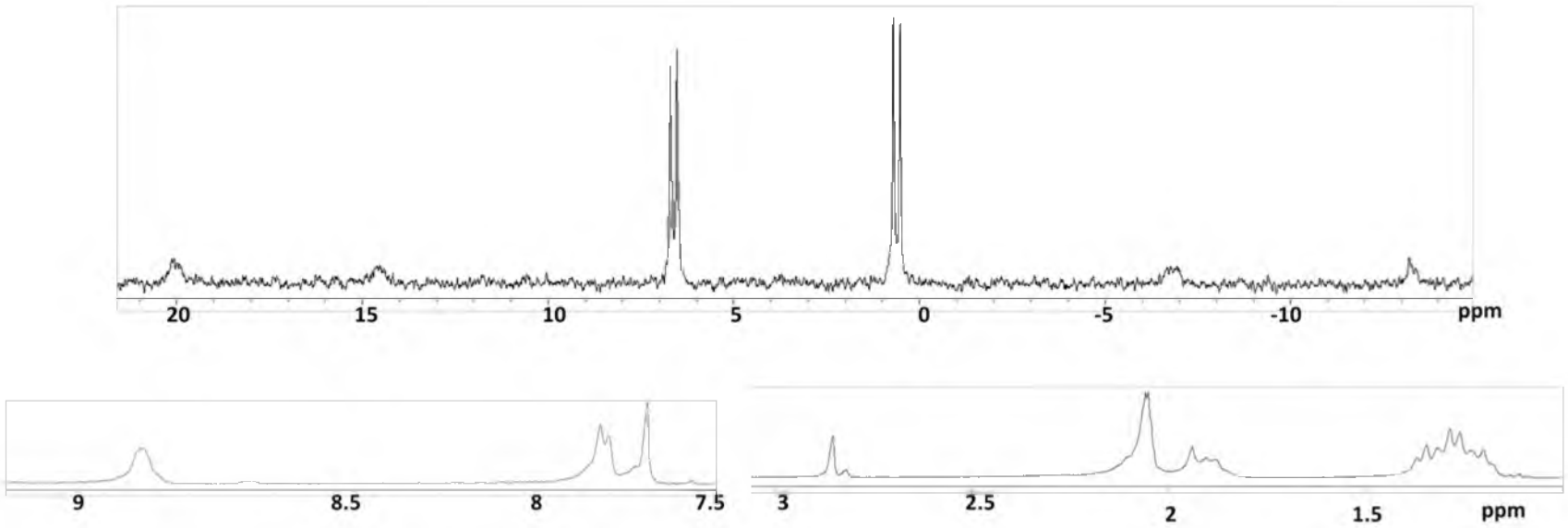

Figure A.1: $^{31}P\{^{1}H\}$ and ^{1}H NMR Spectra of **2.05A.**.

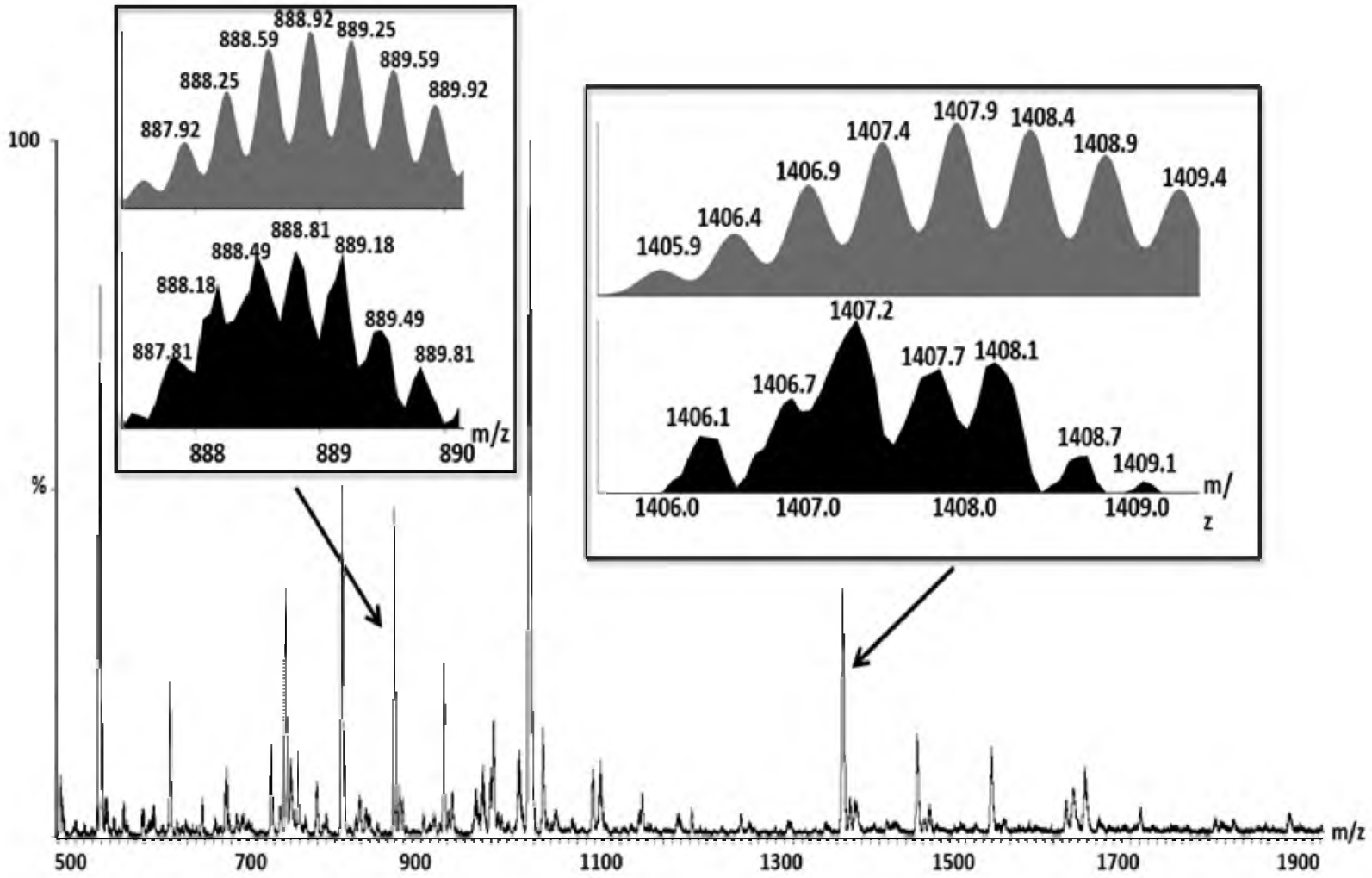

Figure A.2: ESI-MS spectra of the $[M–2•OTf]^{2+}$ and $[M–3•OTf]^{3+}$ charge states for **2.05A**.

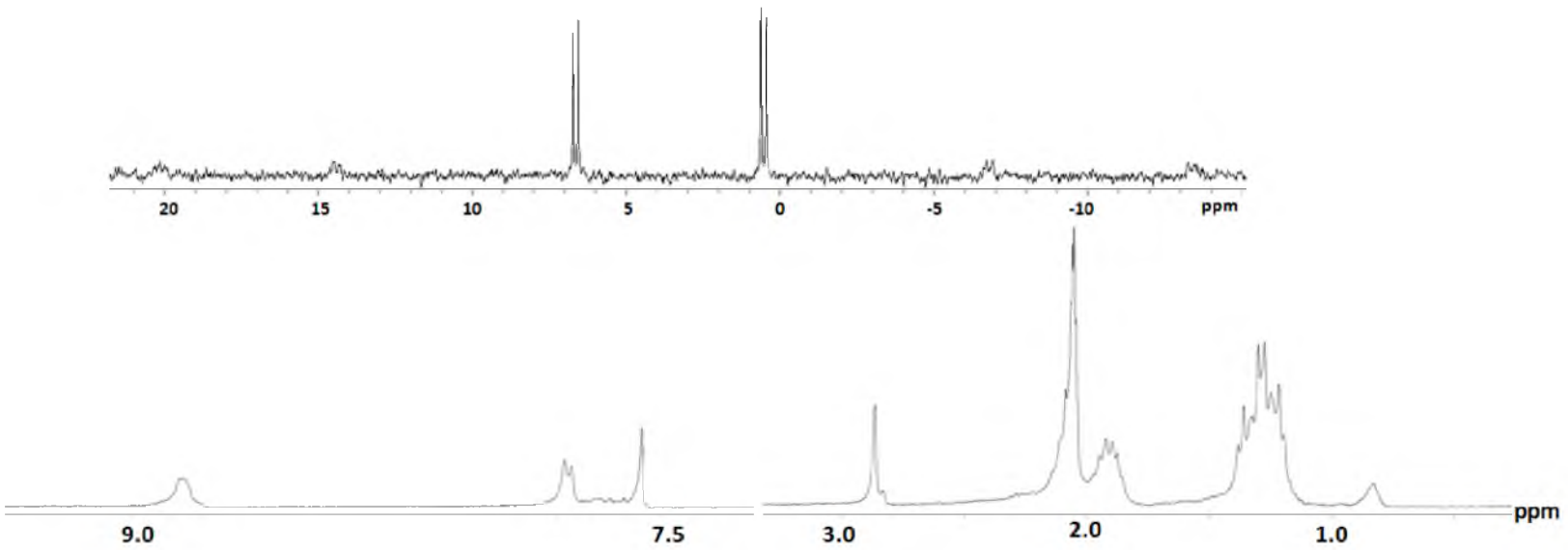

Figure A.3: $^{31}P\{^{1}H\}$ and ^{1}H NMR Spectra of **2.05b**

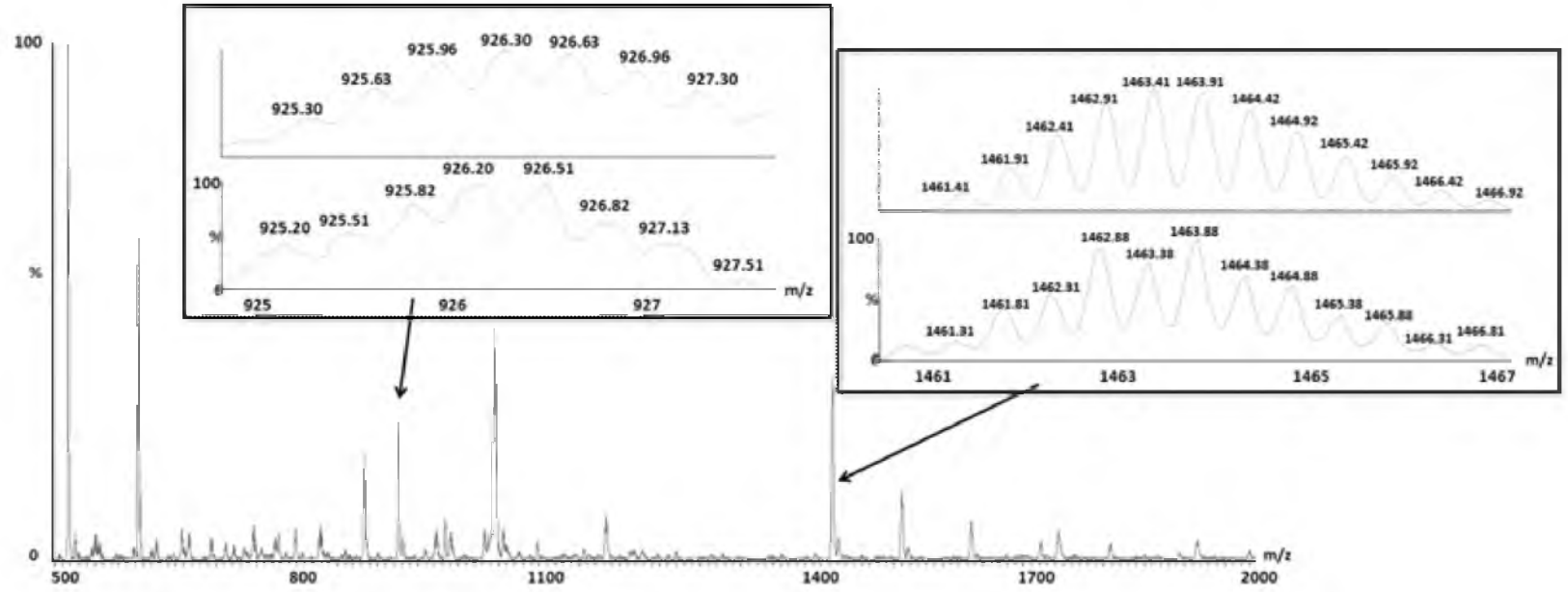

Figure A.4: ESI-MS spectra of the $[M–2•OTf]^{2+}$ and $[M–3•OTf]^{3+}$ charge states for **2.05b**.

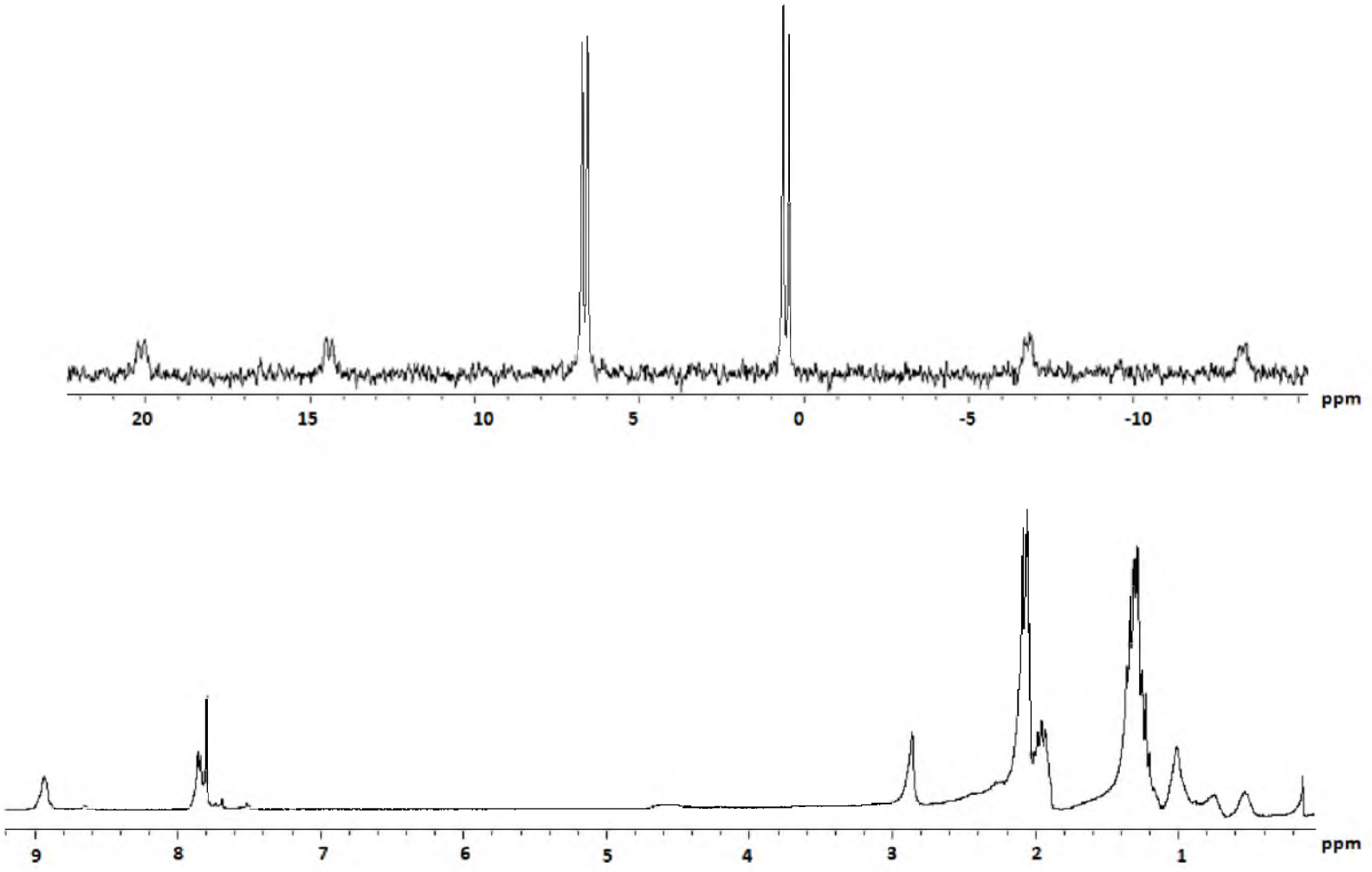

Figure A.5: $^{31}P\{^{1}H\}$ and ^{1}H NMR Spectra of **2.05c**.

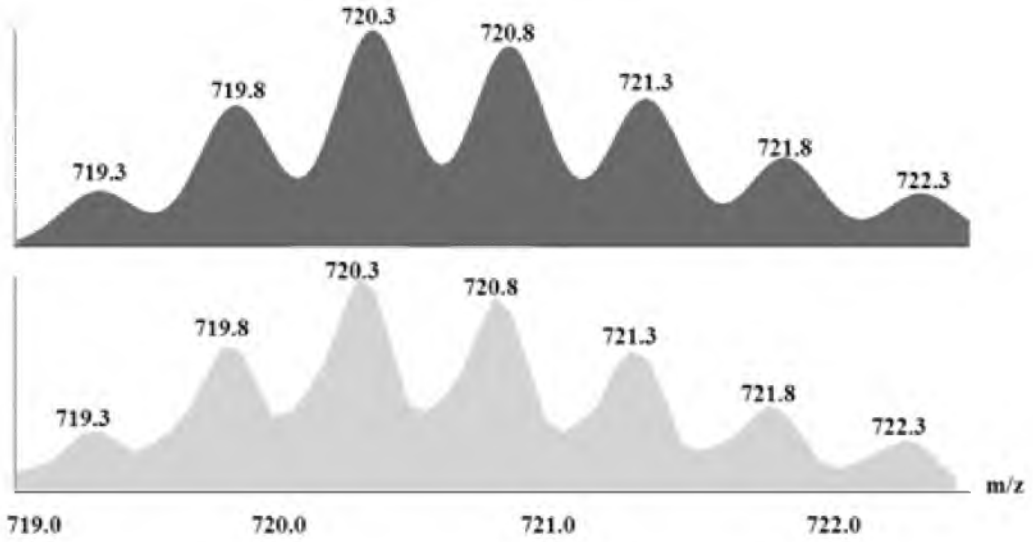

Figure A.6: ESI-MS showing a +2 charge state of self assembly **2.05c** confirming a 1:1 structure.

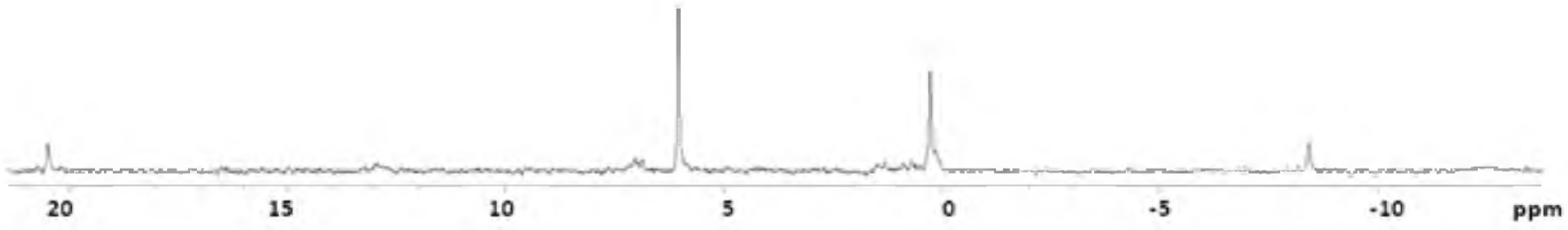

Figure A.7: $^{31}P\{^{1}H\}$ mixture of self-assemblies formed from procedure **2.06**. Peaks are in good agreement with literature reported values.

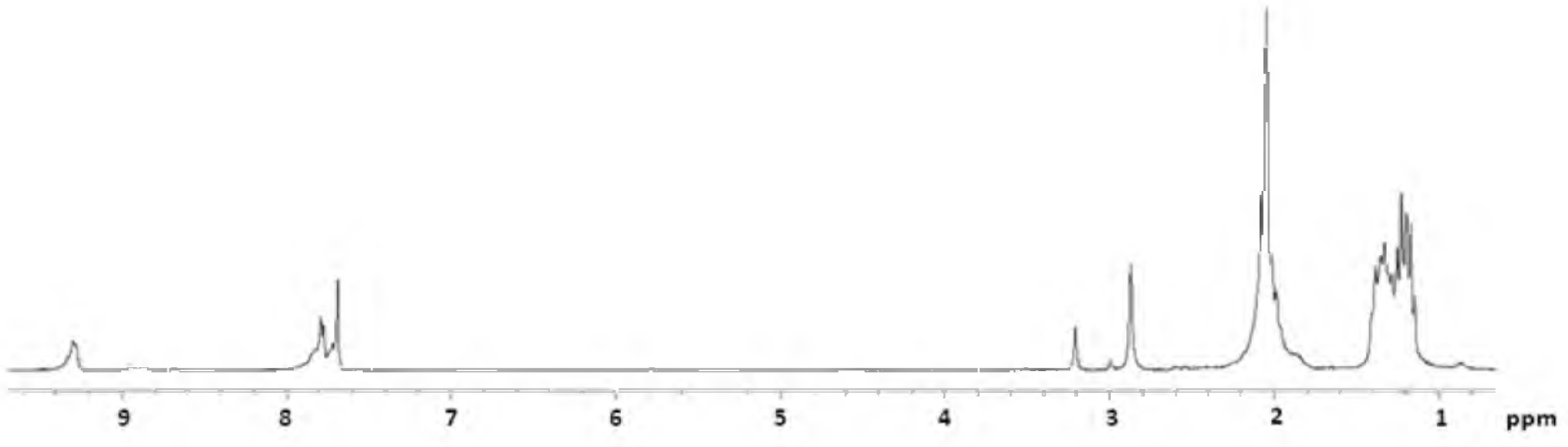

Figure A.8: ^{1}H mixture of self-assemblies formed from procedure **2.06**.

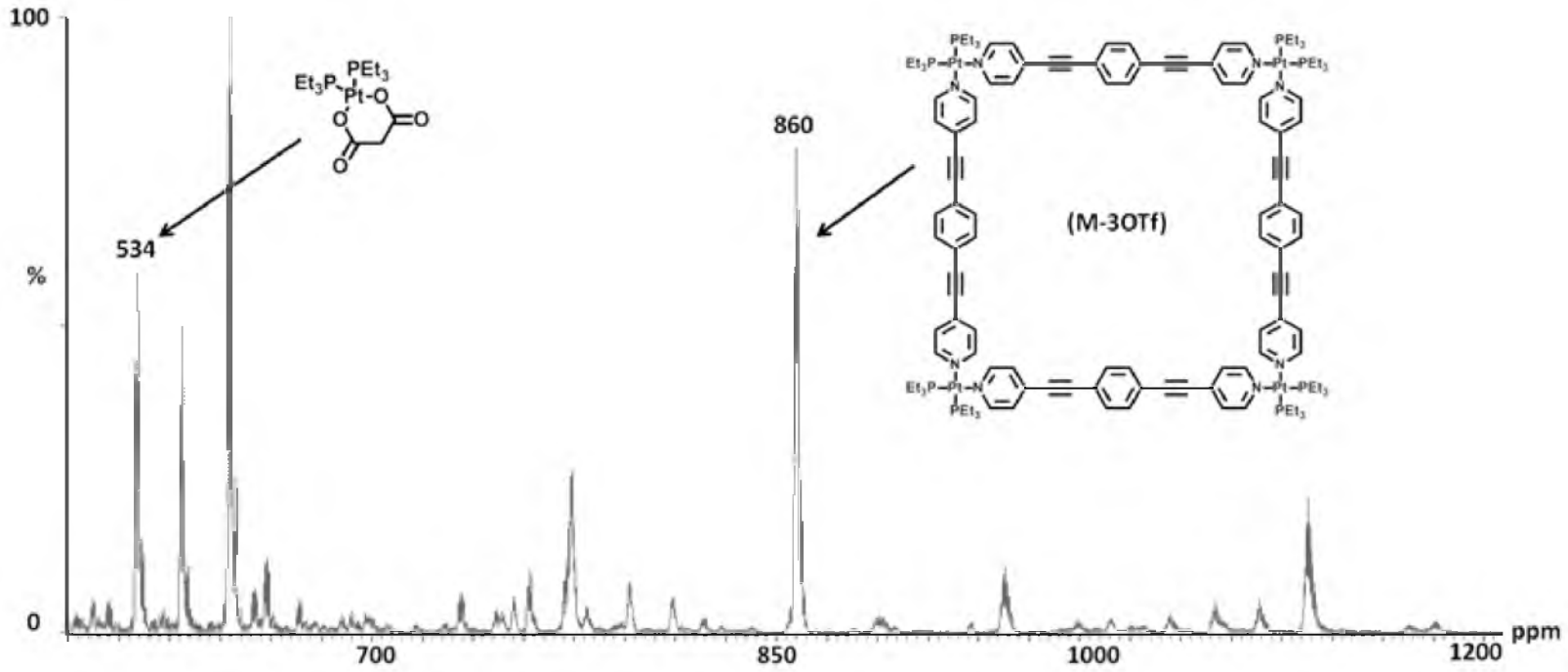

Figure A.9: MS displaying the crude mixture of **2.06**. Both products are present.

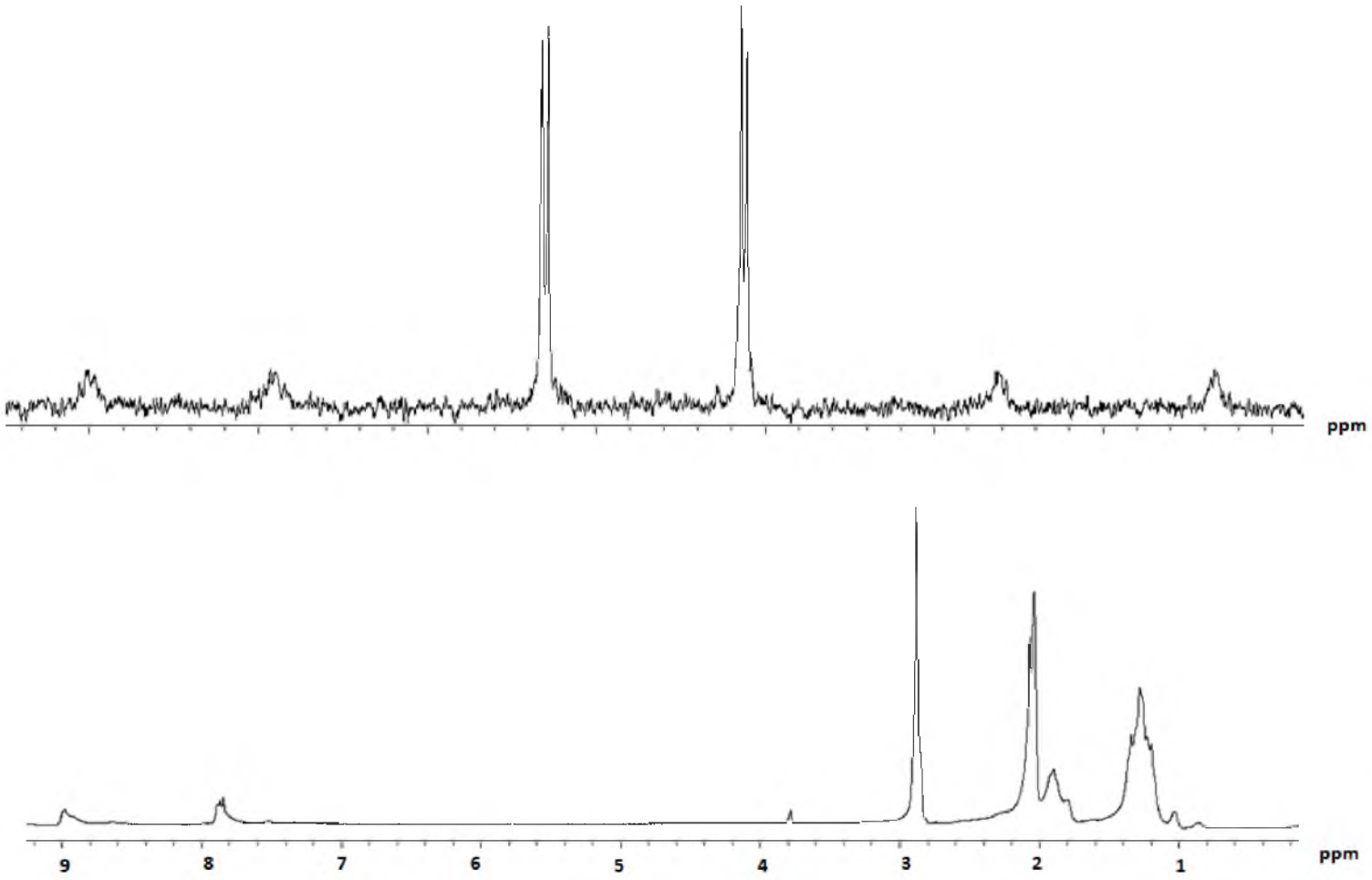

Figure A.10: $^{31}P\{^{1}H\}$ and ^{1}H of self-assembly **2.07**.

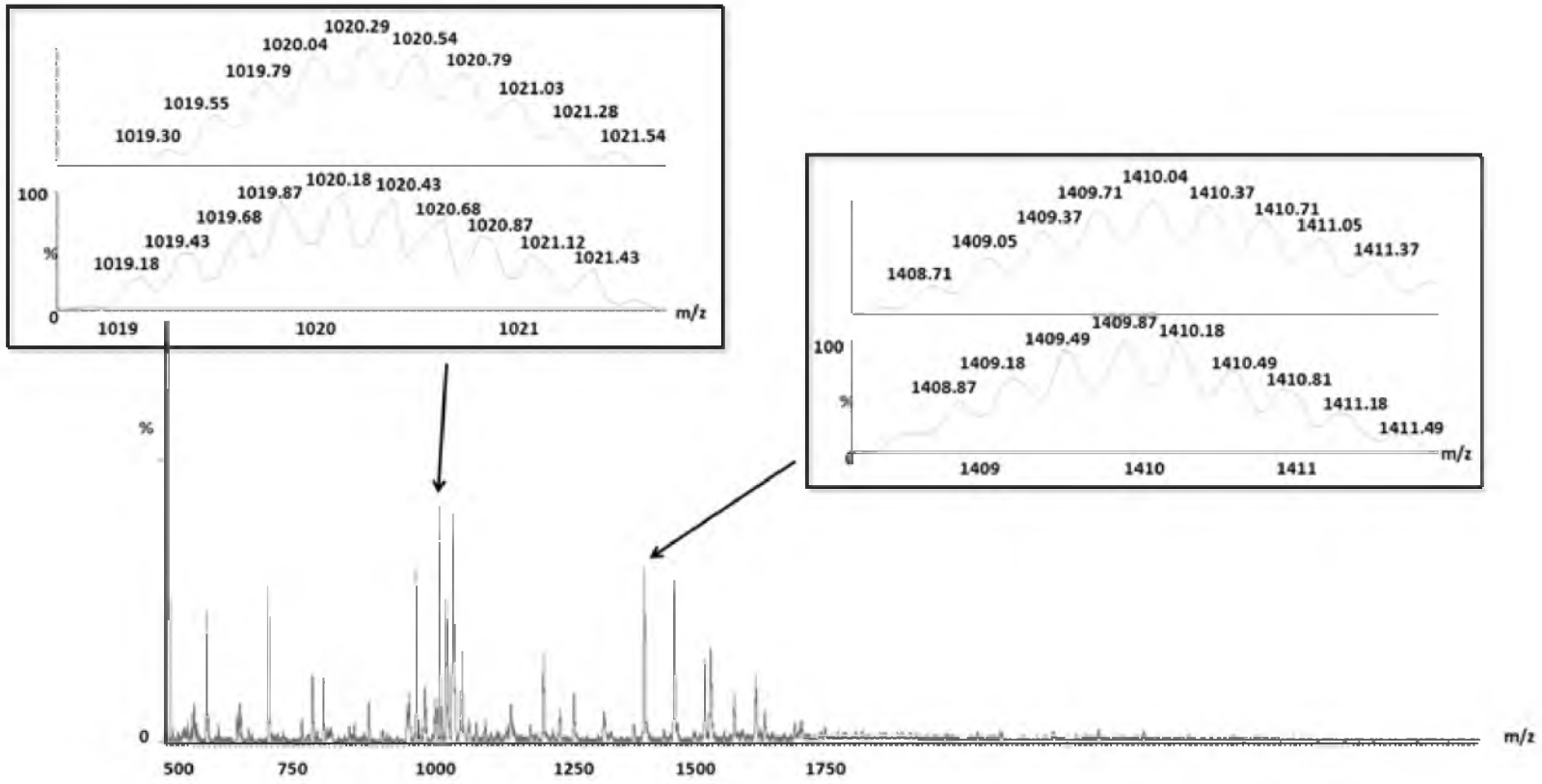

Figure A.11: ESI-MS displaying the $[M–3•OTf]^{3+}$ and $[M–4•OTf]^{4+}$ charge states of **2.07**.

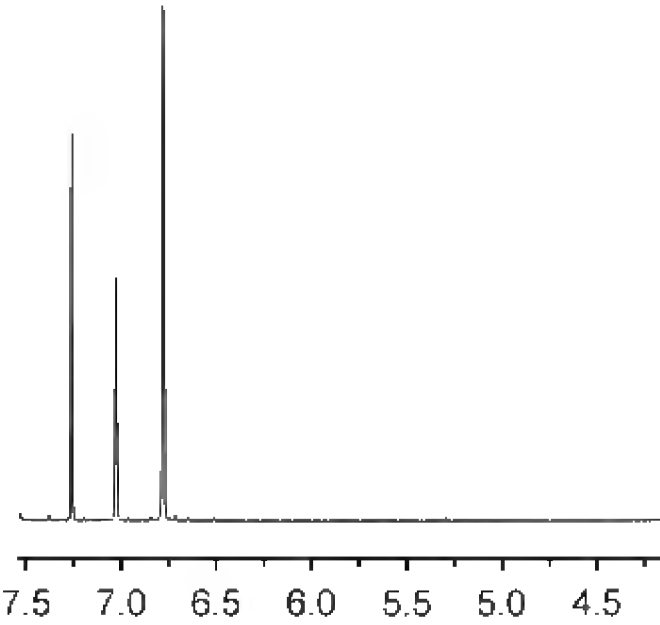

Figure A.12:

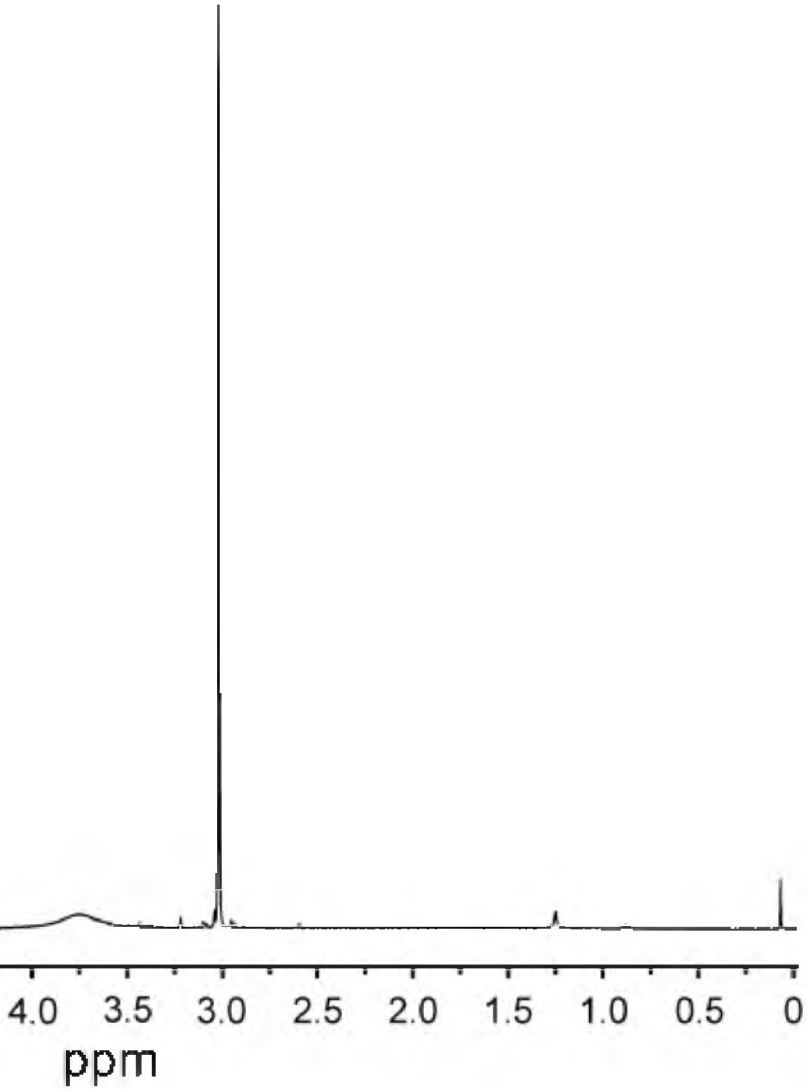

^{1}H NMR spectra of **3.03**.

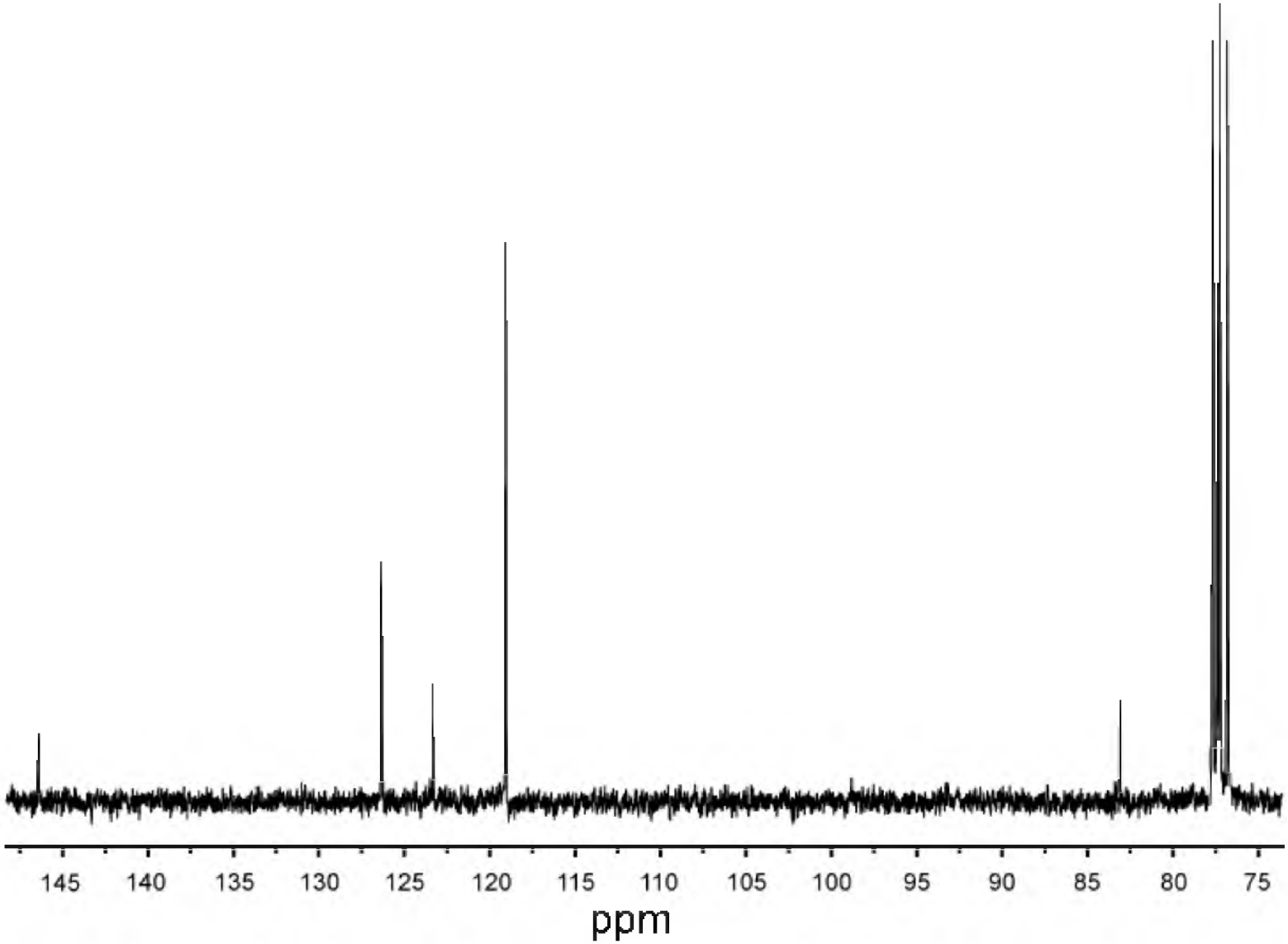

Figure A.13: ^{13}C NMR spectra of **3.03**.

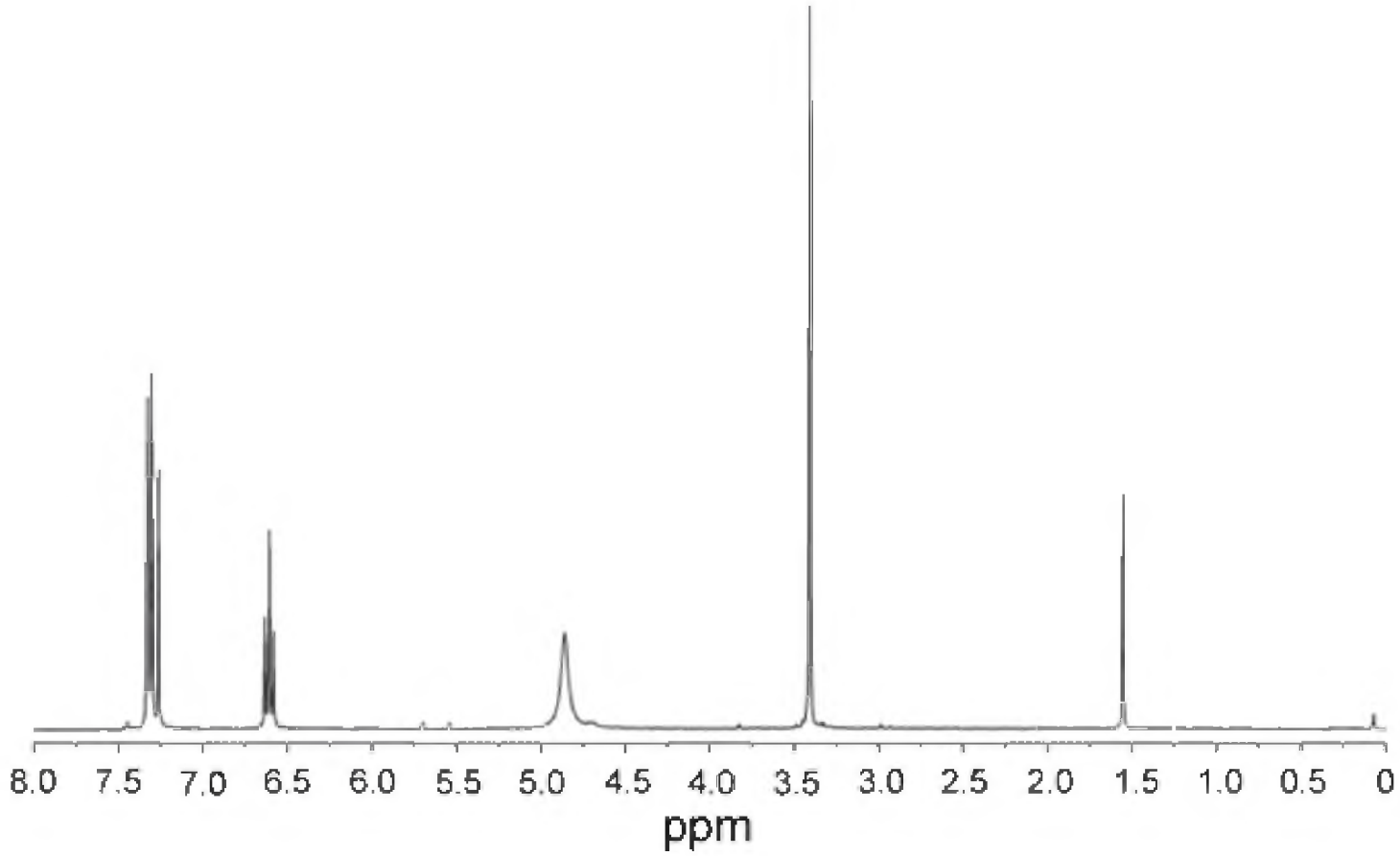

Figure A.14: ^{1}H NMR spectra of **3.04**.

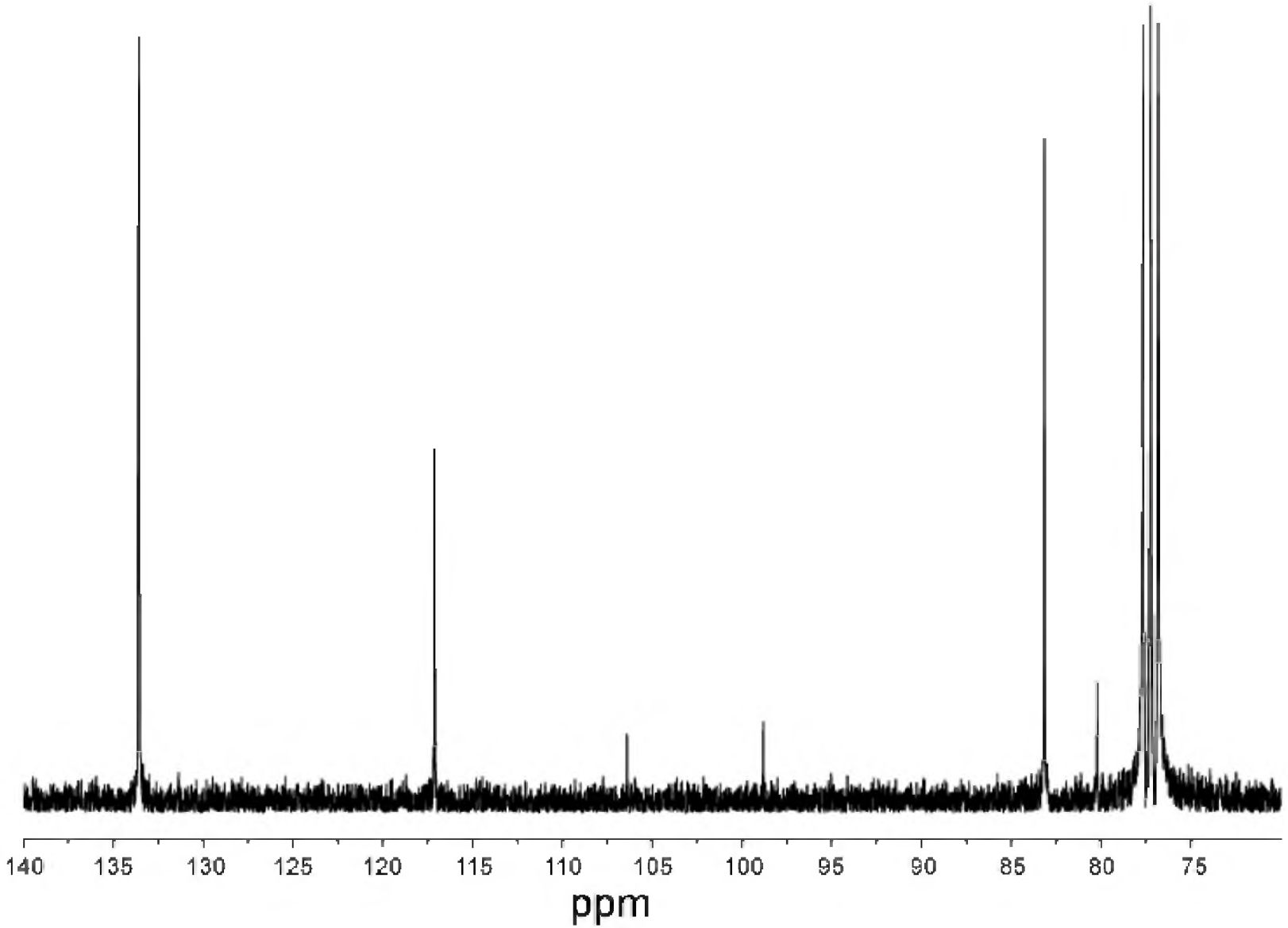

Figure A.15: ^{13}C NMR spectra of **3.04**.

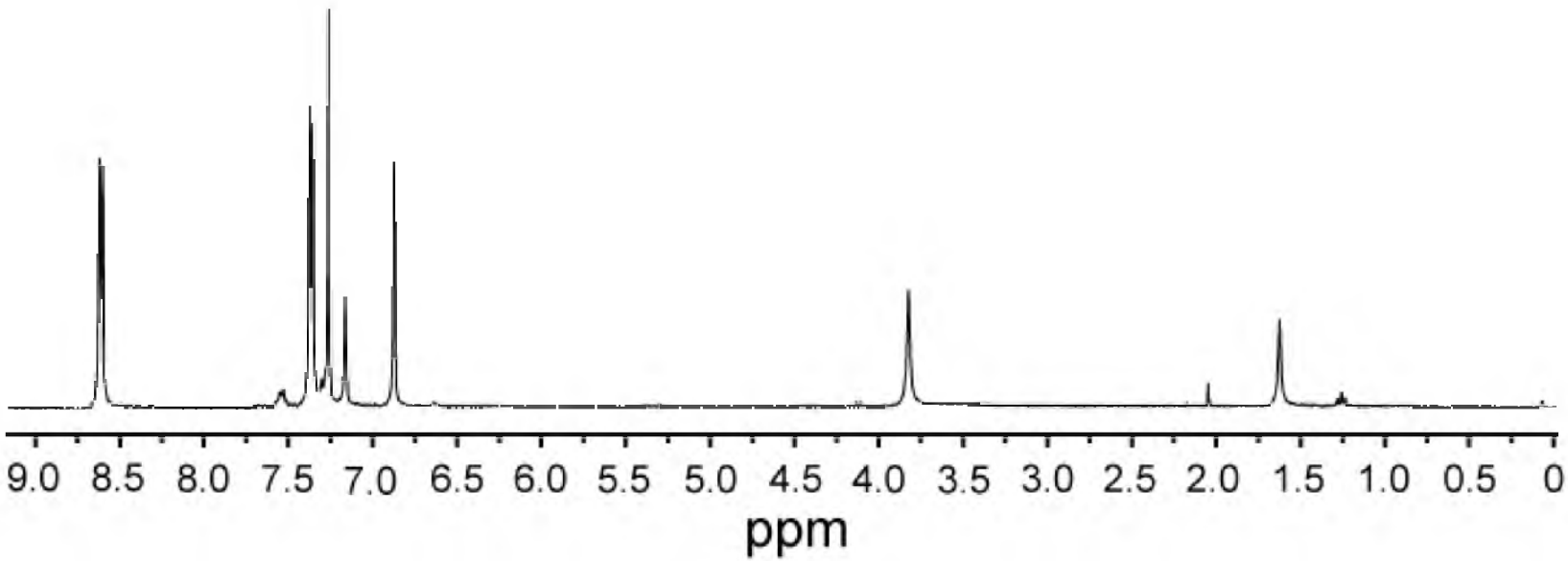

Figure A.16: ^{1}H NMR spectra of **3.05**.

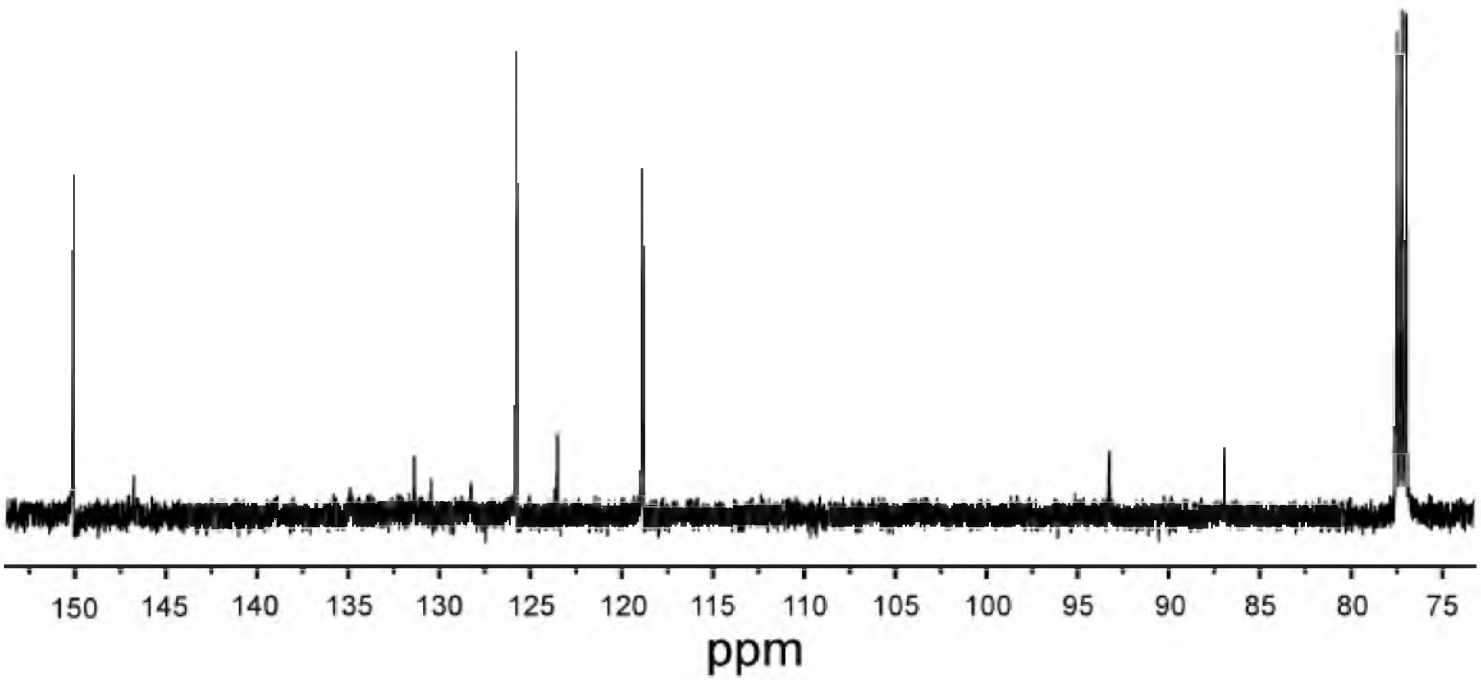

Figure A.17: ^{13}C NMR spectra of **3.05**.

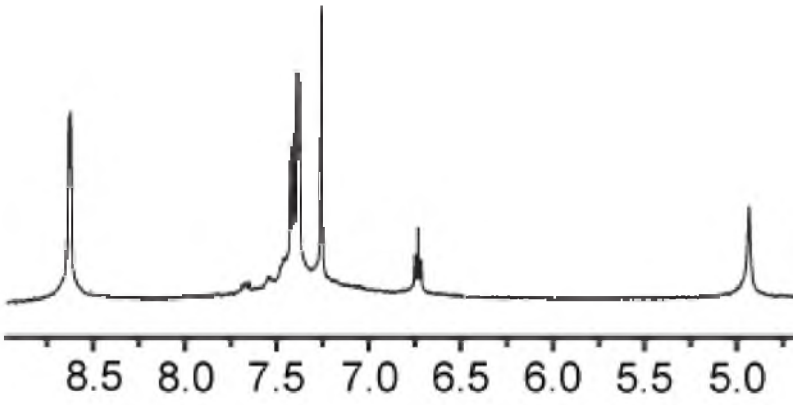

Figure A.18:

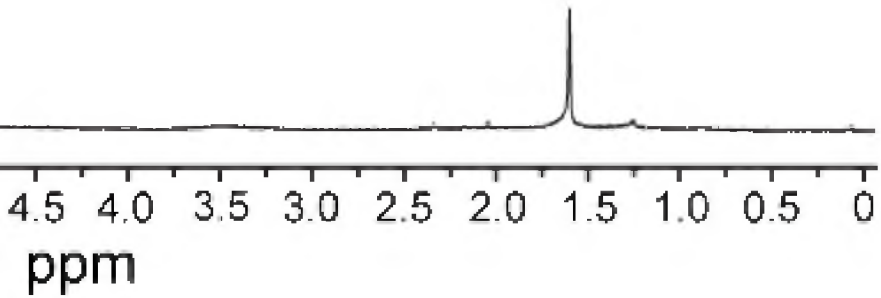

^{1}H NMR spectra of **3.06**.

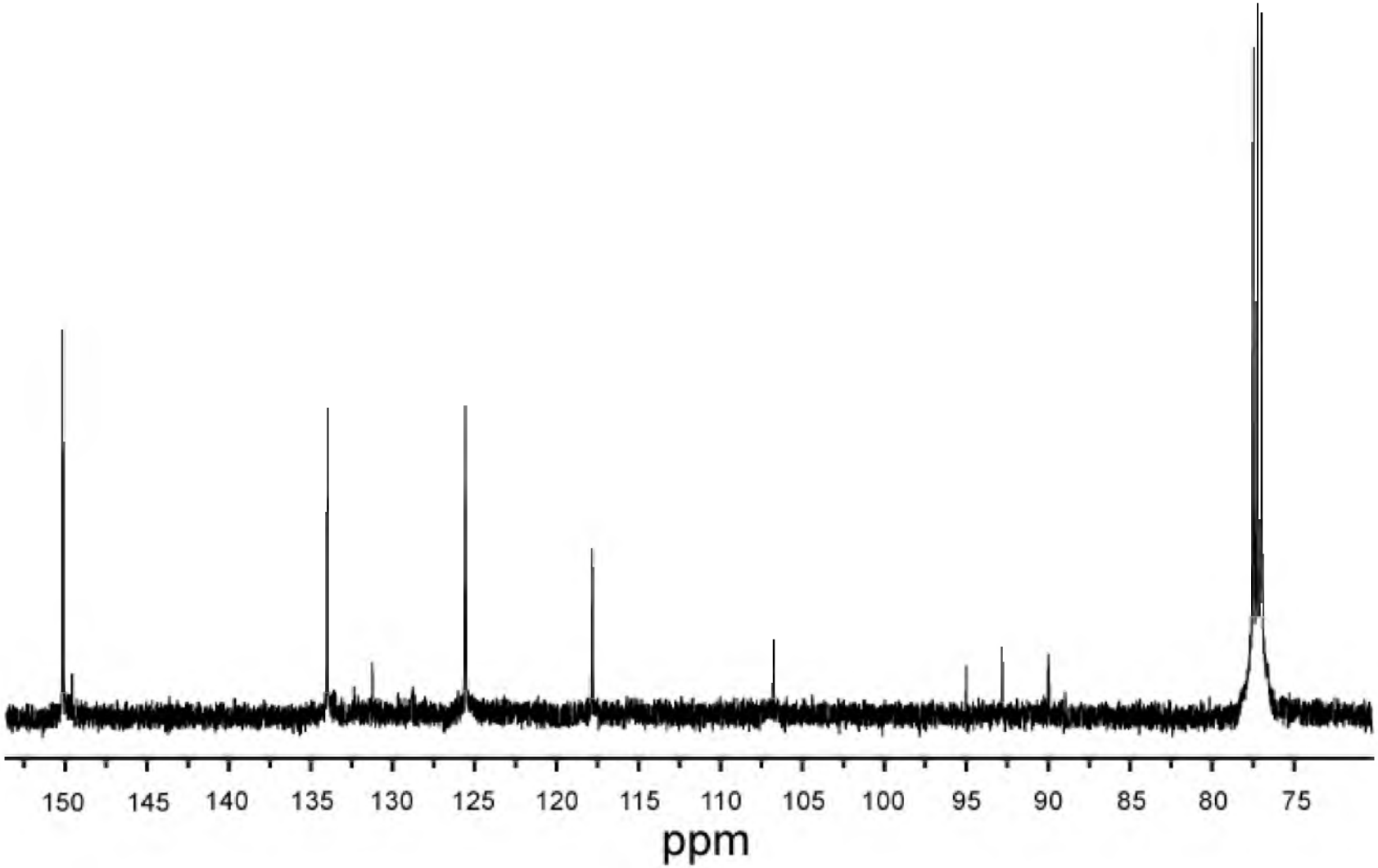

Figure A.19: ^{13}C NMR spectra of **3.06**.

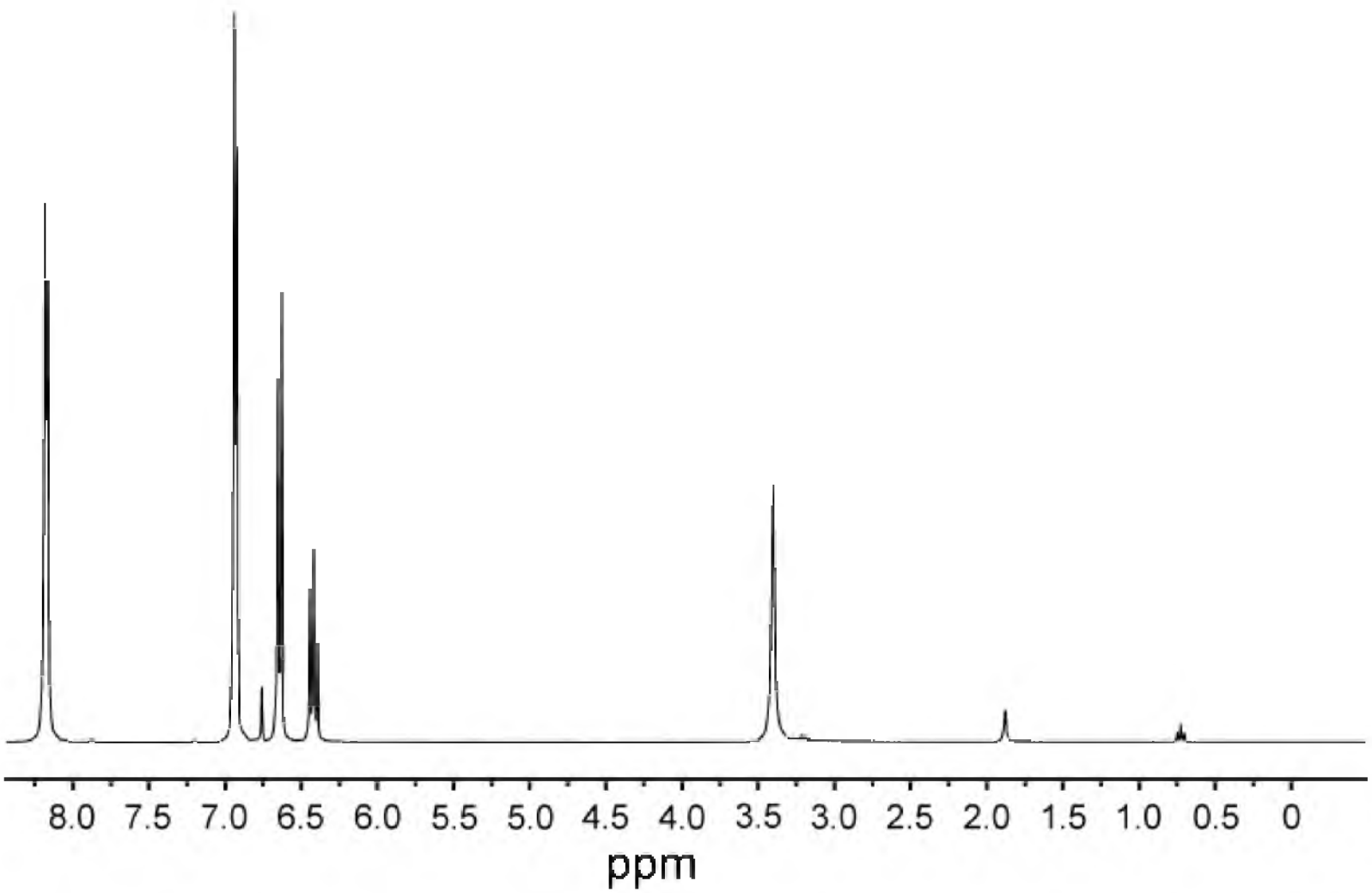

Figure A.20: ^{1}H NMR spectra of **3.08**.

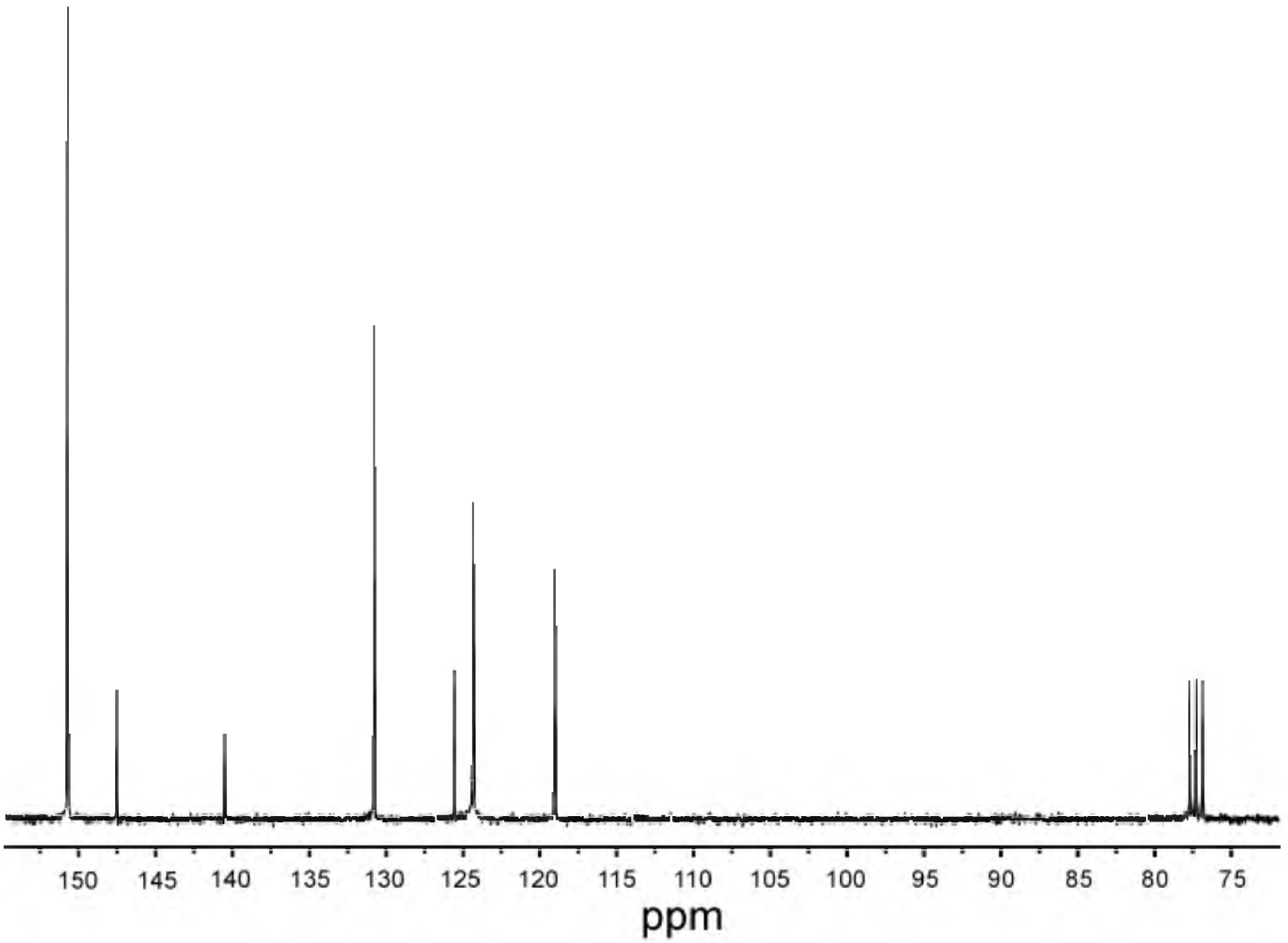

Figure A.21: ^{13}C NMR spectra of **3.08**.

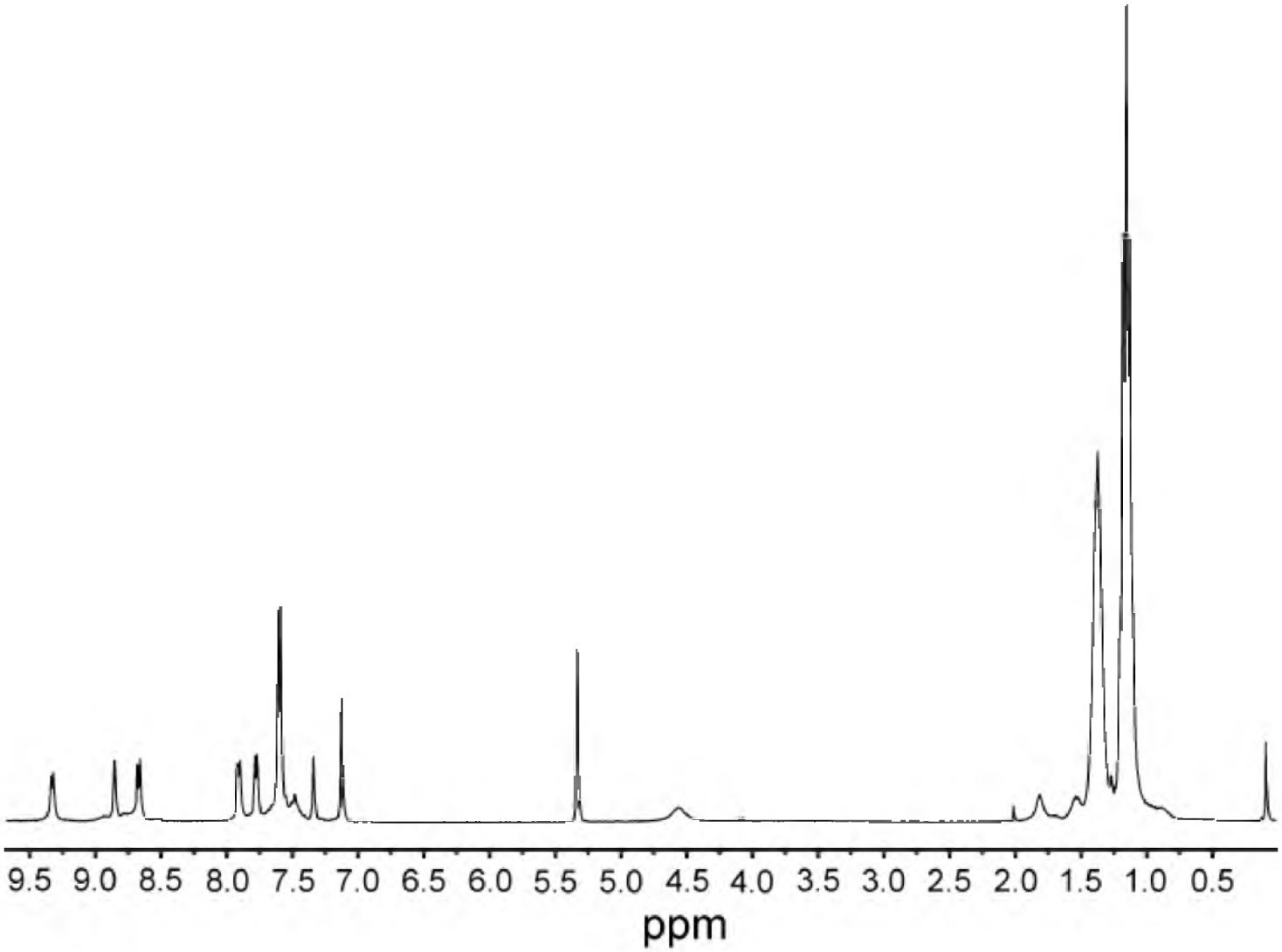

Figure A.22: ^{1}H NMR spectra of **3.10**.

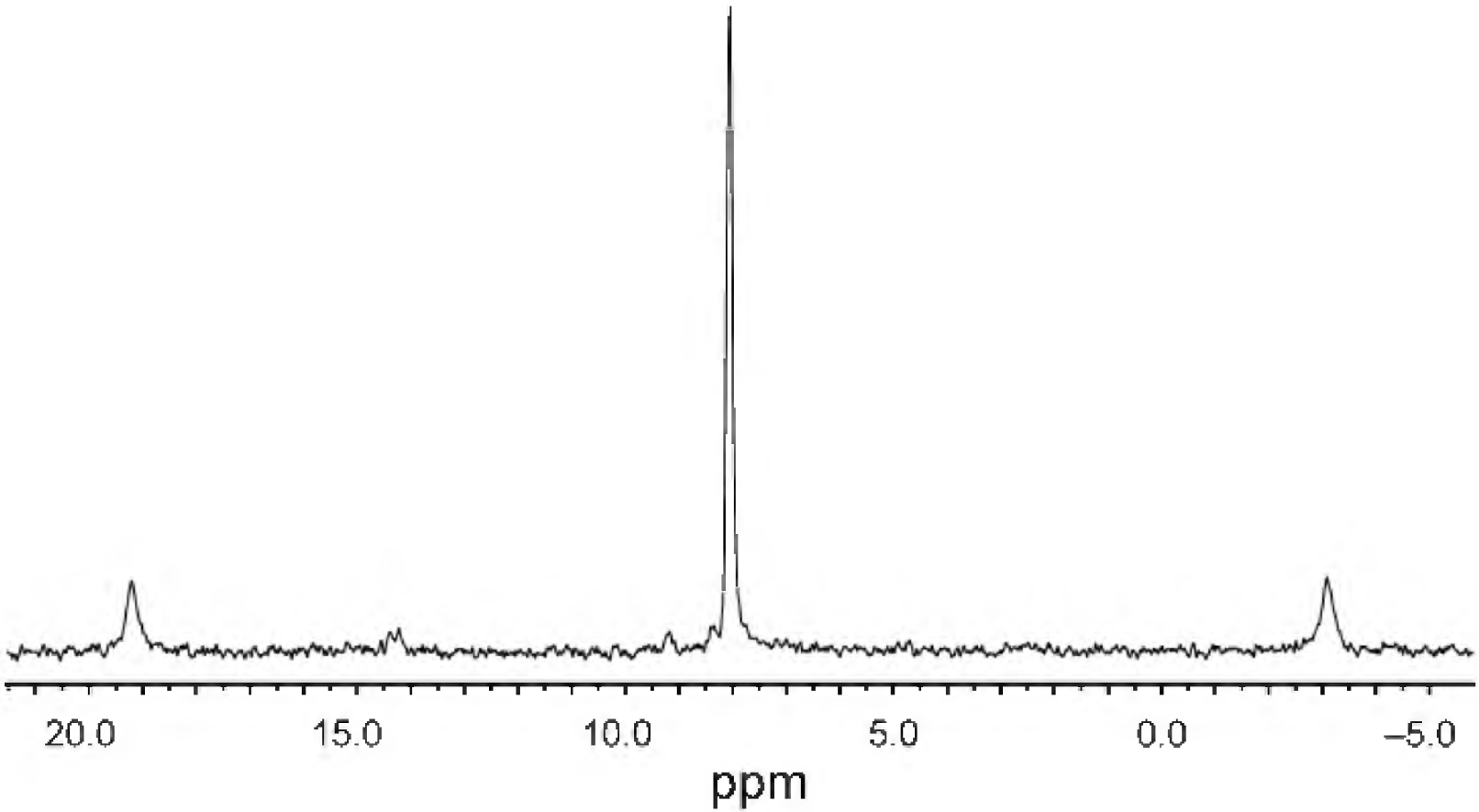

Figure A.23: $^{31}P\{^{1}H\}$ NMR spectra of **3.10**.

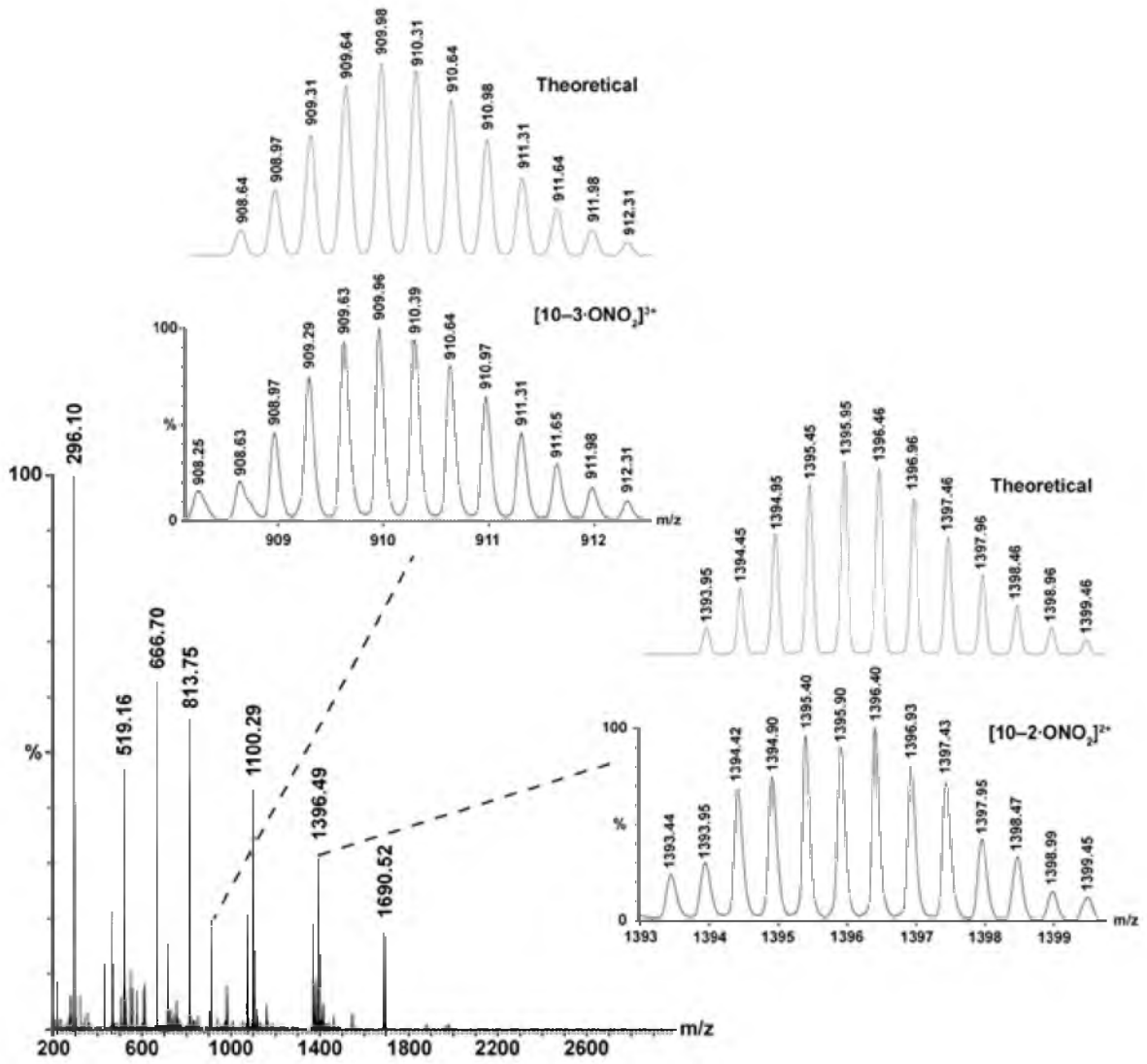

Figure A.24: ESI-MS spectra of the $[M–2•ONO_2]^{2+}$ and $[M–3•ONO_2]^{3+}$ charge states for **3.10**.

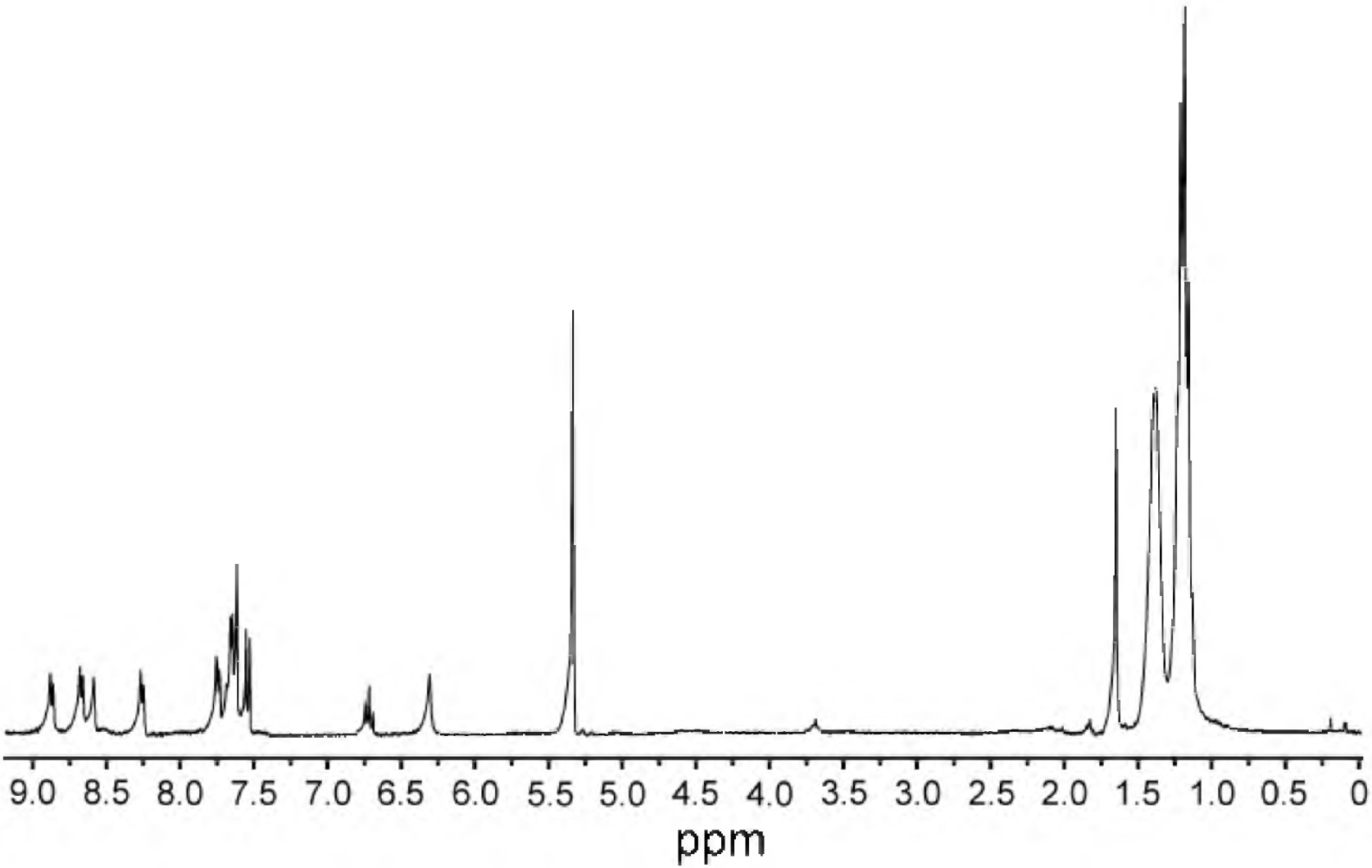

Figure A.25: ^{1}H NMR spectra of **3.11**.

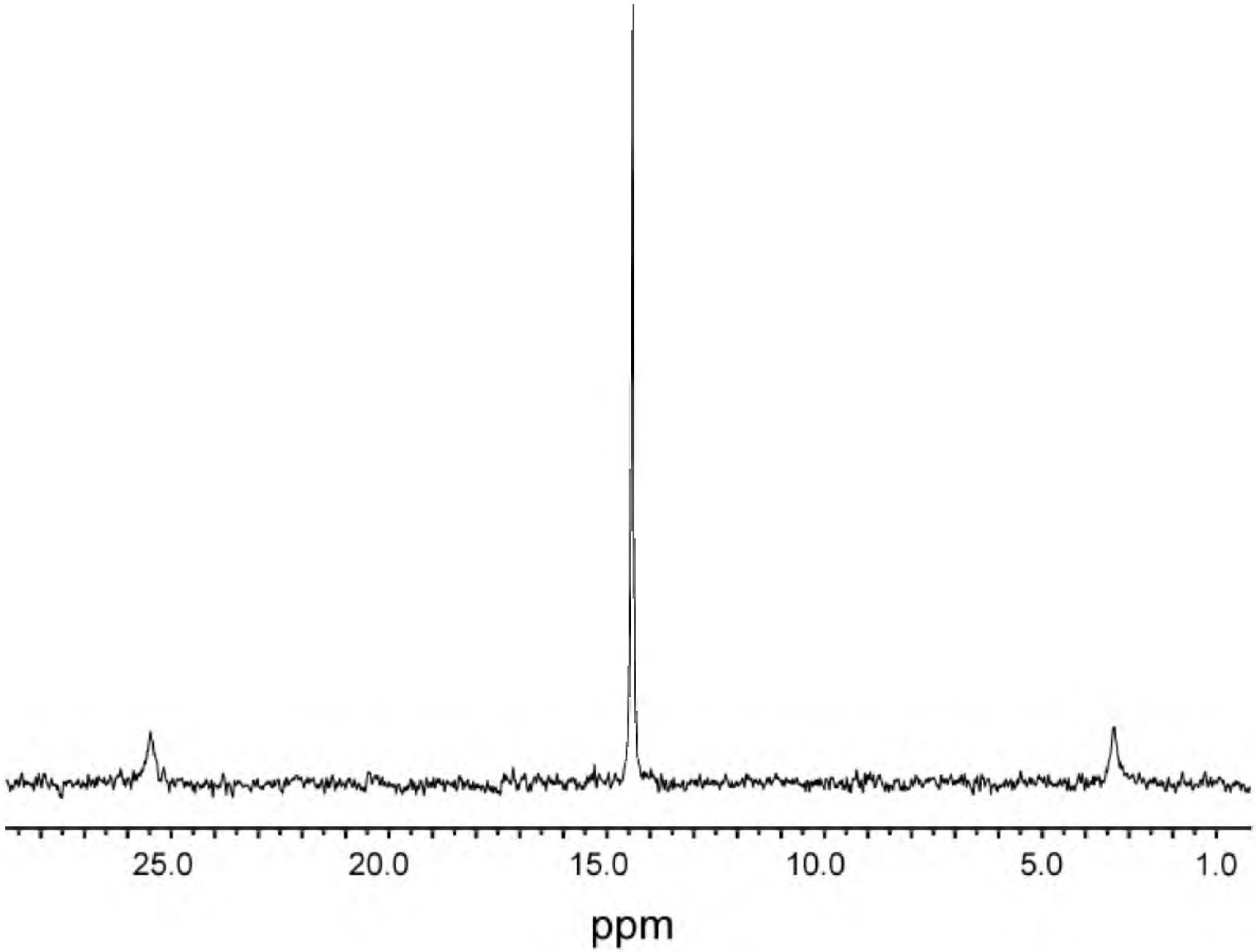

Figure A.26: $^{31}P\{^{1}H\}$ NMR spectra of **3.11**.

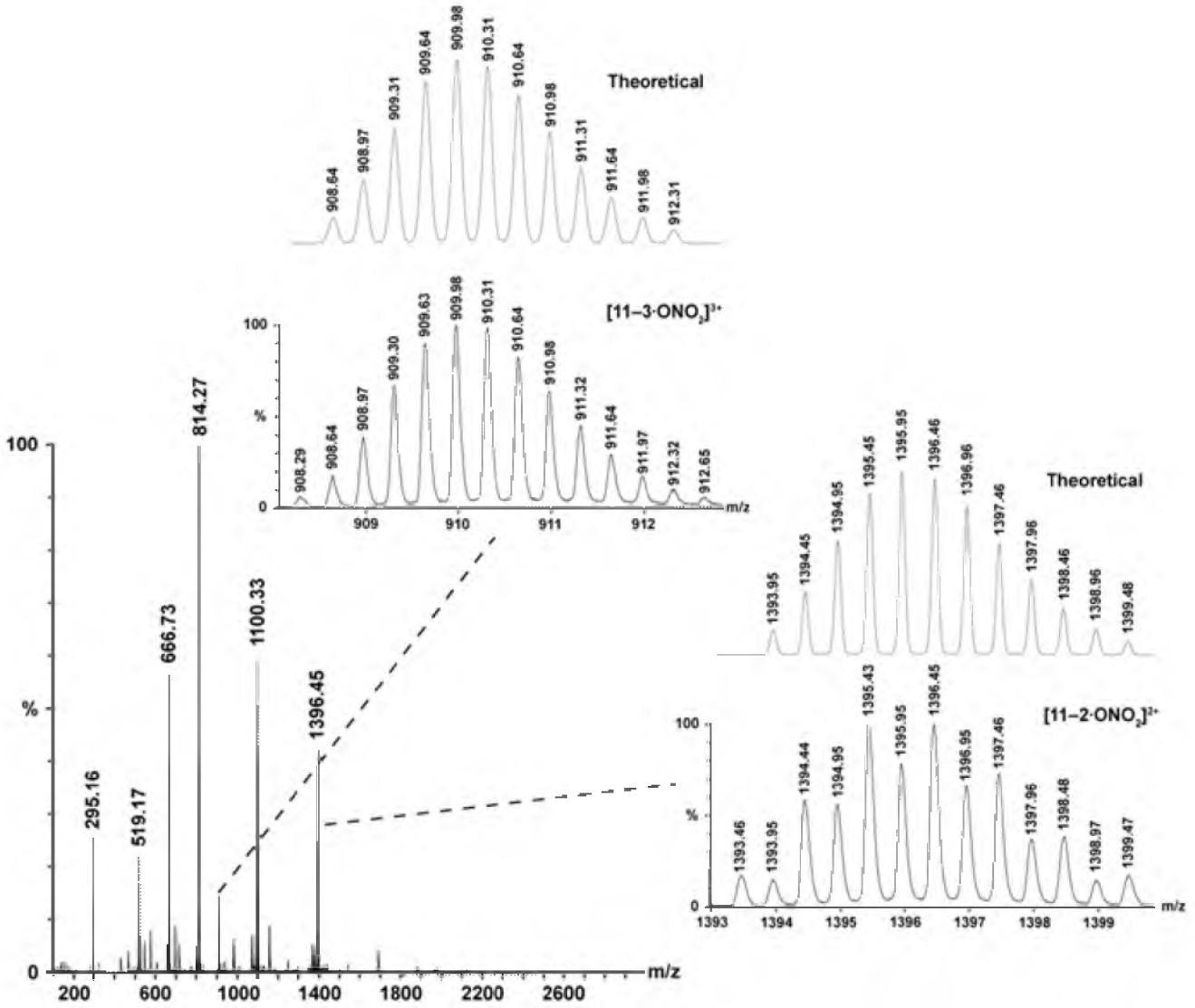

Figure A.27: ESI-MS spectra of the $[M–2•ONO_2]^{2+}$ and $[M–3•ONO_2]^{3+}$ charge states for **3.11**.

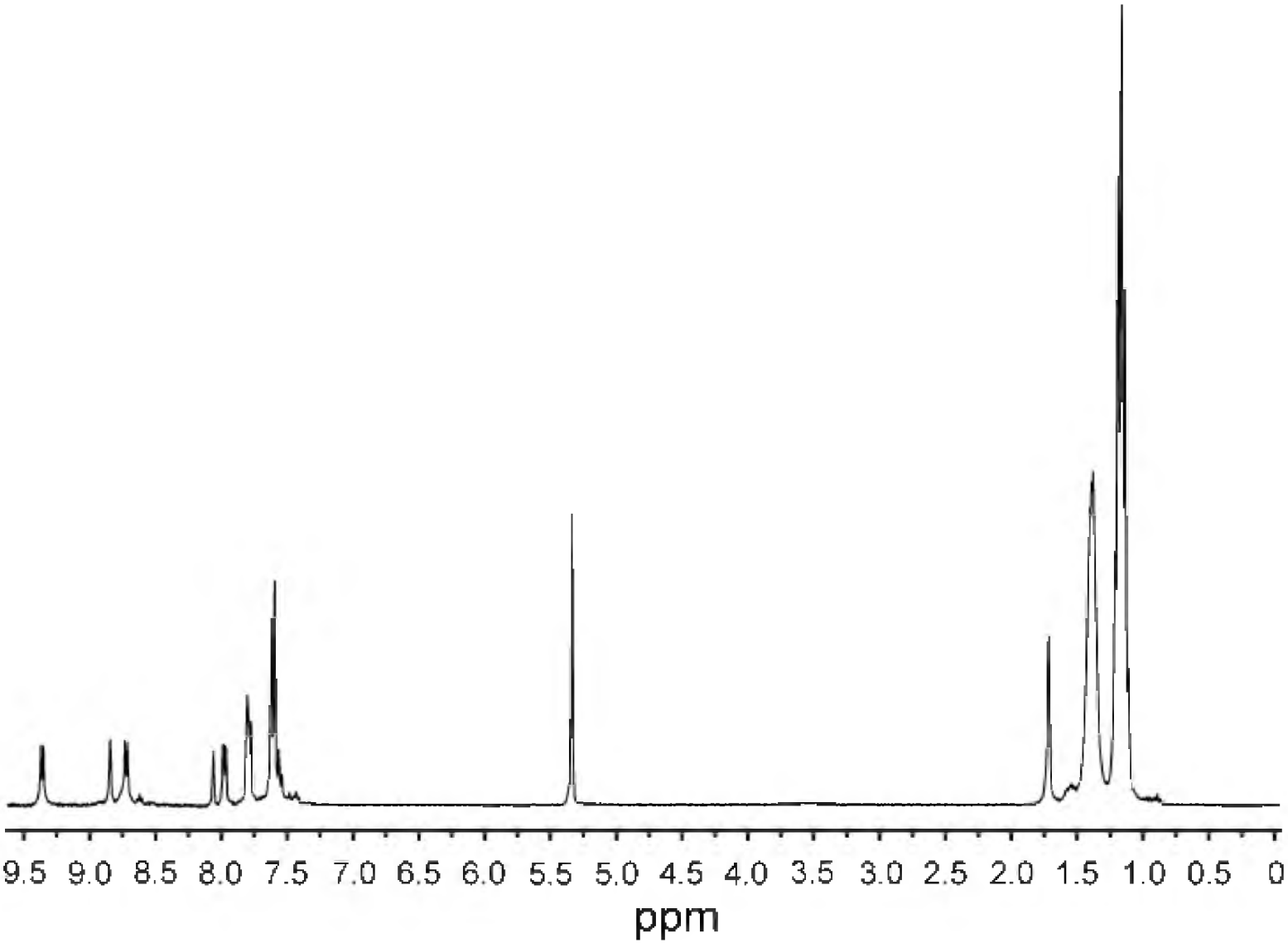

Figure A.28: ^{1}H NMR spectra of **3.12**.

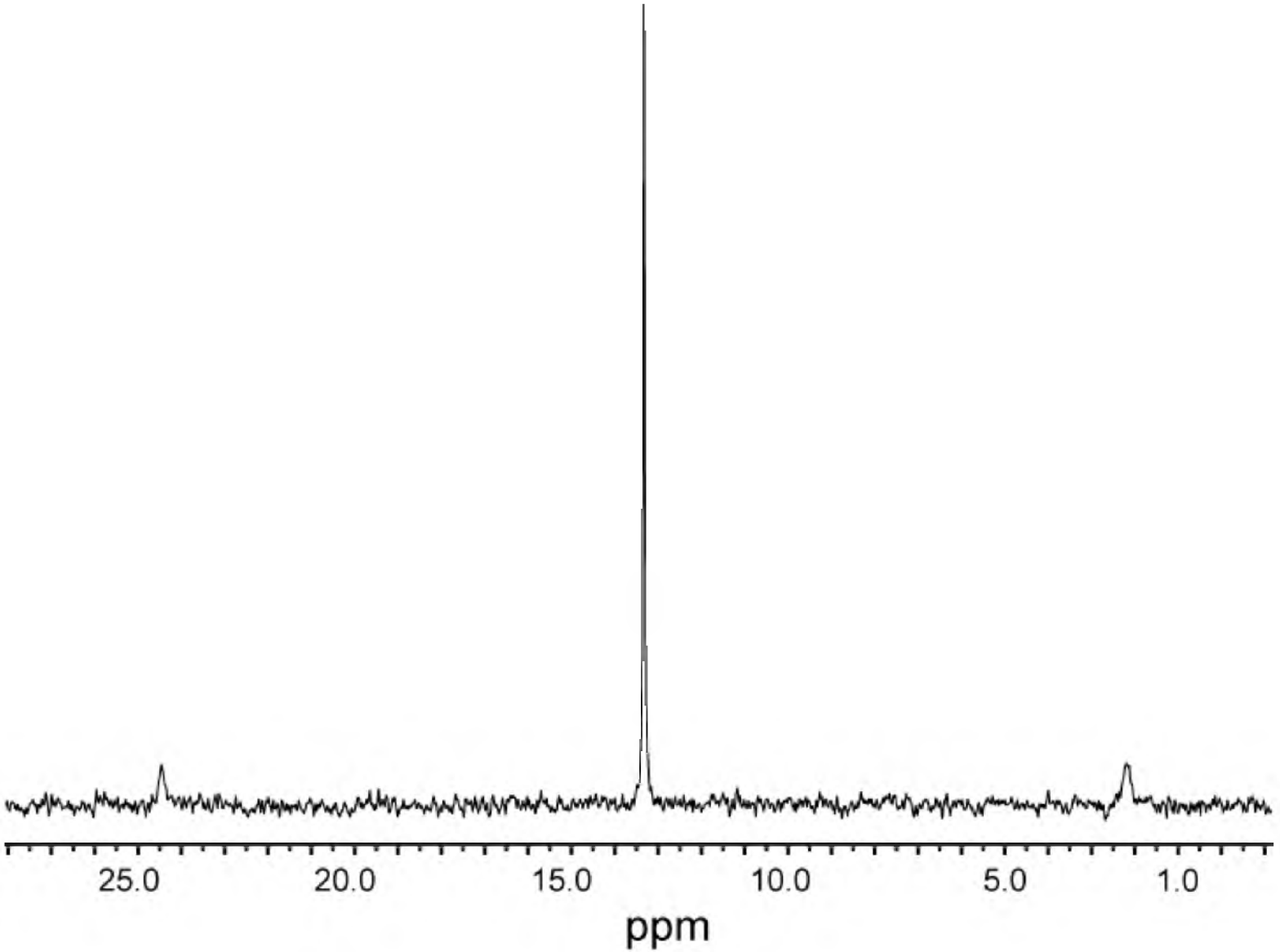

Figure A.29: $^{31}P\{^{1}H\}$ NMR spectra of **3.12**.

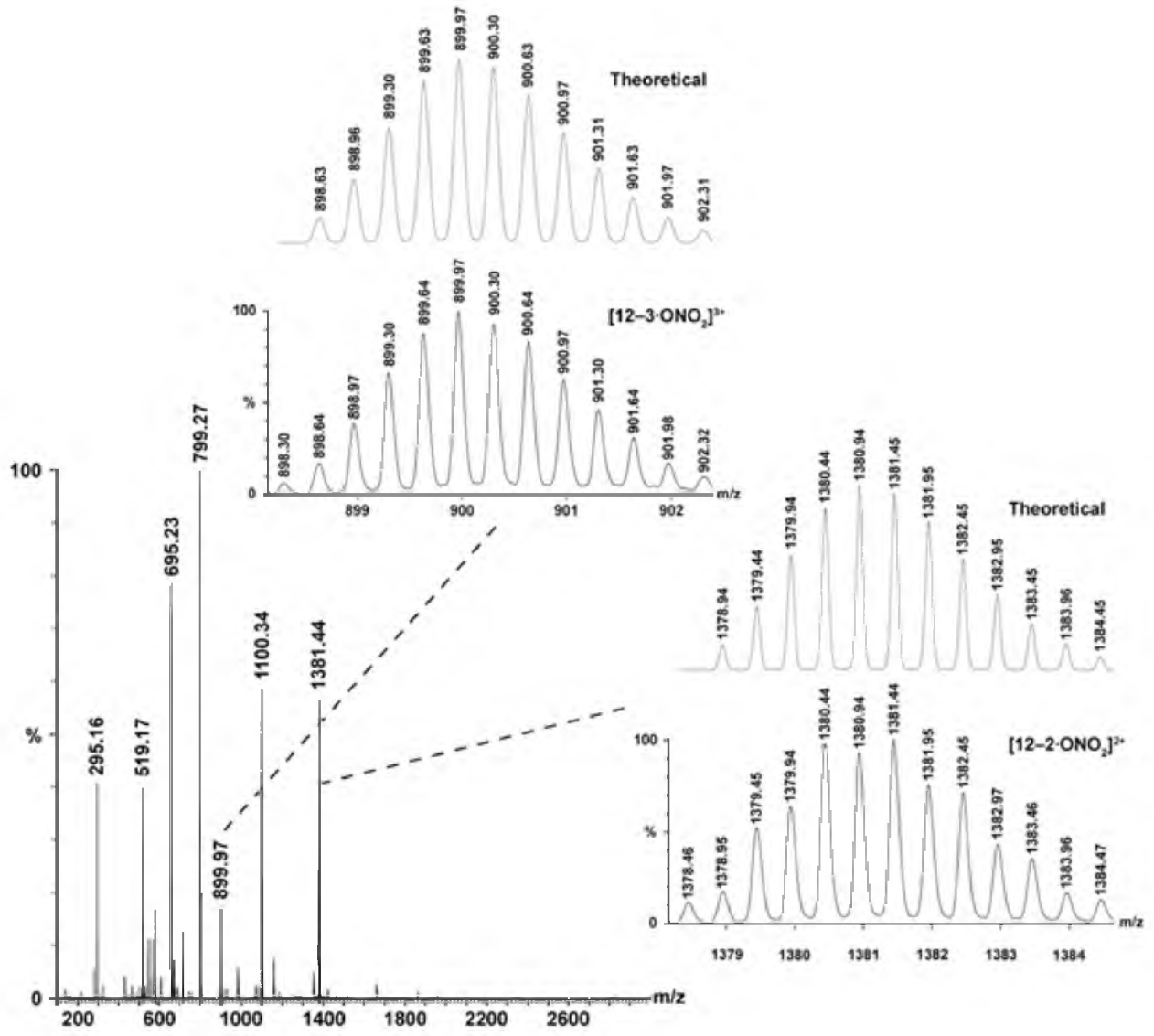

Figure A.30: ESI-MS spectra of the $[M–2•ONO_2]^{2+}$ and $[M–3•ONO_2]^{3+}$ charge states for **3.12**.

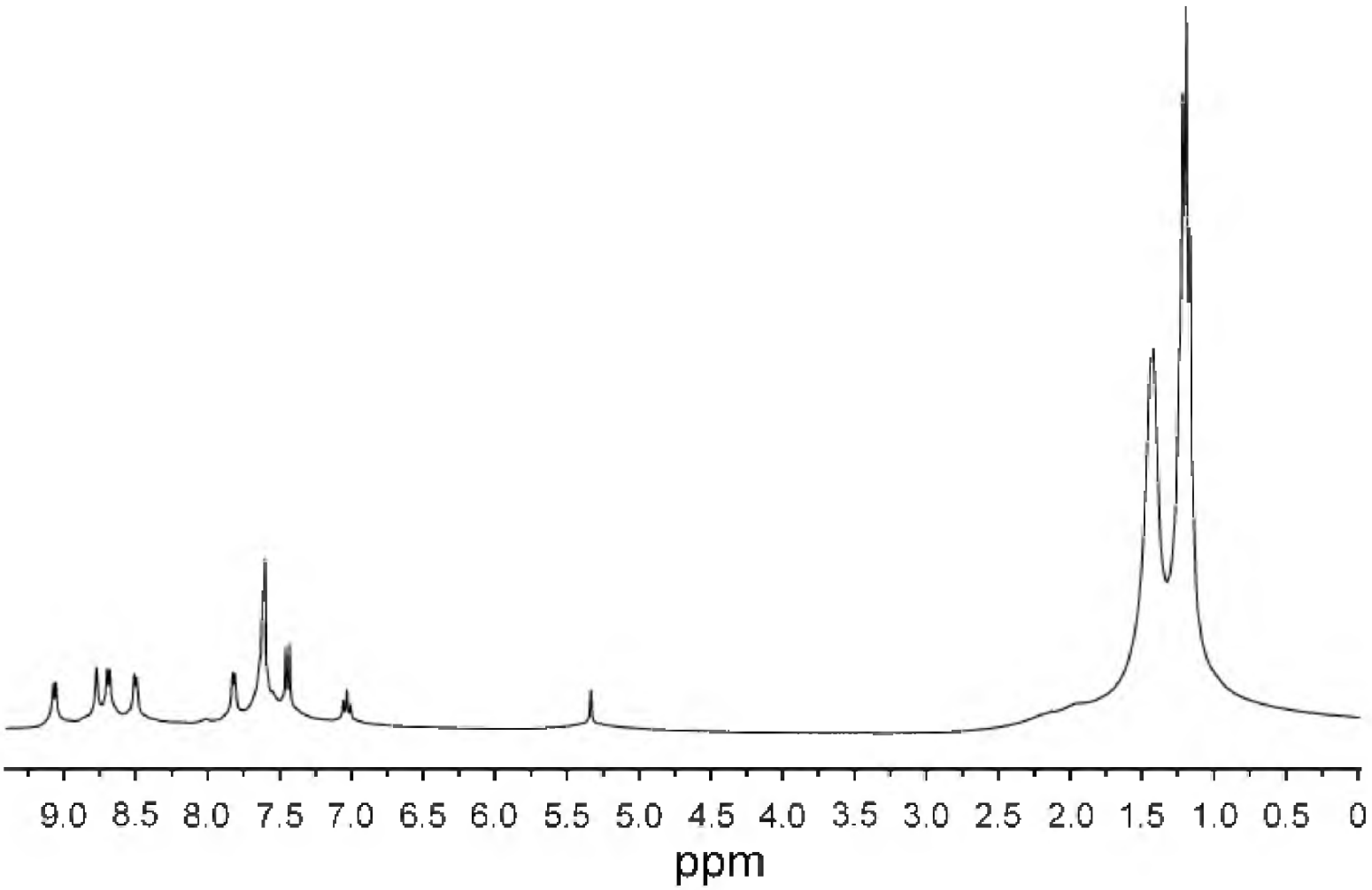

Figure A.31: ^{1}H NMR spectra of **3.13**.

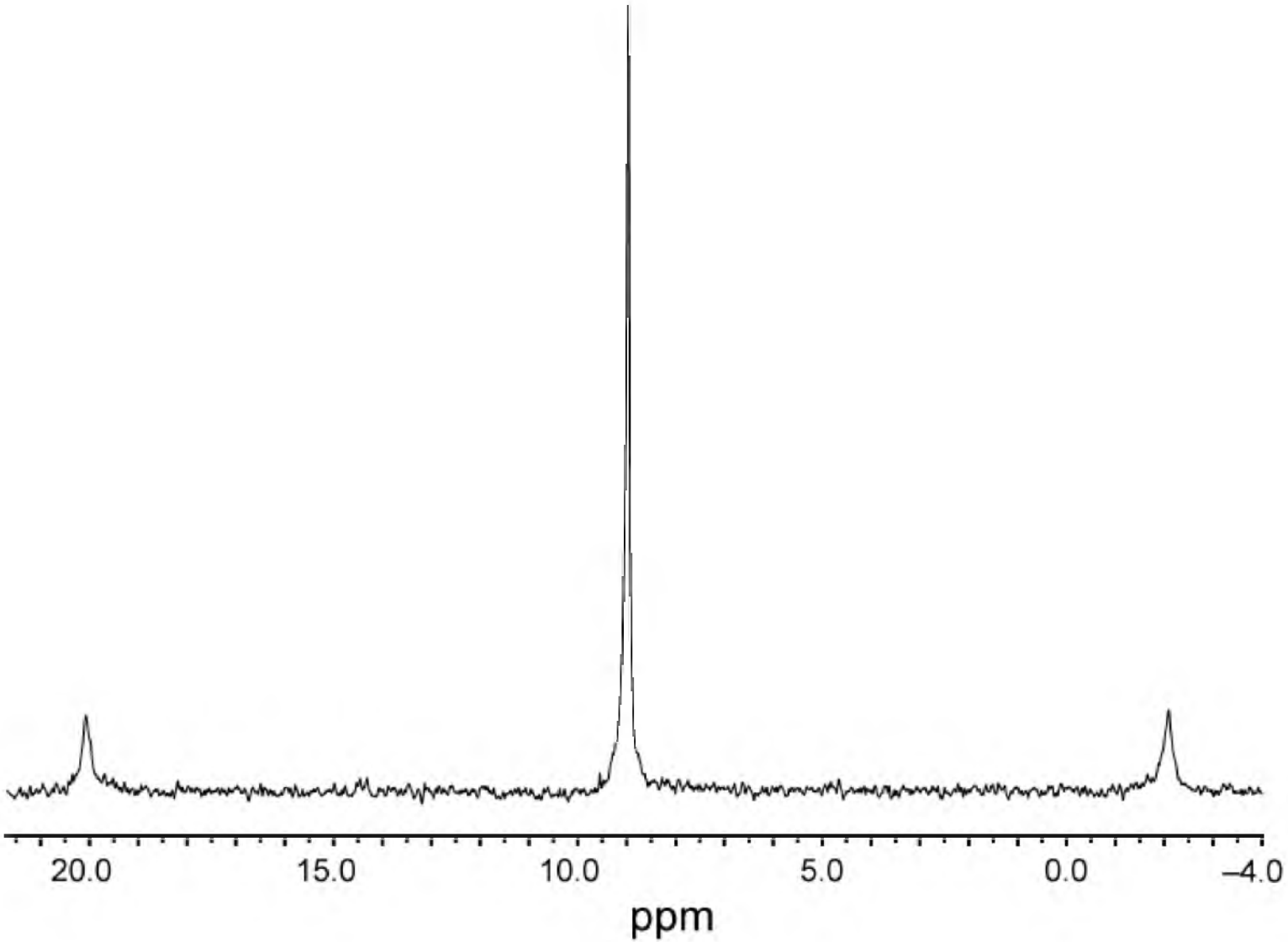

Figure A.32: $^{31}P\{^{1}H\}$ NMR spectra of **3.13**.

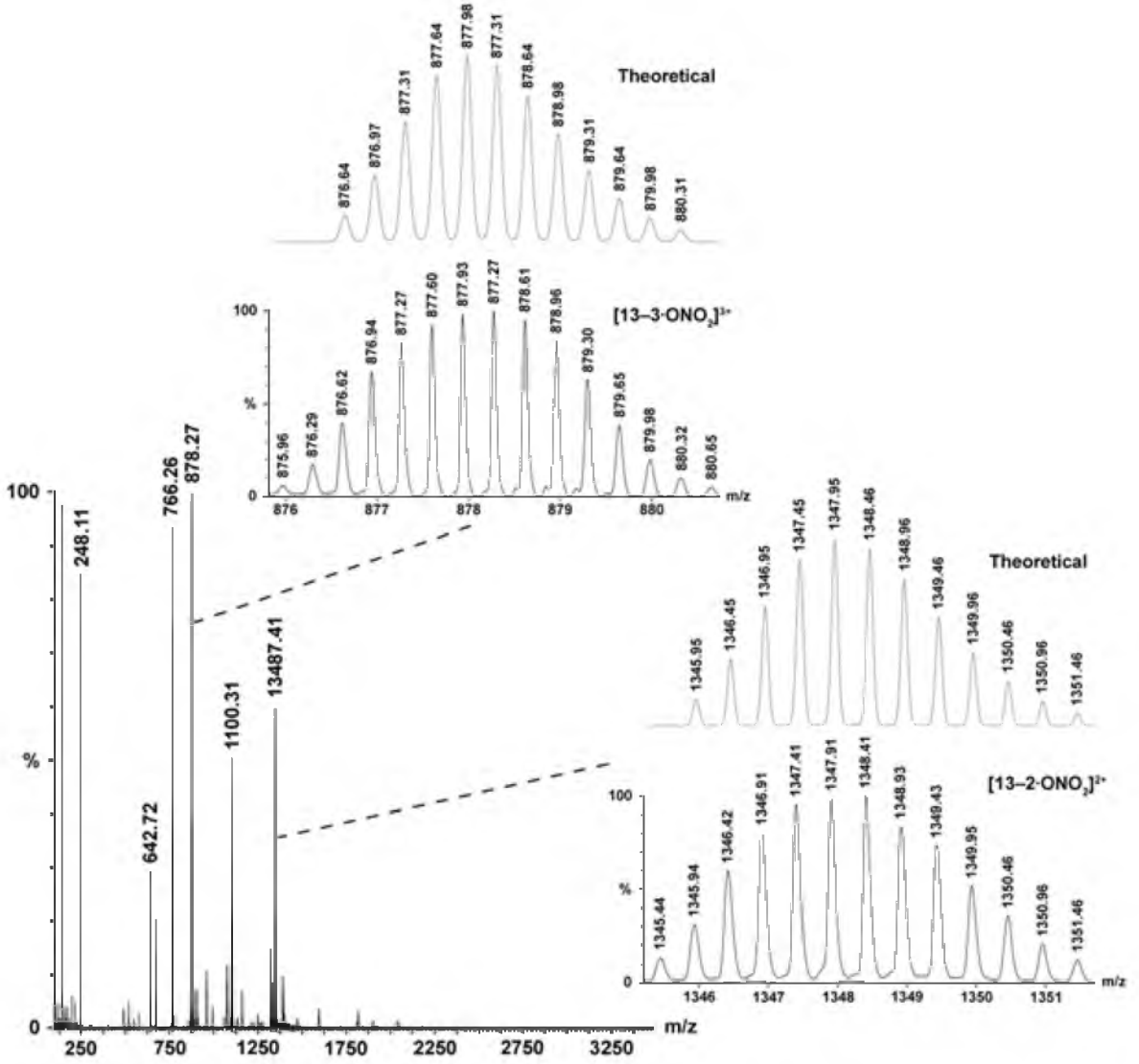

Figure A.33: ESI-MS spectra of the $[M–2•ONO_2]^{2+}$ and $[M–3•ONO_2]^{3+}$ charge states for **3.13**.

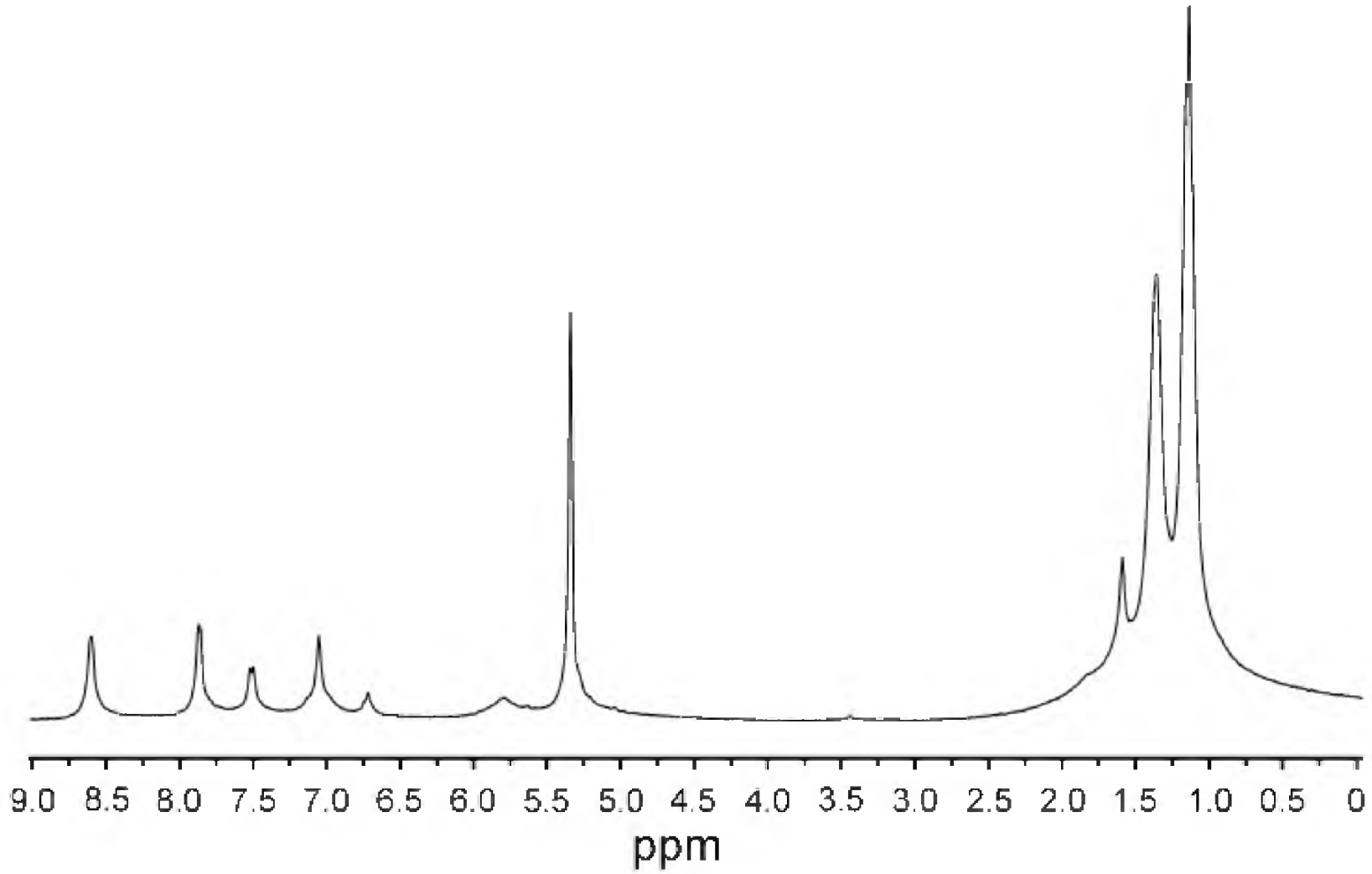

Figure A.34: ^{1}H NMR spectra of **3.14**.

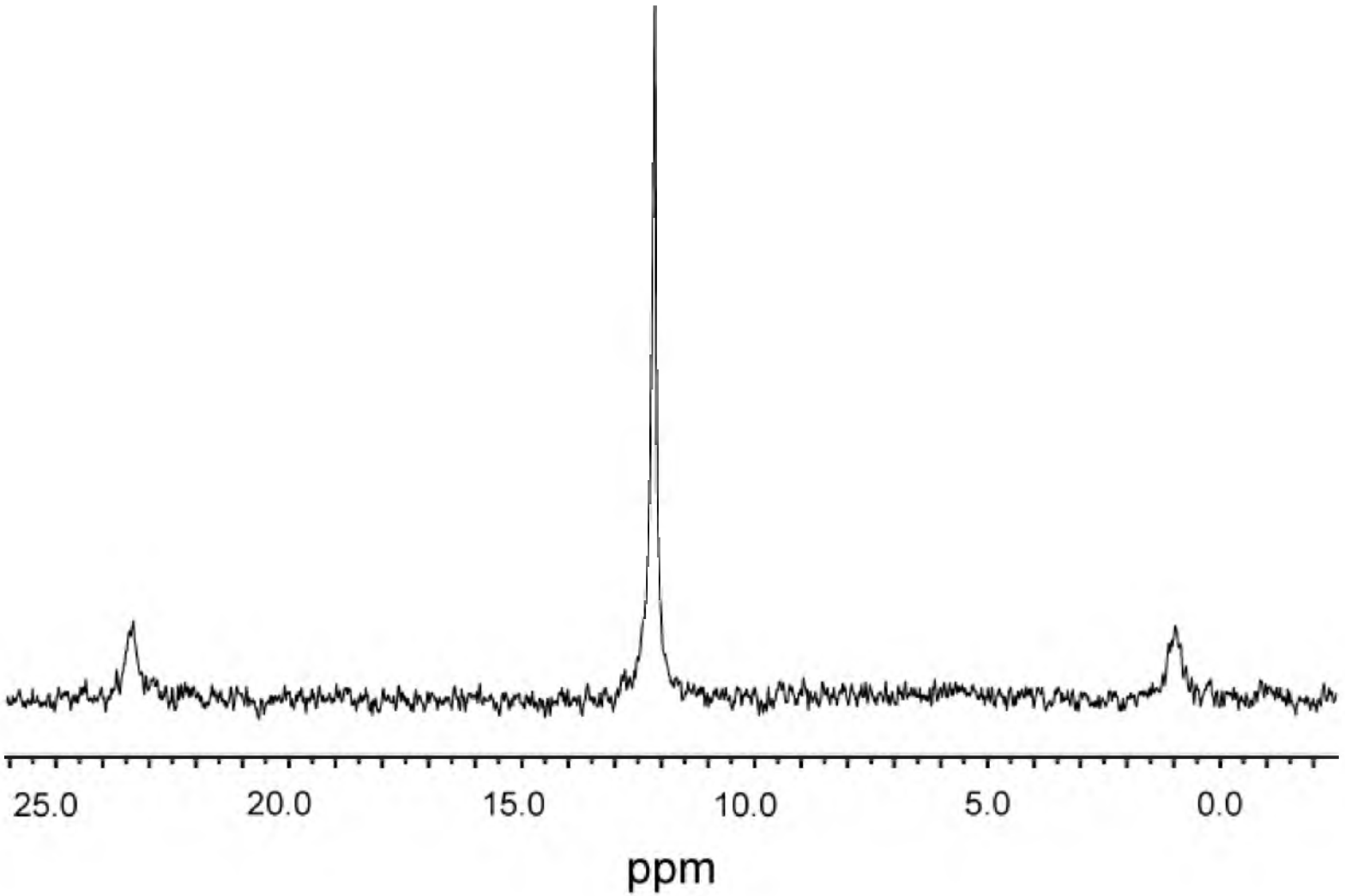

Figure A.35: $^{31}P\{^{1}H\}$ NMR spectra of **3.14**.

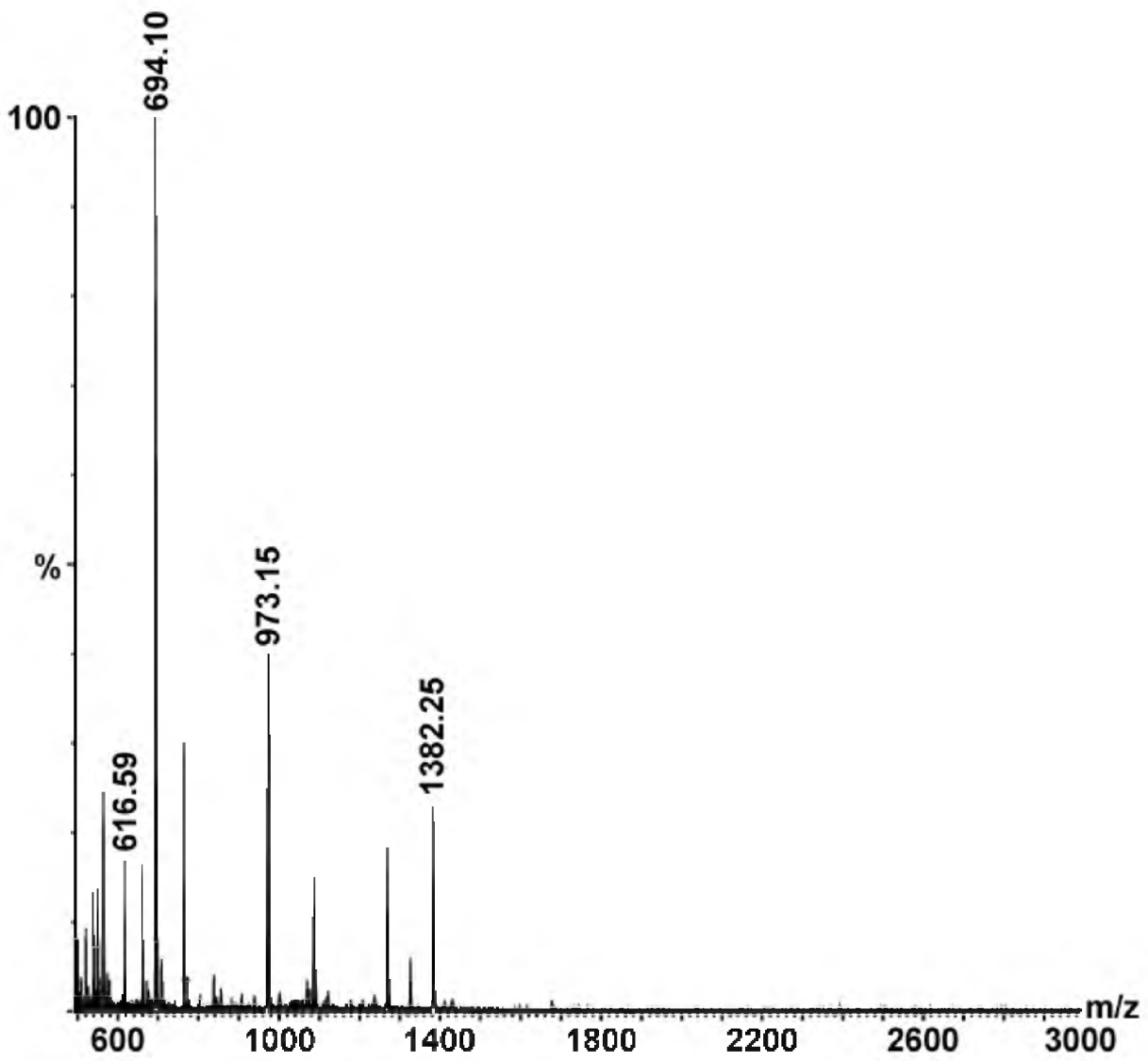

Figure A.36: ESI-MS spectrum of **3.14**.

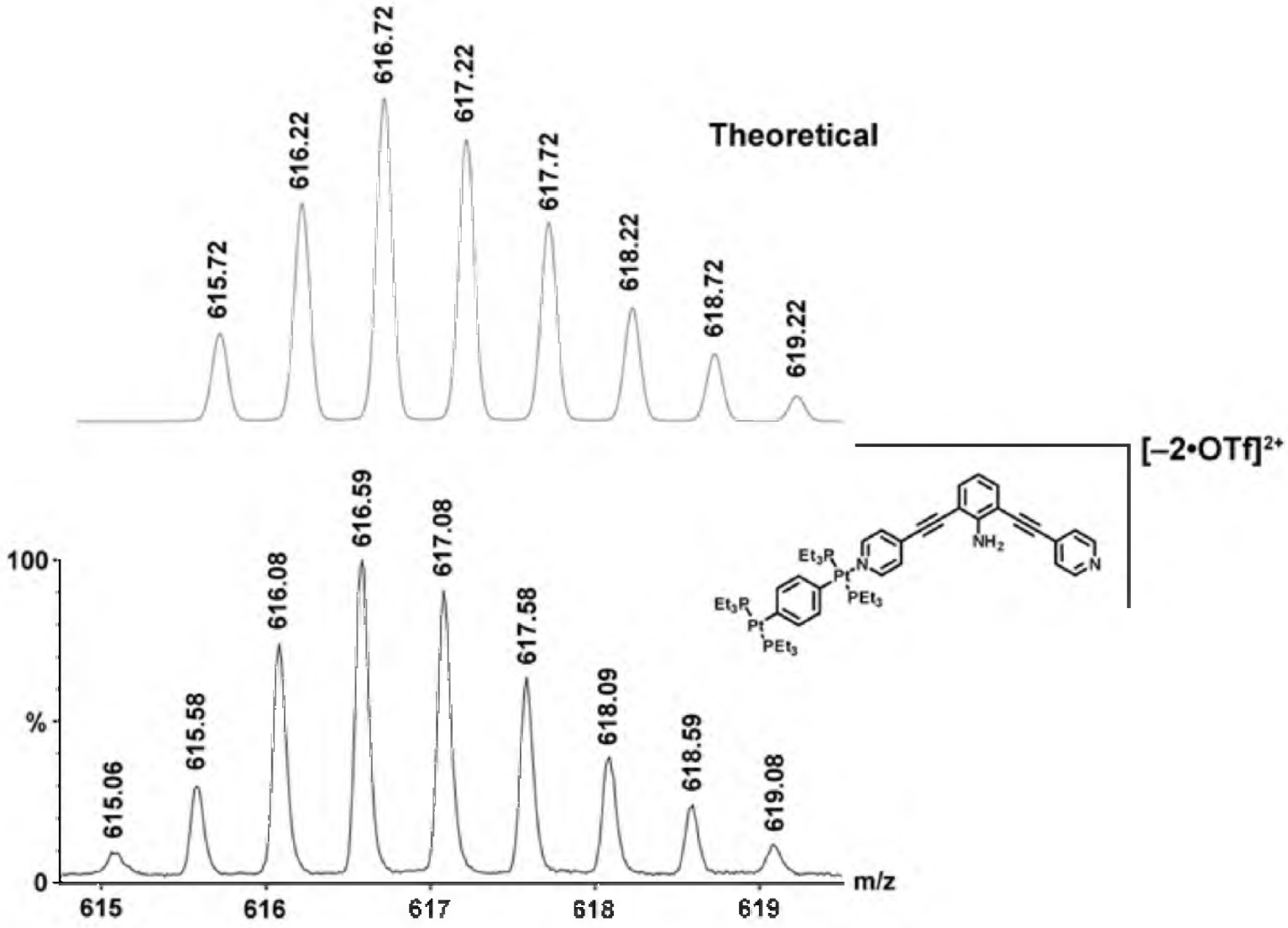

Figure A.37: ESI-MS spectrum of a fragment of **3.14**.

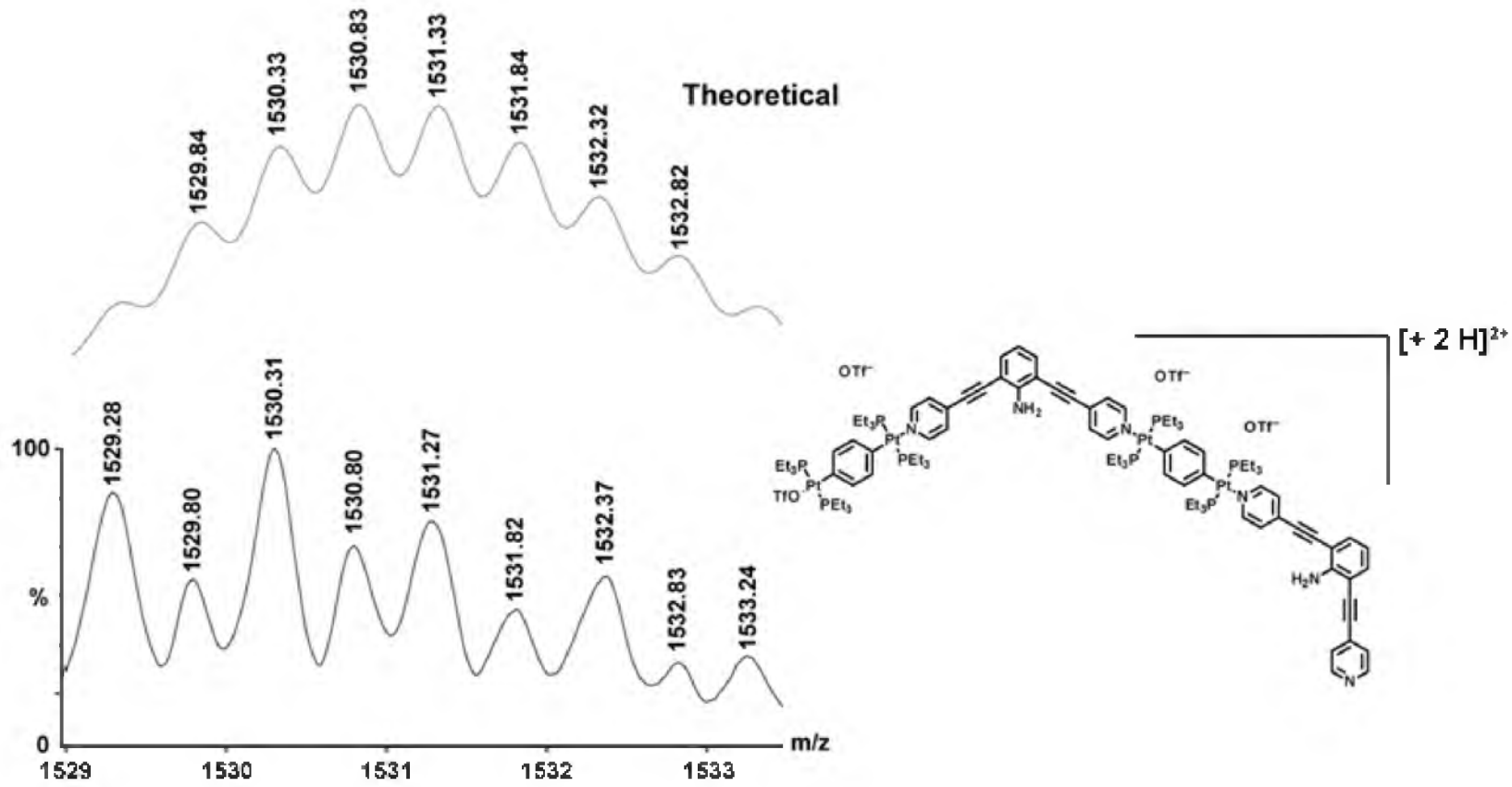

Figure A.38: ESI-MS spectrum of a fragment of **3.14**.

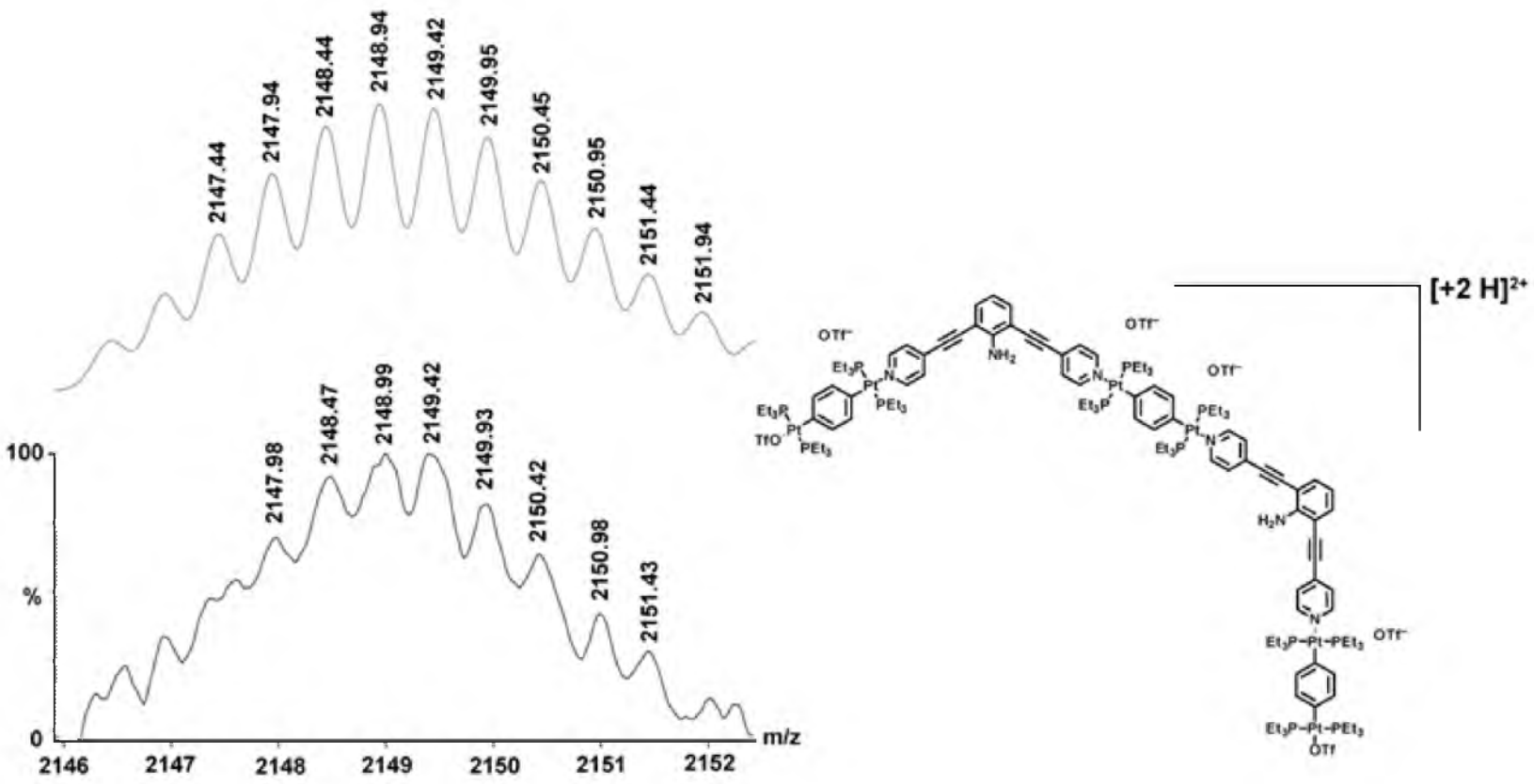

Figure A.39: ESI-MS Spectrum of a fragment of **3.14**.

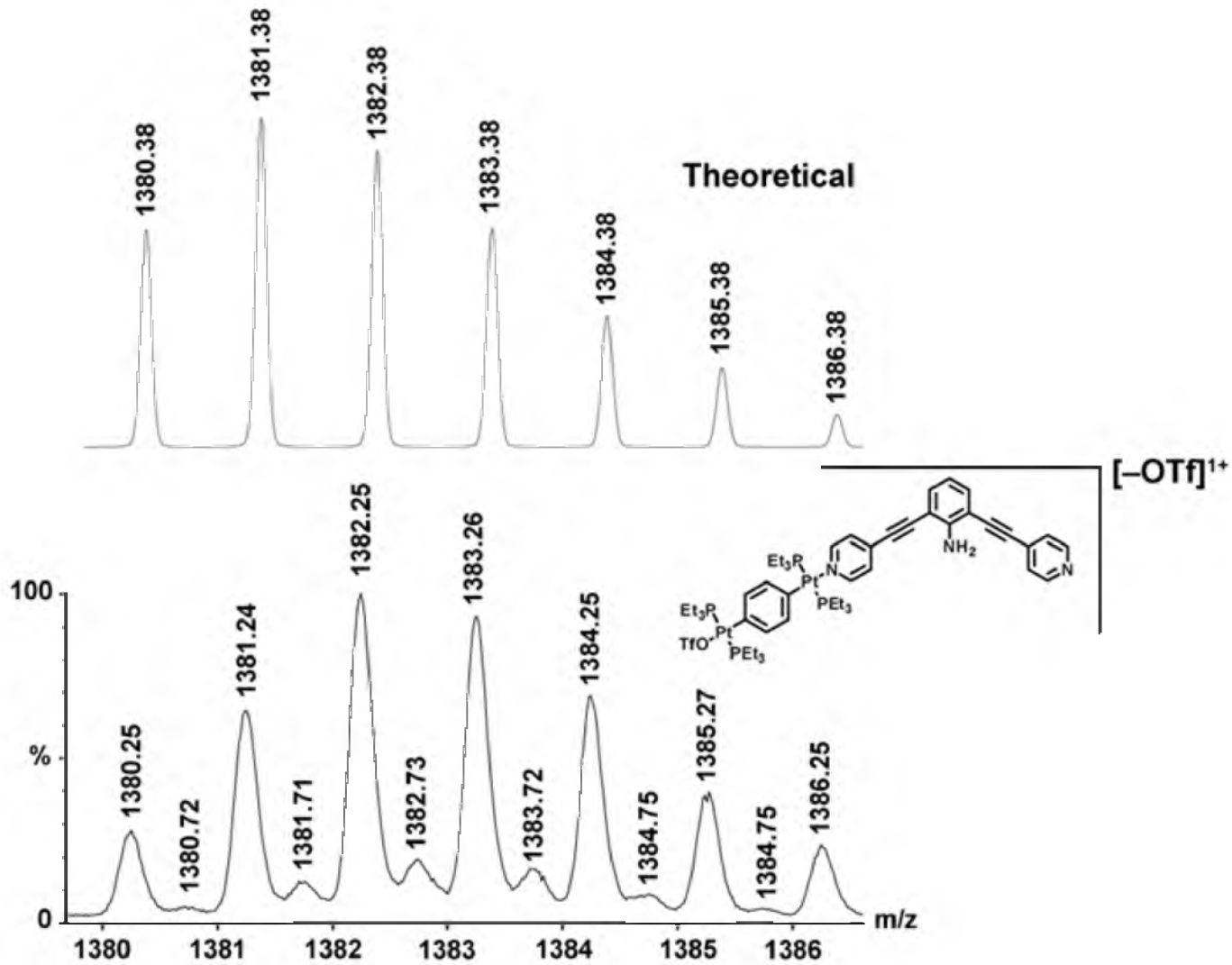

Figure A.40: ESI-MS Spectrum of a fragment of **3.14**.

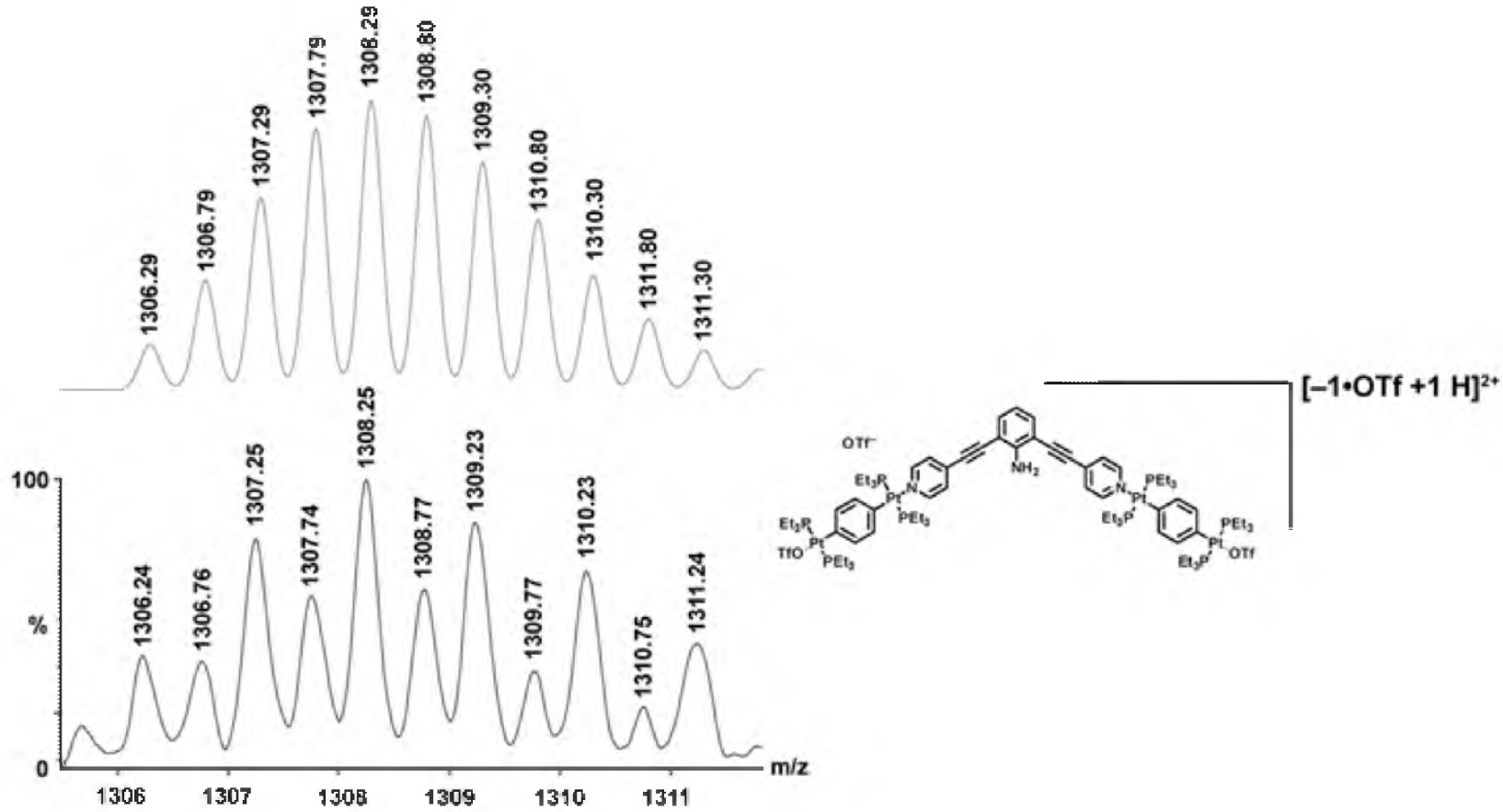

Figure A.41: ESI-MS Spectrum of a fragment of **3.14**.

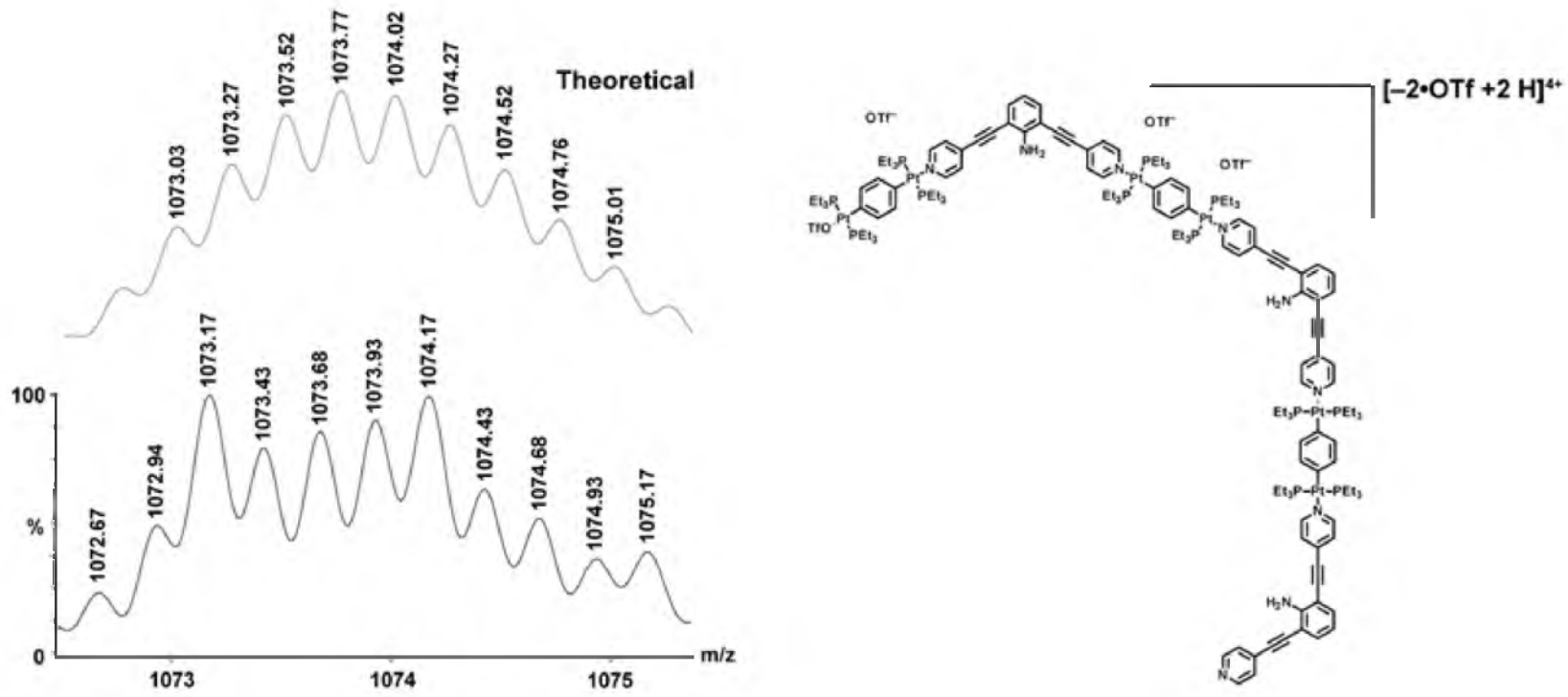

Figure A.42: ESI-MS Spectrum of a fragment of **3.14**.

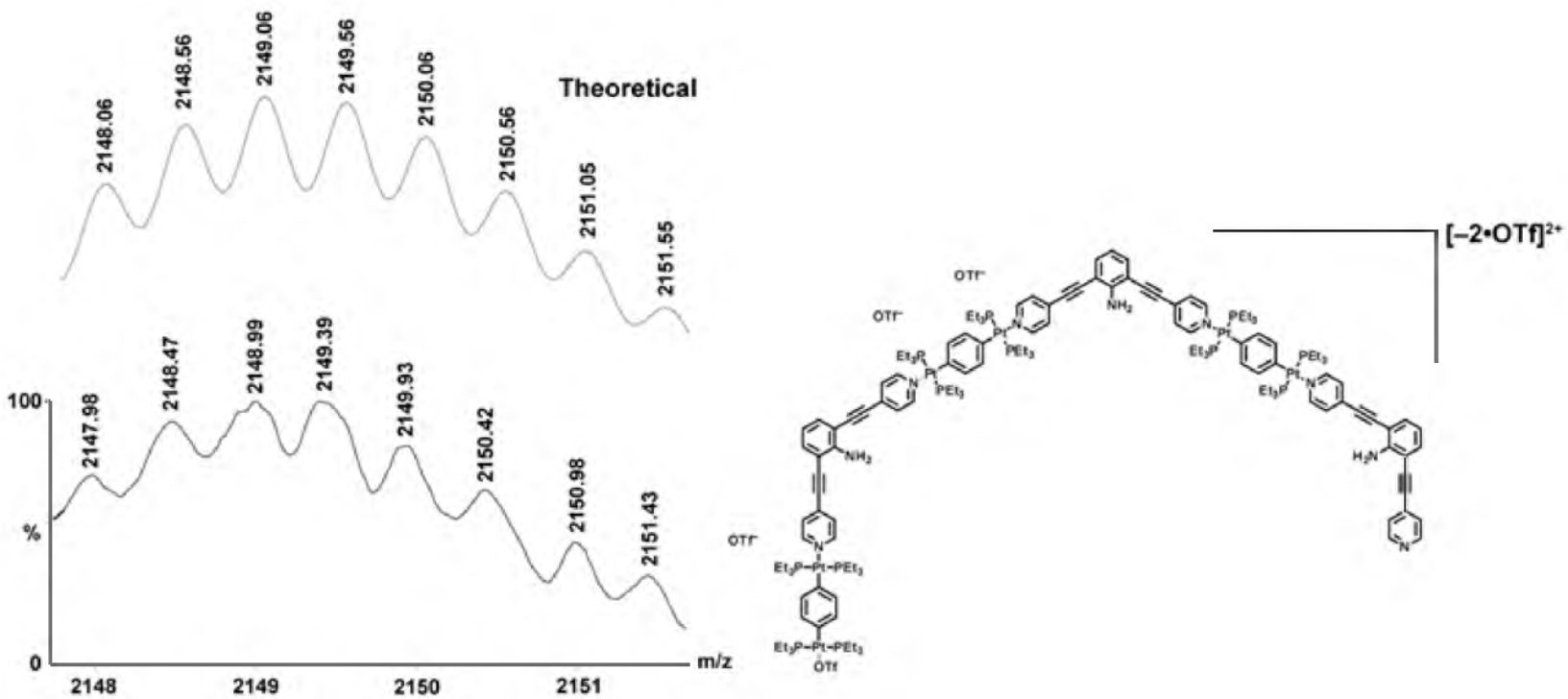

Figure A.43: ESI-MS Spectrum of a fragment of **3.14**.

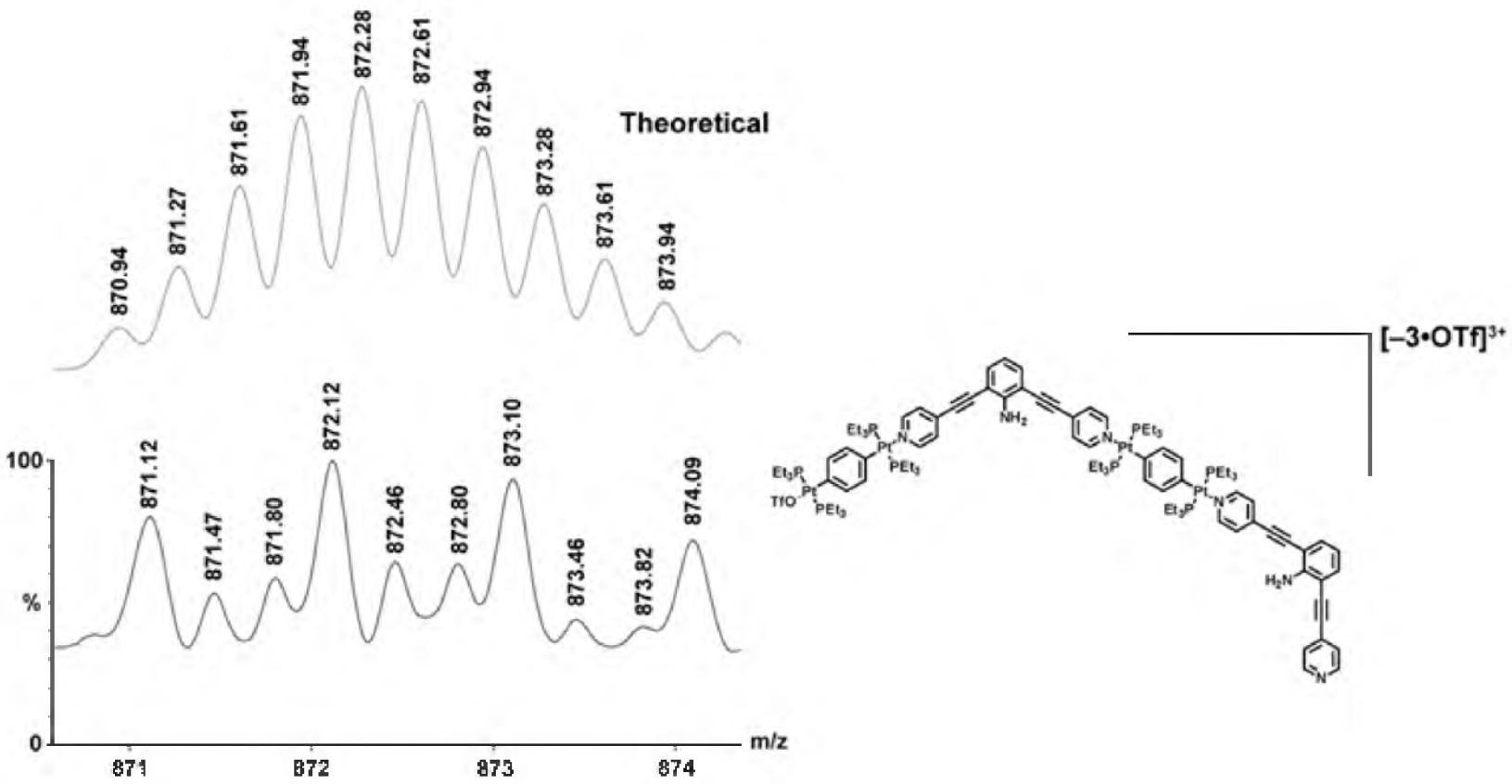

Figure A.44: ESI-MS Spectrum of a fragment of **3.14**.

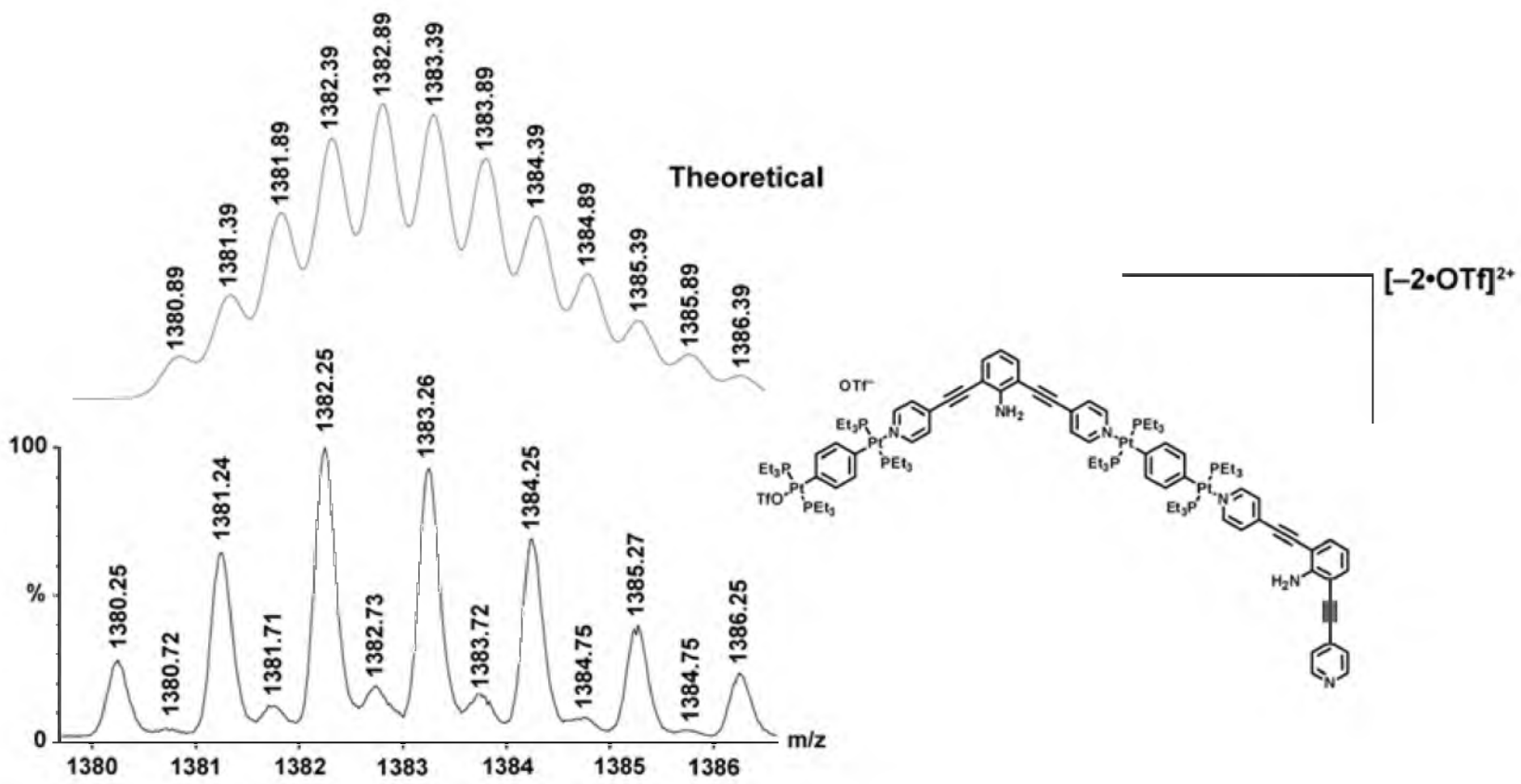

Figure A.45: ESI-MS Spectrum of a fragment of **3.14**.

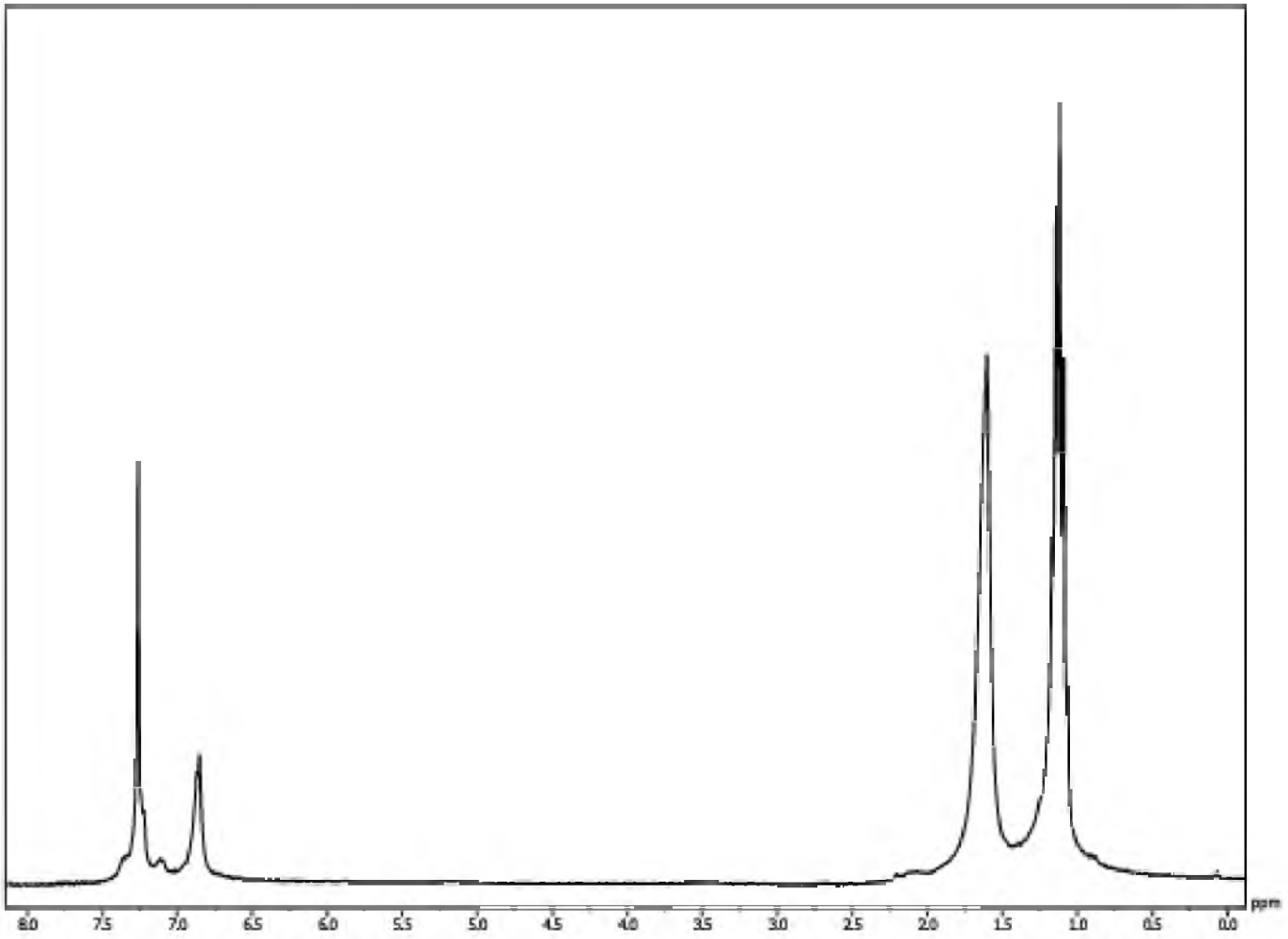

Figure A.46: ^{1}H NMR spectra of **4.03**.

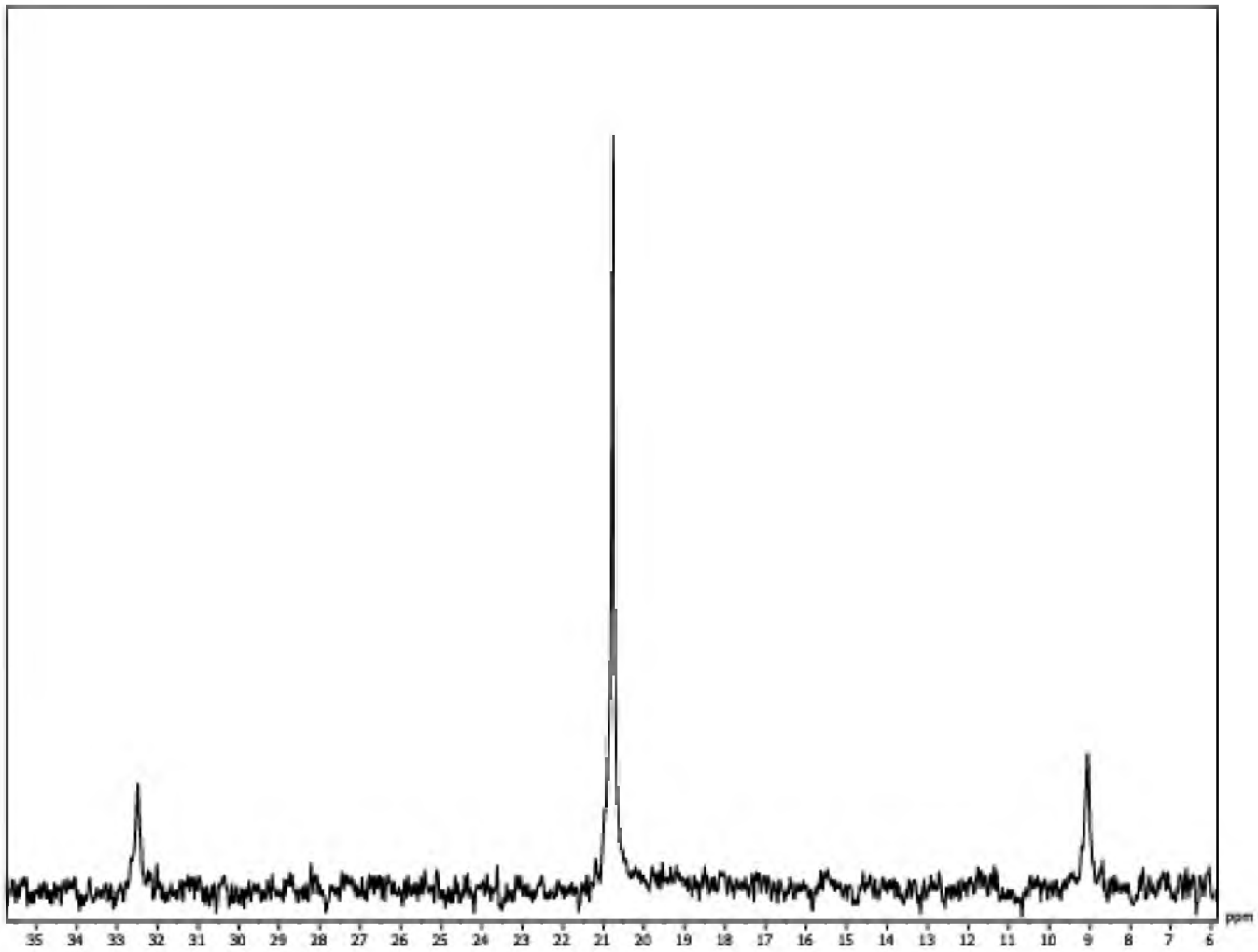

Figure A.47: $^{31}P\{^{1}H\}$ NMR spectra of **4.03**.

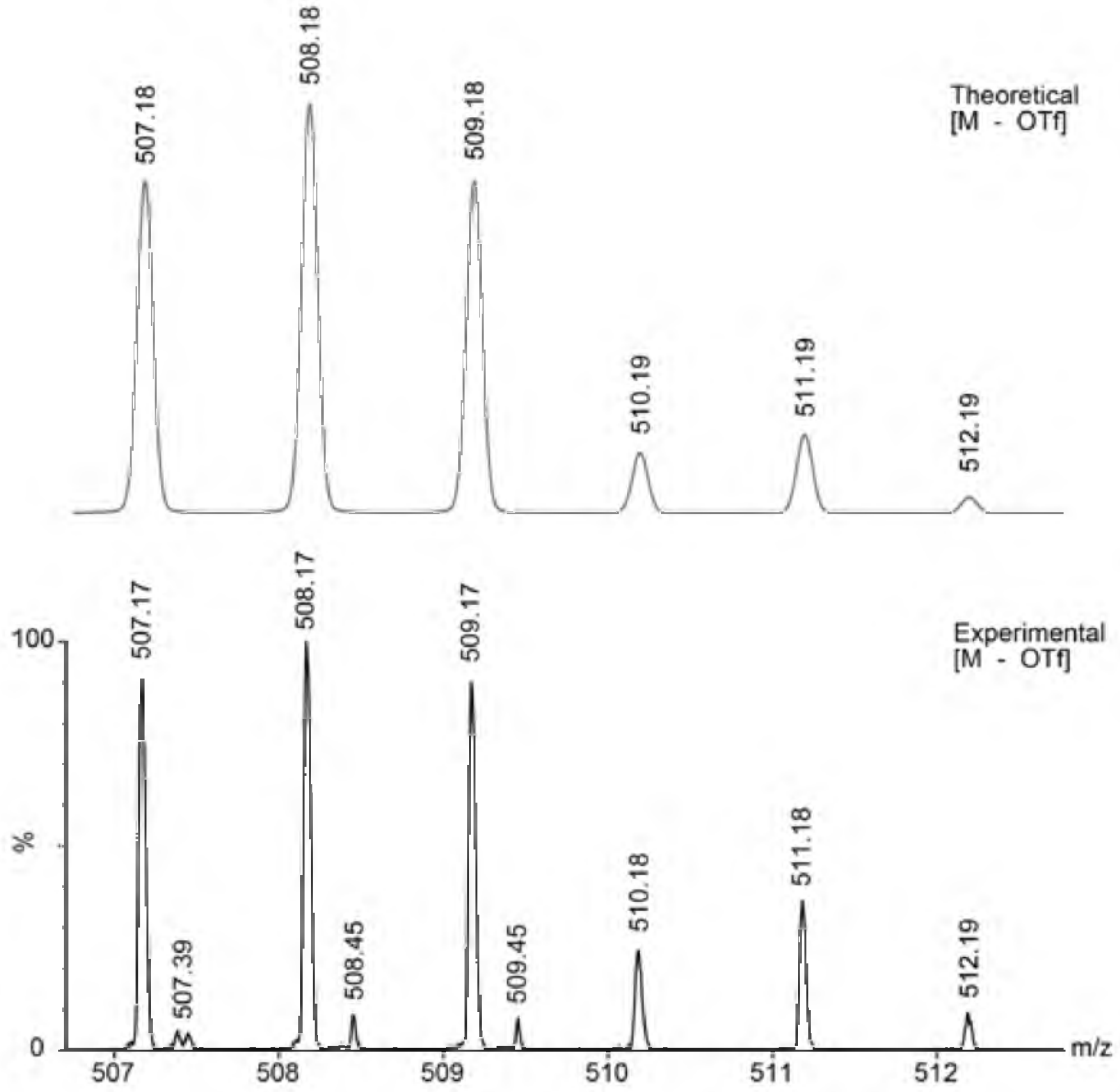

Figure A.48: ESI-MS spectrum of the $[M–OTf]^{1+}$ charge state of **4.03**.

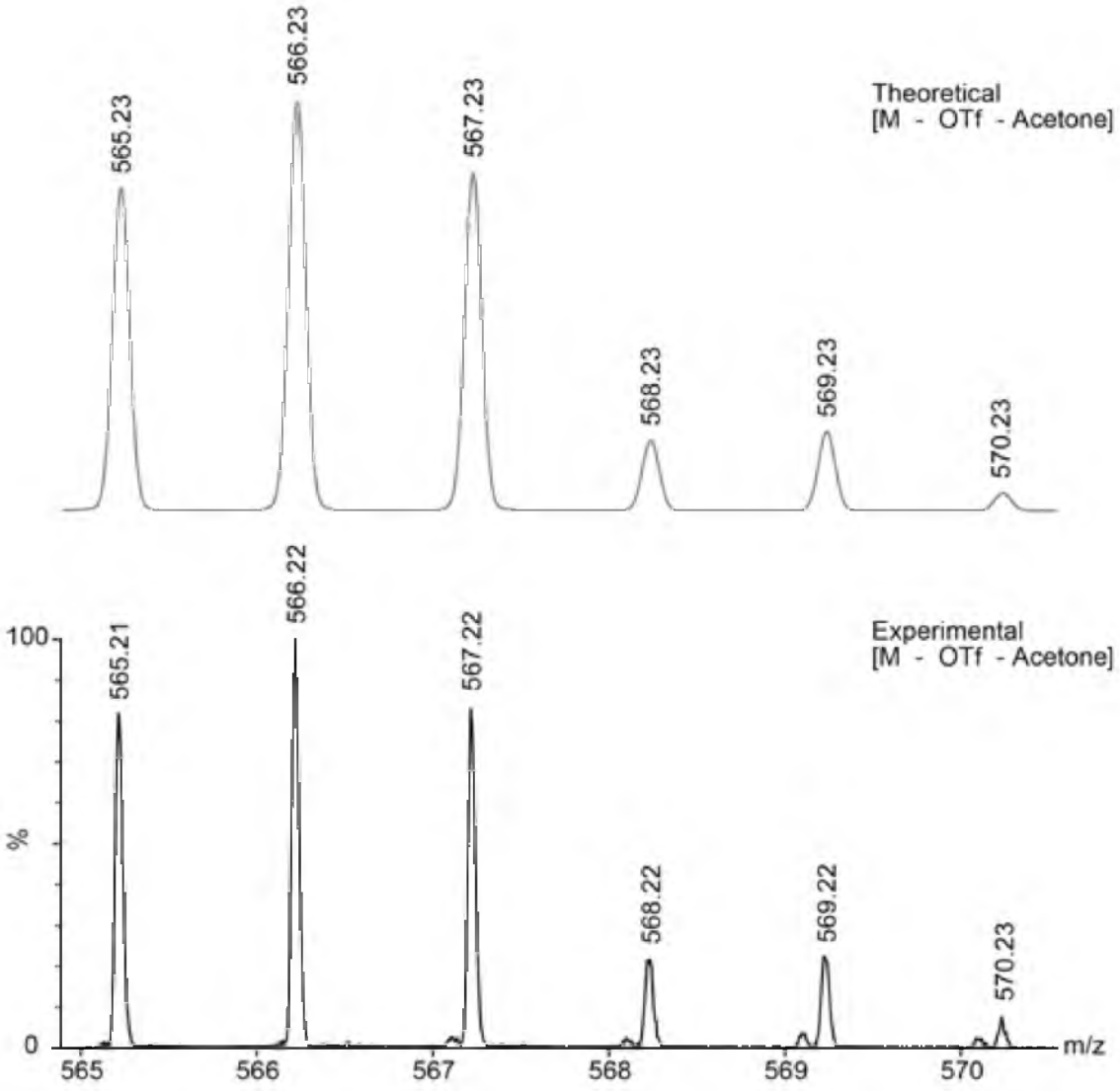

Figure A.49: ESI-MS spectrum of the [M–OTf–Acetone] charge state of **4.03**.

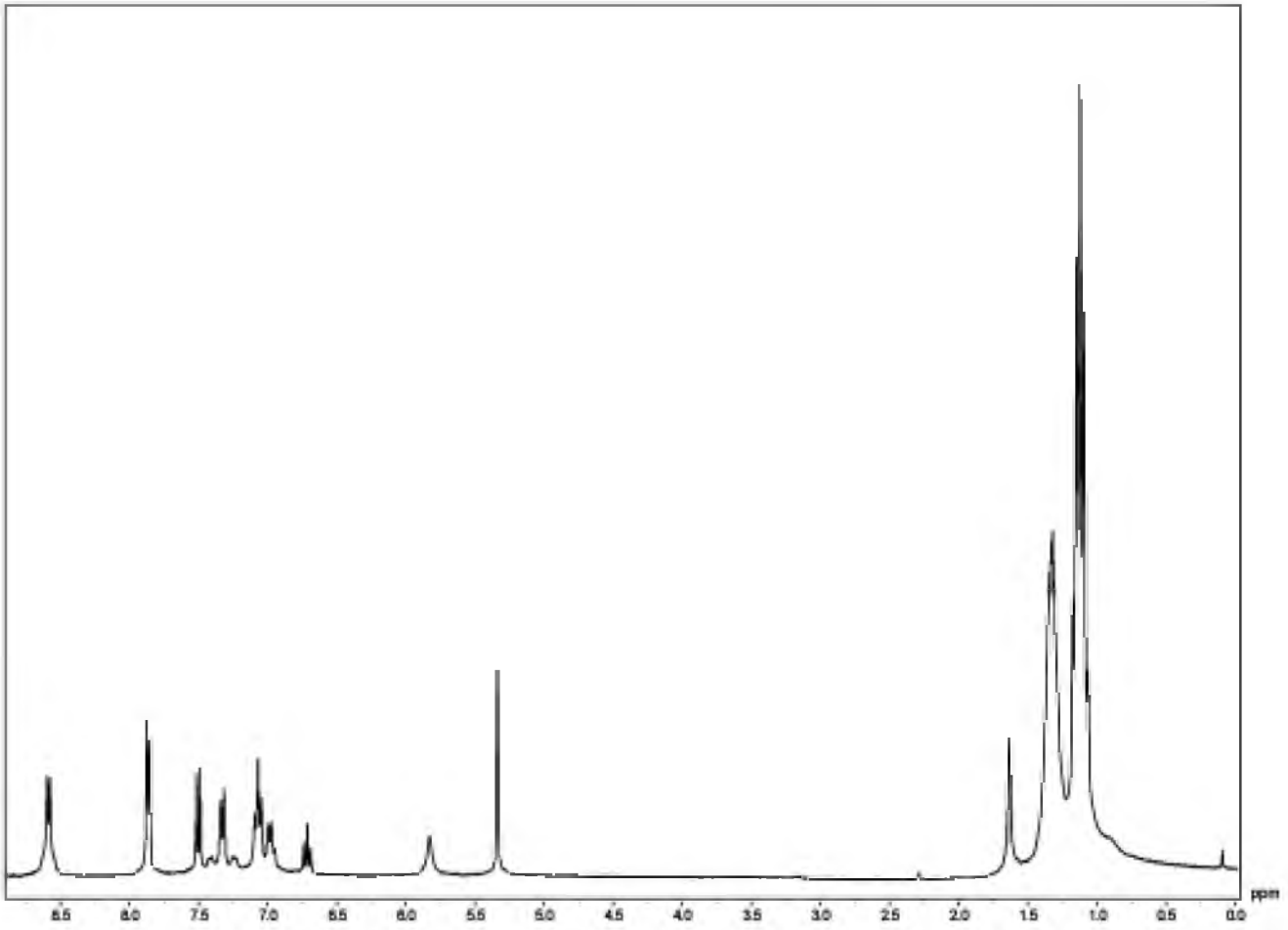

Figure A.50: ^{1}H NMR spectra of **4.04**.

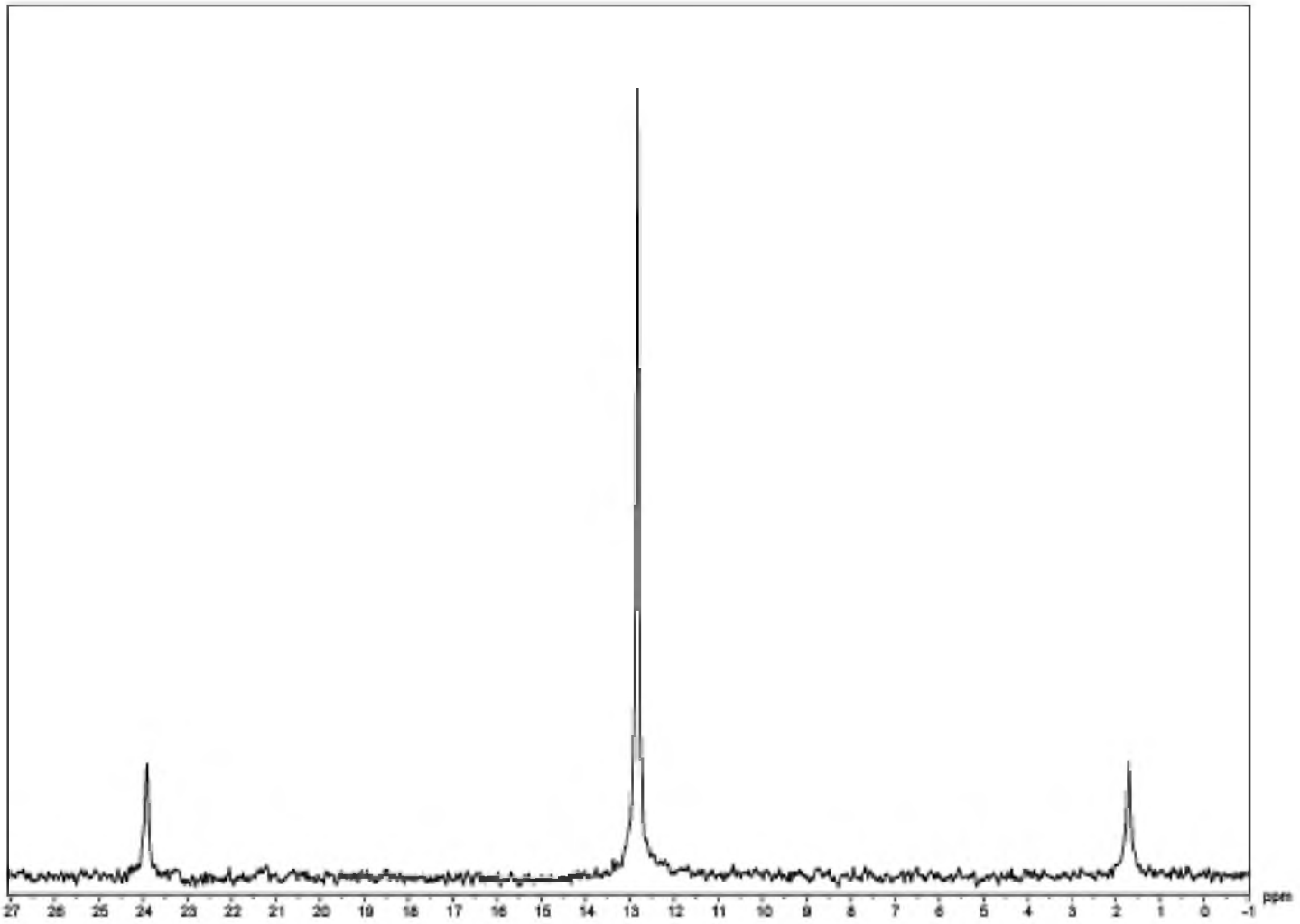

Figure A.51: $^{31}P\{^{1}H\}$ NMR spectra of **4.04**.

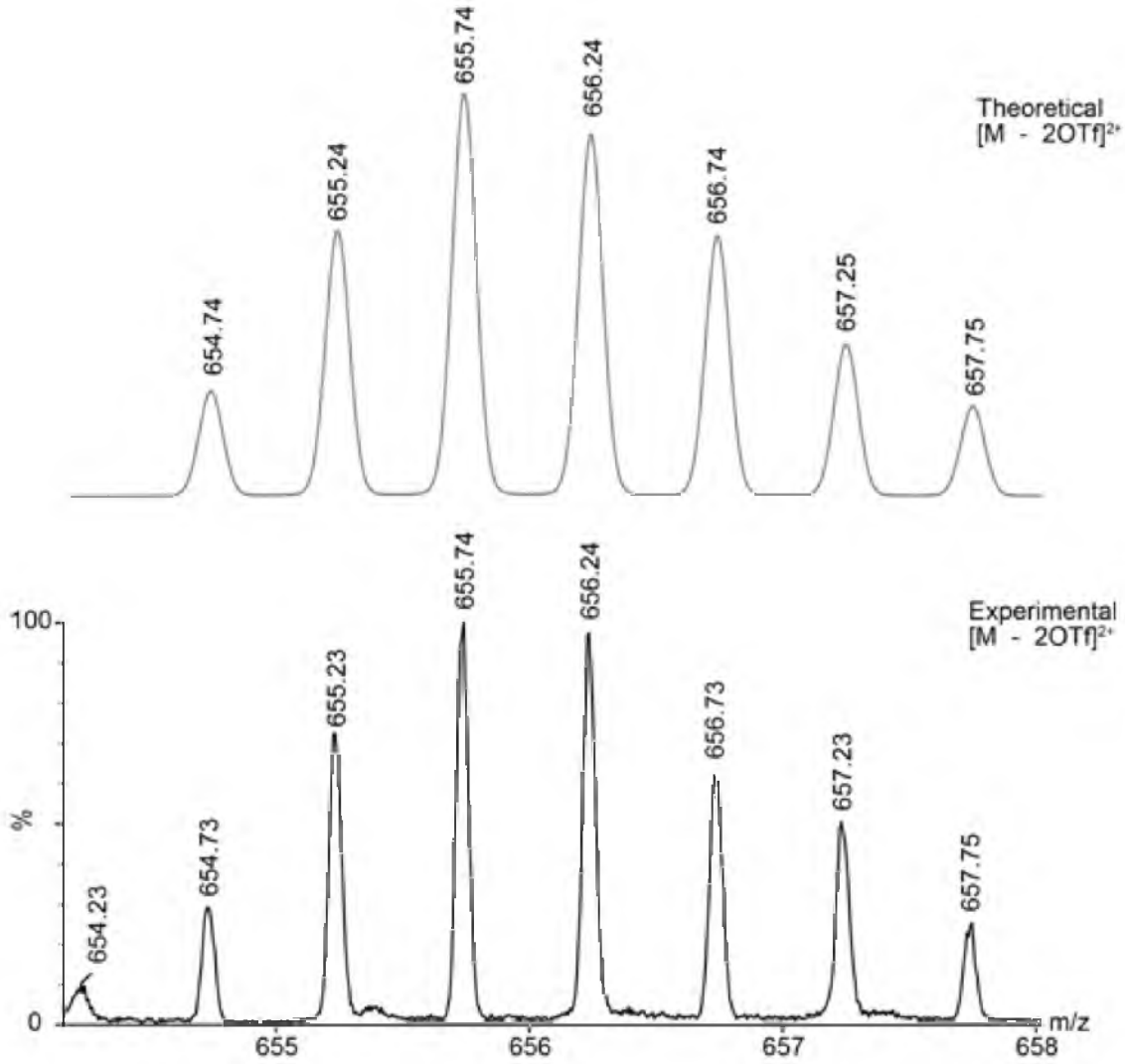

Figure A.52: ESI-MS spectrum of the $[M–2•OTf]^{2+}$ charge state of **4.04**.

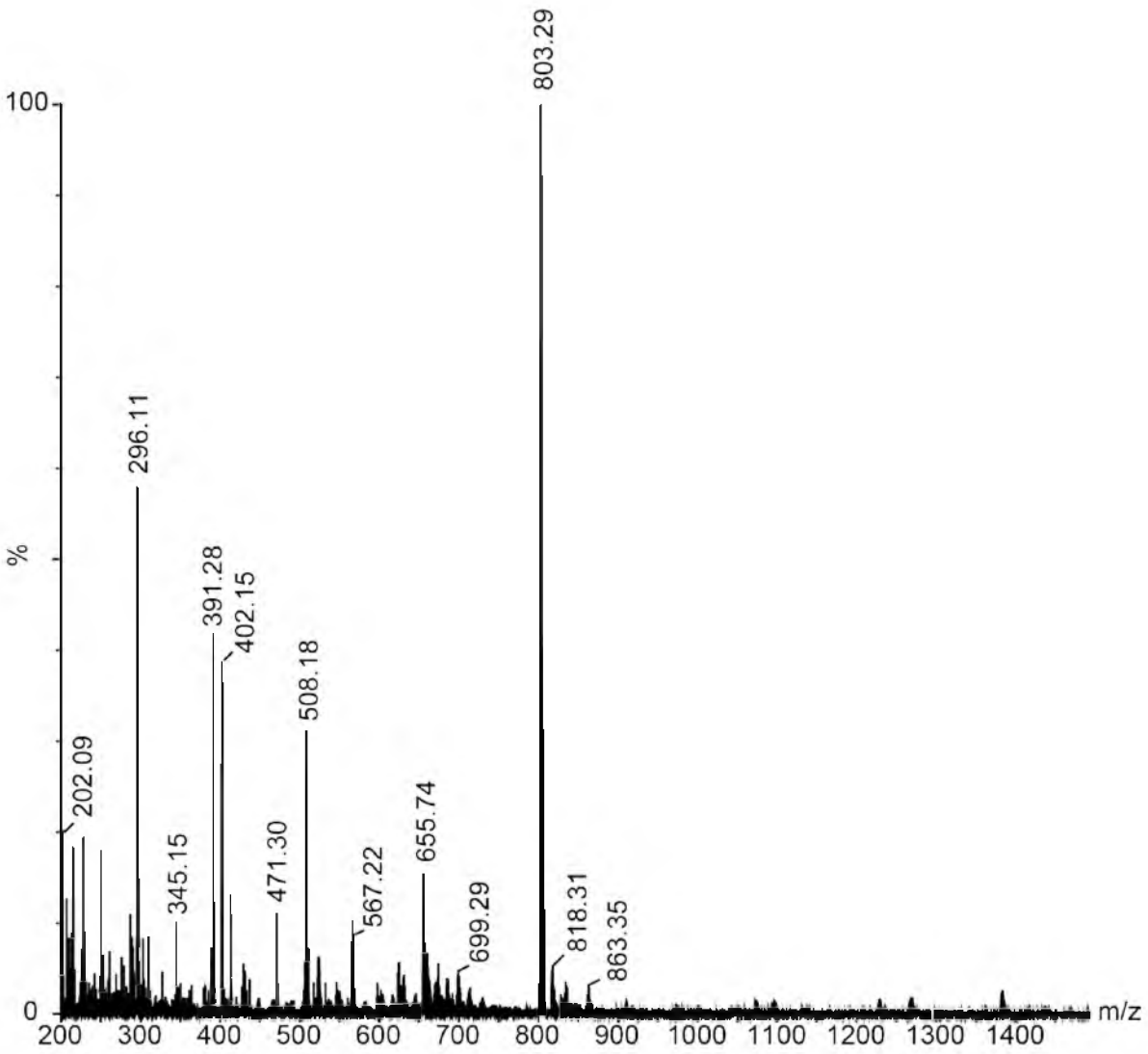

Figure A.53: ESI-MS spectrum of **4.04**.

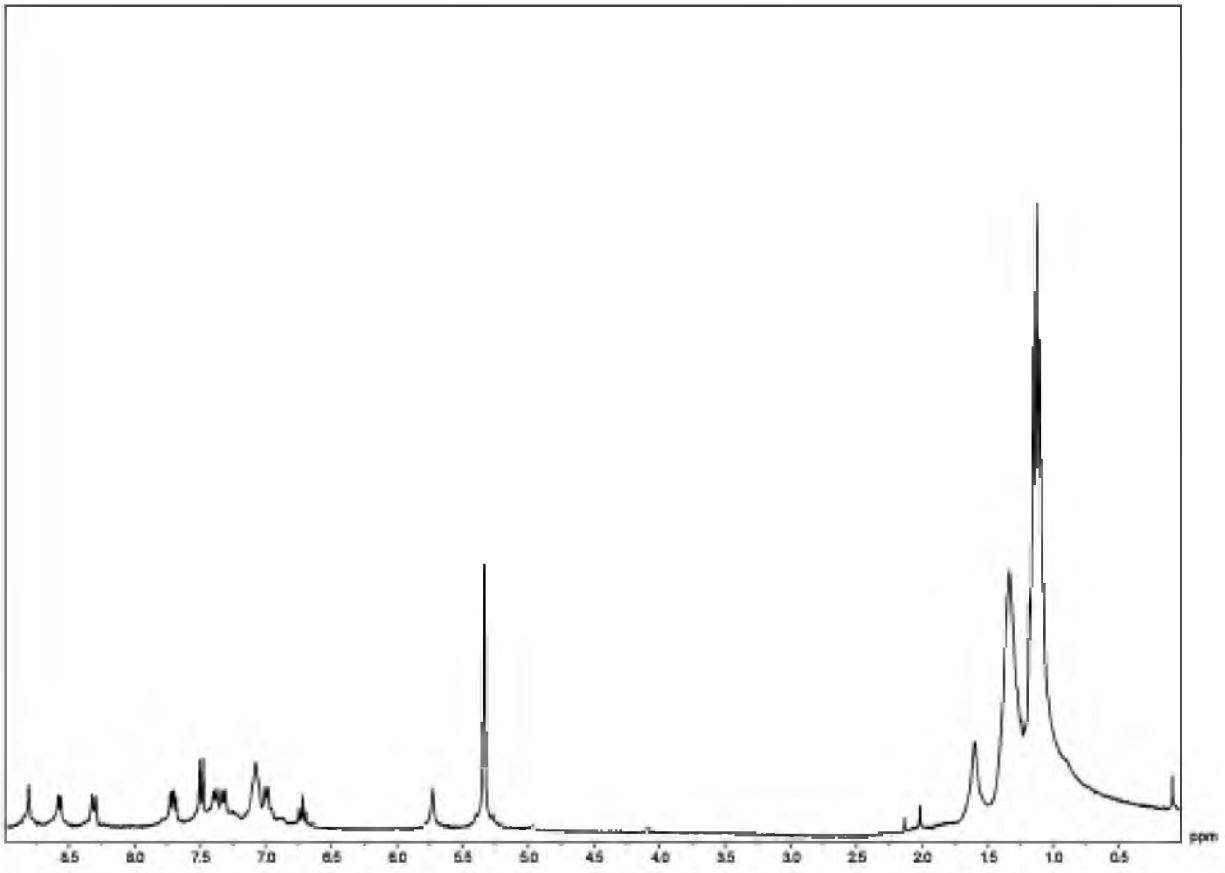

Figure A.54: ^{1}H NMR spectra of **4.05A.**.

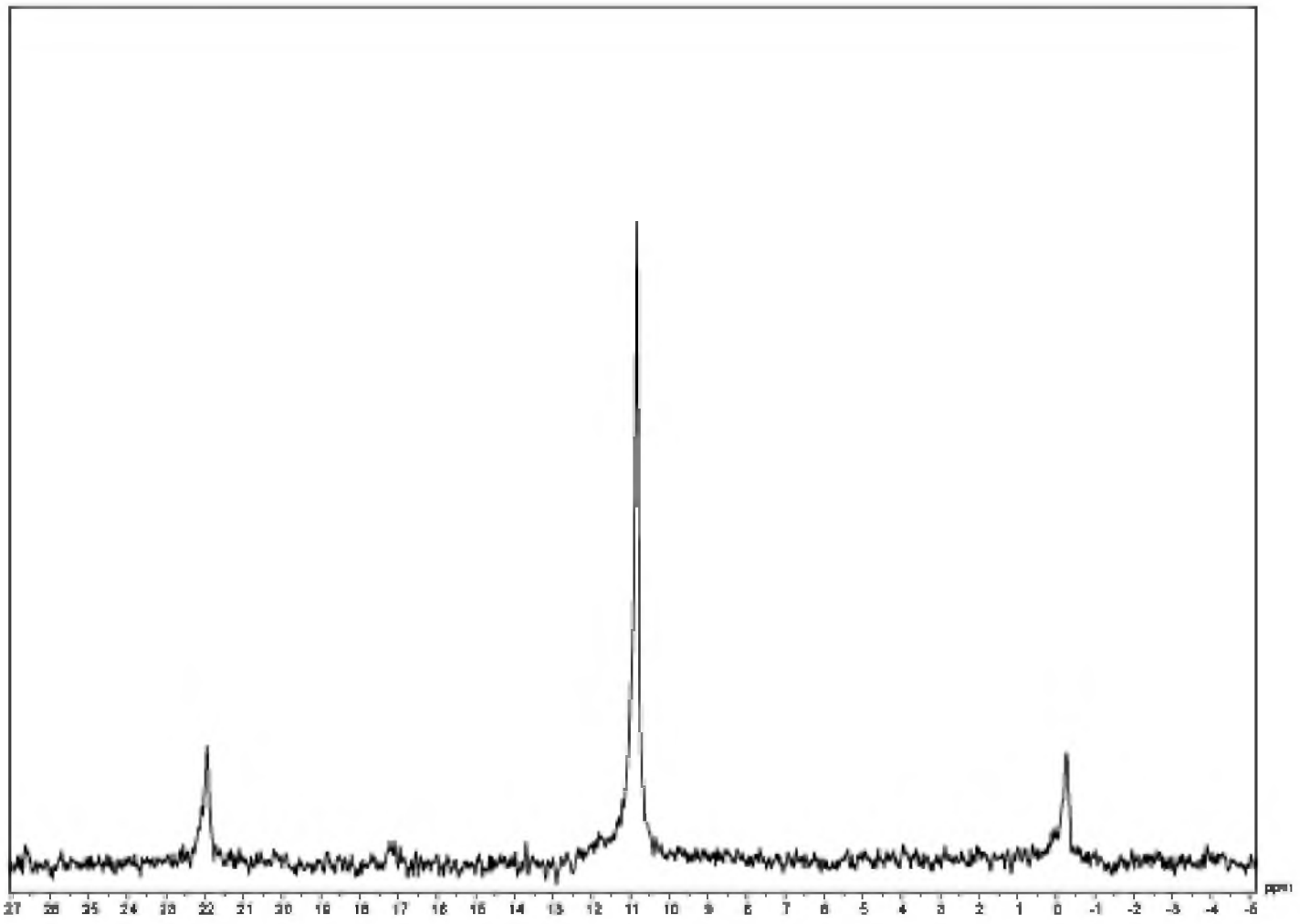

Figure A.55: $^{31}P\{^{1}H\}$ NMR spectra of **4.05A.**.

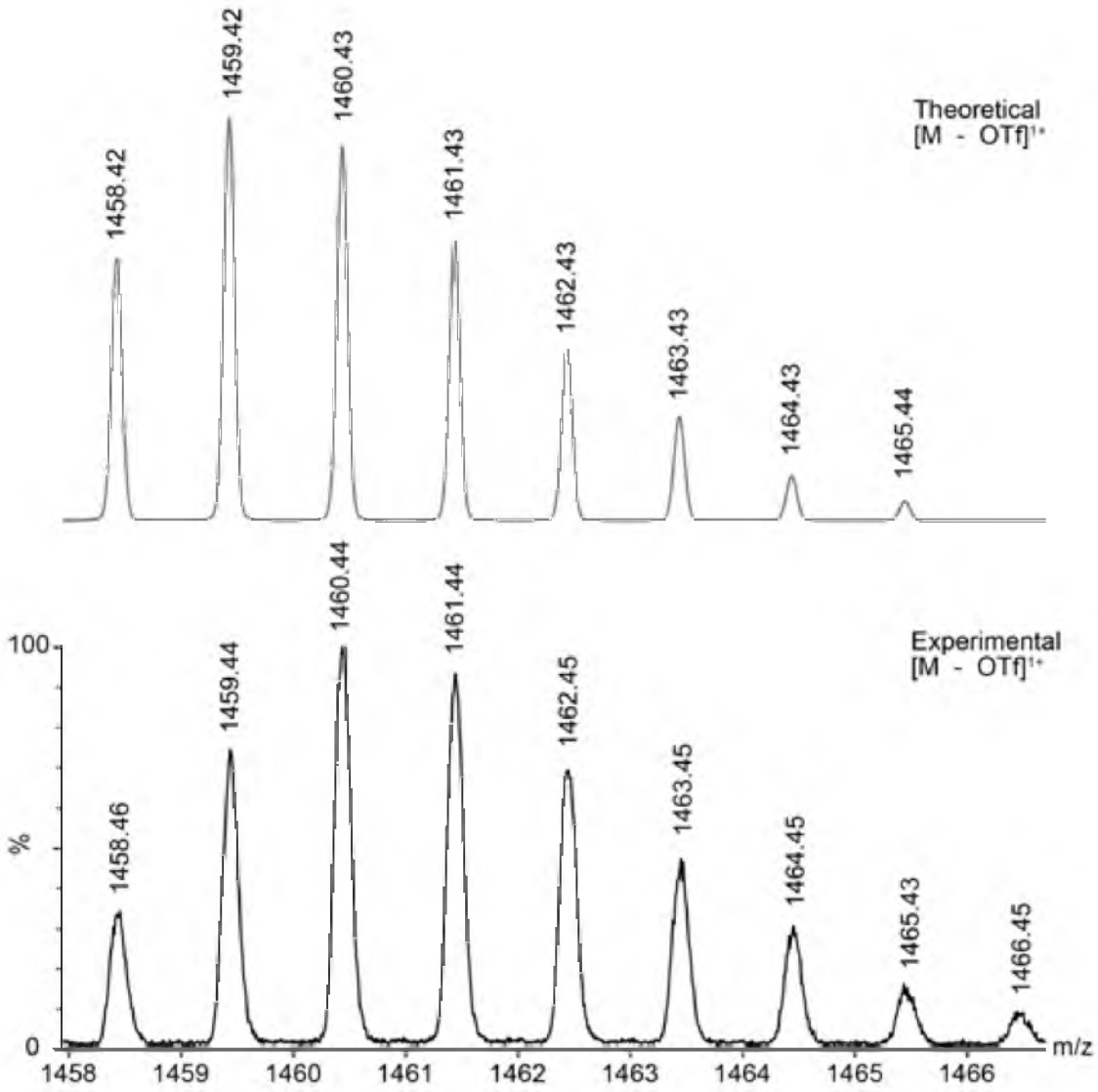

Figure A.56: ESI-MS spectrum of the $[M–OTf]^{1+}$ charge state of **4.05A.**.

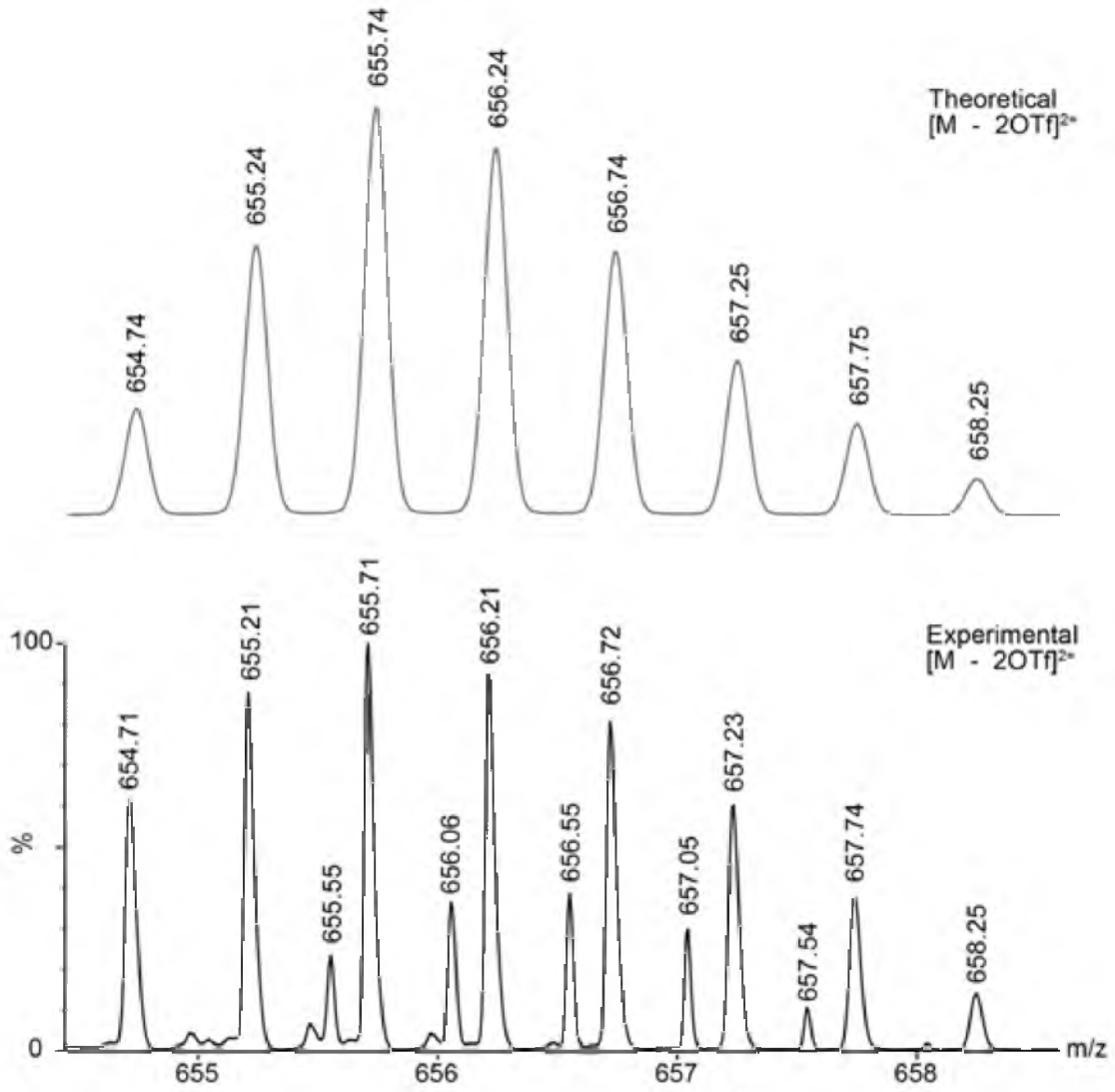

Figure A.57: ESI-MS spectrum of the $[M–2•OTf]^{2+}$ charge state of **4.05A.**.

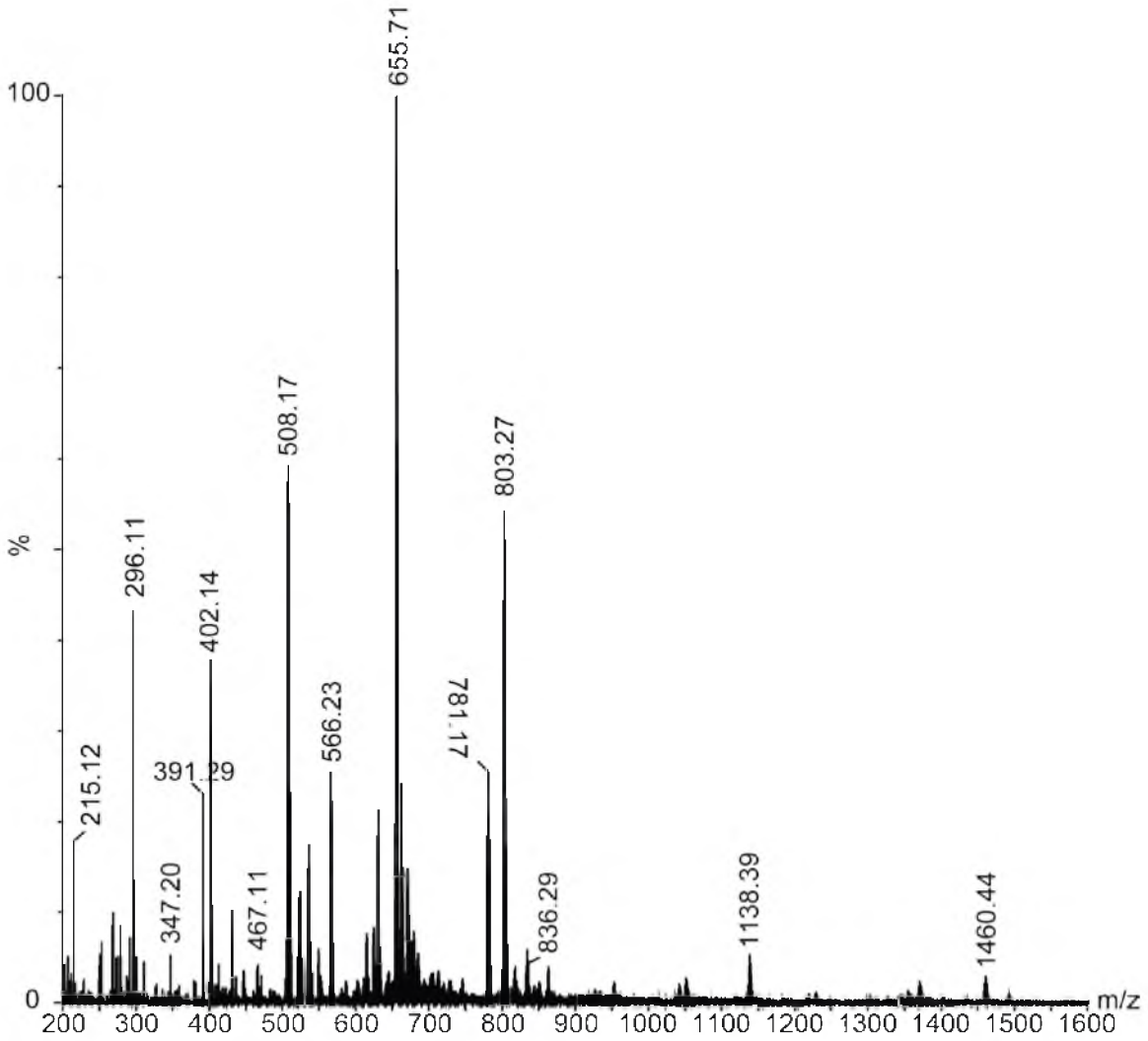

Figure A.58: ESI-MS spectrum of **4.05A.**.

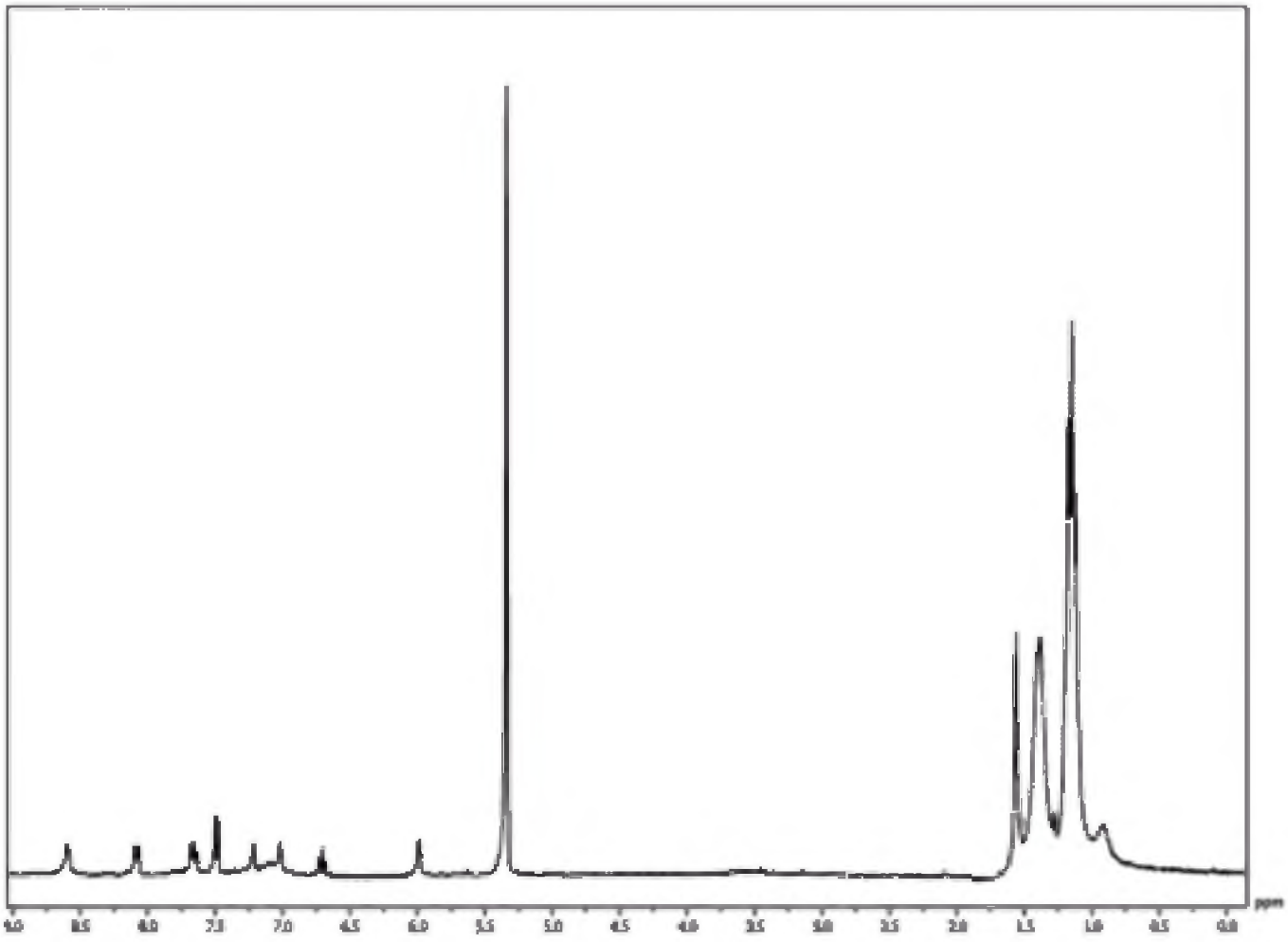

Figure A.59: ^{1}H NMR spectra of **4.06**.

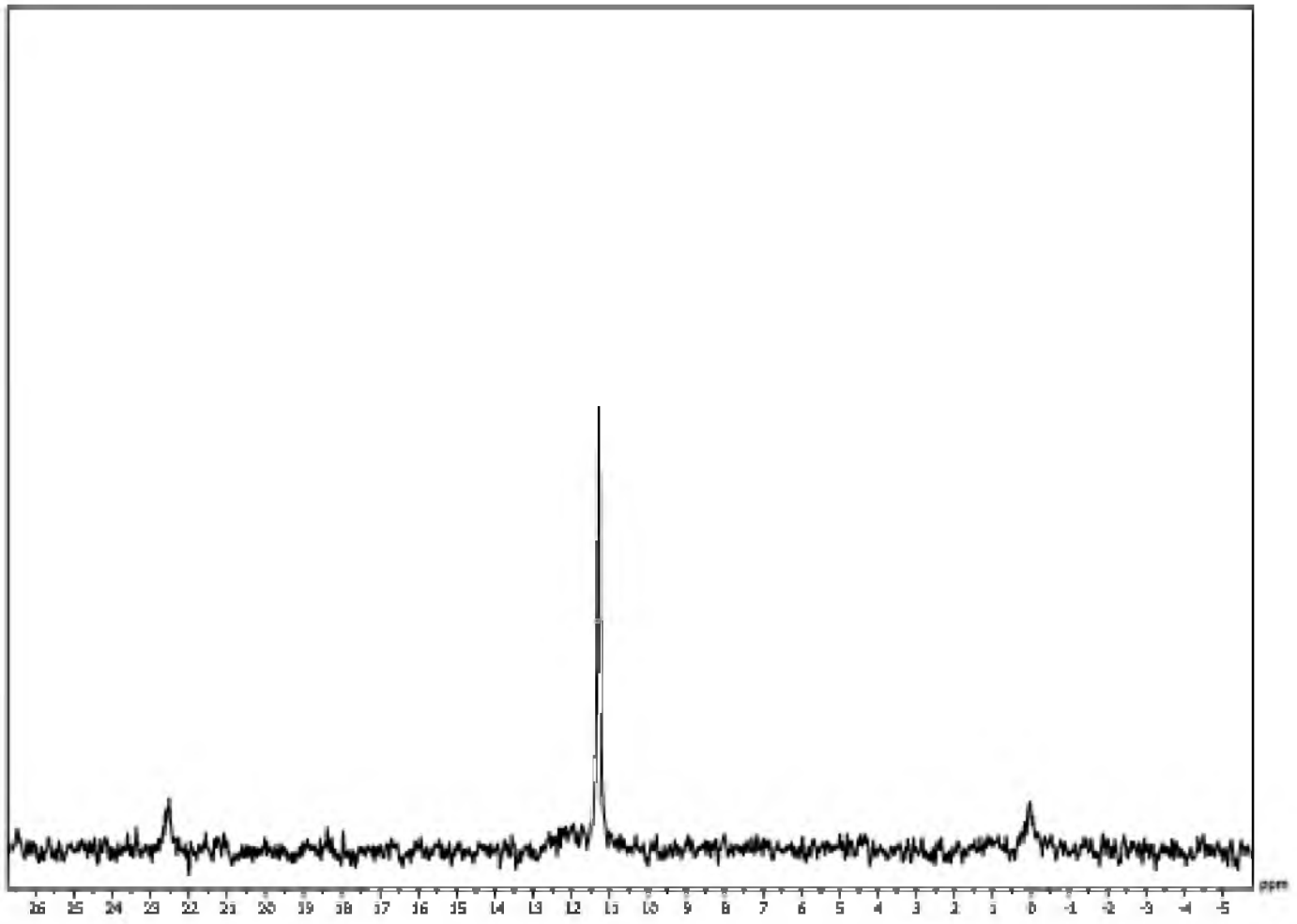

Figure A.60: $^{31}P\{^{1}H\}$ NMR spectra of **4.06**.

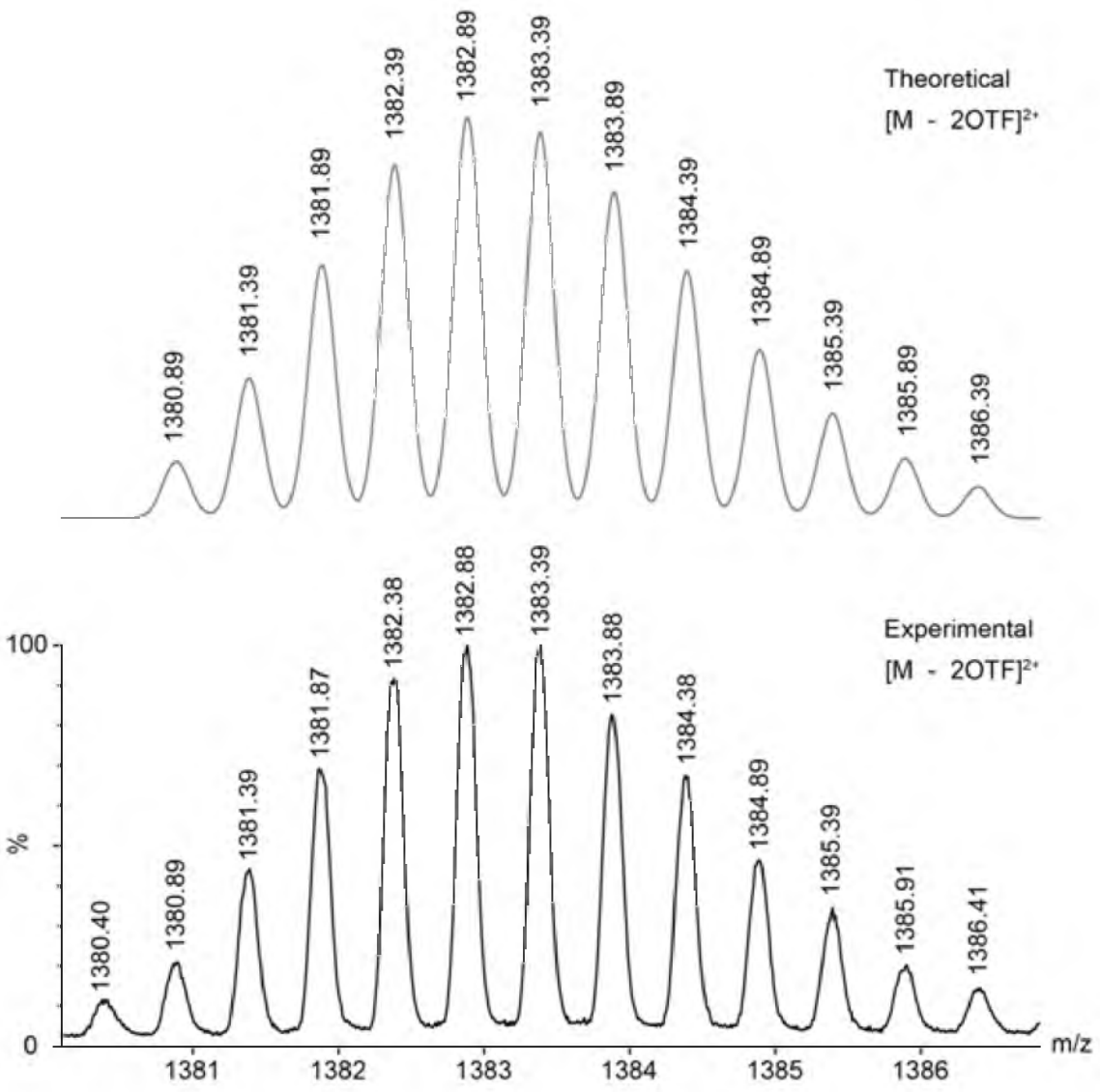

Figure A.61: ESI-MS spectrum of the $[M–2•OTf]^{2+}$ charge state of **4.06**.

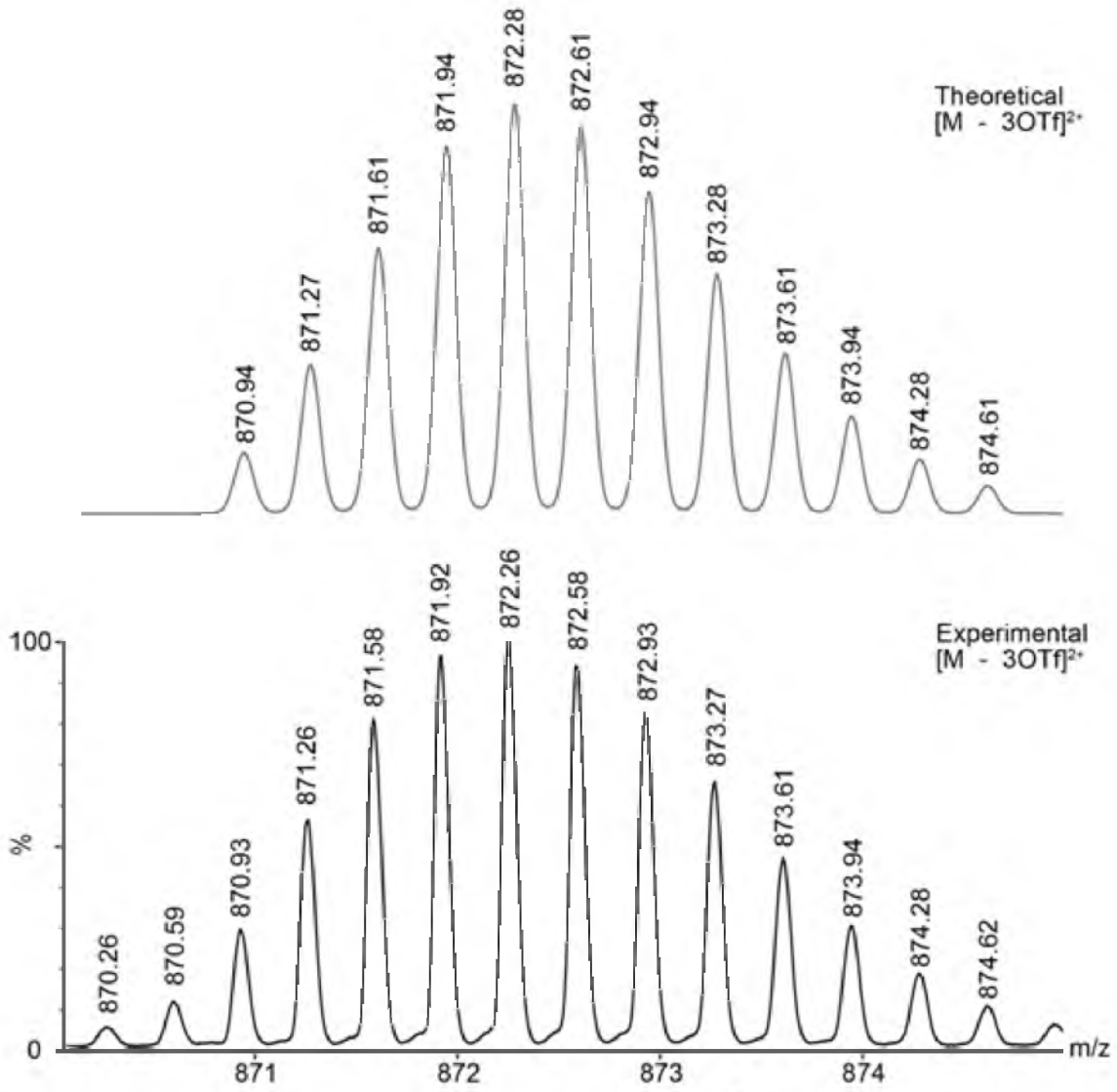

Figure A.62: ESI-MS spectrum of the $[M–3•OTf]^{3+}$ charge state of **4.06**.

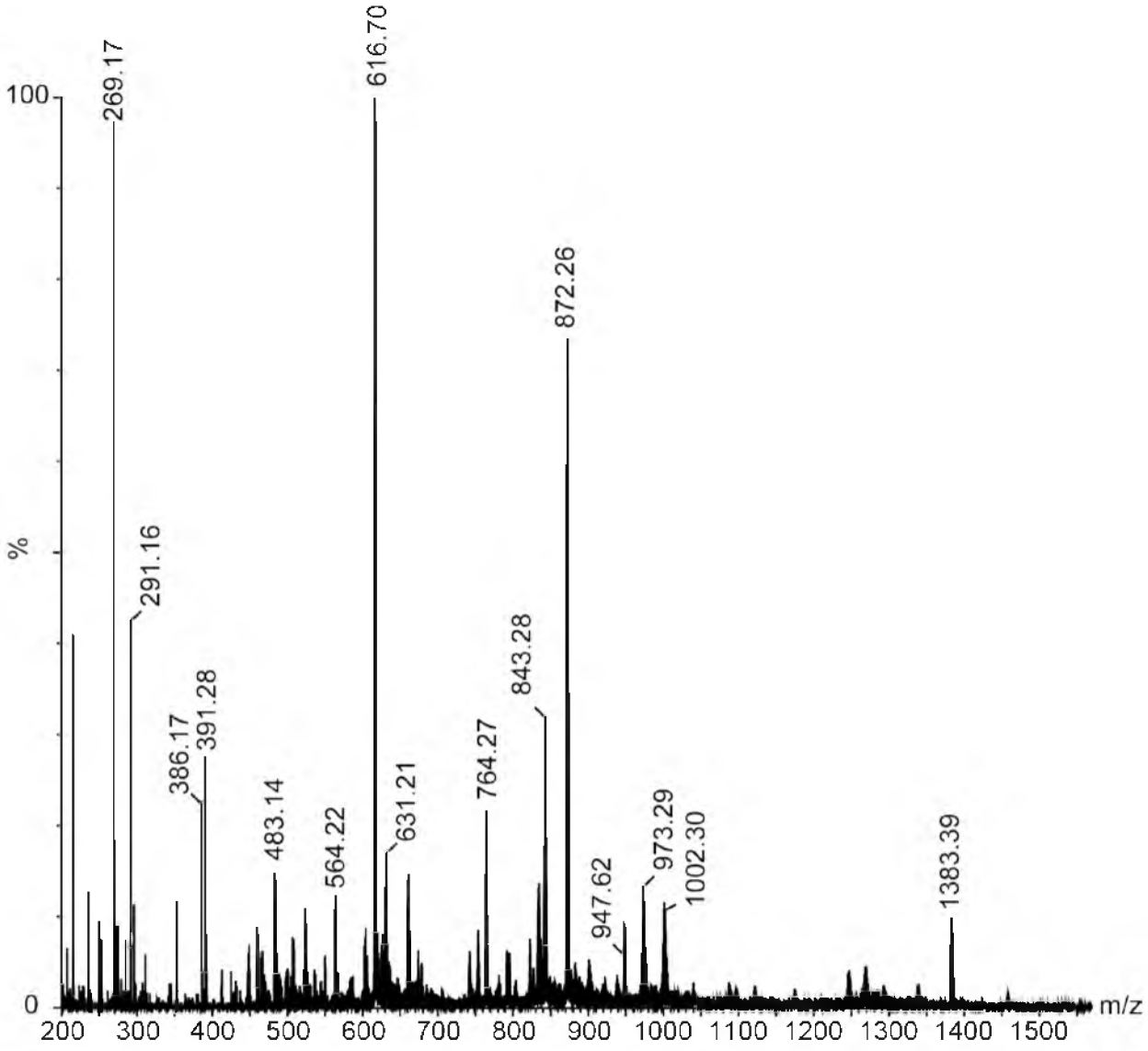

Figure A.63: ESI-MS spectrum of **4.06**.

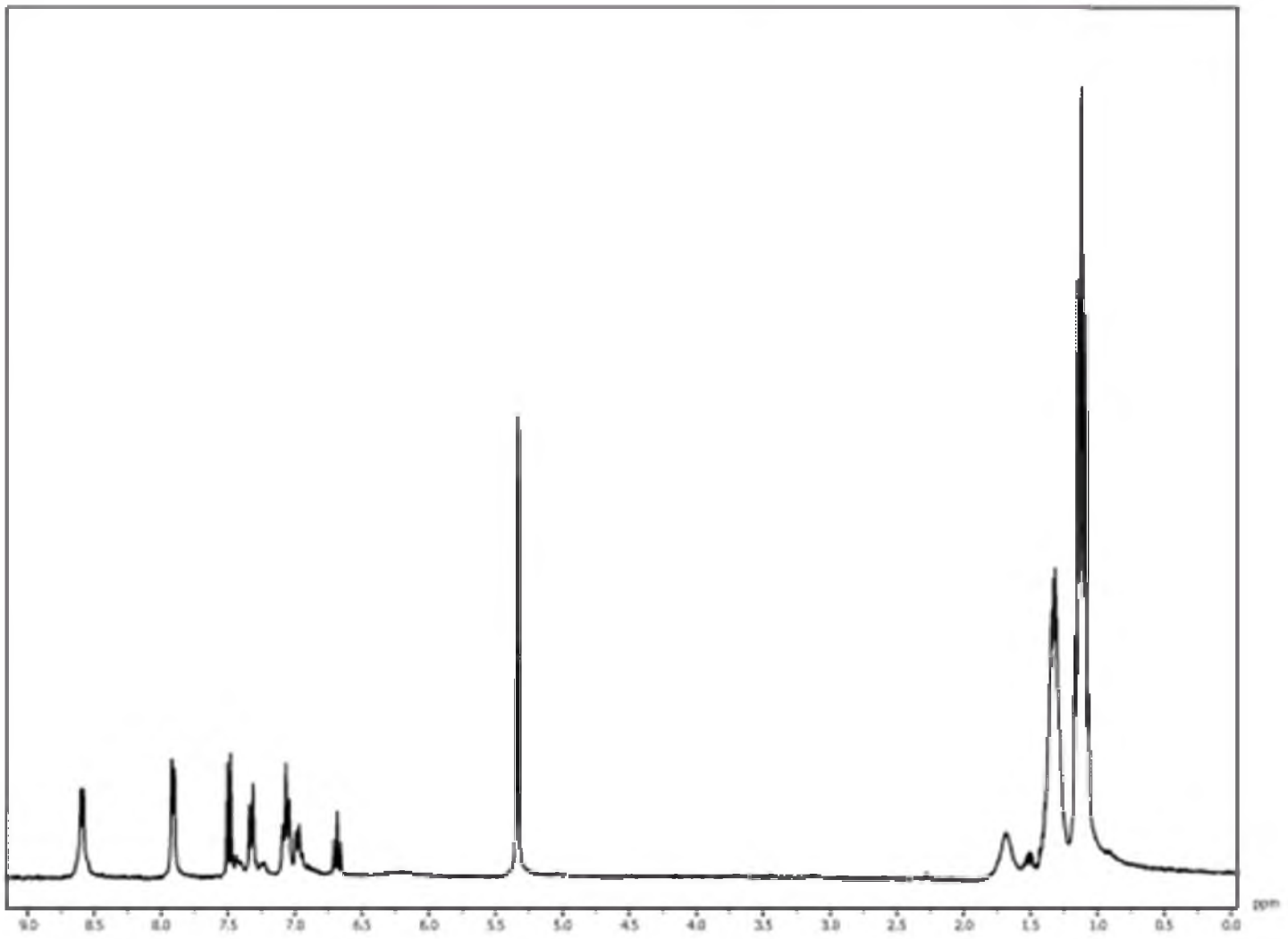

Figure A.64: ^{1}H NMR spectra of **4.07**.

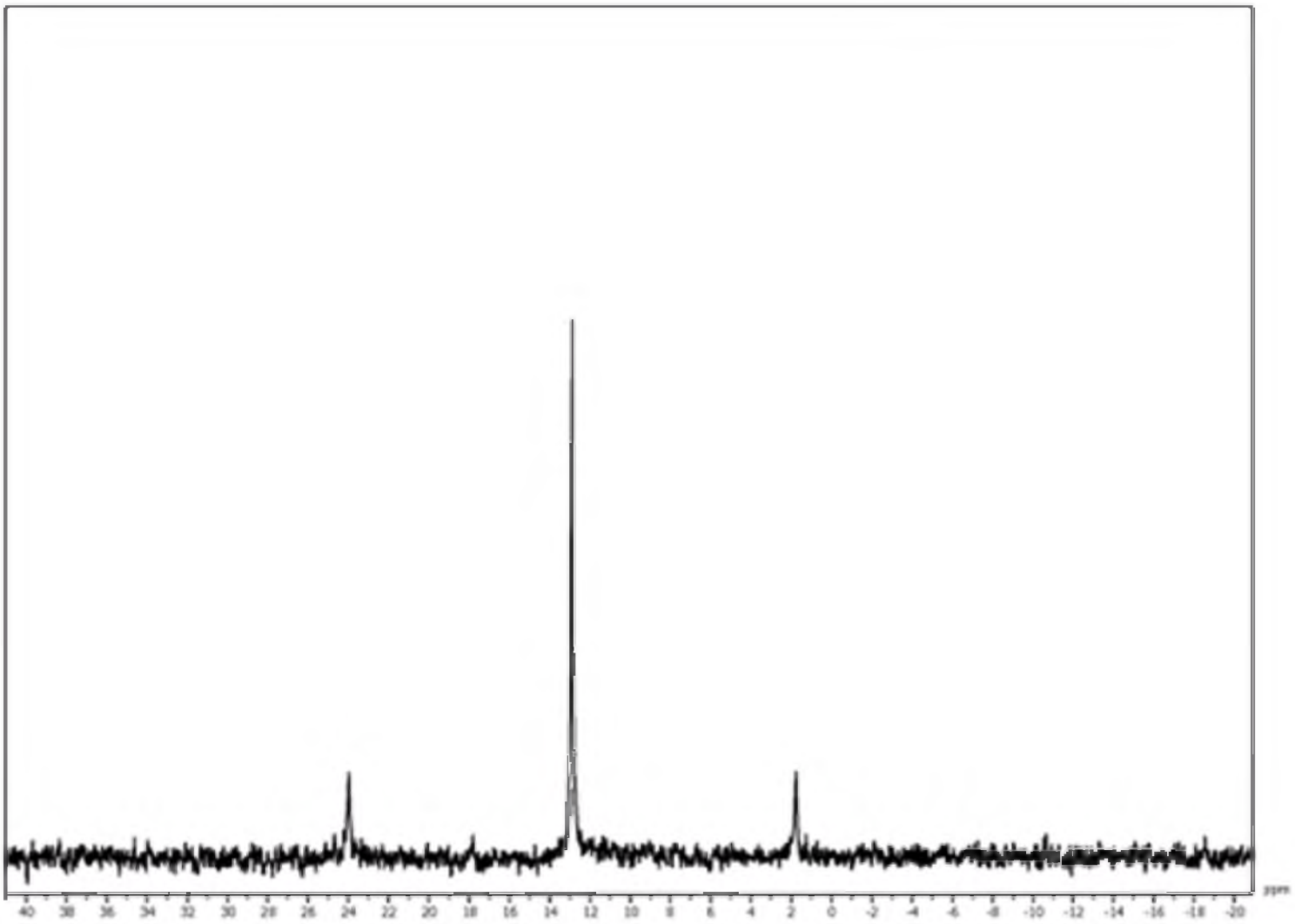

Figure A.65: $^{31}P\{^{1}H\}$ NMR spectra of **4.07**.

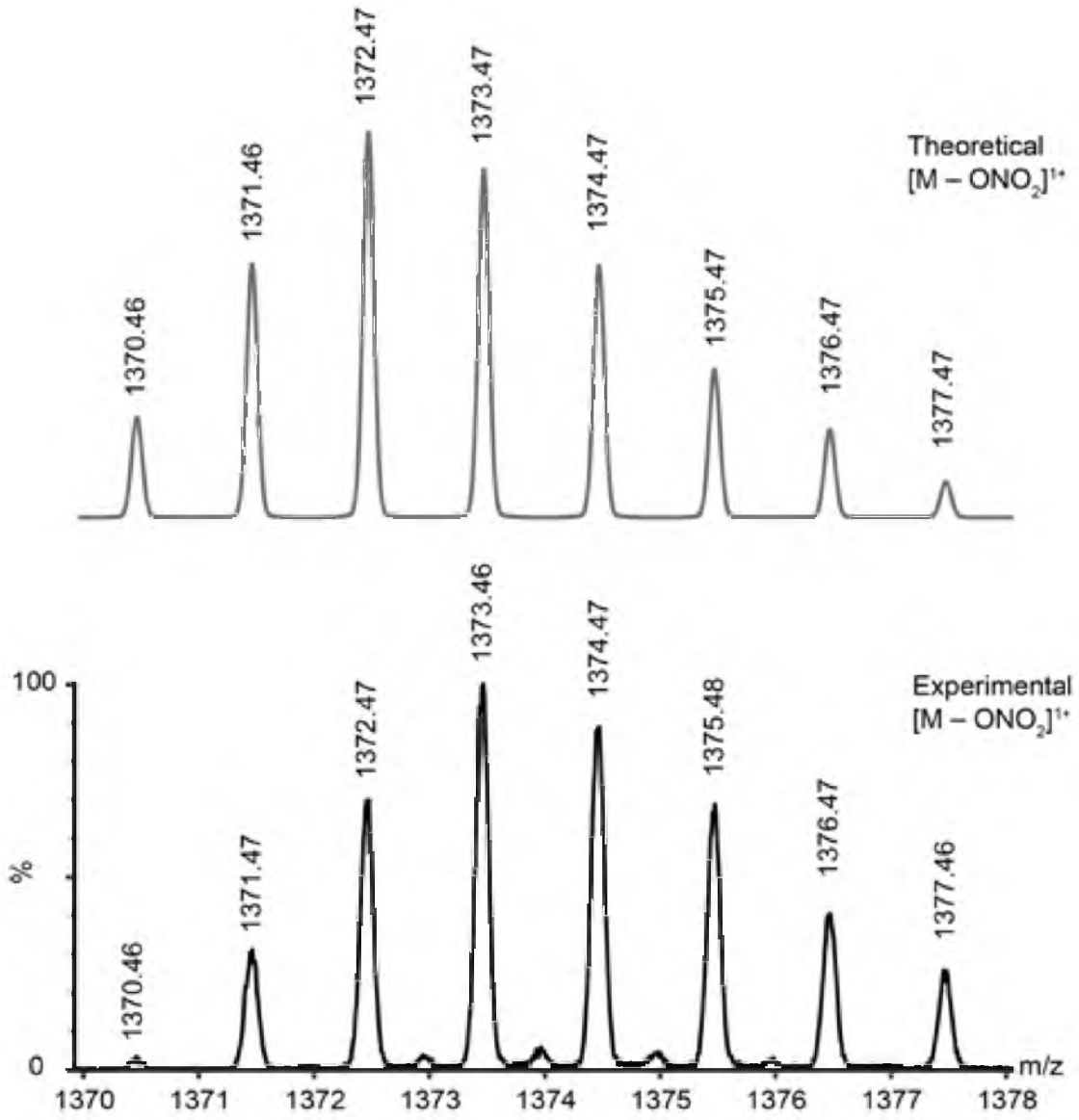

Figure A.66: ESI-MS spectrum of the $[M–NO_3]^{1+}$ charge state of **4.07**.

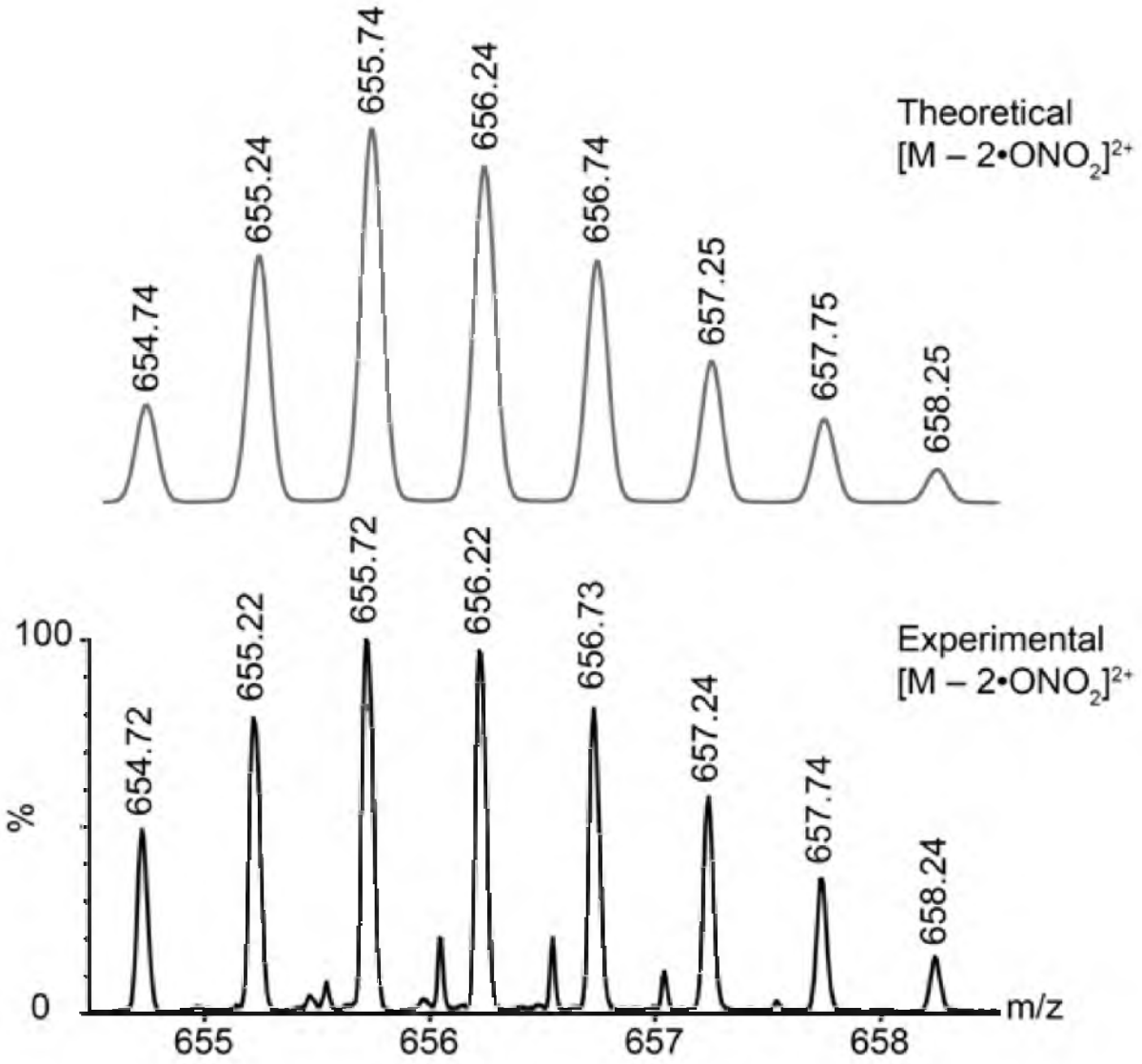

Figure A.67: ESI-MS spectrum of the $[M–2•NO_3]^{2+}$ charge state of **4.07**.

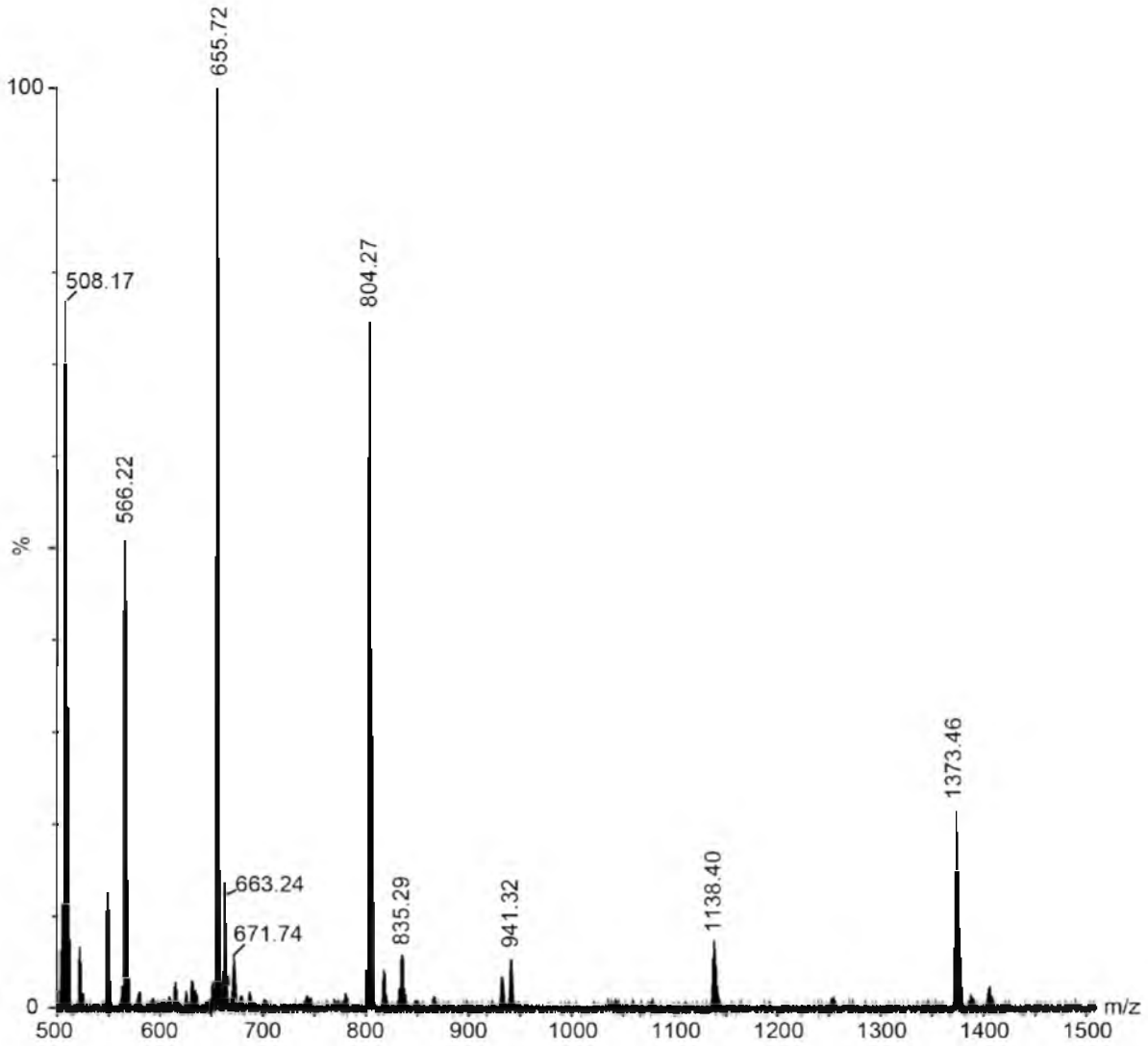

Figure A.68: ESI-MS spectrum of **4.07**.

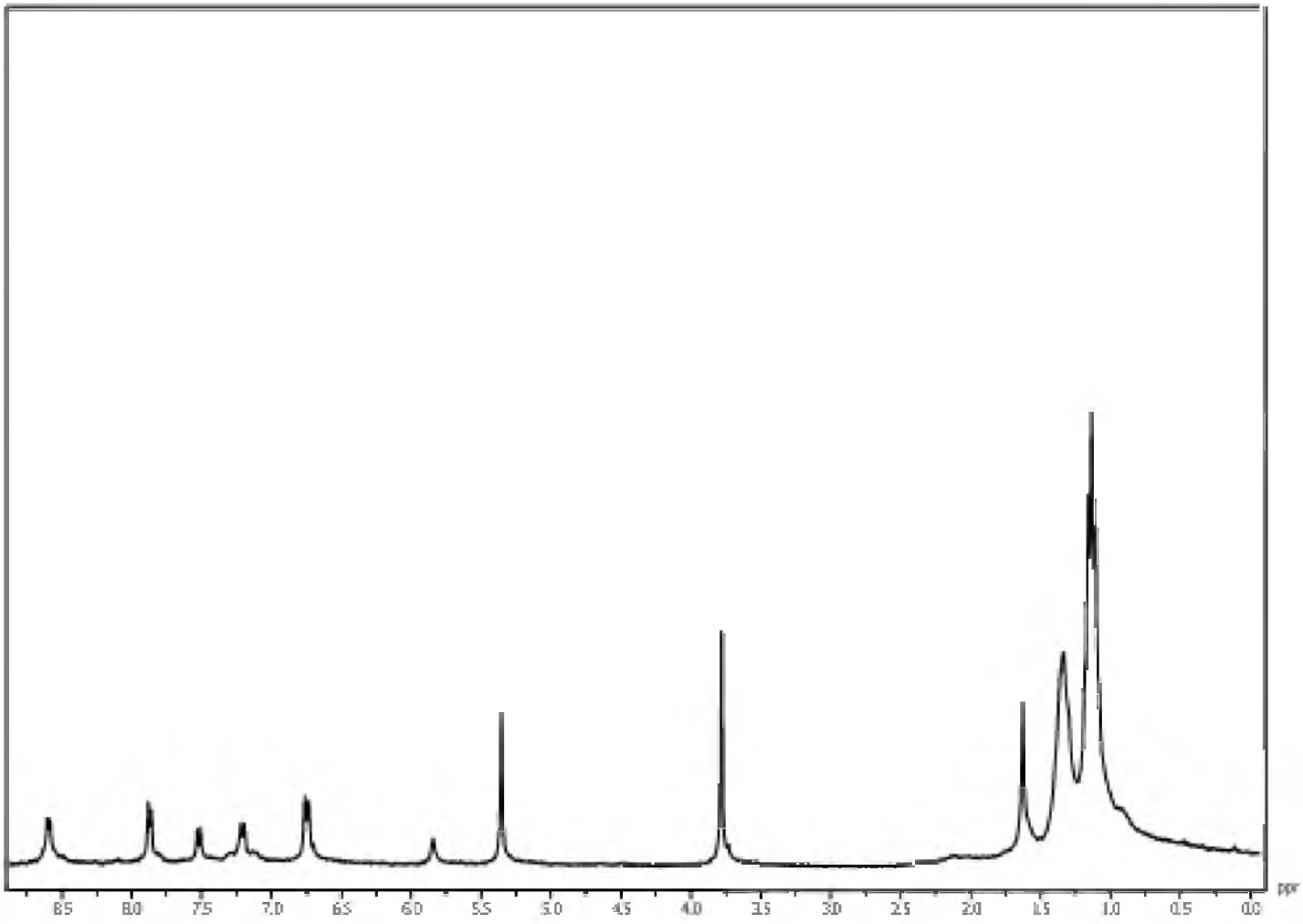

Figure A.69: ^{1}H NMR spectra of **4.13**.

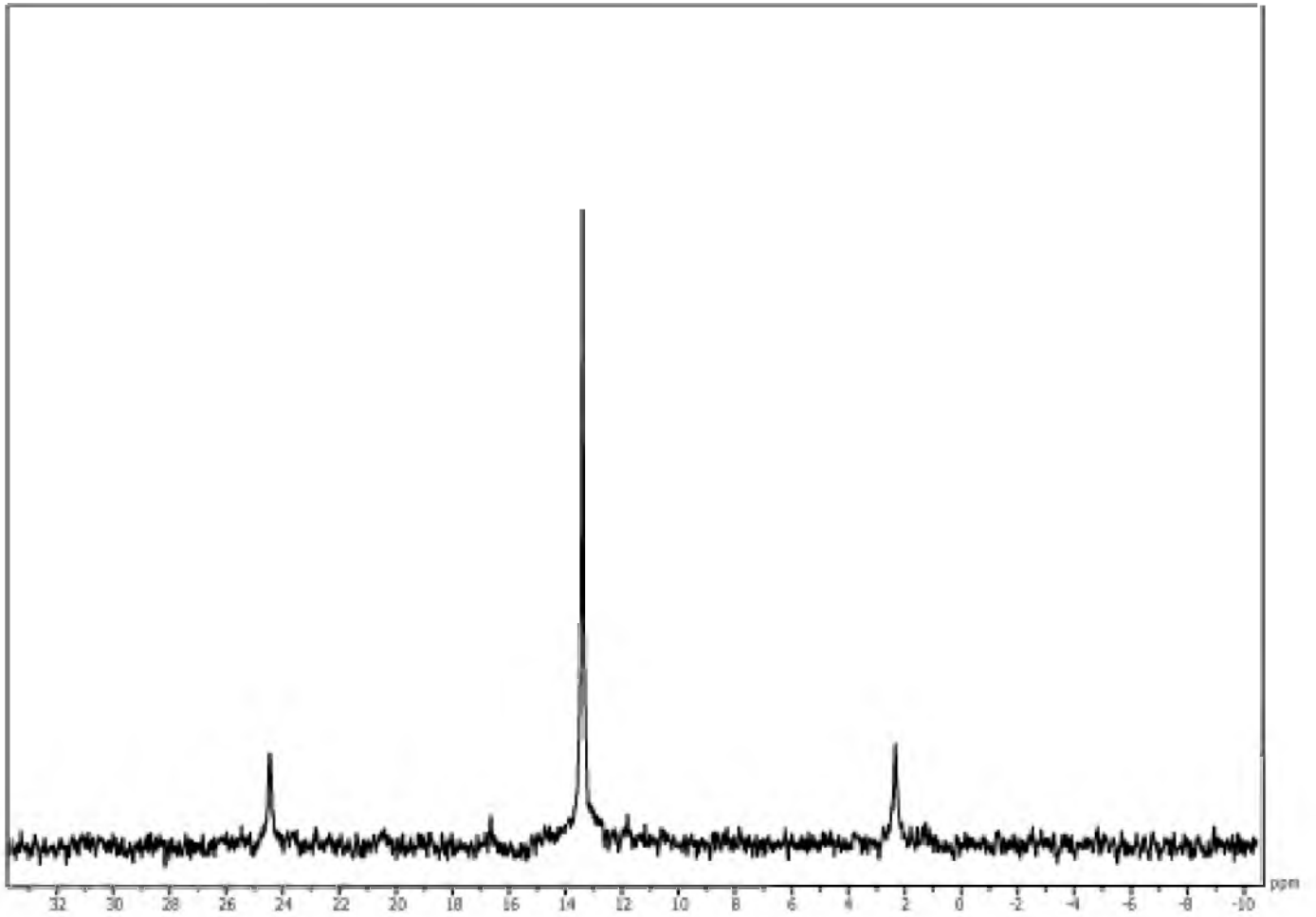

Figure A.70: $^{31}P\{^{1}H\}$ NMR spectra of **4.13**.

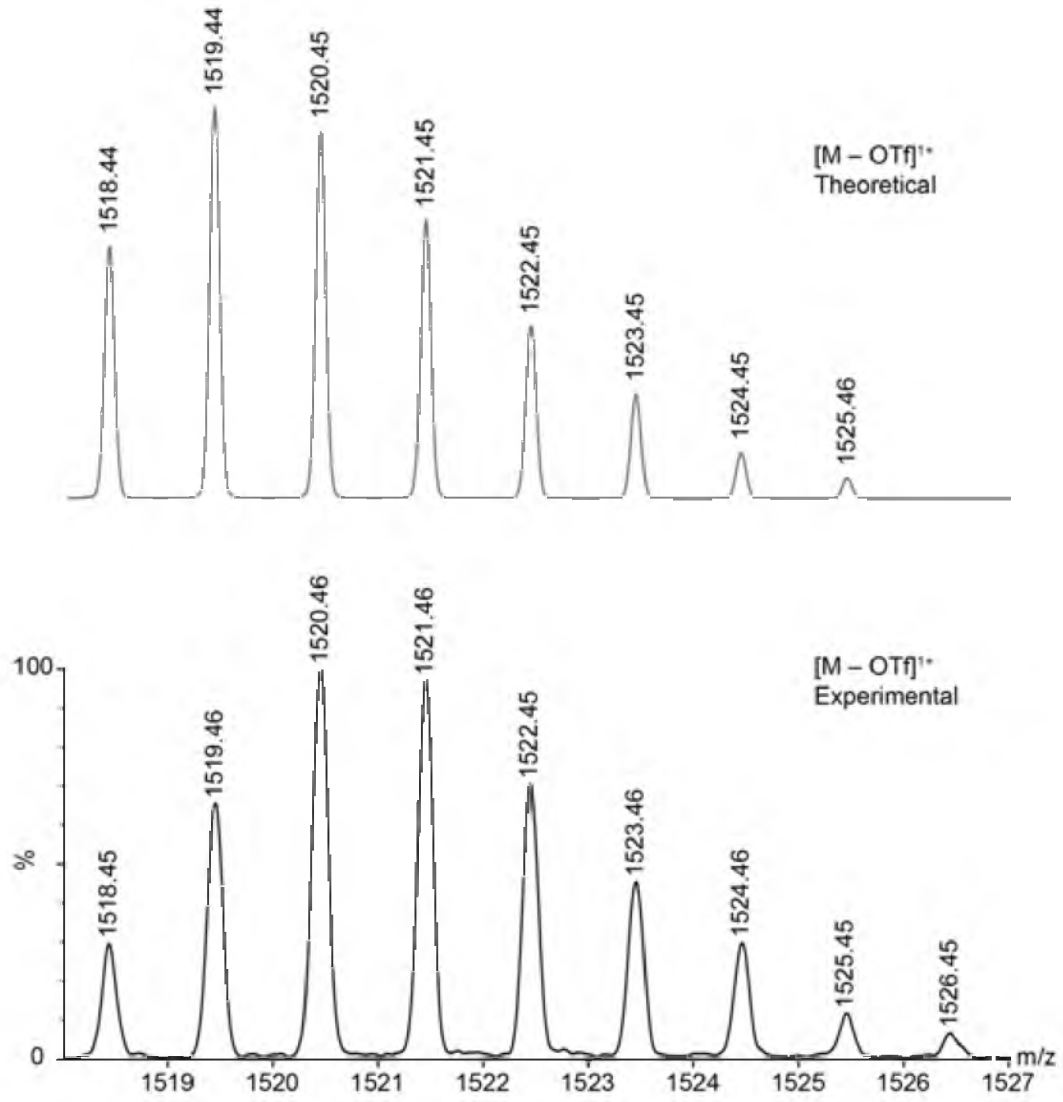

Figure A.71: ESI-MS spectrum of the $[M–OTf]^{1+}$ charge state of **4.13**.

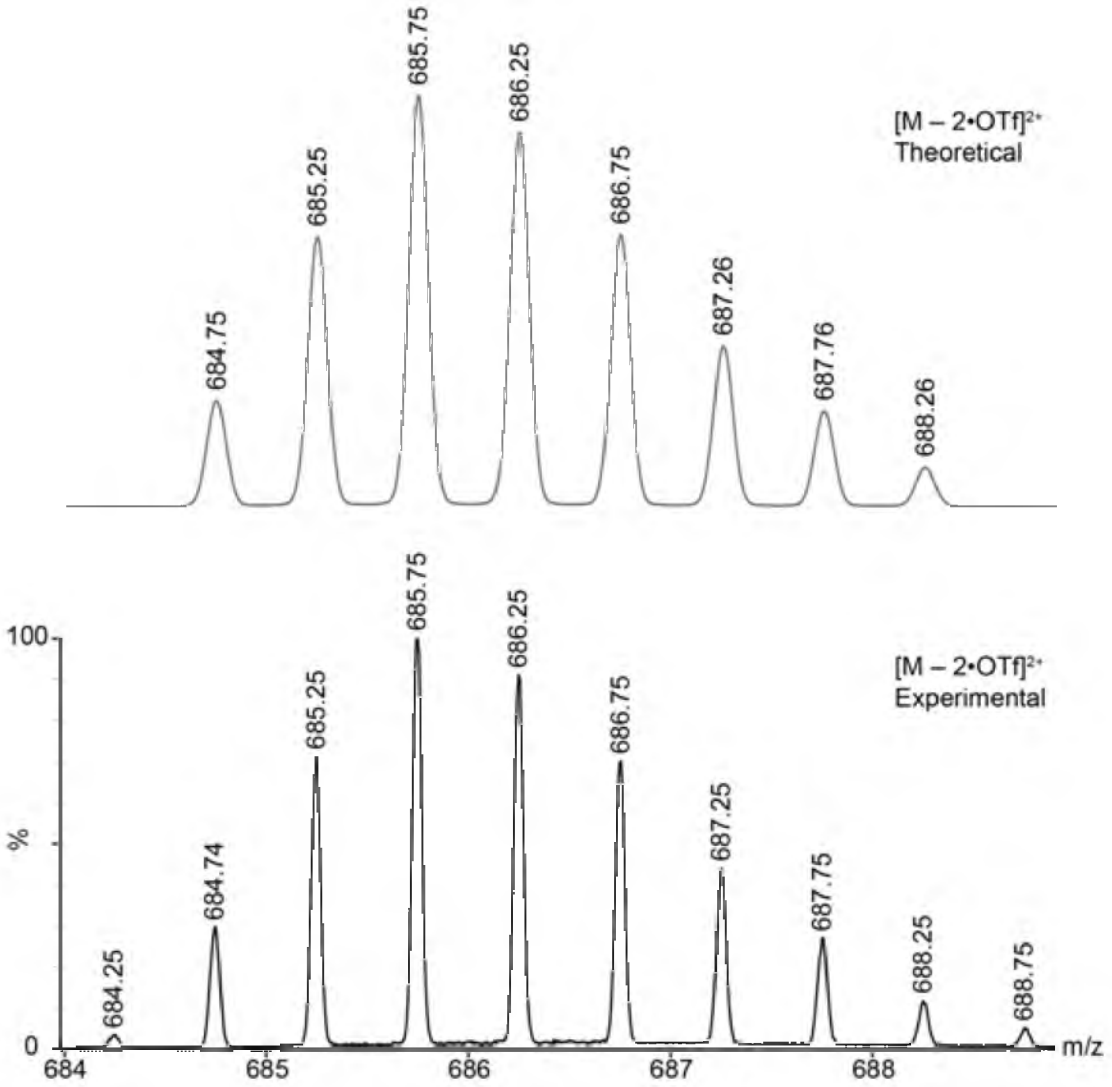

Figure A.72: ESI-MS spectrum of the $[M–2•OTf]^{2+}$ charge state of **4.13**.

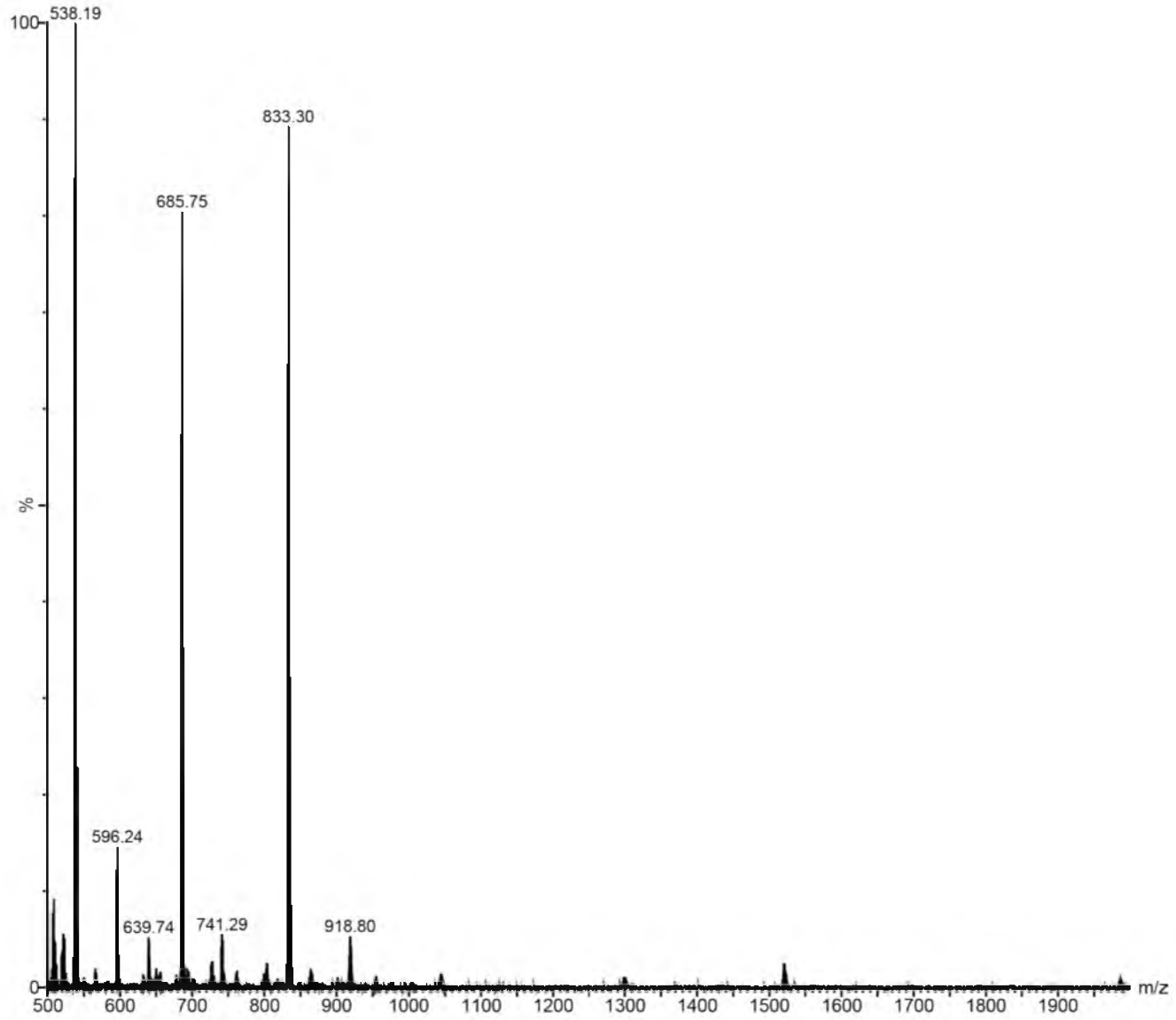

Figure A.73: ESI-MS spectrum of **4.13**.

Figure A.74:

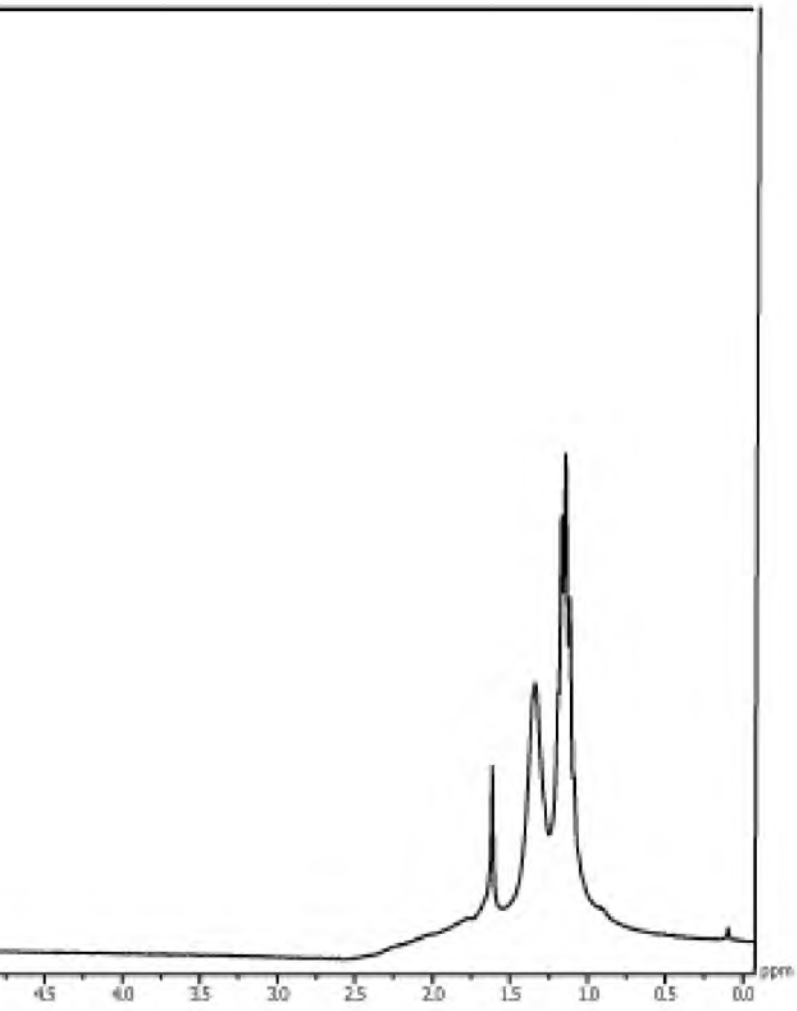

^{1}H NMR spectra of **4.14**.

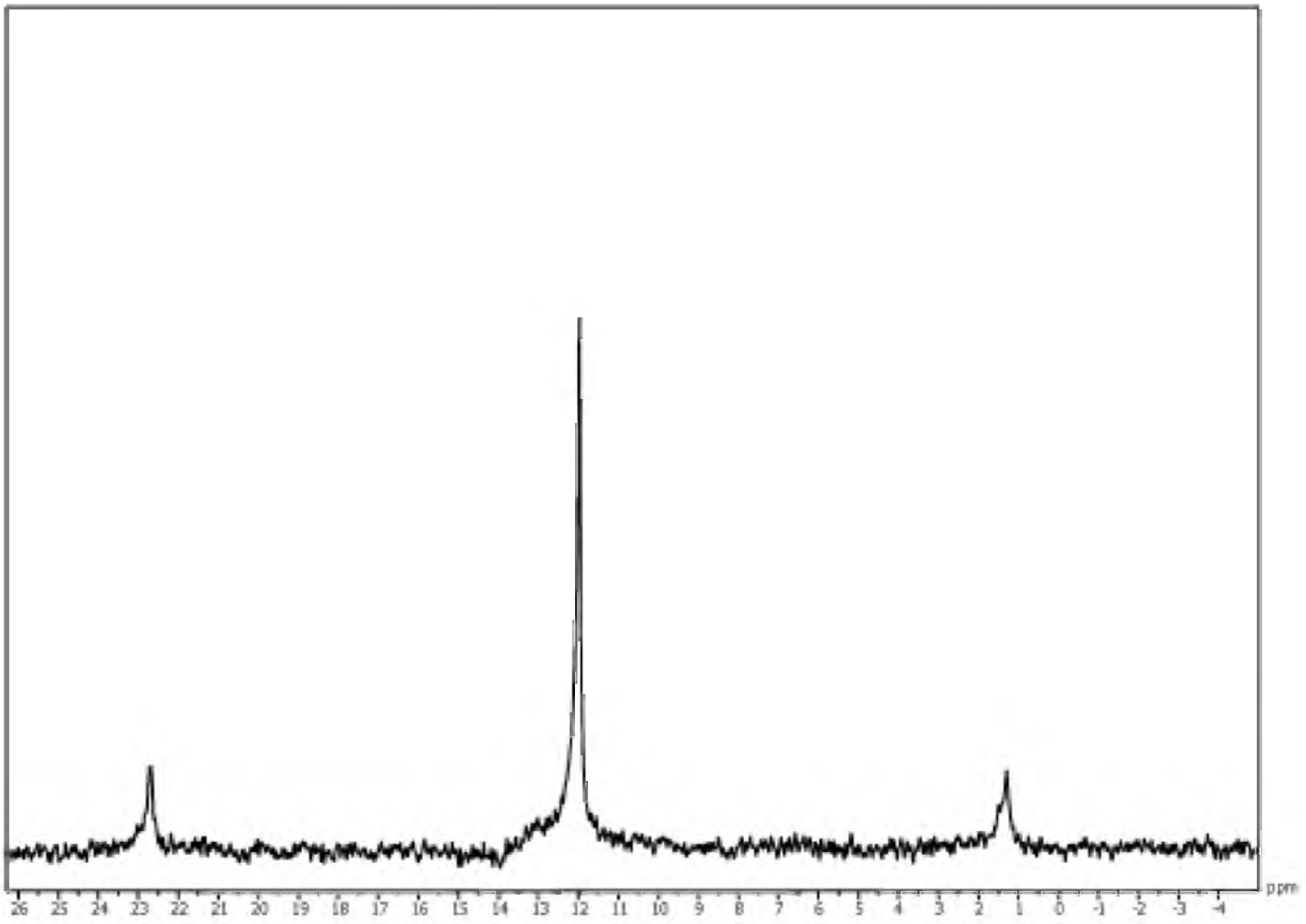

Figure A.75: $^{31}P\{^{1}H\}$ NMR spectra of **4.14**.

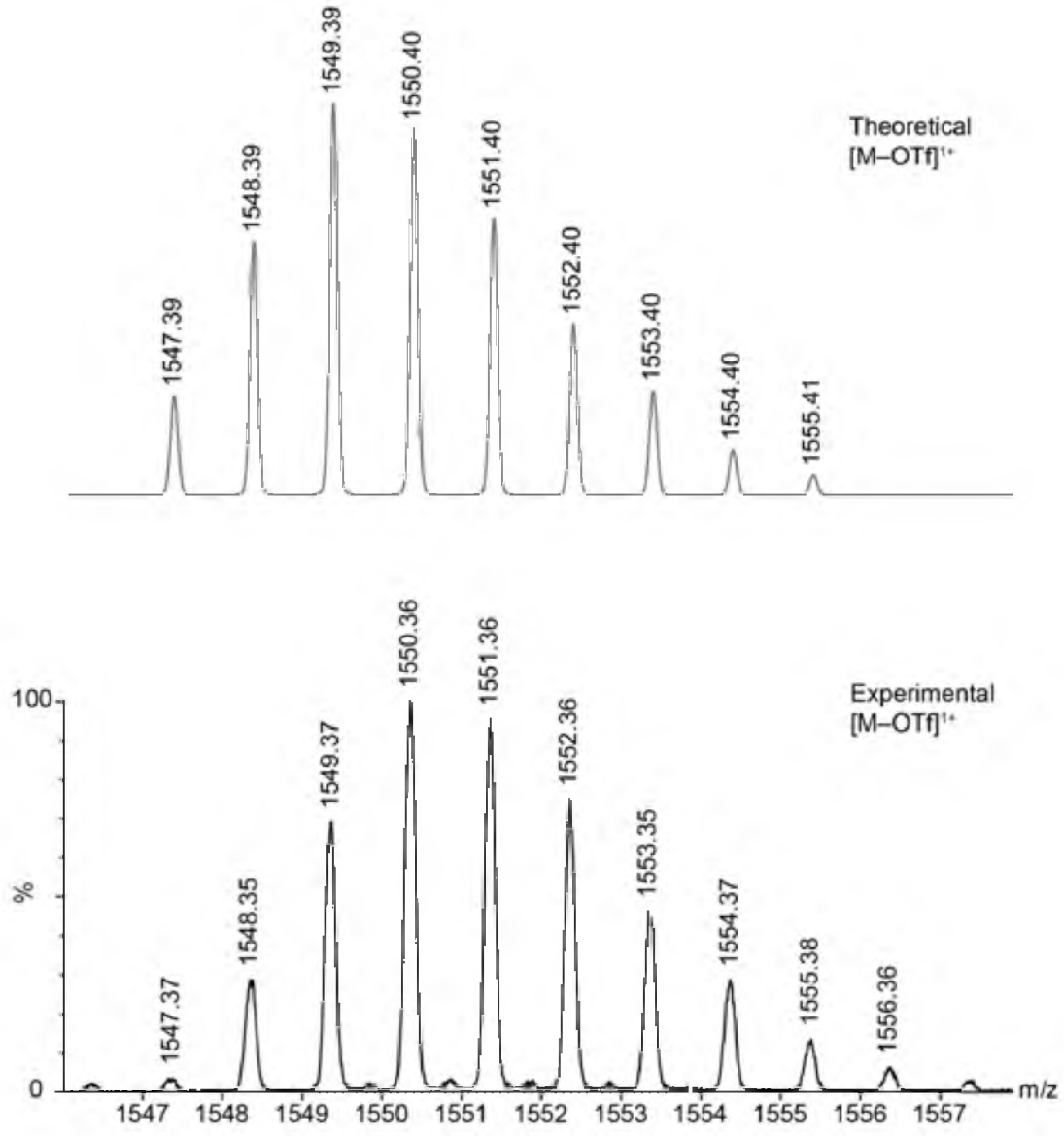

Figure A.76: ESI-MS spectrum of the $[M–OTf]^{1+}$ charge state of **4.14**.

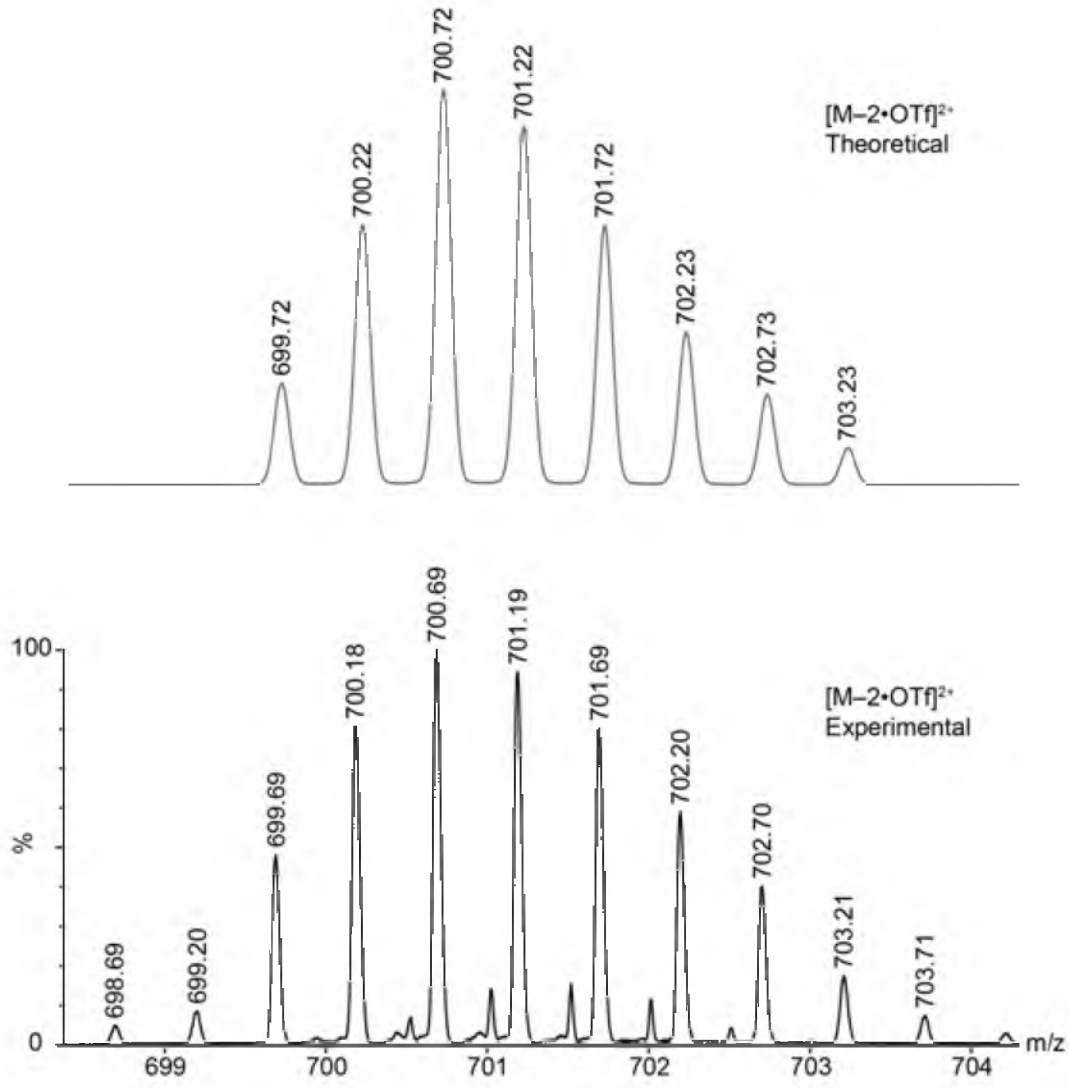

Figure A.77: ESI-MS spectrum of the $[M–2•OTf]^{2+}$ charge state of **4.14**.

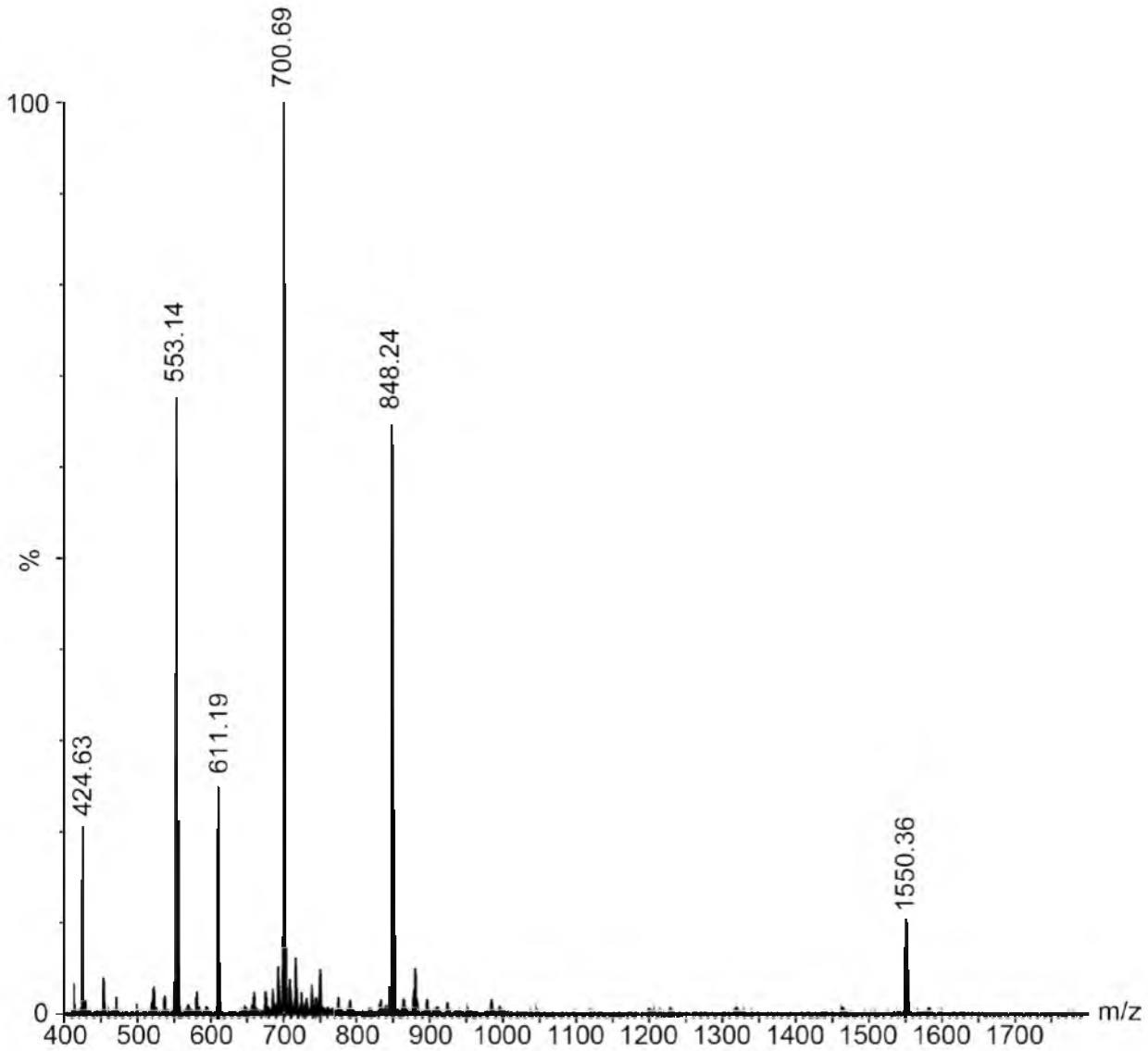

Figure A.78: ESI-MS spectrum of **4.14**.

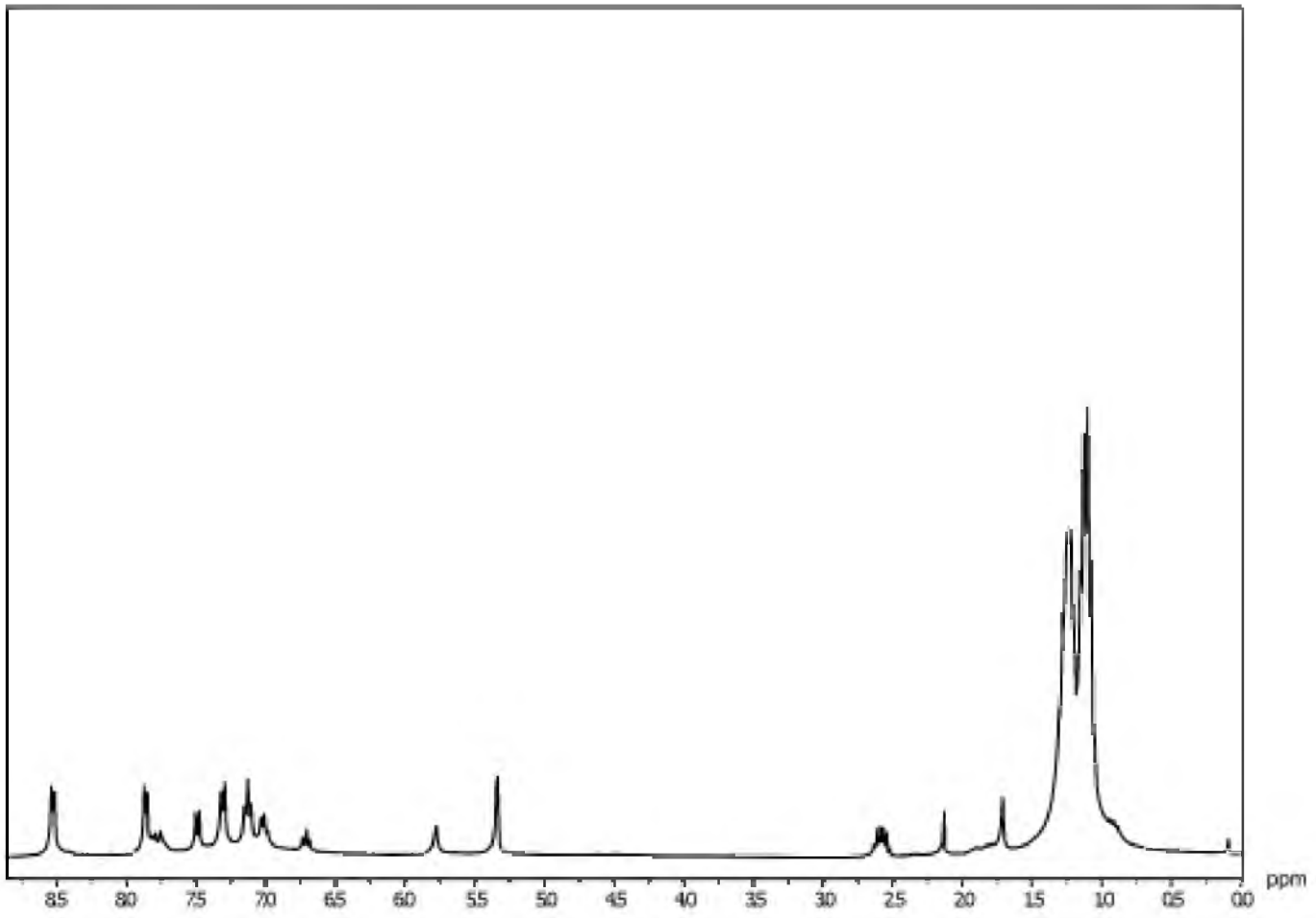

Figure A.79: ^{1}H NMR spectra of **4.15**.

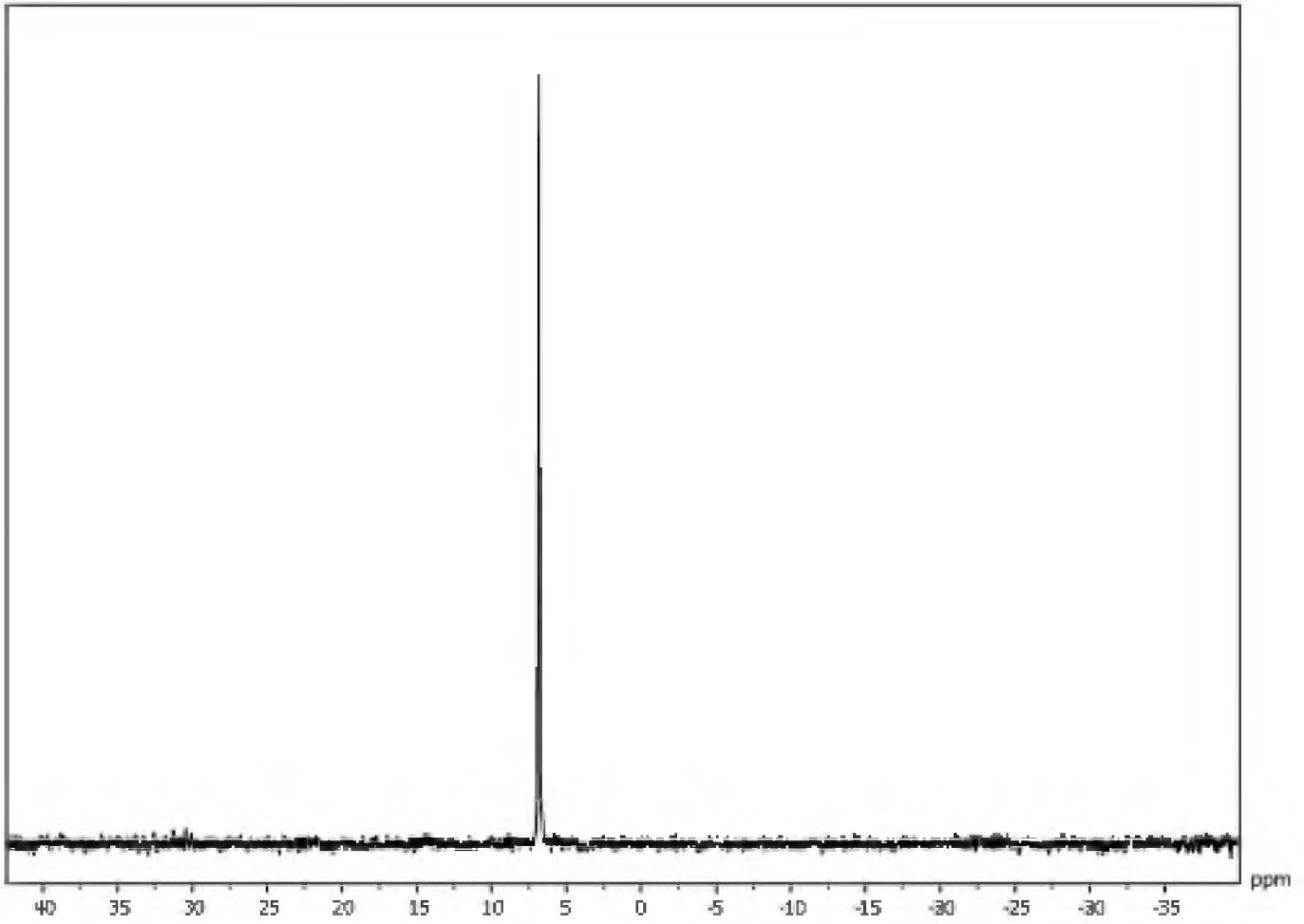

Figure A.80: $^{31}P\{^{1}H\}$ NMR spectra of **4.15**.

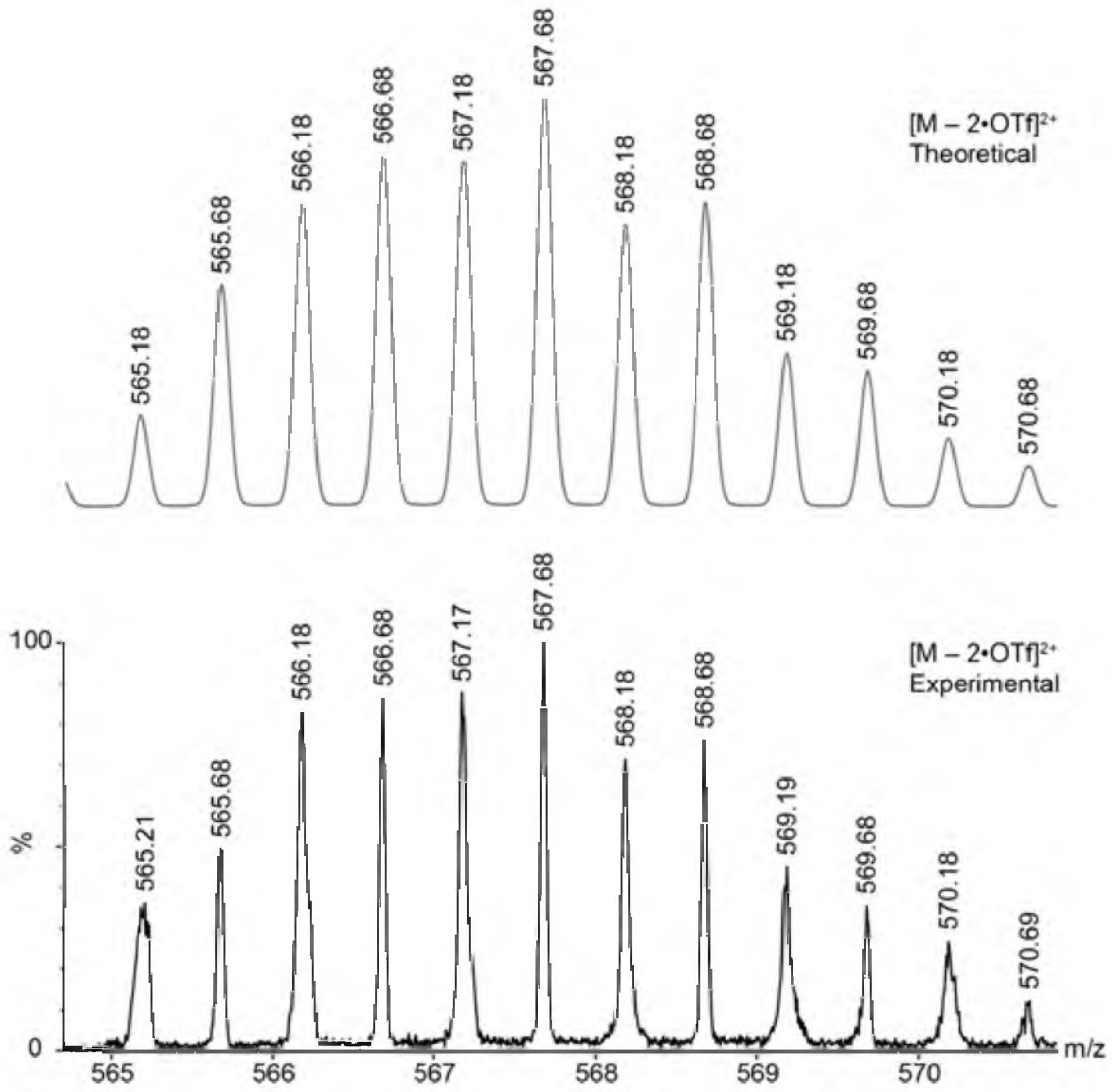

Figure A.81: ESI-MS spectrum of the $[M–2•OTf]^{2+}$ charge state of **4.15**.

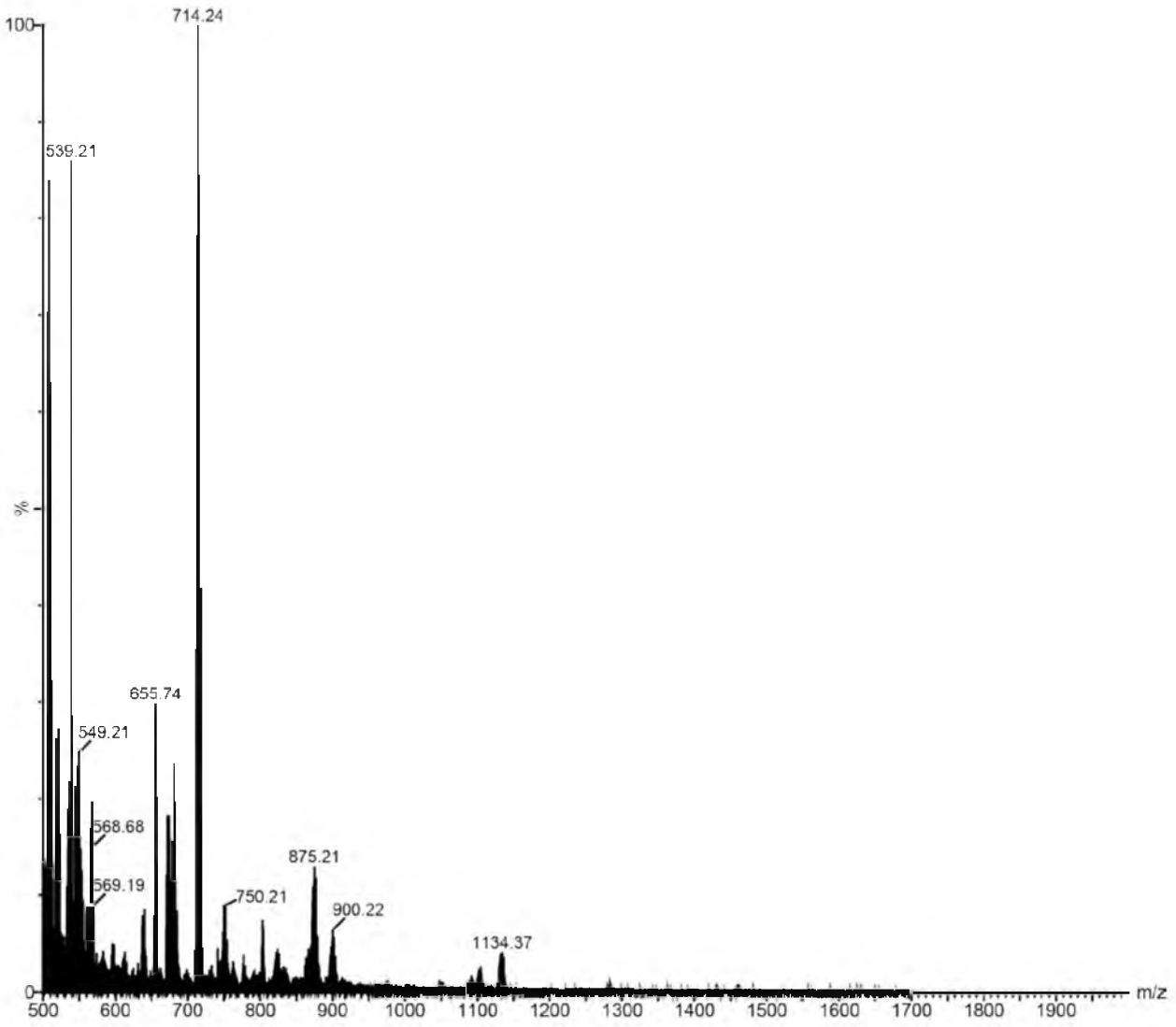

Figure A.82: ESI-MS spectrum of **4.15**.

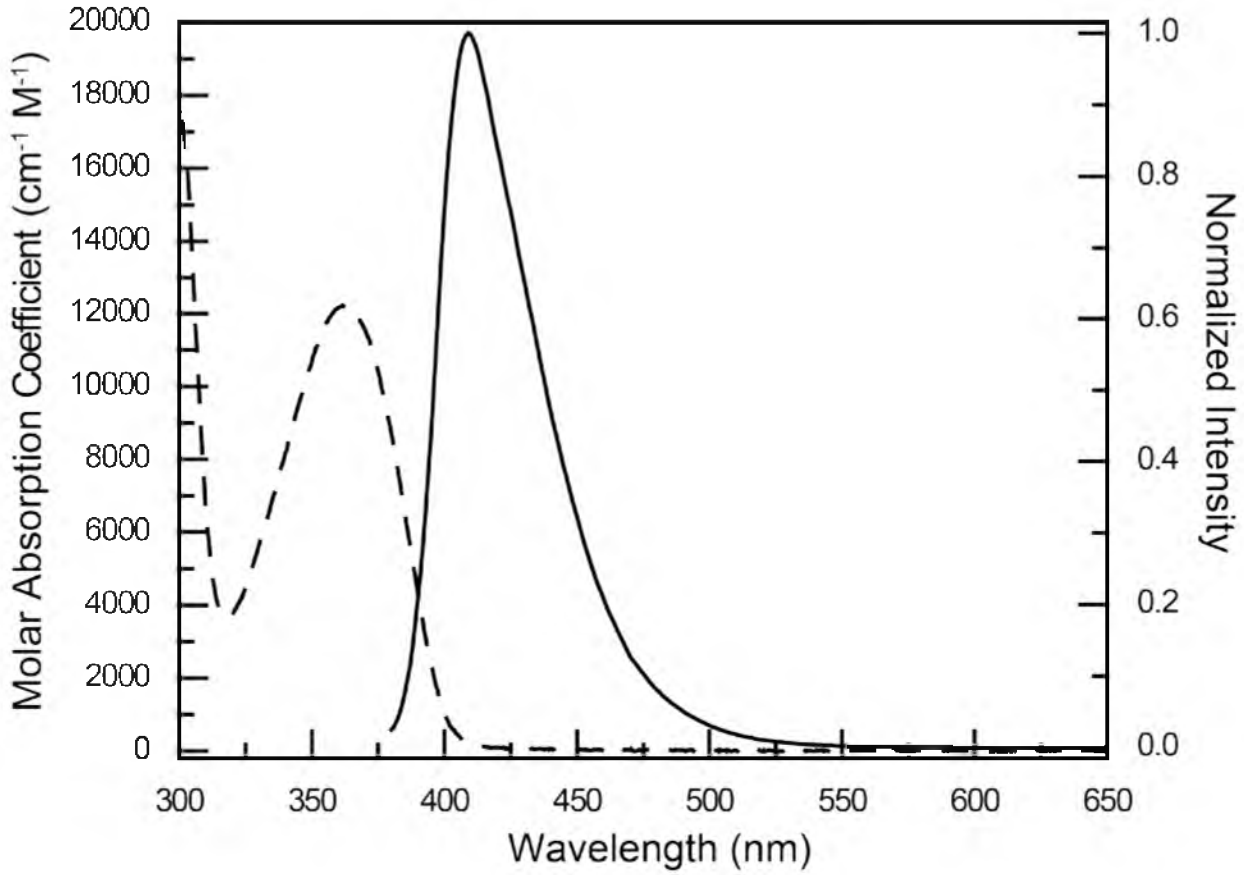

Figure A.83: Absorption (dashed) and emission (solid) profiles of **4.02**.

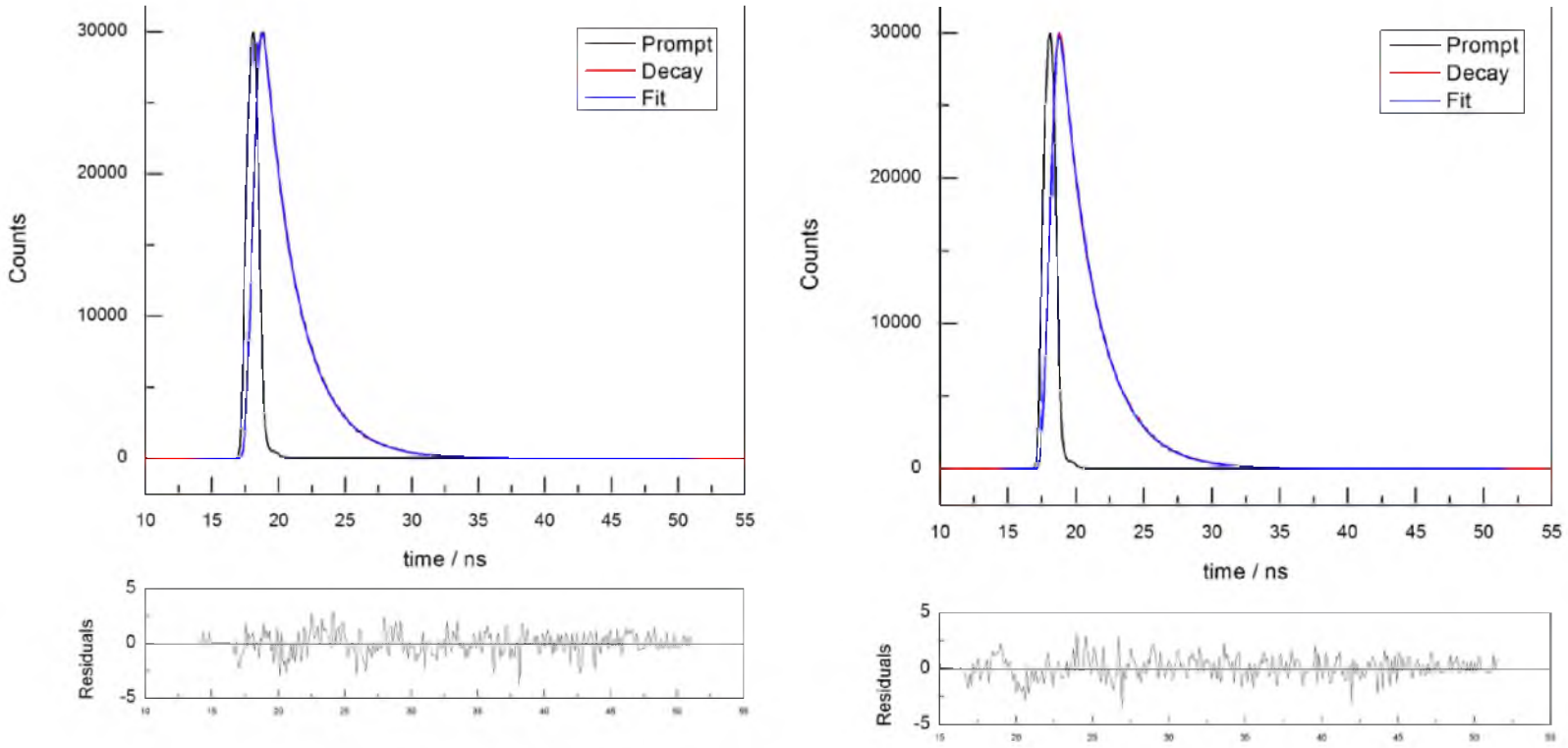

Figure A.84: Excited-state lifetime traces for **4.01** (left) and **4.02** (right).

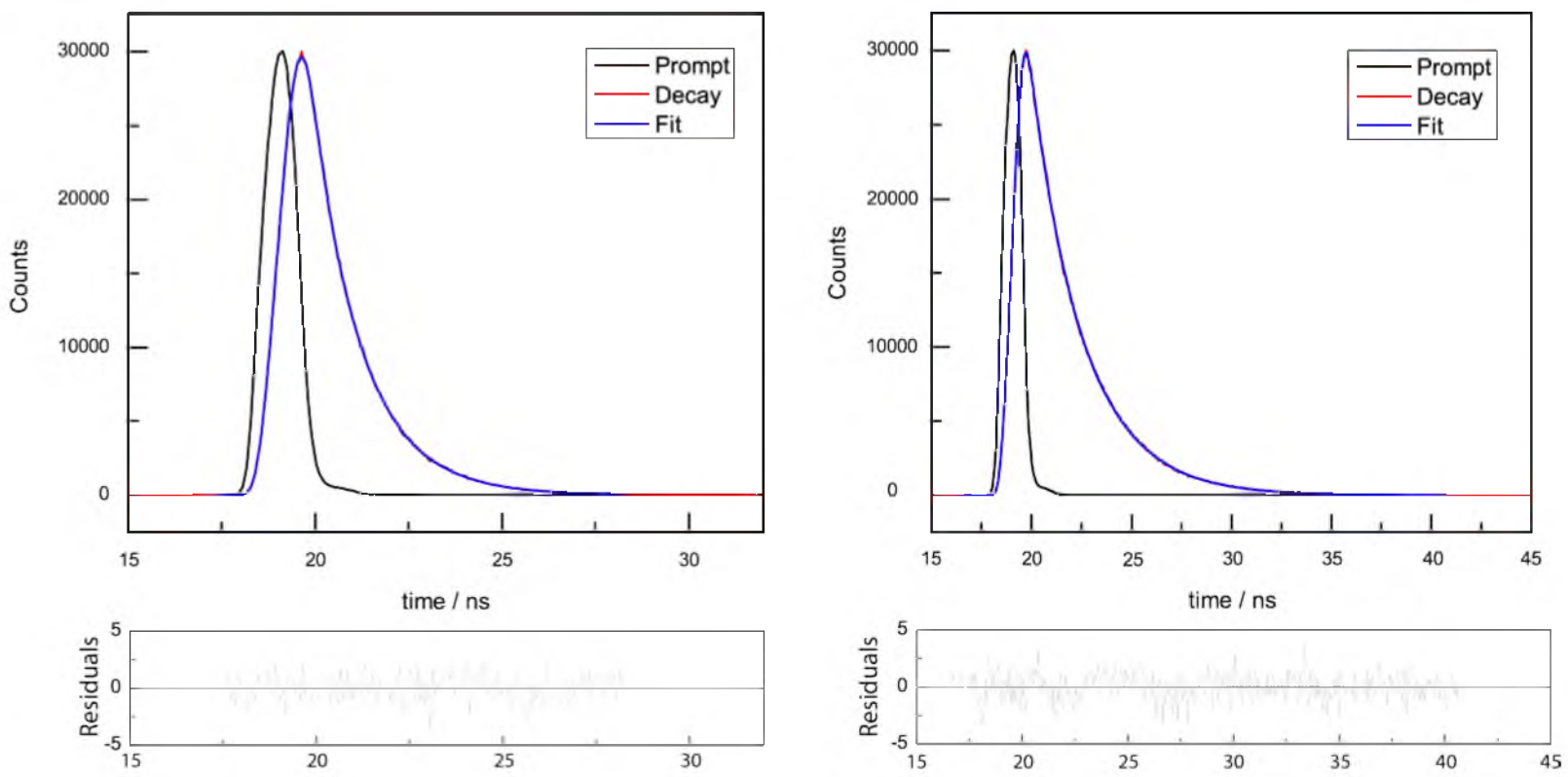

Figure A.85: Excited-state lifetime traces for **4.04** (left) and **4.05A.** (right).

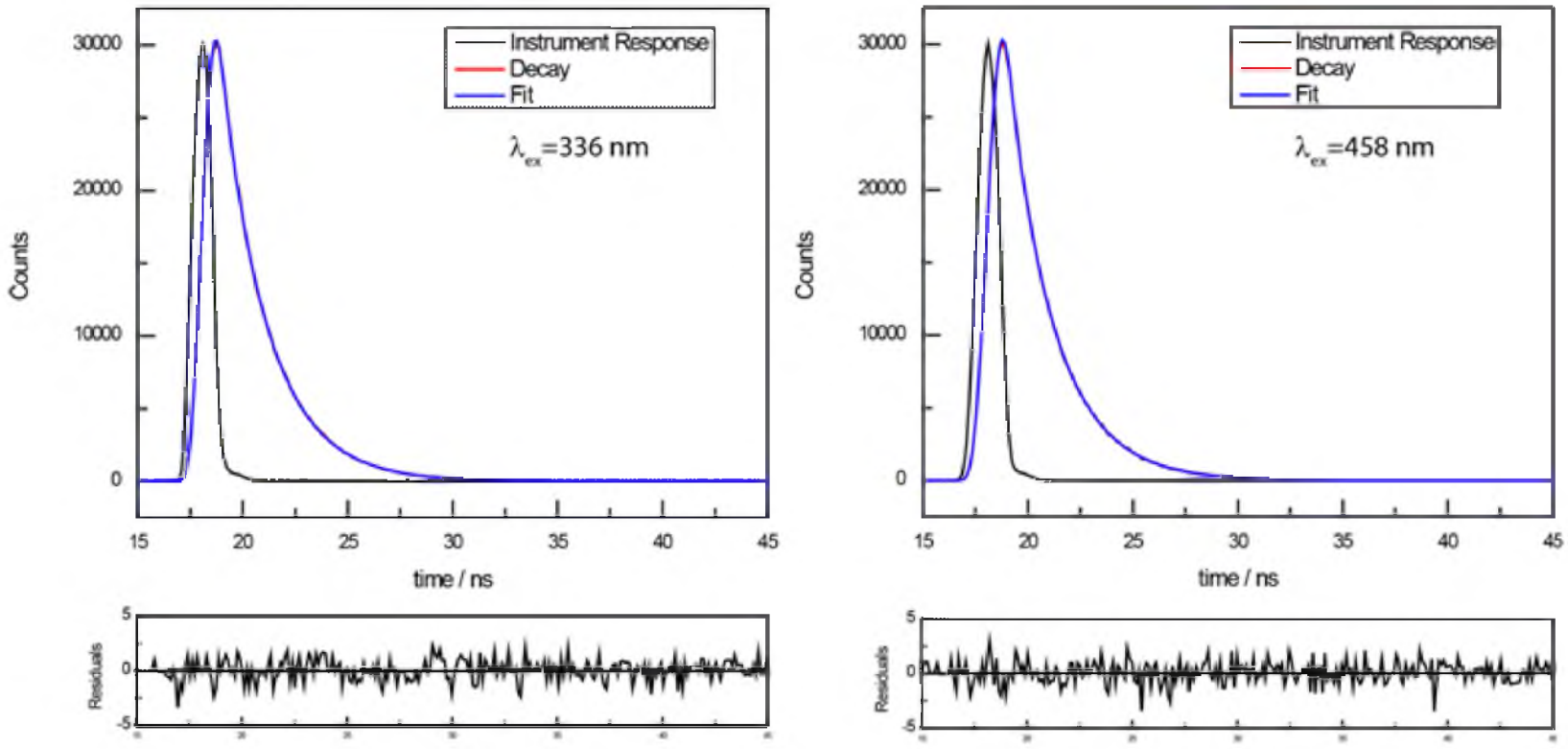

Figure A.86: Excited-state lifetime traces for **4.13** at 336 nm (left) and 458 nm (right).

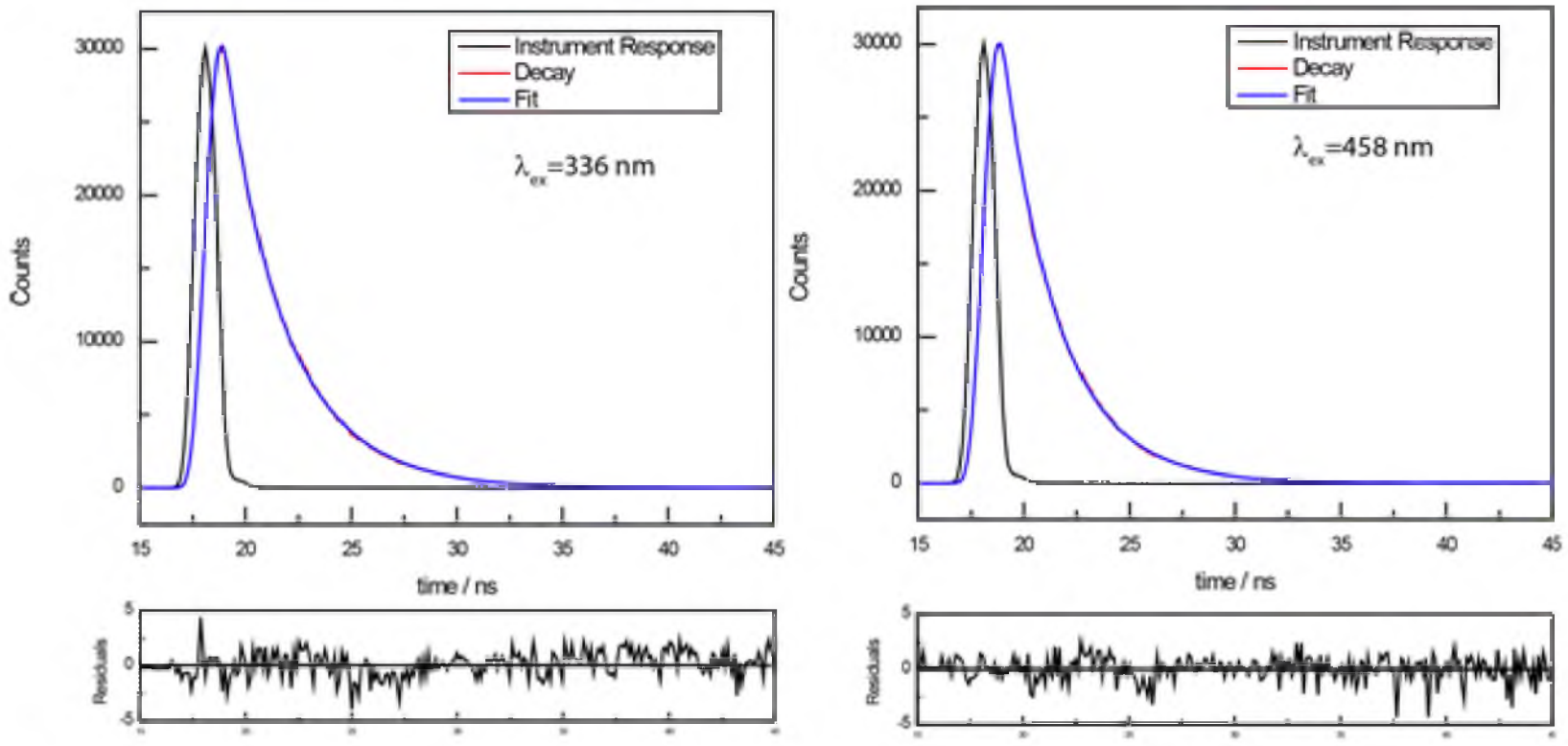

Figure A.87: Excited-state lifetime traces for **4.14** at 336 nm (left) and 458 nm (right).

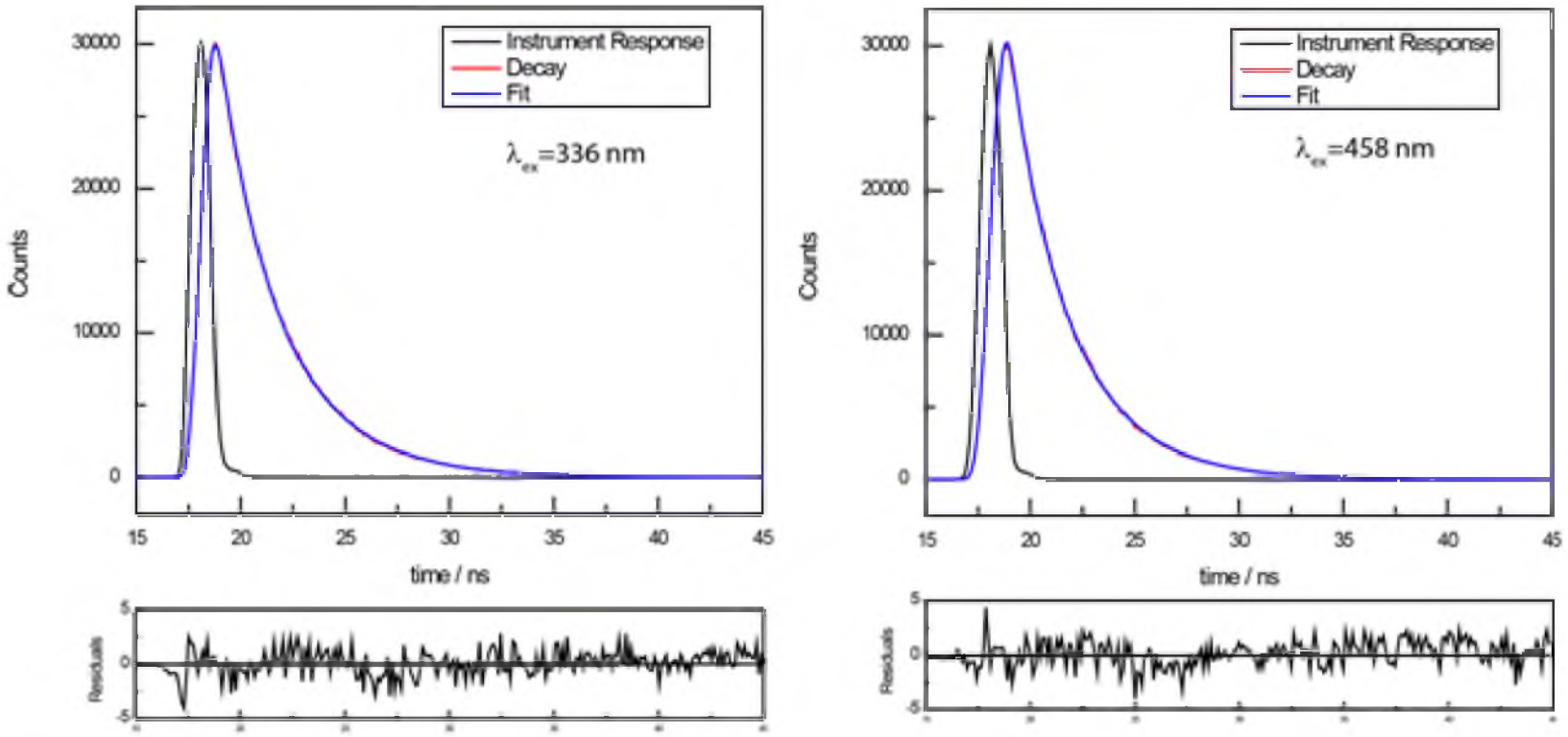

Figure A.88: Excited-state lifetime traces for **4.15** at 336 nm (left) and 458 nm (right).

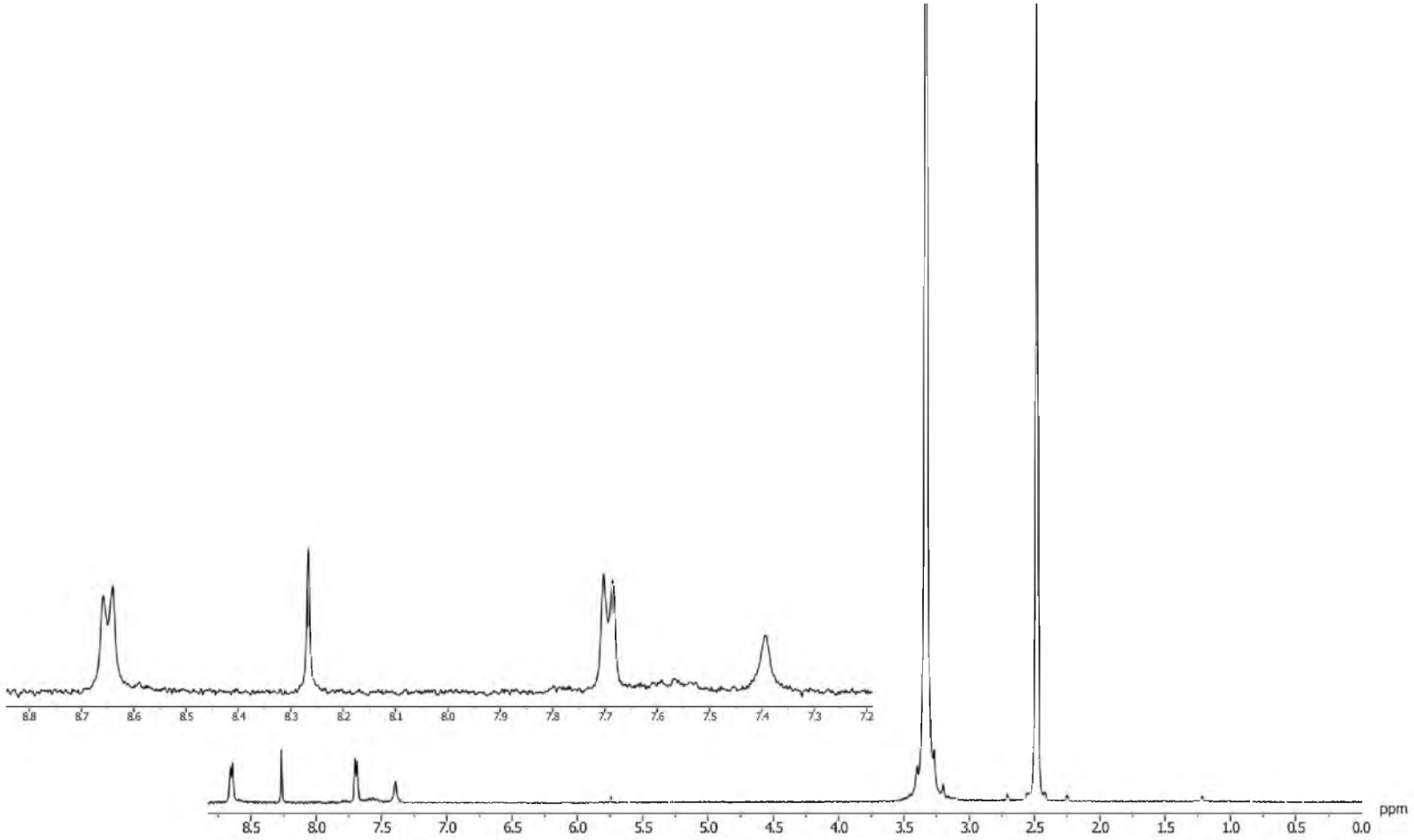

Figure A.89: ^{1}H NMR spectra of **5.01**.

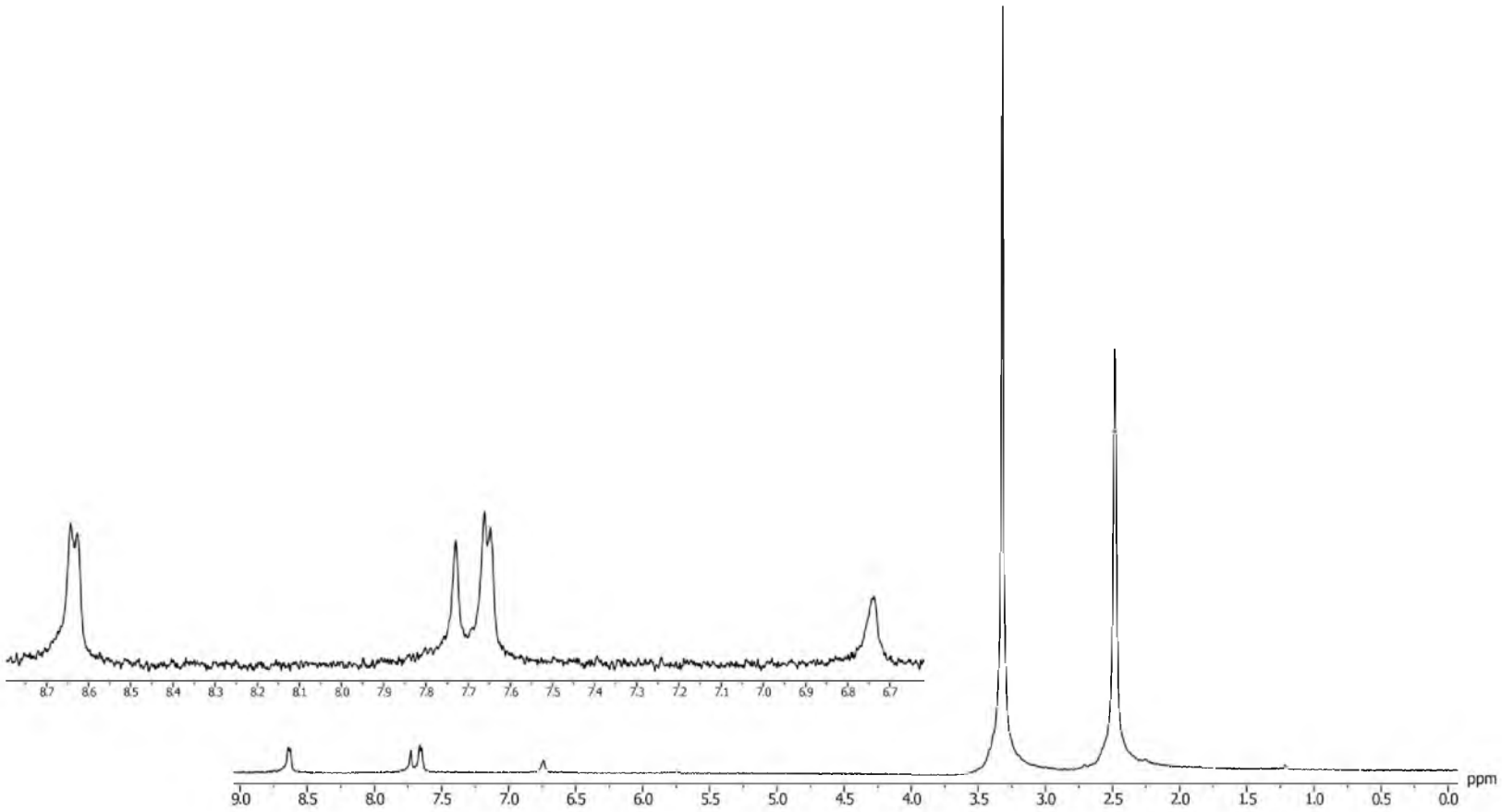

Figure A.90: ^{1}H NMR spectra of **5.02**.

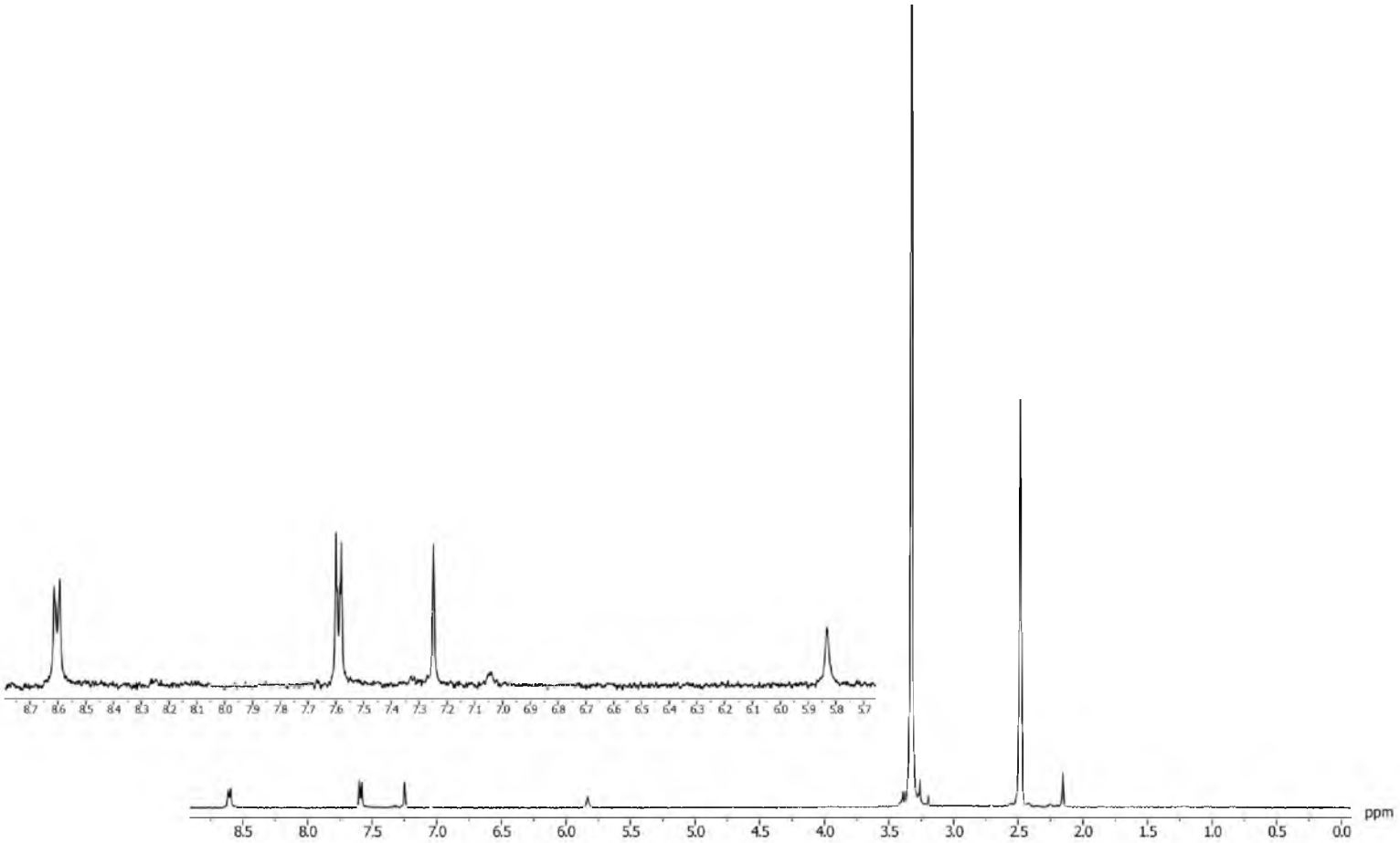

Figure A.91: ^{1}H NMR spectra of **5.04**.

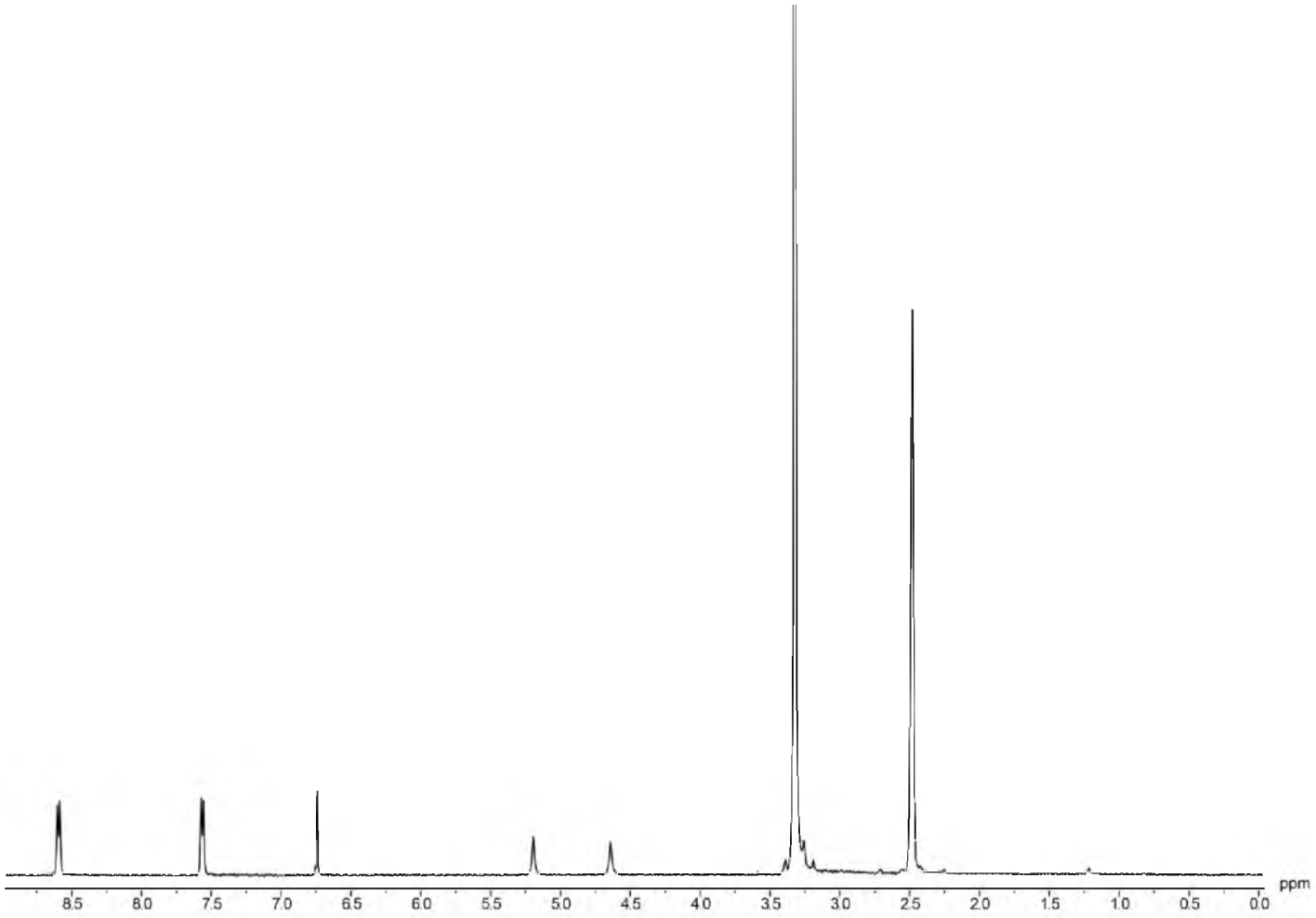

Figure A.92: ^{1}H NMR spectra of **5.05**.

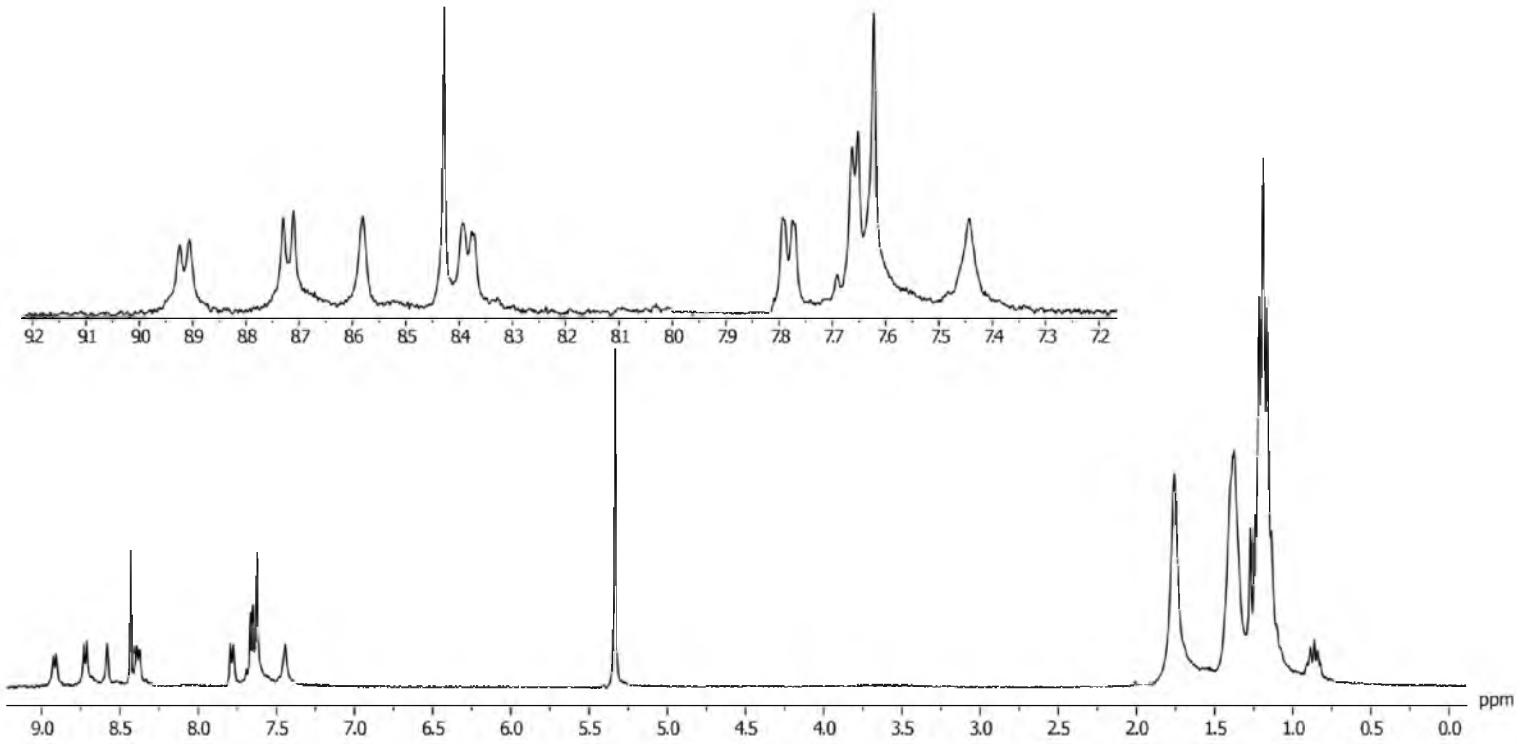

Figure A.93: ^{1}H NMR spectra of **5.07**.

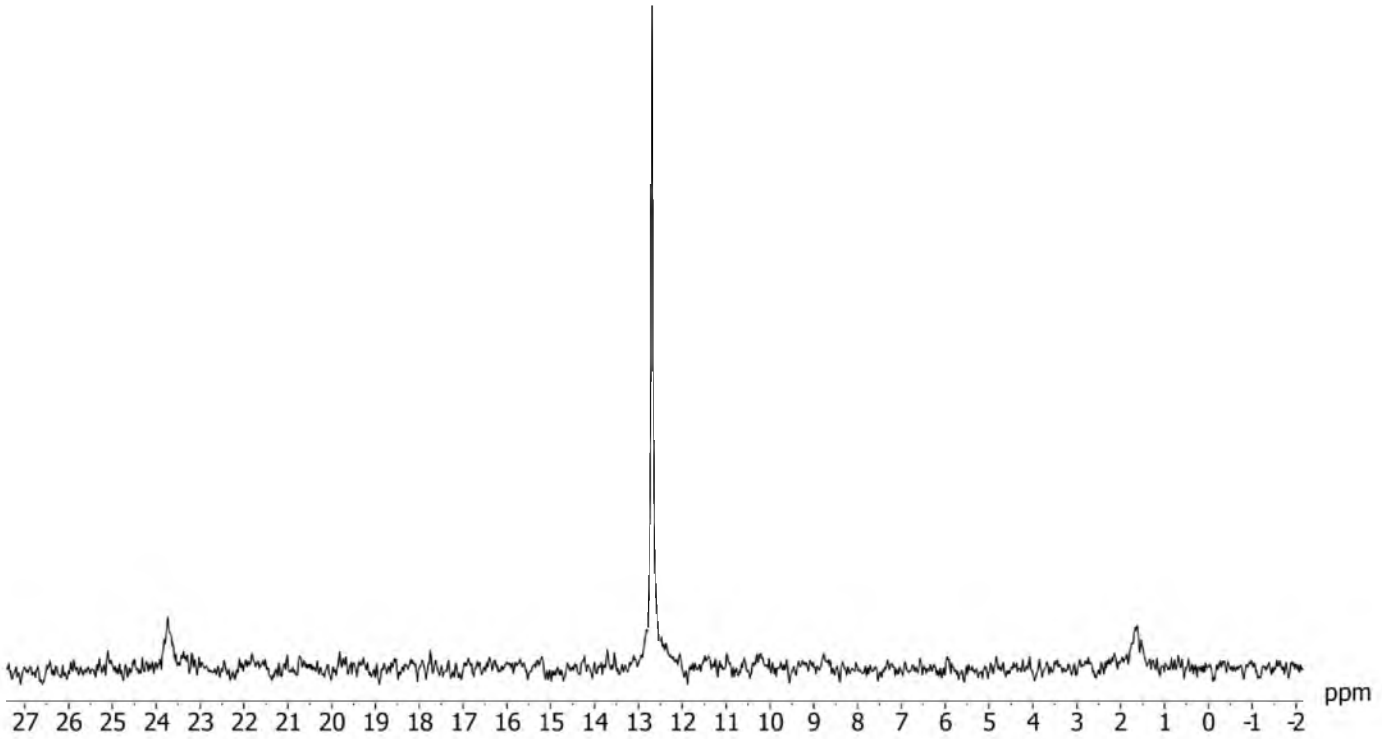

Figure A.94. $^{31}P\{^{1}H\}$ NMR Spectra of **5.07**.

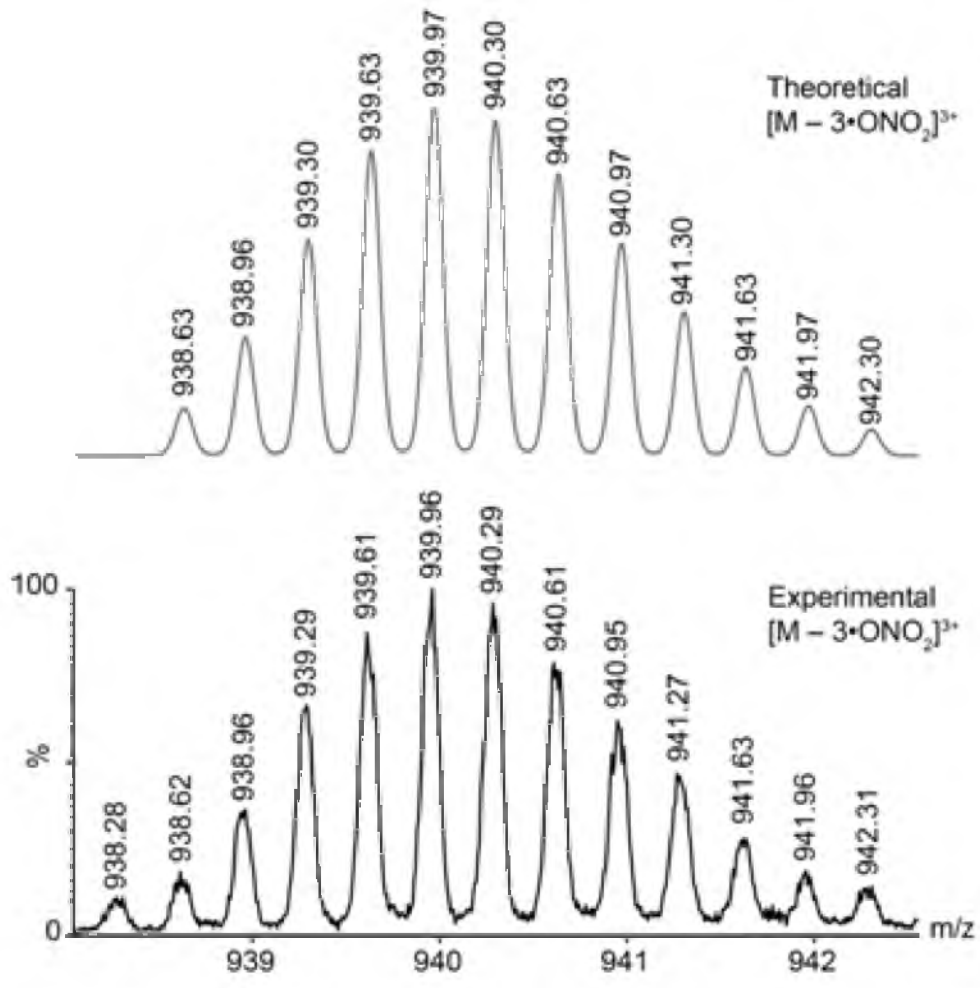

Figure A.95: ESI-MS Spectrum of $[M–3•ONO_2]^{3+}$ of **5.07**.

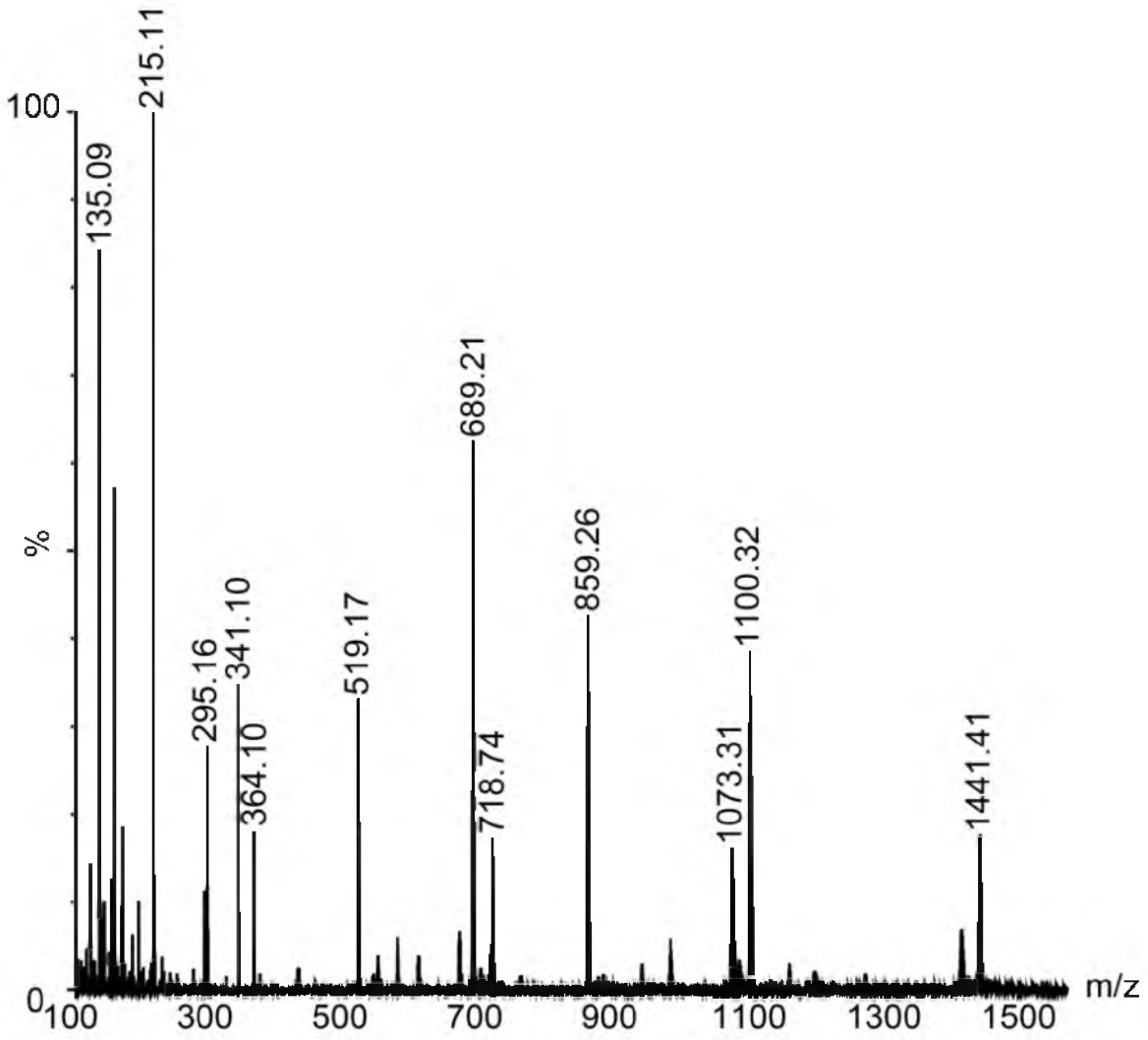

Figure A.96: ESI-MS Spectrum of **5.07**.

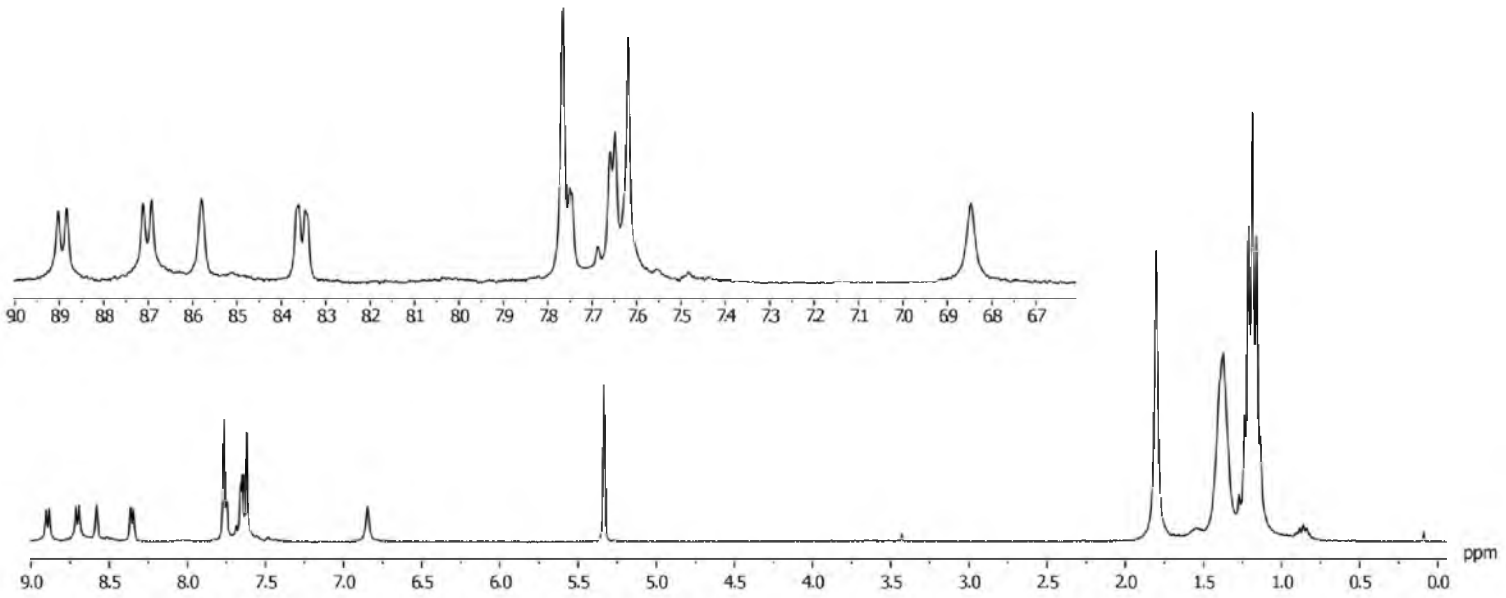

Figure A.97: ^{1}H NMR Spectrum of **5.08**.

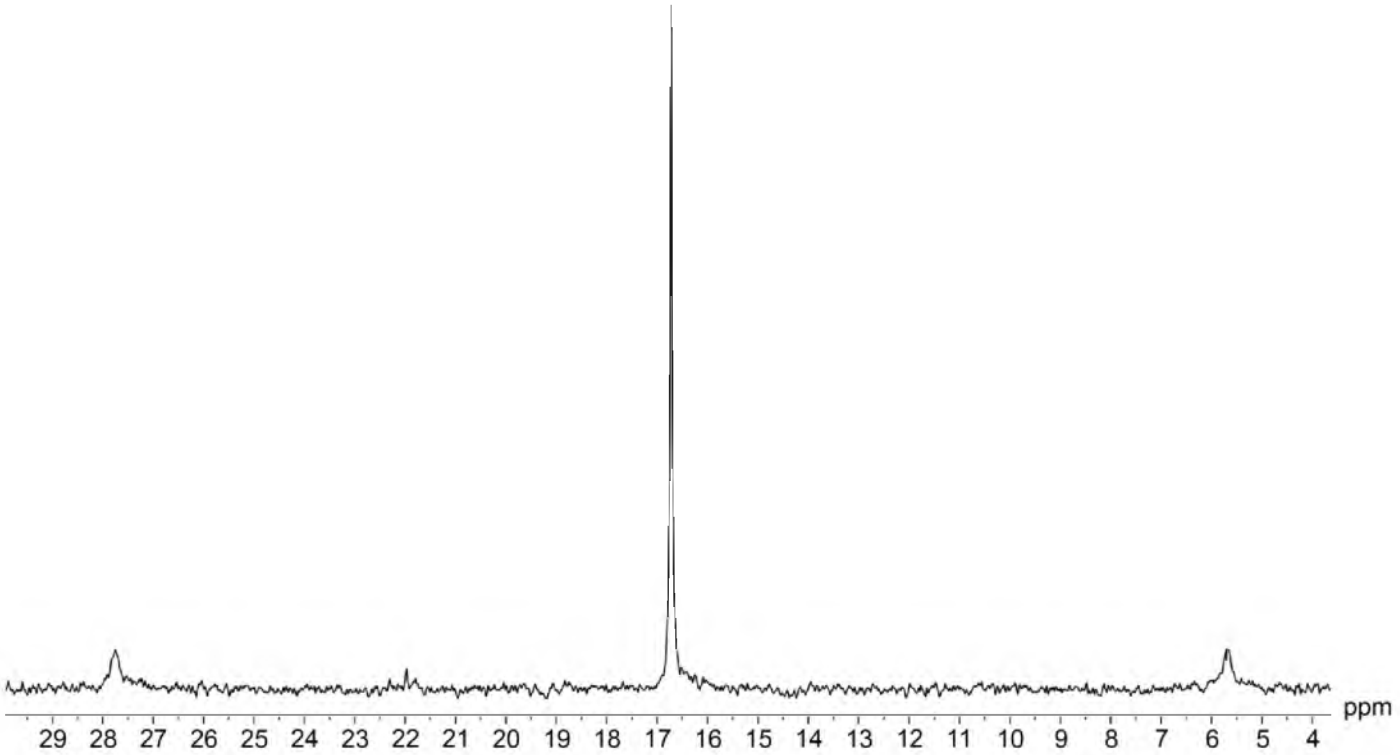

Figure A.98: $^{31}P\{^{1}H\}$ NMR Spectra of **5.08**.

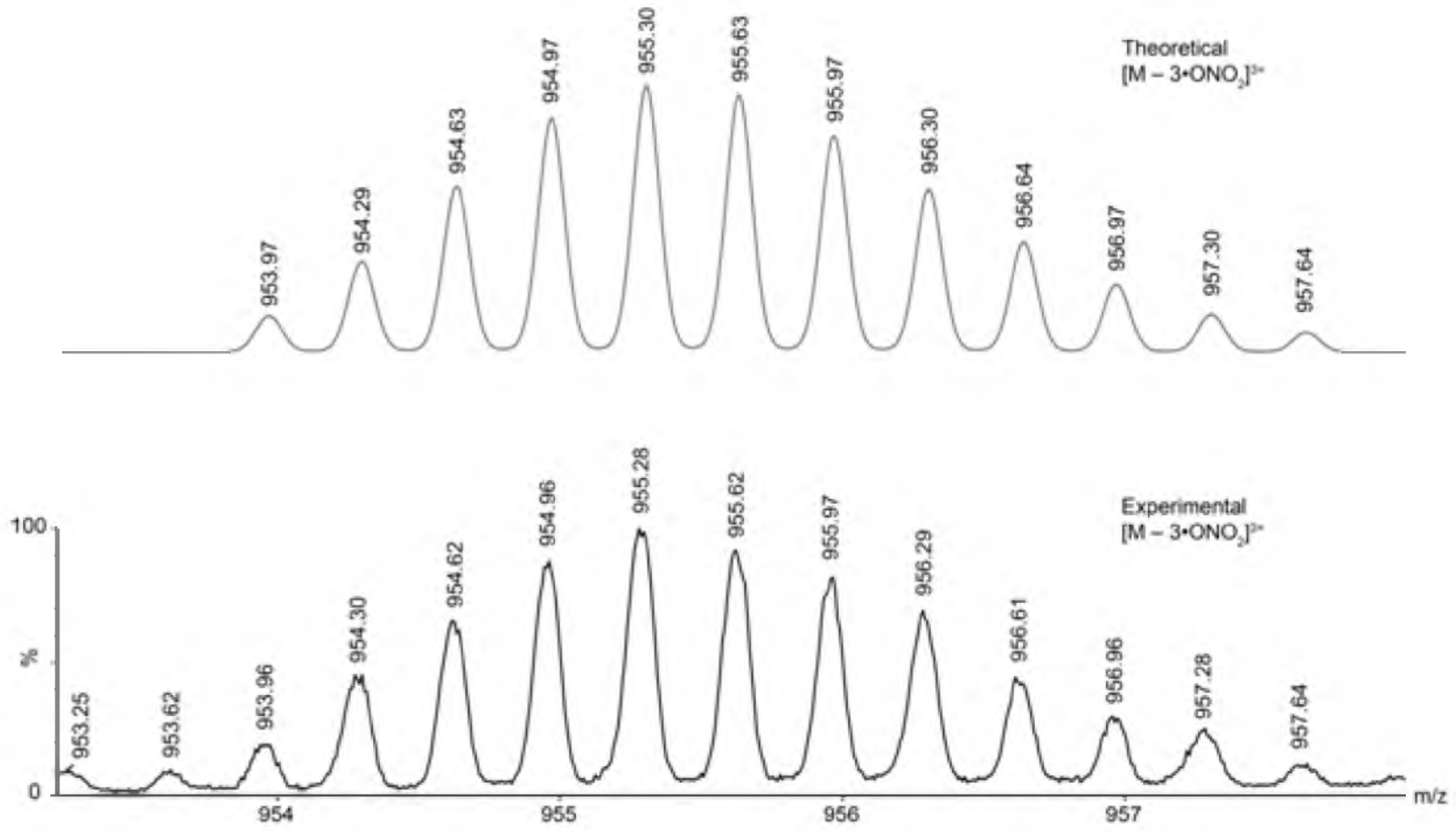

Figure A.99: ESI-MS Spectrum of $[M–3•ONO_2]^{3+}$ of **5.08**.

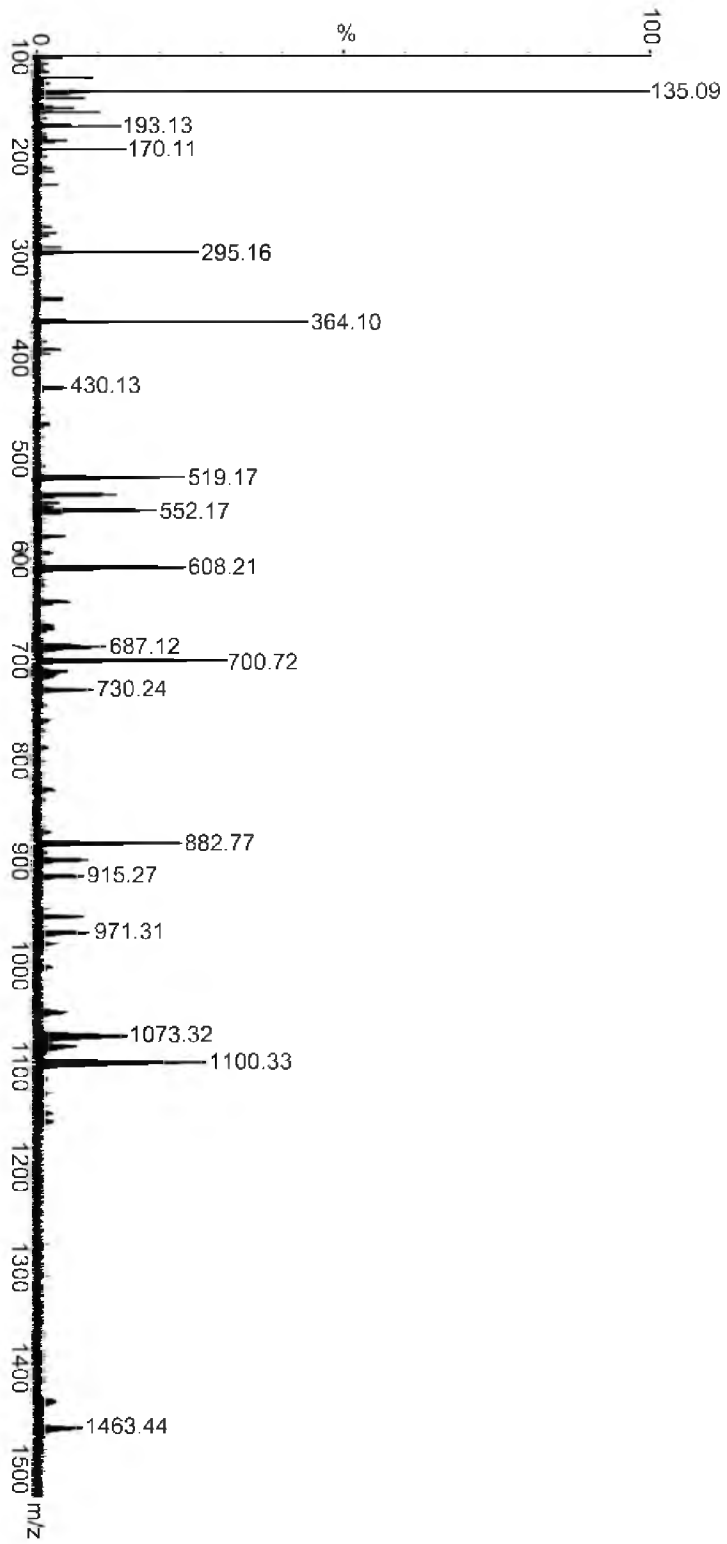

Figure A.100: ESI-MS Spectrum of **5.08**.

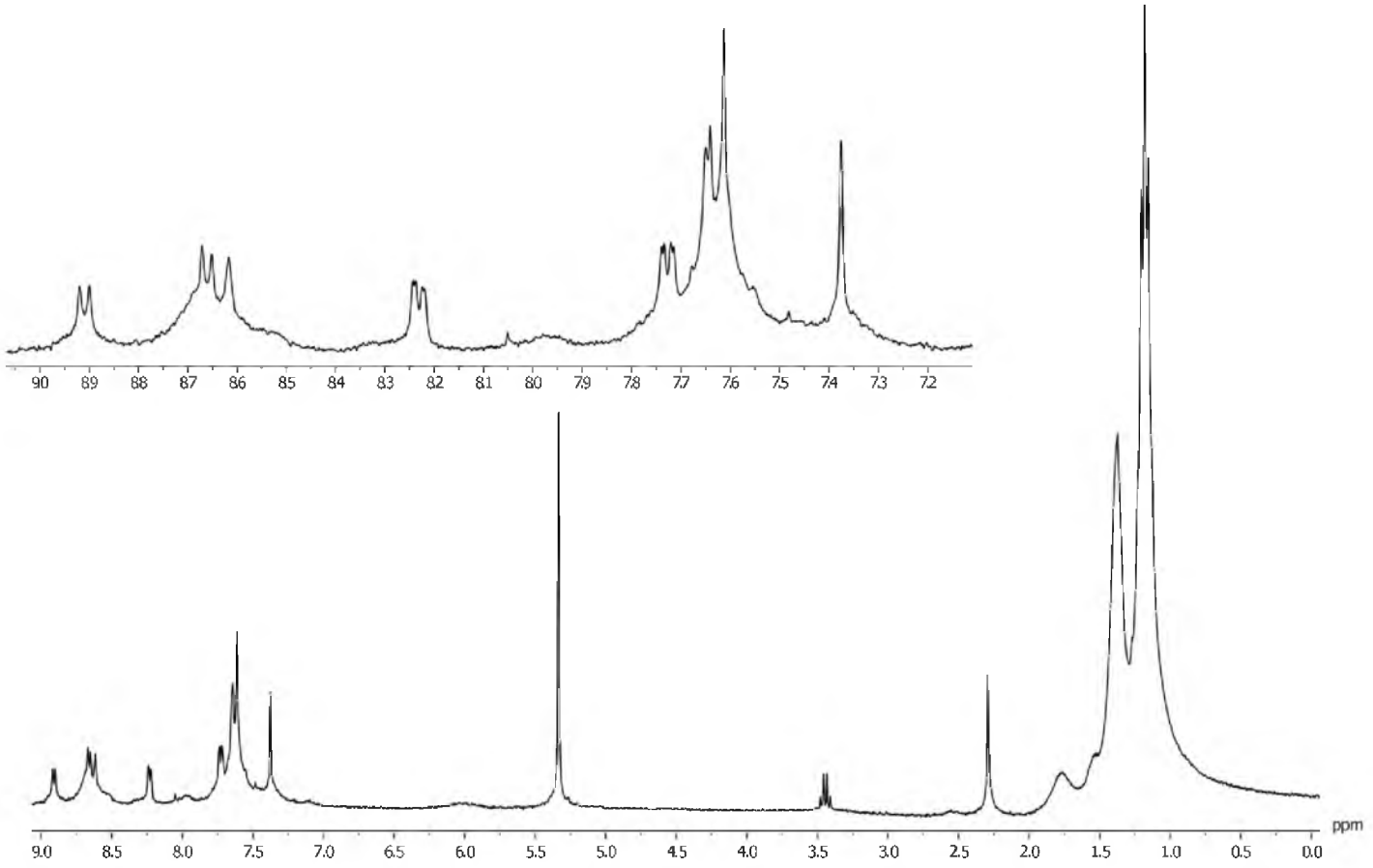

Figure A.101: ^{1}H NMR Spectra of **5.10**.

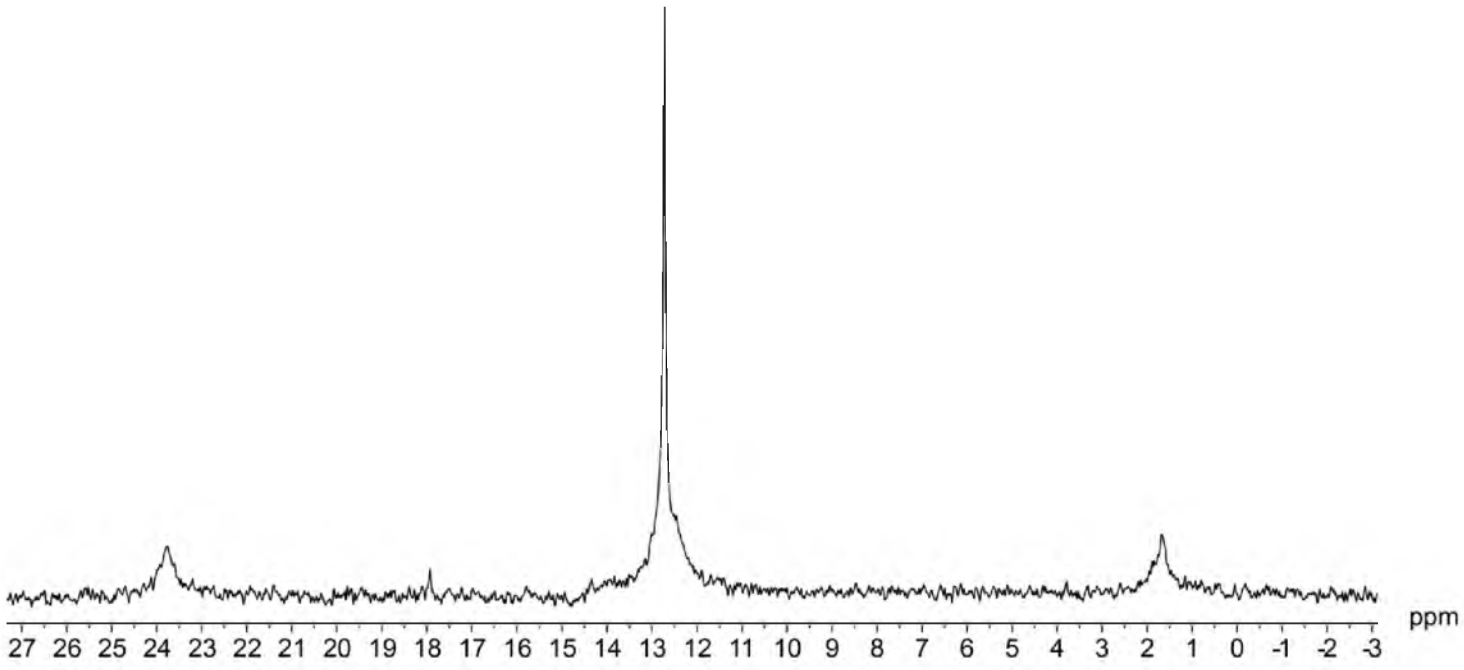

Figure A.102: $^{31}P\{^{1}H\}$ NMR Spectra of **5.10**.

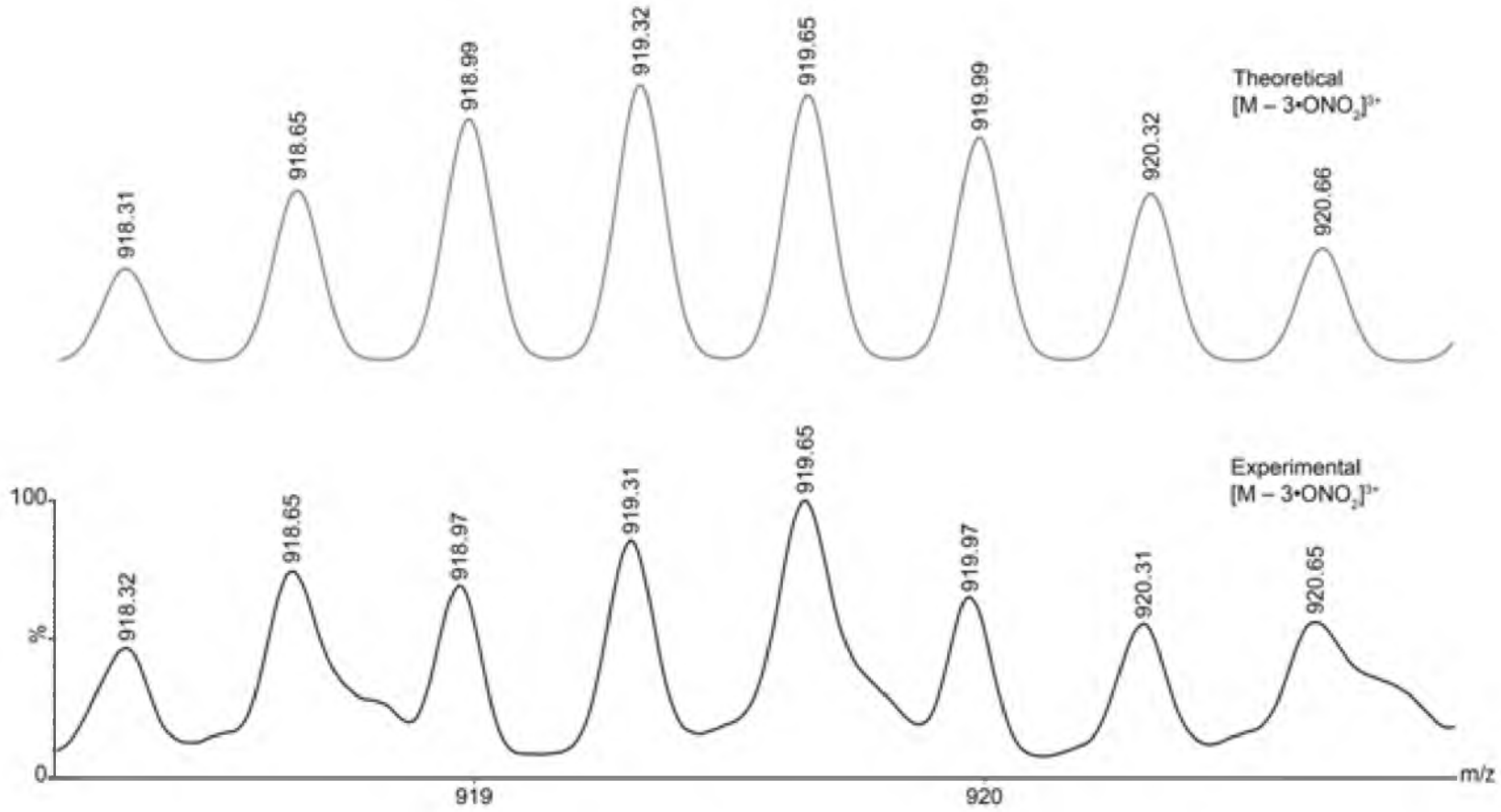

Figure A.103: ESI-MS Spectrum of $[M–3•ONO_2]^{3+}$ of **5.10**.

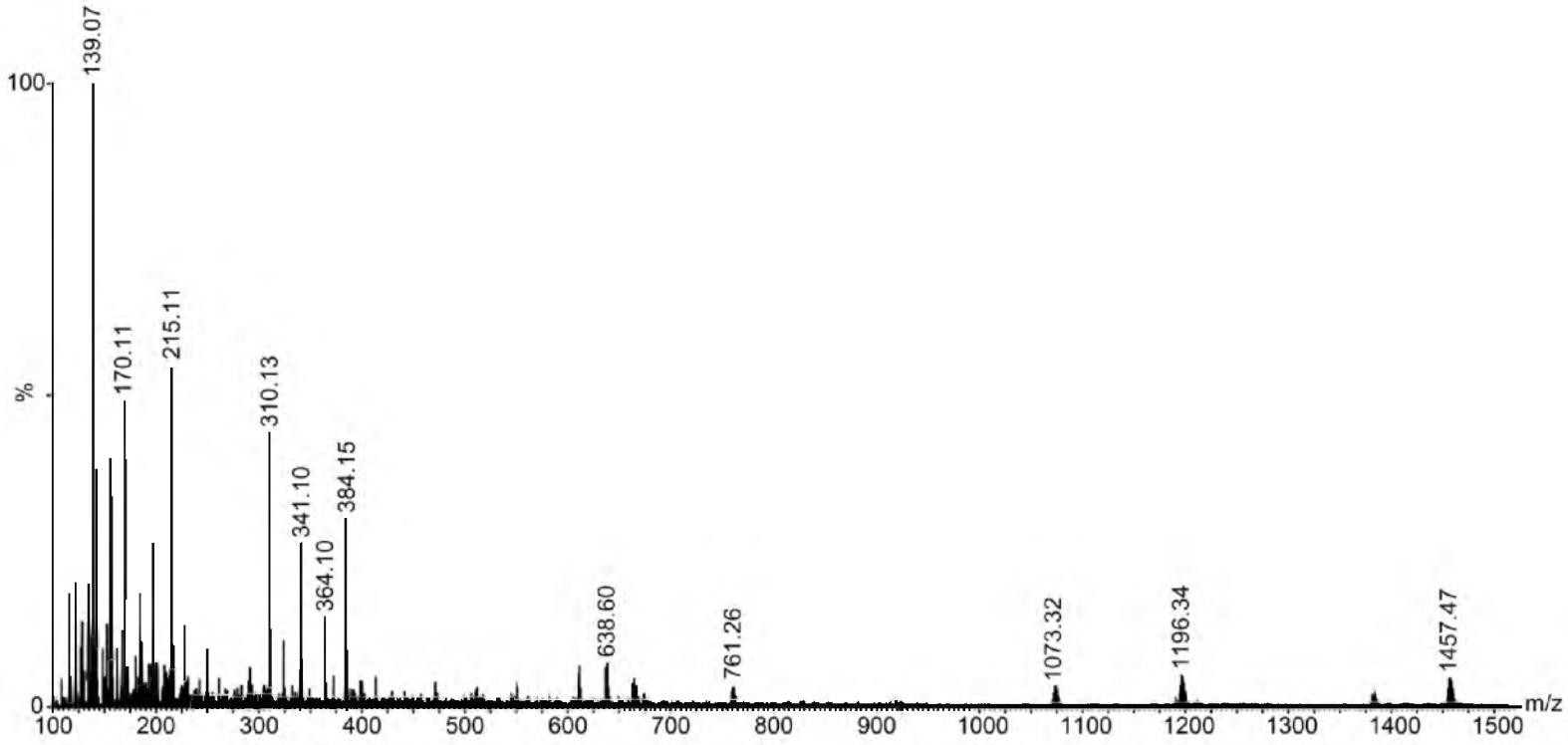

Figure A.104: ESI-MS Spectrum of **5.10**.

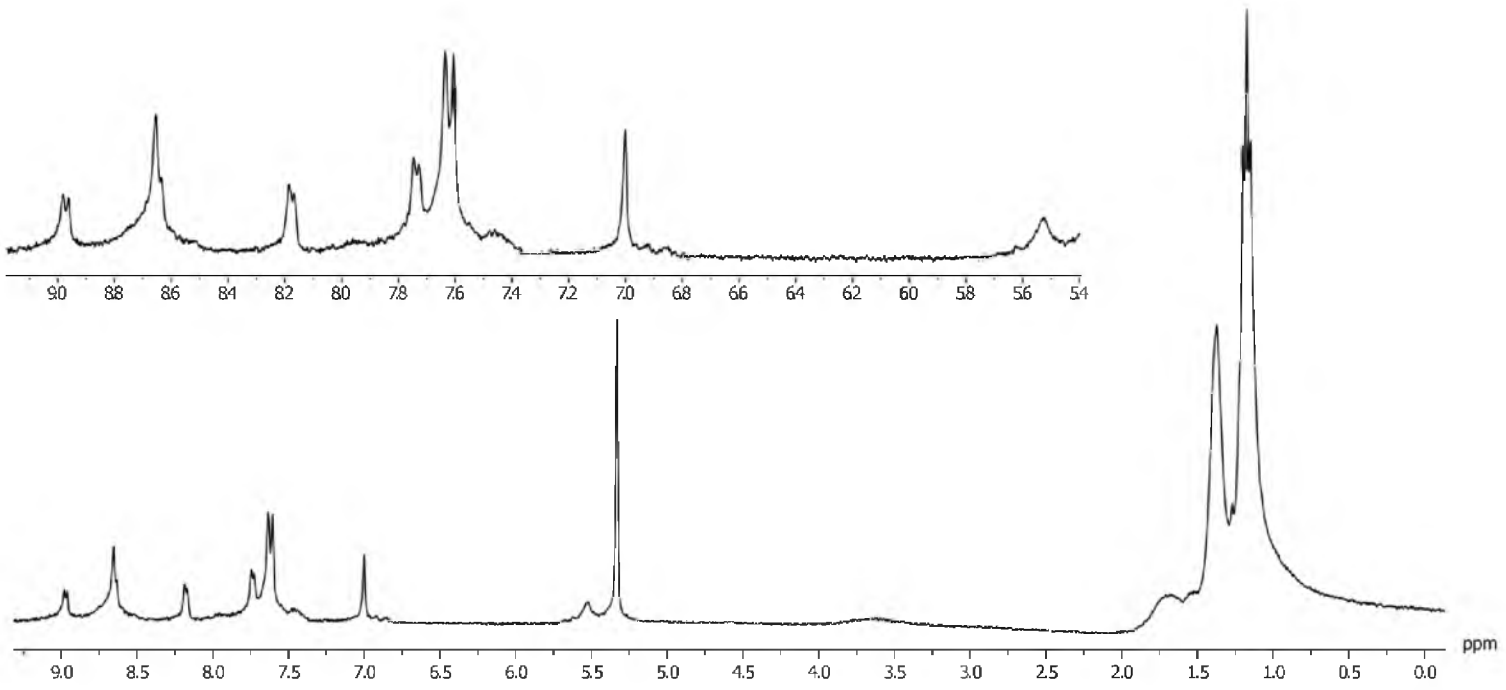

Figure A.105: ^{1}H NMR Spectrum of **5.11**.

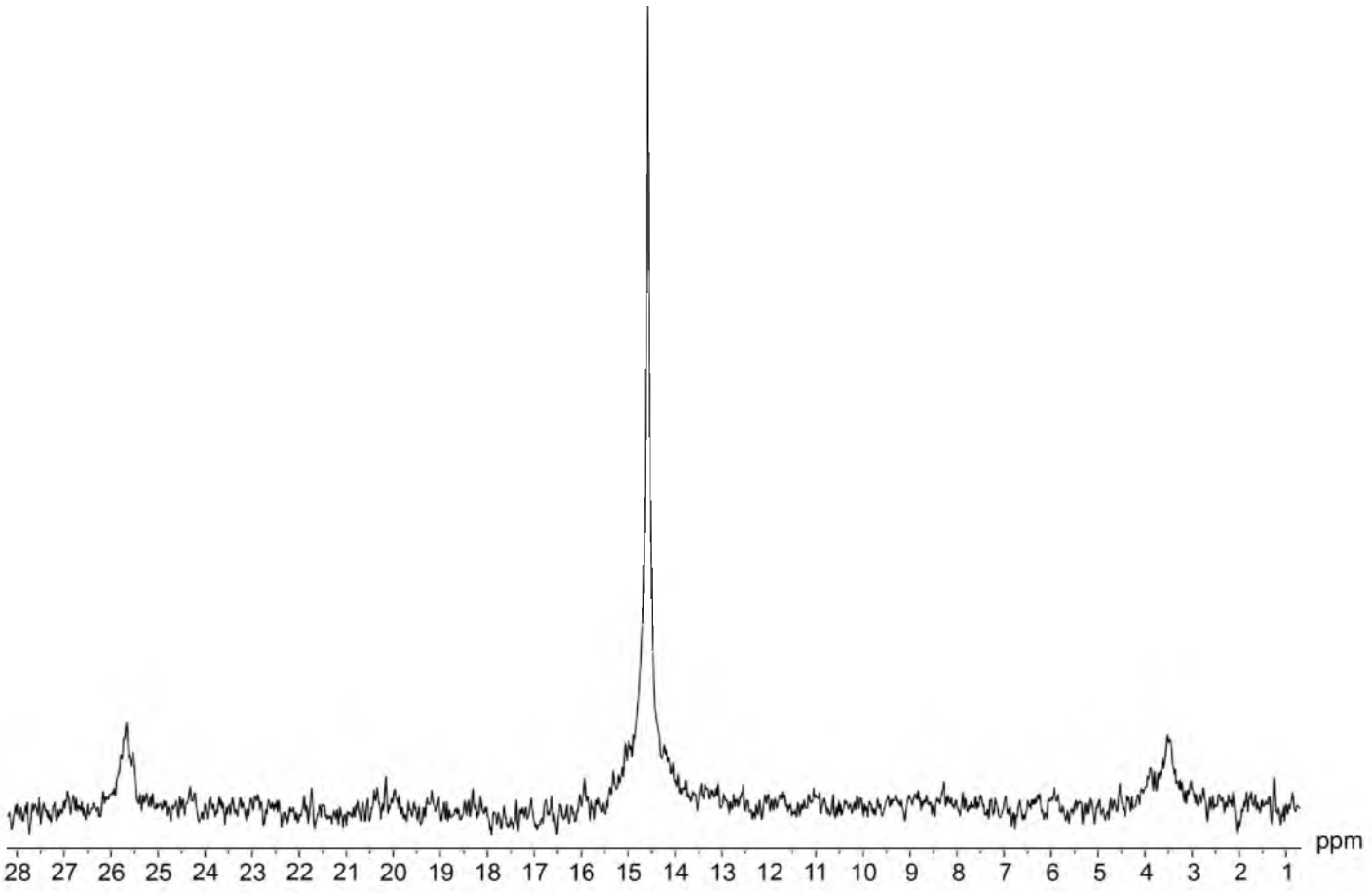

Figure A.106: $^{31}P\{^{1}H\}$ NMR Spectrum of **5.11**.

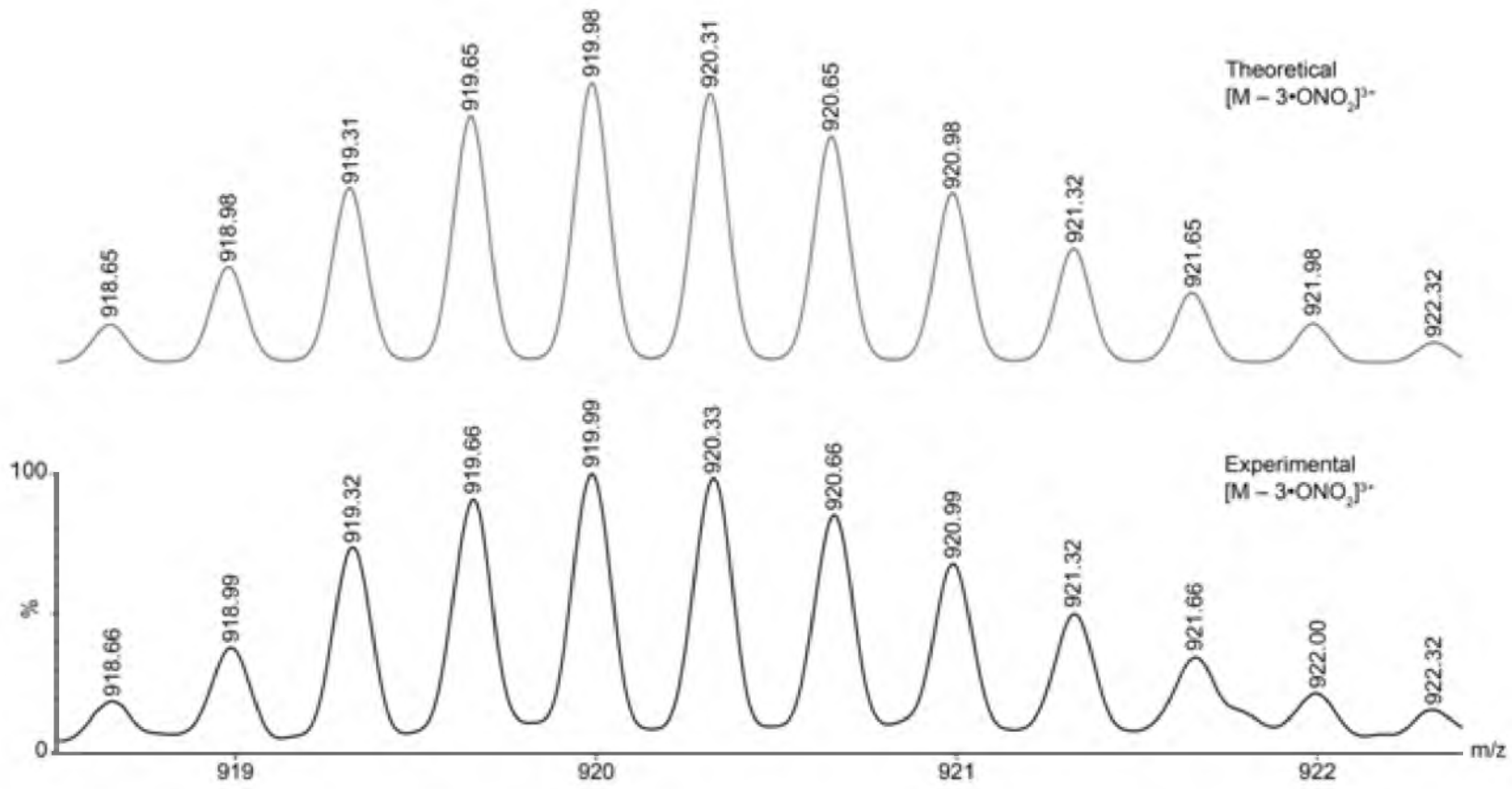

Figure A.107: ESI-MS Spectrum of $[M–3•ONO_2]^{3+}$ of **5.11**.

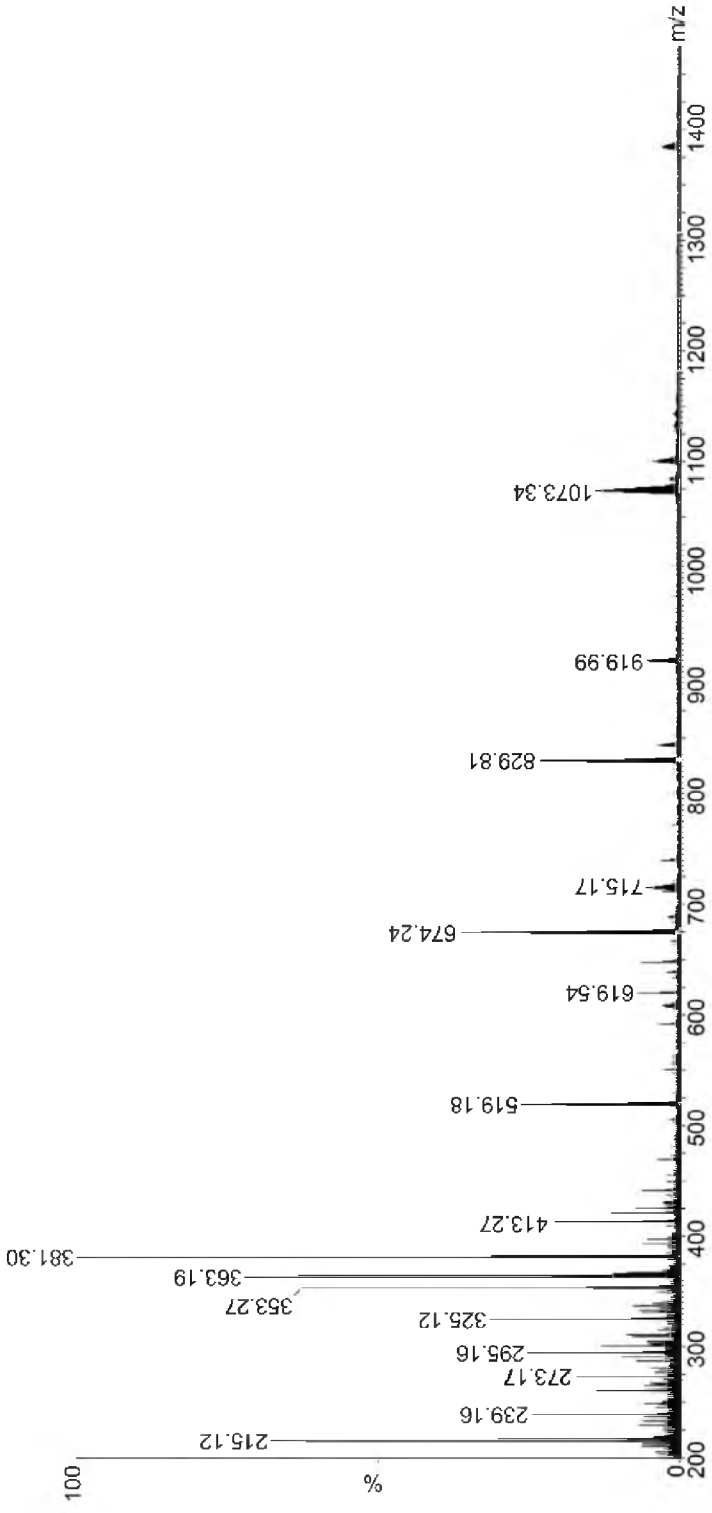

Figure A.108: ESI-MS Spectrum of **5.11**.

Table A.1. Excited-state lifetimes for 4.01, 4.02, 4.04, and 4.05a.

Compound	τ_1 (10^{-9}s)	% Contribution	τ_2 (10^{-9}s)	% Contribution	χ^2
4.01	1.33	3.4	2.59	96.6	1.11
4.02	2.55	100			1.05
4.04	1.37	83.6	0.69	16.4	1.19
5a.	2.58	97.7	0.55	2.3	1.18

Table A.2. Excited-state lifetimes for 4.13–4.15

Compound	τ_1 (10^{-9}s) 336 [458] / nm	% Contribution 336 [458] / nm	τ_2 (10^{-9}s) 336 [458] / nm
4.13	2.20 [2.20]	95.8 [94.6]	0.41 [0.34]
4.14	2.62 [2.64]	95.5 [96.7]	0.30 [0.33]
4.15	3.26 [3.00]	88.5 [94.3]	1.4 [0.73]

% Contribution 336 [458] / nm
4.2 [5.4]
4.5 [3.3]
11.5 [5.7]

Theoretical Excited-States from TD-DFT with a non-zero Oscillator Strength

Compound 3.10-PH_3:

Excited State 2: Singlet-A

2.5751 eV 481.48 nm f=0.3030

<S**2>=0.000

349 -> 354 0.47011

350 -> 353 0.49359

352 -> 354 0.16966

Excited State 4: Singlet-A

2.6604 eV 466.04 nm f=0.0432

<S**2>=0.000

351 -> 353 0.59719

352 -> 355 -0.37509

Excited State 5: Singlet-A

2.6657 eV 465.11 nm f=0.0266

<S**2>=0.000

349 -> 354 -0.14260

351 -> 356 -0.36917

352 -> 354 0.57088

Excited State 6: Singlet-A

2.6657 eV 465.10 nm f=0.0005

<S**2>=0.000

351 -> 354 0.59570

352 -> 356 -0.36423

Excited State 7: Singlet-A

2.6855 eV 461.68 nm f=0.0009

<S**2>=0.000

349 -> 355 0.48235

350 -> 356 0.48828

Excited State 10: Singlet-A

2.8222 eV 439.32 nm f=0.0015

<S**2>=0.000

351 -> 353 0.37126

352 -> 355 0.59029

Excited State 11: Singlet-A

2.8227 eV 439.25 nm f=0.0112

<S**2>=0.000

350 -> 353 -0.17645

351 -> 356 0.57072

352 -> 354 0.36729

Excited State 14: Singlet-A

2.8376 eV 436.93 nm f=0.0007

<S**2>=0.000

349 -> 354 0.49341

350 -> 353 -0.45735

351 -> 356 -0.17953

Excited State 17: Singlet-A

3.1841 eV 389.39 nm f=0.0190

<S**2>=0.000

347 -> 353 0.59450

348 -> 355 0.38017

Excited State 20: Singlet-A

3.1866 eV 389.07 nm f=0.0043

<S**2>=0.000

347 -> 356 0.37705

348 -> 354 0.59727

Excited State 21: Singlet-A

3.2127 eV 385.92 nm f=0.0002

<S**2>=0.000

351 -> 357 0.48727

352 -> 357 0.16303

352 -> 358 -0.45468

Excited State 22: Singlet-A

3.2128 eV 385.91 nm f=0.0099

<S**2>=0.000

351 -> 358 0.48654

352 -> 357 -0.45446

352 -> 358 -0.16528

Excited State 26: Singlet-A

3.3499 eV 370.11 nm f=0.0427

<S**2>=0.000

347 -> 353 -0.38078

348 -> 355 0.59174

Excited State 30: Singlet-A

3.4280 eV 361.68 nm f=0.0016

<S**2>=0.000

351 -> 362 0.48986

352 -> 361 0.48702

Excited State 32: Singlet-A

3.4294 eV 361.53 nm f=2.4633

<S**2>=0.000

345 -> 356 0.48181

346 -> 355 0.50153

Excited State 35: Singlet-A

3.5857 eV 345.77 nm f=0.7839

<S**2>=0.000

345 -> 353 0.38476

346 -> 354 0.58111

Excited State 37: Singlet-A

3.6005 eV 344.35 nm f=0.0287

<S**2>=0.000

345 -> 353 0.58688

346 -> 354 -0.39308

Excited State 39: Singlet-A

3.6405 eV 340.57 nm f=0.0002

<S**2>=0.000

349 -> 357 0.45438

349 -> 359 -0.16696

350 -> 357 0.21395

350 -> 359 -0.41743

352 -> 357 0.11531

Excited State 44: Singlet-A

3.6748 eV 337.39 nm f=0.0003

<S**2>=0.000

345 -> 356 0.50905

346 -> 355 -0.48964

Excited State 55: Singlet-A

3.7510 eV 330.53 nm f=0.0003

<S**2>=0.000

347 -> 359 -0.34879

347 -> 360 0.34784

348 -> 359 0.45888

348 -> 360 -0.17192

Excited State 56: Singlet-A

3.7510 eV 330.53 nm f=0.0007

<S**2>=0.000

347 -> 359 0.34669

347 -> 360 0.34573

348 -> 359 0.17422

348 -> 360 0.46120

Excited State 57: Singlet-A

3.7954 eV 326.67 nm f=0.0001

<S**2>=0.000

349 -> 361 0.52886

350 -> 363 -0.36666

351 -> 367 -0.10692

352 -> 361 0.14668

352 -> 368 0.14433

Excited State 60: Singlet-A

3.7964 eV 326.58 nm f=0.0005

<S**2>=0.000

349 -> 364 0.32183

350 -> 362 0.48475

350 -> 367 -0.11560

351 -> 366 -0.19776

351 -> 367 -0.11192

352 -> 365 0.25243

Compound 3.11-PH_3:

Excited State 2: Singlet-A

2.5835 eV 479.91 nm f=0.2018

<S**2>=0.000

351 -> 356 0.23262

352 -> 354 0.65540

Excited State 3: Singlet-A

2.5866 eV 479.34 nm f=0.0330

<S**2>=0.000

351 -> 353 0.66208

352 -> 355 0.24603

Excited State 6: Singlet-A

2.7054 eV 458.29 nm f=1.1438

<S**2>=0.000

349 -> 354 -0.48211

350 -> 353 0.49267

Excited State 7: Singlet-A

2.8017 eV 442.53 nm f=0.0099

<S**2>=0.000

351 -> 353 -0.24656

352 -> 355 0.66183

Excited State 10: Singlet-A

2.8064 eV 441.80 nm f=0.0364

<S**2>=0.000

351 -> 356 0.66020

352 -> 354 -0.24569

Excited State 13: Singlet-A

3.0380 eV 408.12 nm f=0.0547

<S**2>=0.000

349 -> 355 -0.48296

350 -> 356 0.49353

Excited State 14: Singlet-A

3.0413 eV 407.67 nm f=0.0001

<S**2>=0.000

345 -> 354 0.10120

346 -> 353 0.10233

349 -> 356 -0.47236

350 -> 355 0.50113

Excited State 16: Singlet-A

3.1152 eV 398.00 nm f=0.0041

<S**2>=0.000

347 -> 353 0.65883

348 -> 355 0.25394

Excited State 17: Singlet-A

3.1163 eV 397.85 nm f=0.0031

<S**2>=0.000

347 -> 356 0.25064

348 -> 354 0.65824

Excited State 21: Singlet-A

3.1956 eV 387.98 nm f=0.0006

<S**2>=0.000

351 -> 357 0.48795

352 -> 357 0.24556

352 -> 358 -0.42164

Excited State 22: Singlet-A

3.1957 eV 387.97 nm f=0.0090

<S**2>=0.000

351 -> 358 0.48664

352 -> 357 -0.42157

352 -> 358 -0.24818

Excited State 25: Singlet-A

3.3350 eV 371.77 nm f=0.0180

<S**2>=0.000

347 -> 353 -0.25516

348 -> 355 0.65833

Excited State 29: Singlet-A

3.4178 eV 362.77 nm f=0.0007

<S**2>=0.000

351 -> 361 0.38493

351 -> 362 -0.30374

352 -> 361 -0.35617

352 -> 362 0.34237

Excited State 30: Singlet-A

3.4178 eV 362.76 nm f=0.0007

<S**2>=0.000

351 -> 361 0.30600

351 -> 362 0.38642

352 -> 361 0.34120

352 -> 362 0.35372

Excited State 32: Singlet-A

3.4615 eV 358.18 nm f=0.0005

<S**2>=0.000

351 -> 364 0.48539

352 -> 363 0.49336

Excited State 34: Singlet-A

3.5082 eV 353.41 nm f=2.3945

<S**2>=0.000

345 -> 356 0.48388

346 -> 355 0.50427

Excited State 35: Singlet-A

3.6001 eV 344.39 nm f=0.0959

<S**2>=0.000

345 -> 353 -0.31645

346 -> 354 0.62335

Excited State 36: Singlet-A

3.6003 eV 344.37 nm f=0.0015

<S**2>=0.000

345 -> 354 -0.38831

346 -> 353 0.58314

Excited State 37: Singlet-A

3.6145 eV 343.02 nm f=0.8230

<S**2>=0.000

345 -> 353 0.61819

346 -> 354 0.29741

Excited State 38: Singlet-A

3.6312 eV 341.45 nm f=0.0031

<S**2>=0.000

345 -> 354 0.57602

346 -> 353 0.37160

Excited State 45: Singlet-A

3.7358 eV 331.88 nm f=0.0003

<S**2>=0.000

347 -> 359 0.41628

347 -> 360 -0.24526

348 -> 359 0.43919

348 -> 360 -0.22416

Excited State 46: Singlet-A

3.7359 eV 331.87 nm f=0.0004

<S**2>=0.000

347 -> 359 -0.24800

347 -> 360 -0.42168

348 -> 359 0.22114

348 -> 360 0.43400

Excited State 47: Singlet-A

3.7538 eV 330.29 nm f=0.0004

<S**2>=0.000

351 -> 365 -0.21550

351 -> 366 -0.44121

352 -> 365 0.46431

352 -> 366 0.19312

Excited State 48: Singlet-A

3.7538 eV 330.29 nm f=0.0001

<S**2>=0.000

351 -> 365 -0.44306

351 -> 366 0.21604

352 -> 365 -0.18997

352 -> 366 0.46121

Excited State 50: Singlet-A

3.7542 eV 330.25 nm f=0.0001

<S**2>=0.000

351 -> 367 0.39168

351 -> 368 0.29889

352 -> 367 0.27047

352 -> 368 0.41974

Excited State 51: Singlet-A

3.7696 eV 328.91 nm f=0.0001

<S**2>=0.000

345 -> 355 0.45954

345 -> 356 0.20608

346 -> 355 -0.21310

346 -> 356 -0.44418

Excited State 52: Singlet-A

3.7697 eV 328.90 nm f=0.0004

<S**2>=0.000

345 -> 355 -0.20619

345 -> 356 0.46490

346 -> 355 -0.43863

346 -> 356 0.21282

Excited State 55: Singlet-A

3.8408 eV 322.81 nm f=0.0001

<S**2>=0.000

349 -> 359 0.44429

350 -> 357 0.51430

Excited State 57: Singlet-A

3.8415 eV 322.75 nm f=0.0023

<S**2>=0.000

349 -> 357 0.49891

350 -> 359 0.45916

Excited State 58: Singlet-A

3.8417 eV 322.73 nm f=0.0001

<S**2>=0.000

349 -> 358 0.49841

350 -> 360 0.45884

Compound 3.12-PH_3:

Excited State 2: Singlet-A

2.5742 eV 481.64 nm f=0.0384

<S**2>=0.000

343 -> 347 -0.38943

344 -> 345 0.58915

Excited State 3: Singlet-A

2.5780 eV 480.94 nm f=0.0554

<S**2>=0.000

343 -> 346 0.58849

344 -> 348 0.39029

Excited State 6: Singlet-A

2.7274 eV 454.58 nm f=0.0013

<S**2>=0.000

343 -> 347 0.58953

344 -> 345 0.39025

Excited State 7: Singlet-A

2.7293 eV 454.28 nm f=0.0053

<S**2>=0.000

343 -> 346 -0.39116

344 -> 348 0.58884

Excited State 9: Singlet-A

3.0994 eV 400.03 nm f=0.0164

<S**2>=0.000

341 -> 345 0.58425

342 -> 347 0.39649

Excited State 12: Singlet-A

3.1018 eV 399.72 nm f=0.0033

<S**2>=0.000

341 -> 348 -0.39475

342 -> 346 0.58579

Excited State 13: Singlet-A

3.1994 eV 387.52 nm f=0.0001

<S**2>=0.000

343 -> 350 -0.48353

344 -> 349 0.48920

Excited State 14: Singlet-A

3.1995 eV 387.52 nm f=0.0100

<S**2>=0.000

343 -> 349 -0.48352

344 -> 350 0.48887

Excited State 17: Singlet-A

3.2578 eV 380.58 nm f=0.0061

<S**2>=0.000

341 -> 345 -0.39732

342 -> 347 0.58413

Excited State 22: Singlet-A

3.4205 eV 362.47 nm f=0.0002

<S**2>=0.000

343 -> 353 -0.22864

343 -> 354 0.43737

344 -> 353 0.44327

344 -> 354 -0.21478

Excited State 23: Singlet-A

3.4206 eV 362.47 nm f=0.0007

<S**2>=0.000

343 -> 353 0.43673

343 -> 354 0.22602

344 -> 353 0.21737

344 -> 354 0.44398

Excited State 24: Singlet-A

3.4324 eV 361.22 nm f=1.5737

<S**2>=0.000

337 -> 346 -0.10031

339 -> 348 0.47492

340 -> 347 0.49351

Excited State 28: Singlet-A

3.6193 eV 342.57 nm f=0.6351

<S**2>=0.000

339 -> 345 -0.36564

340 -> 346 0.58249

Excited State 30: Singlet-A

3.6396 eV 340.65 nm f=0.0271

<S**2>=0.000

339 -> 345 0.59237

340 -> 346 0.38216

Excited State 32: Singlet-A

3.6611 eV 338.65 nm f=2.5610

<S**2>=0.000

335 -> 345 -0.24450

337 -> 346 0.45961

338 -> 345 0.43789

340 -> 347 0.14910

Excited State 38: Singlet-A

3.7013 eV 334.97 nm f=0.0403

<S**2>=0.000

339 -> 348 0.51558

340 -> 347 -0.47582

Excited State 41: Singlet-A

3.7382 eV 331.67 nm f=0.0001

<S**2>=0.000

341 -> 351 -0.21046

341 -> 352 -0.44664

342 -> 351 0.47389

342 -> 352 0.14440

Excited State 42: Singlet-A

3.7382 eV 331.67 nm f=0.0009

<S**2>=0.000

341 -> 351 -0.44723

341 -> 352 0.21241

342 -> 351 -0.14255

342 -> 352 0.47302

Excited State 43: Singlet-A

3.7464 eV 330.94 nm f=0.0001

<S**2>=0.000

343 -> 357 0.46614

343 -> 358 0.17084

344 -> 357 0.19398

344 -> 358 0.45979

Excited State 50: Singlet-A

3.8719 eV 320.22 nm f=0.0030

<S**2>=0.000

341 -> 361 0.23105

342 -> 362 0.23507

343 -> 363 -0.43062

344 -> 364 0.43246

Excited State 51: Singlet-A

3.8794 eV 319.59 nm f=0.1209

<S**2>=0.000

335 -> 348	-0.14000
336 -> 346	0.48161
337 -> 347	0.11609
338 -> 348	-0.47557

Excited State 55: Singlet-A

3.8868 eV 318.99 nm f=0.0468

<S**2>=0.000

335 -> 345	0.36006
336 -> 347	0.34238
337 -> 346	-0.23151
338 -> 345	0.43195

Compound 3.13-PH_3:

Excited State 2: Singlet-A

2.6749 eV 463.50 nm f=0.0234

<S**2>=0.000

327 -> 329	-0.23465
327 -> 331	-0.36705
328 -> 329	0.53108
328 -> 331	-0.16199

Excited State 3: Singlet-A

2.6772 eV 463.11 nm f=0.0360

<S**2>=0.000

327 -> 330	0.53190
327 -> 332	0.16065
328 -> 330	0.23547
328 -> 332	-0.36546

Excited State 6: Singlet-A

2.8118 eV 440.95 nm f=0.0009

<S**2>=0.000

327 -> 329	-0.19322
327 -> 331	0.54997
328 -> 329	0.35267
328 -> 331	0.18857

Excited State 7: Singlet-A

2.8136 eV 440.65 nm f=0.0010

<S**2>=0.000

327 -> 330	0.34861
327 -> 332	-0.18237
328 -> 330	0.19643
328 -> 332	0.55344

Excited State 9: Singlet-A

3.1163 eV 397.86 nm f=0.0001

<S**2>=0.000

327 -> 333 -0.24128

327 -> 334 0.45900

328 -> 333 0.42196

328 -> 334 0.16072

Excited State 10: Singlet-A

3.1165 eV 397.83 nm f=0.0096

<S**2>=0.000

327 -> 333 0.42588

327 -> 334 -0.14998

328 -> 333 0.22953

328 -> 334 0.46502

Excited State 11: Singlet-A

3.1280 eV 396.37 nm f=0.0001

<S**2>=0.000

327 -> 335 -0.32826

327 -> 336 0.48260

328 -> 335 0.35785

Excited State 13: Singlet-A

3.2117 eV 386.04 nm f=0.0250

<S**2>=0.000

325 -> 329 -0.12374

325 -> 331 -0.39096

326 -> 329 0.56086

Excited State 14: Singlet-A

3.2123 eV 385.97 nm f=0.0003

<S**2>=0.000

325 -> 330 -0.12177

325 -> 332 -0.38357

326 -> 330 0.55420

Excited State 16: Singlet-A

3.2145 eV 385.70 nm f=0.0016

<S**2>=0.000

325 -> 330 0.56422

326 -> 330 0.12400

326 -> 332 -0.39626

Excited State 18: Singlet-A

3.2776 eV 378.27 nm f=0.5194

<S**2>=0.000

323 -> 330 -0.48863

324 -> 329 0.49344

Excited State 20: Singlet-A

3.3552 eV 369.53 nm f=0.0042

<S**2>=0.000

325 -> 329 -0.10841

325 -> 331 0.56778

326 -> 329 0.39304

Excited State 21: Singlet-A

3.3567 eV 369.37 nm f=0.0002

<S**2>=0.000

325 -> 330 0.39046

326 -> 330 0.11222

326 -> 332 0.57013

Excited State 23: Singlet-A

3.3888 eV 365.86 nm f=0.0039

<S**2>=0.000

327 -> 341 -0.23149

327 -> 342 0.11268

328 -> 339 -0.11892

328 -> 341 -0.44012

328 -> 342 0.45188

Excited State 24: Singlet-A

3.3889 eV 365.85 nm f=0.0024

<S**2>=0.000

327 -> 339 -0.11880

327 -> 341 0.41901

327 -> 342 0.47144

328 -> 341 -0.22602

328 -> 342 -0.12327

Excited State 25: Singlet-A

3.4330 eV 361.16 nm f=0.0192

<S**2>=0.000

323 -> 331 0.49622

324 -> 332 -0.49527

Excited State 26: Singlet-A

3.4345 eV 361.00 nm f=0.0010

<S**2>=0.000

327 -> 343 0.20569

327 -> 344 0.13577

328 -> 338 0.10116

328 -> 340 0.10902

328 -> 343 0.44824

328 -> 344 0.43716

Excited State 27: Singlet-A

3.4346 eV 360.99 nm f=0.0014

<S**2>=0.000

327 -> 338 -0.10117

327 -> 340 0.10966

327 -> 343 -0.41514

327 -> 344 0.46871

328 -> 343 0.20691

328 -> 344 -0.13893

Excited State 32: Singlet-A

3.5119 eV 353.04 nm f=0.0003

<S**2>=0.000

327 -> 338 -0.18905

327 -> 340 0.31735

328 -> 335 0.14339

328 -> 338 0.53552

328 -> 340 0.17013

Excited State 39: Singlet-A

3.6658 eV 338.22 nm f=0.0002

<S**2>=0.000

325 -> 335 0.46788

325 -> 336 -0.32709

326 -> 335 -0.14851

326 -> 336 0.36254

Excited State 40: Singlet-A

3.6658 eV 338.22 nm f=0.0007

<S**2>=0.000

325 -> 335 0.14177

325 -> 336 0.36515

326 -> 335 0.46184

326 -> 336 0.33564

4.04–$(PCH_3)_3$

Excited State 1: Singlet-A

2.7481 eV 451.16 nm f=0.9253

<S**2>=0.000

219 -> 220 0.67603

Excited State 2: Singlet-A

2.9883 eV 414.90 nm f=0.0135

<S**2>=0.000

217 -> 221 0.23674

218 -> 220 0.64502

219 -> 221 0.15097

Excited State 3: Singlet-A

3.0011 eV 413.12 nm f=0.0036

<S**2>=0.000

217 -> 220 0.62136

218 -> 221 0.29254

219 -> 220 0.15182

Excited State 4: Singlet-A

3.1521 eV 393.33 nm f=0.0109

<S**2>=0.000

214 -> 220 0.12170

217 -> 221 -0.13932

218 -> 220 -0.11046

219 -> 221 0.67088

Excited State 5: Singlet-A

3.2790 eV 378.12 nm f=0.0880

<S**2>=0.000

217 -> 220 -0.27291

218 -> 221 0.63670

219 -> 220 -0.12451

Excited State 6: Singlet-A

3.3045 eV 375.20 nm f=0.0003

<S**2>=0.000

217 -> 221 0.64661

218 -> 220 -0.26173

219 -> 221 0.10076

Excited State 7: Singlet-A

3.4198 eV 362.55 nm f=0.0001

<S**2>=0.000

216 -> 220 0.65838

216 -> 221 0.25626

Excited State 8: Singlet-A

3.4228 eV 362.23 nm f=0.0001

<S**2>=0.000

215 -> 220 0.65772

215 -> 221 -0.25796

Excited State 9: Singlet-A

3.4994 eV 354.30 nm f=0.0002

<S**2>=0.000

212 -> 220 0.58435

212 -> 221 0.39113

Excited State 10: Singlet-A

3.5004 eV 354.21 nm f=0.0002

<S**2>=0.000

213 -> 220 0.58248

213 -> 221 -0.39393

Excited State 11: Singlet-A

3.6189 eV 342.61 nm f=1.2000

<S**2>=0.000

214 -> 221 0.69684

Excited State 12: Singlet-A

3.6946 eV 335.58 nm f=0.2349

<S**2>=0.000

214 -> 220 0.68610

219 -> 221 -0.11412

Excited State 19: Singlet-A

4.0500 eV 306.13 nm f=0.0005

<S**2>=0.000

218 -> 222 0.17112

219 -> 222 0.65507

Excited State 20: Singlet-A

4.0507 eV 306.08 nm f=0.0013

<S**2>=0.000

218 -> 223 -0.17746

219 -> 223 0.65388

Excited State 23: Singlet-A

4.2731 eV 290.15 nm f=0.0845

<S**2>=0.000

208 -> 221 0.26791

209 -> 220 0.63822

219 -> 224 -0.10748

Excited State 24: Singlet-A

4.3374 eV 285.85 nm f=0.0022

<S**2>=0.000

208 -> 220 0.57234

209 -> 221 0.39347

Excited State 25: Singlet-A

4.3940 eV 282.17 nm f=0.0052

<S**2>=0.000

217 -> 226 -0.10001

217 -> 227 0.34964

218 -> 225 -0.12363

218 -> 226 -0.12983

218 -> 227 0.45541

219 -> 227 0.28036

Excited State 26: Singlet-A

4.3997 eV 281.80 nm f=0.0057

<S**2>=0.000

217 -> 228	-0.38856
218 -> 228	0.47215
219 -> 228	-0.29419

Excited State 27: Singlet-A

4.4046 eV 281.49 nm f=0.0004

<S**2>=0.000

206 -> 220	0.35738
206 -> 221	0.29532
207 -> 220	0.45339
207 -> 221	-0.25056

Excited State 28: Singlet-A

4.4052 eV 281.45 nm f=0.0005

<S**2>=0.000

206 -> 220	0.45364
206 -> 221	0.24718
207 -> 220	-0.35565
207 -> 221	0.29682

Excited State 29: Singlet-A

4.4255 eV 280.16 nm f=0.0001

<S**2>=0.000

217 -> 225	-0.29376
217 -> 226	0.26788
218 -> 225	0.34494
218 -> 226	-0.33598
219 -> 225	-0.22577
219 -> 226	0.20357

Excited State 30: Singlet-A

4.4280 eV 280.00 nm f=0.0006

<S**2>=0.000

217 -> 225	0.24154
217 -> 226	0.26346
217 -> 227	0.13563
218 -> 225	0.32786
218 -> 226	0.32848
218 -> 227	0.17665
219 -> 225	0.19664
219 -> 226	0.21196
219 -> 227	0.10895

4.05–$P(CH_3)_3$

Excited State 1: Singlet-A
2.8901 eV 428.99 nm f=0.6572
<S**2>=0.000
171 ->172 0.70180
Excited State 2: Singlet-A
3.1994 eV 387.53 nm f=0.0103
<S**2>=0.000
171 ->173 0.68910
171 ->175 -0.12791
Excited State 3: Singlet-A
3.3878 eV 365.97 nm f=0.0627
<S**2>=0.000
171 ->174 0.69594
Excited State 4: Singlet-A
3.5171 eV 352.52 nm f=0.0056
<S**2>=0.000
168 ->172 0.17592
171 ->173 0.11402
171 ->175 0.66520
Excited State 5: Singlet-A
3.6150 eV 342.97 nm f=0.0483
<S**2>=0.000
168 ->173 0.18121
169 ->172 0.62900
170 ->173 0.25877
Excited State 6: Singlet-A
3.6170 eV 342.78 nm f=0.0052
<S**2>=0.000
168 ->172 0.21862
169 ->173 0.30645
170 ->172 0.59471
Excited State 7: Singlet-A
3.7310 eV 332.31 nm f=0.7409
<S**2>=0.000
168 ->173 0.63712
170 ->173 -0.26565
Excited State 8: Singlet-A
3.7762 eV 328.33 nm f=0.1222
<S**2>=0.000
168 ->172 0.59882
168 ->174 0.13829
170 ->172 -0.26374
171 ->175 -0.18090

Excited State 9: Singlet-A

3.8432 eV 322.61 nm f=0.0071

<S**2>=0.000

168 ->177 0.10102

169 ->176 0.39745

169 ->177 0.25817

170 ->176 0.24323

170 ->177 0.39492

171 ->176 0.14333

Excited State 10: Singlet-A

3.8432 eV 322.61 nm f=0.0028

<S**2>=0.000

168 ->176 0.10177

169 ->176 -0.26014

169 ->177 0.39934

170 ->176 0.39413

170 ->177 -0.24036

171 ->177 0.13887

Excited State 13: Singlet-A

3.8790 eV 319.63 nm f=0.0162

<S**2>=0.000

168 ->173 0.19204

169 ->172 -0.30095

169 ->174 0.18325

170 ->173 0.56787

170 ->175 -0.10593

Excited State 14: Singlet-A

3.8805 eV 319.51 nm f=0.0083

<S**2>=0.000

168 ->172 -0.15896

169 ->173 0.59573

169 ->175 -0.10047

170 ->172 -0.25850

170 ->174 0.18774

Excited State 15: Singlet-A

3.8868 eV 318.99 nm f=0.0010

<S**2>=0.000

168 ->177 -0.11389

169 ->176 -0.12630

171 ->176 0.67621

Excited State 16: Singlet-A

3.8881 eV 318.88 nm f=0.0001

<S**2>=0.000

168 ->176 -0.11339

169 ->177 -0.12196

171 ->177 0.67915

Excited State 17: Singlet-A

4.0296 eV 307.68 nm f=0.0011

<S**2>=0.000

168 ->172 0.11998

168 ->174 -0.25987

169 ->173 -0.16841

169 ->175 -0.31423

170 ->174 0.52798

Excited State 18: Singlet-A

4.0314 eV 307.54 nm f=0.1555

<S**2>=0.000

168 ->173 0.10056

168 ->175 -0.25125

169 ->174 -0.41993

170 ->173 0.15134

170 ->175 0.45611

Excited State 19: Singlet-A

4.0351 eV 307.26 nm f=0.0001

<S**2>=0.000

171 ->178 0.69934

Excited State 20: Singlet-A

4.0355 eV 307.23 nm f=0.0020

<S**2>=0.000

171 ->179 0.69602

Excited State 21: Singlet-A

4.0766 eV 304.14 nm f=0.0104

<S**2>=0.000

168 ->172 -0.10039

168 ->174 0.60914

169 ->173 -0.10882

169 ->175 -0.26878

170 ->174 0.14074

Excited State 22: Singlet-A

4.0815 eV 303.77 nm f=0.1782

<S**2>=0.000

168 ->175 0.60659

169 ->174 -0.32745

170 ->173 0.10300

Excited State 23: Singlet-A

4.1058 eV 301.97 nm f=0.0001

<S**2>=0.000

166 ->172 -0.18578

166 ->173 0.29383

167 ->172 -0.21286

167 ->173 0.55271

167 ->174 0.11268

Excited State 24: Singlet-A

4.1058 eV 301.97 nm f=0.0001

<S**2>=0.000

166 ->172 0.21291

166 ->173 0.55276

166 ->174 -0.11273

167 ->172 -0.18568

167 ->173 -0.29377

Excited State 29: Singlet-A

4.2955 eV 288.64 nm f=0.0001

<S**2>=0.000

166 ->173 -0.12262

166 ->174 0.18066

166 ->175 -0.31041

167 ->173 -0.10258

167 ->174 0.52425

167 ->175 -0.25983

Excited State 30: Singlet-A

4.2955 eV 288.64 nm f=0.0002

<S**2>=0.000

166 ->173 0.10260

166 ->174 0.52424

166 ->175 0.25971

167 ->173 -0.12257

167 ->174 -0.18075

167 ->175 -0.31043

4.13–$P(CH_3)_3$

Excited State 1: Singlet-A

2.9257 eV 423.77 nm f=0.7154

<S**2>=0.000

219 -> 220 0.70046

Excited State 2: Singlet-A

3.2614 eV 380.16 nm f=0.0019

<S**2>=0.000

217 -> 220 0.16374

217 -> 221 -0.15127

218 -> 220 -0.30193

219 -> 221 0.57790

219 -> 223 -0.10490

Excited State 3: Singlet-A

3.2767 eV 378.38 nm f=0.0093

<S**2>=0.000

217 -> 220 0.55608

217 -> 221 -0.14269

218 -> 220 0.31232

218 -> 221 0.25736

Excited State 4: Singlet-A

3.2835 eV 377.60 nm f=0.0109

<S**2>=0.000

217 -> 220 -0.26714

217 -> 221 0.21033

218 -> 220 0.46789

218 -> 221 0.11540

219 -> 221 0.37737

Excited State 5: Singlet-A

3.4640 eV 357.92 nm f=0.0592

<S**2>=0.000

219 -> 222 0.69381

Excited State 6: Singlet-A

3.5555 eV 348.71 nm f=0.0034

<S**2>=0.000

217 -> 221 0.30496

218 -> 220 -0.29390

218 -> 221 0.52238

218 -> 222 -0.18633

Excited State 7: Singlet-A

3.5568 eV 348.58 nm f=0.0073

<S**2>=0.000

217 -> 220 0.29300

217 -> 221 0.52275

217 -> 222 0.18615

218 -> 221 -0.30448

Excited State 8: Singlet-A

3.5761 eV 346.71 nm f=0.0079

<S**2>=0.000

214 -> 220 0.13728

216 -> 220 -0.10164

219 -> 221 0.10443

219 -> 223 0.66510

Excited State 9: Singlet-A

3.7109 eV 334.11 nm f=0.0015

<S**2>=0.000

214 -> 220 0.27740

215 -> 220 0.29303

215 -> 221 0.21658

216 -> 220 0.51512

216 -> 221 0.14180

Excited State 10: Singlet-A

3.7111 eV 334.09 nm f=0.0041

<S**2>=0.000

214 -> 220 -0.17864

215 -> 220 0.58251

215 -> 221 -0.14782

216 -> 220 -0.23698

216 -> 221 0.19812

Excited State 11: Singlet-A

3.7206 eV 333.23 nm f=0.0904

<S**2>=0.000

214 -> 221 -0.11366

217 -> 222 0.37830

217 -> 223 -0.11954

218 -> 221 0.19790

218 -> 222 0.34047

218 -> 223 0.39782

Excited State 12: Singlet-A

3.7239 eV 332.94 nm f=0.0059

<S**2>=0.000

217 -> 221 0.19547

217 -> 222 -0.34182

217 -> 223 0.40394

218 -> 222 0.39022

218 -> 223 0.12266

Excited State 13: Singlet-A

3.7741 eV 328.51 nm f=0.7456

<S**2>=0.000

214 -> 221 0.56225

216 -> 221 -0.37104

Excited State 14: Singlet-A

3.7887 eV 327.25 nm f=0.0012

<S**2>=0.000

213 -> 220 0.55020

213 -> 221 0.41063

213 -> 222 -0.13186

Excited State 15: Singlet-A

3.7893 eV 327.20 nm f=0.0020

<S**2>=0.000

212 -> 220 0.55133

212 -> 221 -0.40924

212 -> 222 -0.13080

Excited State 16: Singlet-A

3.8108 eV 325.35 nm f=0.1164

<S**2>=0.000

214 -> 220 0.56967

216 -> 220 -0.32982

219 -> 223 -0.17552

Excited State 17: Singlet-A

3.9718 eV 312.16 nm f=0.0003

<S**2>=0.000

214 -> 220 -0.10817

214 -> 221 0.22768

215 -> 220 -0.15959

215 -> 221 0.45526

216 -> 220 -0.17936

216 -> 221 0.38151

216 -> 222 -0.10269

Excited State 18: Singlet-A

3.9728 eV 312.08 nm f=0.0003

<S**2>=0.000

214 -> 220 -0.10090

214 -> 221 -0.28485

215 -> 220 0.20778

215 -> 221 0.44231

215 -> 222 0.11385

216 -> 220 -0.12456

216 -> 221 -0.35811

Excited State 19: Singlet-A

4.0008 eV 309.90 nm f=0.0038

<S**2>=0.000

217 -> 222 -0.31083

217 -> 223 -0.12559

218 -> 222 -0.30787

218 -> 223 0.53553

Excited State 20: Singlet-A

4.0020 eV 309.80 nm f=0.0003

<S**2>=0.000

217 -> 222 0.30927

217 -> 223 0.53842

218 -> 222 -0.30689

218 -> 223 0.13102

Excited State 21: Singlet-A

4.1084 eV 301.78 nm f=0.0048

<S**2>=0.000

214 -> 220 0.10541

214 -> 222 0.53674

216 -> 222 -0.40646

Excited State 22: Singlet-A

4.1191 eV 301.00 nm f=0.2222

<S**2>=0.000

213 -> 220 -0.11898

213 -> 222 -0.16934

213 -> 223 -0.14118

214 -> 223 0.49724

216 -> 223 -0.36983

Excited State 23: Singlet-A

4.1205 eV 300.90 nm f=0.0354

<S**2>=0.000

213 -> 220 0.29136

213 -> 221 -0.21751

213 -> 222 0.41375

213 -> 223 0.35009

214 -> 223 0.19789

216 -> 223 -0.14648

Excited State 24: Singlet-A

4.1222 eV 300.77 nm f=0.0106

<S**2>=0.000

212 -> 220 0.30787

212 -> 221 0.23189

212 -> 222 0.43655

212 -> 223 -0.37192

214 -> 223 0.10816

Excited State 25: Singlet-A

4.1685 eV 297.43 nm f=0.0014

<S**2>=0.000

214 -> 222 0.22912

214 -> 223 0.19330

215 -> 222 0.37893

215 -> 223 0.26635

216 -> 221 0.10206

216 -> 222 0.32522

216 -> 223 0.25295

Excited State 26: Singlet-A

4.1697 eV 297.35 nm f=0.0011

<S**2>=0.000

214 -> 222 -0.26015

214 -> 223 0.19297

215 -> 221 -0.11727

215 -> 222 0.39364

215 -> 223 -0.31704

216 -> 222 -0.27838

216 -> 223 0.19015

Excited State 27: Singlet-A

4.3071 eV 287.86 nm f=0.0001

<S**2>=0.000

211 -> 220 0.46844

211 -> 221 0.35820

211 -> 222 -0.13484

213 -> 220 0.15313

213 -> 221 -0.25282

213 -> 222 -0.11803

213 -> 223 -0.13284

Excited State 28: Singlet-A

4.3078 eV 287.81 nm f=0.0002

<S**2>=0.000

210 -> 220 0.50566

210 -> 221 -0.38887

210 -> 222 -0.14361

212 -> 220 -0.10396

212 -> 221 -0.16929

4.14–$P(CH_3)_3$

Excited State 1: Singlet-A

2.7225 eV 455.40 nm f=0.9315

<S**2>=0.000

241 -> 242 0.70337

Excited State 2: Singlet-A

3.1199 eV 397.40 nm f=0.0117

<S**2>=0.000

238 -> 242 -0.11379

241 -> 243 0.69119

Excited State 3: Singlet-A

3.3950 eV 365.20 nm f=0.0344

<S**2>=0.000

238 -> 242 0.15114

239 -> 243 -0.28100

240 -> 242 0.62734

Excited State 4: Singlet-A

3.3979 eV 364.88 nm f=0.2062

<S**2>=0.000

239 -> 242 0.60150

240 -> 243 -0.36755

Excited State 5: Singlet-A

3.5550 eV 348.76 nm f=1.0690

<S**2>=0.000

238 -> 243 0.48347

239 -> 242 -0.27517

240 -> 243 -0.42757

Excited State 6: Singlet-A

3.6411 eV 340.51 nm f=0.0001

<S**2>=0.000

232 -> 242 -0.11072

232 -> 243 -0.16580

233 -> 242 0.56468

233 -> 243 0.35825

Excited State 7: Singlet-A

3.6412 eV 340.51 nm f=0.0002

<S**2>=0.000

232 -> 242 0.56467

232 -> 243 -0.35825

233 -> 242 0.11072

233 -> 243 -0.16580

Excited State 8: Singlet-A

3.6718 eV 337.67 nm f=0.1643

<S**2>=0.000

238 -> 242 0.53476

239 -> 243 -0.34278

240 -> 242 -0.27260

241 -> 243 0.11142

Excited State 9: Singlet-A

3.7189 eV 333.39 nm f=0.0546

<S**2>=0.000

238 -> 242 0.41030

239 -> 243 0.54900

240 -> 242 0.15429

Excited State 10: Singlet-A

3.7344 eV 332.00 nm f=0.1320

<S**2>=0.000

238 -> 243 0.50629

239 -> 242 0.24753

240 -> 243 0.42288

Excited State 14: Singlet-A

3.8102 eV 325.40 nm f=0.0003

<S**2>=0.000

234 -> 242 0.52635

235 -> 242 -0.38855

235 -> 243 0.25650

Excited State 18: Singlet-A

4.0268 eV 307.90 nm f=0.0018

<S**2>=0.000

241 -> 245 0.68809

Excited State 19: Singlet-A

4.0832 eV 303.65 nm f=0.0001

<S**2>=0.000

234 -> 242 -0.10858

234 -> 243 -0.18538

235 -> 242 0.24269

235 -> 243 0.62691

Excited State 27: Singlet-A

4.1925 eV 295.73 nm f=0.0001

<S**2>=0.000

230 -> 242 0.26962

230 -> 243 0.14223

230 -> 246 0.38724

230 -> 247 0.39215

231 -> 242 0.10157

231 -> 246 0.14571

231 -> 247 -0.13113

233 -> 246 0.10067

233 -> 247 0.12680

4.15–$P(CH_3)_3$

Excited State 1: Singlet-A

2.7803 eV 445.94 nm f=0.8717

<S**2>=0.000

219 -> 220 0.70299

Excited State 2: Singlet-A

3.1947 eV 388.10 nm f=0.0111

<S**2>=0.000

216 -> 220 -0.13249

219 -> 221 0.69149

Excited State 3: Singlet-A

3.2247 eV 384.48 nm f=0.0054

<S**2>=0.000

217 -> 220 0.28534

217 -> 221 -0.16612

218 -> 220 0.58406

218 -> 221 -0.21839

Excited State 4: Singlet-A

3.2308 eV 383.76 nm f=0.0066

<S**2>=0.000

217 -> 220 0.57858

217 -> 221 0.22666

218 -> 220 -0.28395

218 -> 221 -0.17633

Excited State 5: Singlet-A

3.5279 eV 351.44 nm f=0.1153

<S**2>=0.000

216 -> 221 -0.13535

217 -> 220 0.28288

217 -> 221 -0.28723

218 -> 221 0.56345

Excited State 6: Singlet-A

3.5371 eV 350.52 nm f=0.0069

<S**2>=0.000

217 -> 221 0.57934

218 -> 220 0.27723

218 -> 221 0.29209

Excited State 7: Singlet-A

3.5664 eV 347.65 nm f=0.0005

<S**2>=0.000

213 -> 220 0.59865

213 -> 221 -0.36861

Excited State 8: Singlet-A

3.5740 eV 346.91 nm f=0.0005

<S**2>=0.000

212 -> 220 0.58805

212 -> 221 0.38528

Excited State 9: Singlet-A

3.6276 eV 341.78 nm f=0.0085

<S**2>=0.000

215 -> 220 0.66150

215 -> 221 -0.24101

Excited State 10: Singlet-A

3.6285 eV 341.69 nm f=1.1662

<S**2>=0.000

216 -> 221 0.67927

218 -> 221 0.12736

Excited State 11: Singlet-A

3.6339 eV 341.19 nm f=0.0004

<S**2>=0.000

214 -> 220 0.66002

214 -> 221 0.25200

Excited State 12: Singlet-A

3.6999 eV 335.10 nm f=0.2480

<S**2>=0.000

216 -> 220 0.68194

219 -> 221 0.12945

Excited State 13: Singlet-A

3.8245 eV 324.18 nm f=0.0072

<S**2>=0.000

211 -> 224 0.10313

217 -> 224 0.55482

218 -> 224 -0.35546

219 -> 224 0.11789

Excited State 14: Singlet-A

3.8249 eV 324.15 nm f=0.0114

<S**2>=0.000

211 -> 225 0.10596

217 -> 225 0.33922

218 -> 225 0.56410

219 -> 225 0.11980

Excited State 19: Singlet-A

4.0896 eV 303.17 nm f=0.0001

<S**2>=0.000

216 -> 222 0.10845

219 -> 222 0.59493

219 -> 223 -0.34174

Excited State 20: Singlet-A

4.0899 eV 303.14 nm f=0.0015

<S**2>=0.000

216 -> 223 -0.10940

219 -> 222 0.34220

219 -> 223 0.59418

Excited State 21: Singlet-A

4.0983 eV 302.52 nm f=0.0247

<S**2>=0.000

207 -> 225 0.17716

213 -> 225 0.67622

Excited State 22: Singlet-A

4.1006 eV 302.36 nm f=0.0212

<S**2>=0.000

206 -> 224 0.18003

212 -> 224 0.67663

Excited State 23: Singlet-A

4.2198 eV 293.82 nm f=0.0550

<S**2>=0.000

210 -> 221 0.27667

211 -> 220 0.63740

Excited State 24: Singlet-A

4.2718 eV 290.24 nm f=0.0013

<S**2>=0.000

210 -> 220 0.58678

211 -> 221 0.37555

Excited State 25: Singlet-A

4.3236 eV 286.76 nm f=0.0071

<S**2>=0.000

218 -> 225 -0.10457

219 -> 225 0.68258

Excited State 26: Singlet-A

4.3243 eV 286.71 nm f=0.0056

<S**2>=0.000

217 -> 224 -0.12521

219 -> 224 0.68359

Excited State 29: Singlet-A

4.4060 eV 281.40 nm f=0.0006

<S**2>=0.000

202 -> 220 -0.18241

209 -> 220 0.14757

215 -> 225 0.63387